TRANSITION METAL-BASED NANOCOMPOSITE FOR THE ELECTROCHEMICAL DETECTION OF PHARMACEUTICAL DRUGS

SHAMIMA AKHTER

FACULTY OF SCIENCE
UNIVERSITI MALAYA
KUALA LUMPUR

2022

TRANSITION METAL-BASED NANOCOMPOSITE FOR THE ELECTROCHEMICAL DETECTION OF PHARMACEUTICAL DRUGS

SHAMIMA AKHTER

THESIS SUBMITTED IN FULFILMENT OF THE REQUIREMENTS FOR THE DEGREE OF DOCTOR OF PHILOSOPHY

DEPARTMENT OF CHEMISTRY
FACULTY OF SCIENCE
UNIVERSITI MALAYA
KUALA LUMPUR

2022

UNIVERSITI MALAYA

ORIGINAL LITERARY WORK DECLARATION

Name of Candidate: **SHAMIMA AKHTER**

Matric No: **SHC160026/17042846**

Name of Degree: **DOCTOR OF PHILOSOPHY**

Title of Thesis:

TRANSITION METAL-BASED NANOCOMPOSITE FOR THE ELECTROCHEMICAL DETECTCTION OF PHARMACEUTICAL DRUGS

Field of Study:

NANOTECHNOLOGY

I do solemnly and sincerely declare that:

(1) I am the sole author/writer of this Work;
(2) This Work is original;
(3) Any use of any work in which copyright exists was done by way of fair dealing and for permitted purposes and any excerpt or extract from, or reference to or reproduction of any copyright work has been disclosed expressly and sufficiently and the title of the Work and its authorship have been acknowledged in this Work;
(4) I do not have any actual knowledge nor do I ought reasonably to know that the making of this work constitutes an infringement of any copyright work;
(5) I hereby assign all and every rights in the copyright to this Work to the University of Malaya ("UM"), who henceforth shall be owner of the copyright in this Work and that any reproduction or use in any form or by any means whatsoever is prohibited without the written consent of UM having been first had and obtained;
(6) I am fully aware that if in the course of making this Work I have infringed any copyright whether intentionally or otherwise, I may be subject to legal action or any other action as may be determined by UM.

Candidate's Signature Date: 02.03.2022

Subscribed and solemnly declared before,

Witness's Signature Date: 02.03.2022

Name:

Designation:

TRANSITION METAL-BASED NANOCOMPOSITE FOR THE ELECTROCHEMICAL DETECTION OF PHARMACEUTICAL DRUGS

ABSTRACT

The transition metals have gathered attention in the field of nanoscience and nanotechnology due to their extra-ordinary properties such as excellent catalytic properties, facile synthetic approaches and formation of stable complexes, high charge ratio, diverse morphologies, high electrical conductivity, versatile applications and others. In recent years, efforts have been focused on the preparation of nanocomposites by the incorporation of different types of transition metals compounds containing copper, cobalt and nickel in applications such as electrochemical sensing of target analytes. For effective electrochemical detection of the desired analyte, a nanocomposite of functionalized multiwall carbon nanotube (*f*-MWCNTs), chitosan (CTS) and cobalt (Co) was prepared. The excellent electrochemical conductivity of *f*-MWCNTs, high catalytic activity of Co and the synergy of the CTS-Co complex confirms that the *f*-MWCNTs/CTS-Co modified GCE sensor is a potential candidate for the electrochemical determination of paracetamol (PR) in pharmaceutical preparations and human serum. While a hybrid nanocomposite of functionalized multiwall carbon nanotubes MWCNTS$_f$, nitrogen-doped graphene (NGr) and chitosan (CTS) with electrodeposited copper (Cu) metal was prepared for the sensitive determination of an anticancer drug nilutamide (NLM). The presence of MWCNTS$_f$ reduces the agglomeration of the NGr nanosheets which exposes the anchoring site of the NGr. This enables the formation of 3D network of nanocarbons which facilitates electron transfer and electrical conductivity. The CTS facilitates the dispersion of MWCNTS$_f$ and NGr. The presence of transition metal copper (Cu), enhances the electrocatalytic effect of the nanocomposite and proves that the (MWCNTs$_f$–NGr/CTS)-Cu fabricated sensor

possesses great potential for the sensitive determination of NLM in biological sample and pharmaceutical preparations. A tri-metallic metal organic framework Co-Ni-Cu-MOF was synthesized on nickel foam (NF) substrate. Due to the synergy of the catalytic effect of the Co-Ni-Cu tri-metals, high porosity, extended active surface area and enhanced interfacial electron transfer, the Co-Ni-Cu-MOF/NF sensor possesses a strong electrocatalytic effect for the electrochemical determination of anticancer drug nilutamide (NLM) in pharmaceutical preparations and human blood serum. A nanocomposite was synthesized from a combination of nanocellulose (NC), three dimensional polypyrrole (3DPPY) decorated with bimetallic nanoparticles of silver (Ag) and gold (Au) nanoparticles. The addition of NC-3DPPY offers a mechanically robust structure with high porosity and distinct electro-conductivity. In addition, the conjugation of Ag-Au bimetallic nanoparticles provides excellent electro-conductivity and electrocatalytic effect which ultimately accelerate the interfacial electron transfer process. Due to the synergy of the electro-conductivity and electro-catalytic effect, the NC-3DPPY@Ag-Au/GCE sensor showed excellent electrochemical response toward the simultaneous electrochemical determination of anticancer drug methotrexate (MTX) and antibiotic ciprofloxacin (CIF) in biological fluids, commercial dosage forms and water samples. It should be worth mentioning that the synthesized transition metal-based nanocomposite has been fabricated and employed for the first time for the electrochemical detection of pharmaceutical drugs in commercial dosage forms and biological fluids.

Keywords: Transition metals, electrochemical sensor, paracetamol, nilutamide, methotrexate, ciprofloxacin.

KOMPOSIT NANO YANG BERASASKAN KEPADA LOGAM PERALIHAN UNTUK PENDERIA ELEKTROKIMIA UBAT UBATAN FARMASEUTIKAL

ABSTRAK

Logam peralihan telah menarik perhatian di dalam bidang sains nano dan teknologi nano disebabkan oleh sifat luar biasa mereka seperti sifat pemangkin yang sangat baik, kaedah sintesis yang mudah, dan pembentukan kompleks yang stabil, nisbah cas tinggi, kepelbagaian morfologi, kekonduksian elektrik yang tinggi, aplikasi serba boleh dan lain-lain. Banyak usaha telah dilakukan untuk penyediaan nanokomposit dengan menggabungkan pelbagai jenis logam peralihan seperti tembaga, kobalt dan nikel, di dalam aplikasi penderiaan elektrokimia yang sensitif terhadap analit sasaran. Untuk penderiaan analit sasaran tersebut dengan kaedah elektrokimia, suatu bahan komposit nano yang terdiri daripada tiub nano karbon multi dinding berfungsi (*f*-MWCNTs), kitosan (CTS) dan kobalt (Co) disediakan. Bahan komposit nano tersebut mempunyai kekonduksian elektrokimia *f*-MWCNT yang sangat baik, aktiviti pemangkinan Co yang tinggi dan sinergi aktiviti pemangkinan kompleks CTS-Co yang tinggi. Ini menjadikan bahan penderiaan *f*-MWCNTs/CTS-Co yang diubah-suaikan ke atas elektrod gelas karbon (GCE) suatu bahan elektrod yang berpotensi tinggi untuk penentuaan parasetamol (PR) dalam persediaan farmaseutikal dan serum manusia. Sementara bahan komposit-nano hibrid yang terdiri daripada tiub nano karbon multi dinding yang berfungsi (MWCNTS$_f$), graphene didopkan nitrogen (NGr) dan kitosan (CTS) dengan tembaga ter-elektrosadur (Cu), disediakan untuk penentuan sensitif sejenis ubat anti-kanser iaitu nilutamide (NLM). Kehadiran -MWCNTS$_f$ tersebut berupaya untuk mengurangkan pengagregatan NGr yang menyebabkan lebih banyak pendedahan laman penambat pada permukaan NGr dan memungkinkan rangkaian karbon nano 3D yang memudahkan pemindahan elektron dan meningkatkan kekonduksian elektrik. CTS berupaya untuk mempercepatkan penyebaran MWCNTS$_f$ dan NGr. Kehadiran tembaga (Cu) meningkatkan kesan elektro-pemangkinan komposit-nano dan ini membuktikan

bahawa bahan penderia (MWCNTs*f*–NGr/CTS)-Cu mempunyai potensi besar di dalam penentuan sensitif NLM dalam sampel biologi dan persediaan farmaseutikal. Sejenis bahan komposit-nano rangka logam organik tiga-logam iaitu Co-Ni-Cu-MOF disintesis pada logam nikel berbuih (NF). Disebabkan oleh sinergi kesan pemangkinan oleh tiga-logam Co-Ni-Cu, penampilan berliang dan luas permukaan aktif dan pemindahan elektron antara-fasa yang dipertingkatkan, bahan penderia Co-Ni-Cu-MOF/NF mempunyai kesan elektro-pemangkinan yang kuat untuk penentuan elektrokimia suatu ubat anti-kanser iaitu nilutamide (NLM) dalam persediaan farmaseutikal dan serum darah manusia. Satu bahan komposit-nano disintesiskan daripada gabungan nanoselulosa (NC), polipirol tiga dimensi (3DPPY) dan dihiasi dengan aloi nano dwi-logam emas (Au) dan nano-partikel perak (Ag). Penambahan NC-3DPPY telah memberikan suatu struktur mekanik yang kuat dengan keliangan tinggi dengan kekonduksian elektrik yang baik. Sebagai tambahan, konjugasi aloi dwi-logam Au-Ag memberikan kekonduksian elektrik dan kesan elektro-pemangkinan yang sangat baik yang akhirnya mempercepat pemindahan elektron antara-fasa. Oleh kerana terdapat sinergi di antara kesan elektro-kekonduksian dan kesan elektro-pemangkinan, alat penderia bahan NC-3DPPY@Ag-Au/GCE telah menunjukkan tindak balas elektrokimia yang sangat baik terhadap penentuan serentak ubat anti-kanser metotreksat (MTX) dan antibiotik ciprofloxacin (CIF) di dalam sampel cecair biologi, dos komersial dan sampel air. Perlu ditegaskan bahawa, bahan komposit-nano yang berasaskan kepada logam peralihan tersebut adalah pertama kalinya digunakan untuk pengesanan elektrokimia ubat farmasi dalam bentuk dos komersial dan cecair biologi.

Kata kunci: Logam peralihan, penderia elektrokimia, parasetamol, nilutamide, methotrexate, ciprofloxacin.

ACKNOWLEDGEMENTS

All praises be to Allah, for His uncountable blessings, the Allah who is the most Gracious and most Merciful, who gave me the patience and strength and granted me the capability to complete this work.

Firstly, I would like to express my deepest gratitude to my supervisors Professor Dr. Wan Jeffrey Basirun and Professor. Dr. Mohd Rafie Bin Johan for their valuable guidance, continuous support, motivation and encouragement during my PhD journey. Their valuable critical review helped me to enhance the quality of my research writing and immense knowledge.

Next, I would like to express my sincere gratitude to Dr. Samira Bagheri, who was my first supervisor and helped me to start my PhD journey. I would like to extend my gratitude to the research group members to D227 laboratory especially Md. Shalauddin, Nadzirah Sofia and Magaji Ladan for their constructive discussions and sharing of knowledge and helped me in my difficult time.

Finally, my sincere gratitude goes to my parents for their hard work, undemanding love, innumerable sacrifices and unconditional support throughout my life. I can complete my studies and fulfil my dream because of the sacrifices which they made for me to reach until this point. I feel honored and deeply indebted for the support, encouragement, sacrifices, patience and prayers of my loving husband Md. Shalauddin and adorable son Mohammad Zarrar Riyon Tashreef during my difficult times. Without their love and support over the years none of this would have been possible. They have always been there for me and I am gratified for everything they have helped me to achieve. None of this would have been possible without their continuous prayers and support.

TABLE OF CONTENTS

ABSTRACT iii

ABSTRAK v

ACKNOWLEDGEMENTS vivii

TABLE OF CONTENTS Viiviii

LIST OF FIGURES xvxv

LIST OF TABLES xix

LIST OF SYMBOLS AND ABBREVIATIONS XX

LIST OF APPENDICES xxiv

CHAPTER 1: INTRODUCTION 1

1.1 Background 1

1.2 Problem statements 7

1.3 Objectives of the study 7

1.4 Scope of the research 8

1.5 Thesis outline 9

CHAPTER 2: LITERATURE REVIEW 12

2.1 Background 12

2.2 Transition metals and their classification 12

2.3 Non- noble transition metals 13

2.4 Noble transition metals 14

2.5 Metal organic framework based on transition metals 15

2.6 Transition metal and biopolymer composite 17

2.6.1 Chitosan 17

2.6.2 Nanocellulose 18

2.7 Carbon-based nanomaterials……..19

2.7.1 Carbon nanotubes and their functionalization.....20

2.7.2 Nitrogen doped graphene 20

2.8 Nanomaterials and their synthesis approach.....21

2.8.1 Microwave-assisted method 23

2.8.2 Solvothermal synthesis method.....24

2.8.3 Sonochemical synthesis method.....24

2.9 The development of electrochemical devices using nanocomposites……25

2.10 Analyte of interest……..……..25

2.10.1 Paracetamol 26

2.10.2 Nilutamide.....27

2.10.3 Methotrexate.....28

2.10.4 Ciprofloxacin.....29

2.11 Sensor……...……..…….……..30

2.11.1 Chemical sensor 31

2.11.2 Chemically modified electrodes (CMEs). 34

2.12 Electroanalytical techniques…….…….……35

2.12.1 Cyclic voltammetry 37

2.12.2 Pulse voltammetry.....38

2.12.3 Differential pulse voltammetry…….. 38

2.12.4 Chronoamperometry.....39

2.13 Electrochemical impedance spectroscopy (EIS)…….……..40

2.14 The development of electrochemical sensor using nanocomposite materials.....41

2.14.1 Development of metal ions based nanocomposites ……41

CHAPTER 3: METHODOLOGY 46

3.1 Materials 46

3.2 Preparation of transition metal-based nanocomposite 47

3.2.1 Preparation of functionalized MWCNTs (MWCNTs$_f$) 47

3.2.2 Preparation of nitrogen doped graphene (NGr) 47

3.2.3 Synthesis of NC 48

3.2.4 Synthesis of 3DPPY 48

3.2.5 Synthesis of bimetallic Ag-Au nanoparticles 48

3.2.6 Activation of glassy carbon electrode (GCE) 49

3.3 Fabrication of modified sensor 49

3.3.1 Fabrication of (MWCNTs$_f$ –NGr/CTS)-Cu nanocomposite 49

3.3.2 Fabrication of *f*-MWCNTs/CTS-Co nanocomposite 50

3.3.3 Fabrication of Co-Ni-Cu-MOF/NF nanocomposite 51

3.3.4 Fabrication of NC-3DPPY@Ag-Au/GCE sensor 53

3.4 Instrumentations 54

3.4.1 X-ray diffraction (XRD) 54

3.4.2 Raman spectroscopy 55

3.4.3 Fourier transform infrared (FTIR) spectroscopy 55

3.4.4 X-ray photoelectron spectroscopy (XPS) 55

3.4.5 FESEM and EDX analysis 56

3.4.6 Transmission electron microscopy (TEM) 56

3.4.7 Brunauer-Emmett-Teller (BET) analysis 57

3.4.8 Electrochemical analysis 57

3.5 Characteristics of the electrochemical sensor 58

3.5.1 Linearity of calibration curve 58

3.5.2 Sensitivity 59

3.5.3 Limit of detection 59

3.5.4 Stability 59

3.5.5 Reproducibility 60

3.5.6 Selectivity 60

3.5.7 Real sample analysis 60

3.5.8 Standard addition method 61

CHAPTER 4: FUNCTIONALIZED MULTIWALL CARBON NANOTUBE, NITROGEN-DOPED GRAPHENE AND CHITOSAN WITH COPPER FOR NILUTAMIDE DETECTION……....63

4.1 (MWCNTs$_f$–NGr/CTS)-Cu nanocomposite for nilutamide detection……..63

4.2 Aim of the research……..63

4.3 Electrode characterizations……..64

4.3.1 FT-IR spectroscopy analysis 64

4.3.2 Raman spectroscopy analysis 65

4.3.3 Electron microscopy analysis 67

4.4 Electrode characterizations……..69

4.4.1 Electrochemical impedance spectroscopy (EIS) analysis 69

4.4.2 CV of NLM on (MWCNTs$_f$ -NGr/CTS)-Cu/GCE sensor 70

4.5 Optimization of the fabricated sensor ……..72

4.5.1 Scan rate study on (MWCNTs$_f$-NGr/CTS)-Cu sensor 72

4.5.2 CV at different pH 73

4.6 Performance evaluation of the (MWCNTs$_f$ -NGr/CTS)-Cu/GCE sensor ……...75

4.6.1 Analytical performance of (MWCNTs$_f$-NGr/CTS)-Cu sensor 75

4.6.2 Mechanistic pathway of the modified sensor 77

4.6.3 Reproducibility, repeatability and stability 78

4.6.4 Anti-interference study of modified electrode 79

4.6.5 Real sample analysis 80

CHAPTER 5: AMPEROMETRIC DETECTION OF PARACETAMOL BY IMMOBILIZED COBALT ION ON FUNCTIONALIZED MWCNTS-CHITOSAN THIN FILM ……....82

5.1 *f*-MWCNTs/CTS-Co nanocomposite for paracetamol detection 82

5.2 Aim of the research..... 82

5.3 Electrode characterizations..... 83

5.3.1 FTIR spectroscopy analysis 83

5.3.2 FESEM and EDX analysis of *f*-MWCNTs/CTS-Co/GCE..... 84

5.4 Electrochemical characterization..... 87

5.4.1 Electrochemical impedance spectroscopy (EIS) analysis 87

5.4.2 CV of PR on *f*-MWCNTs/CTS-Co/GCE electrode 88

5.5 Optimization of the fabricated sensor..... 90

5.5.1 Scan rate study of *f*-MWCNTs/CTS-Co/GCE sensor..... 90

5.5.2 Analysis of pH variation 90

5.6 Performance evaluation of *f*-MWCNTs/CTS-Co/GCE sensor..... 92

5.6.1 Analytical characterization and method validation..... 92

5.6.2 Interference study..... 93

5.6.3 Reproducibility and stability of the fabricated electrode 95

5.6.4 Recovery study and analytical test results for real samples 95

CHAPTER6: TRI-METALLIC COBALT-NICKEL-COPPER BASED METAL ORGANIC FRAMEWORK NANOSTRUCTURES FOR THE DETECTION OF AN ANTICANCER DRUG NILUTAMIDE ……..97

6.1 Detection of nilutamide using Co-Ni-Cu-MOF/NF sensor ……..97

6.2 Aim of the research..... 97

6.3 Electrode characterizations..... 98

6.3.1 X-ray diffraction analysis.....98

6.3.2 X-ray photoelectron spectroscopy analysis.....98

6.3.3 FESEM,TEM and EDX analysis.....100

6.3.4 BET analysis of fabricated sensor.....103

6.4 Electrochemical characterizations of Co-Ni-Cu-MOF/NF sensor 105

6.4.1 EIS analysis and characterization of effective surface area ……..….105

6.4.2 Electrochemical analysis of Co-Ni-Cu-MOF/NF sensor ……...107

6.5 Optimization of Co-Ni-Cu-MOF/NF sensor 108

6.5.1 Effect of scan rate……...108

6.5.2 Influence of pH ……..111

6.6 Performance evaluation of Co-Ni-Cu-MOF/NF sensor 113

6.6.1 Analytical application of the Co-Ni-Cu-MOF/NF sensor……..113

6.6.2 Interference study of the coexisting substances ……....115

6.6.3 Reproducibility, repeatability and stability of the sensor……...116

6.6.4 Study of real samples ……..…...117

CHAPTER7: NANOCELLULOSE AND 3D-POLYPYRROLE DECORATED WITH SILVER-GOLD BIMETALLIC NANOPARTICLES FOR THE DETECTION OF METHOTREXATE AND CIPROFLOXACIN……119

7.1 NC-3DPPY@Ag-Au nanocomposite for the detection of methotrexate and ciprofloxacin …….....119

7.2 Aim of the research……..…119

7.3 Structural characterization of NC-3DPPY@Ag-Au nanocomposite…….....120

7.3.1 FTIR spectroscopy analysis …..……..…..120

7.3.2 XRD analysis …...……...……121

7.3.3 Surface Morphology analysis of modified electrode ……..…..121

7.4 Electrochemical characterization …….....124

7.4.1 EIS and active surface area calculation for modified sensor ……..124

7.4.2 CV of MTX and CIF at NC-3DPPYT@Ag-Au sensor …..……...…126

7.5 Optimization of the fabricated sensor..….....127

7.5.1 Influence of scan rate……...……127

7.5.2 Analysis of pH variations ……...……129

7.6 Performance evaluation of NC-3DPPYT@Ag-Au sensor.….....132

7.6.1 Analytical application of NC-3DPPY@Ag-Au/GCE sensor.....132

7.6.2 Stability and reproducibility of NC-3DPPY@Ag-Au/GCE ……...…..……134

7.6.3 Selectivity test of NC-3DPPY@Ag-Au/GCE sensor.…….....……135

7.6.4 Real samples analysis ……..……...……136

7.6.5 Determination of MTX and CIF in water sample ……..…….137

CHAPTER 8: CONCLUSIONS AND FUTURE RECOMMENDATIONS……..139

8.1 Conclusions…….....139

8.2 Future recommendations…….....142

REFERENCES.....145

LIST OF PUBLICATIONS AND PAPERS PRESENTED 169

APPENDIX.....171

LIST OF FIGURES

Figure 1.1	:	Flow chart of the research studies……..……..	11
Figure 2.1	:	Transition metals and their versatile applications ……..……..	17
Figure 2.2	:	Synthetic routes of the nanoparticles……	23
Figure 2.3	:	The 3D chemical structure of Paracetamol (N-acetyl-P-aminophenol)…….	26
Figure 2.4	:	The 3D chemical structure of Nilutamide (5,5-dimethyl-3-[4-nitro-3-(trifluoromethyl)phenyl]imidazolidine-2,4-dion)……..	27
Figure 2.5	:	The 3D chemical structure of Methotrexate (MTX) (2,4-diamino-N-10-methyl folic acid)…….....	29
Figure 2.6	:	The 3D chemical structure of Ciprofloxacin (1-cyclopropyl-6-fluoro-1,4 dihydro-4-oxo-7-(1-piperazinyl)-3-quinoline carboxylic acid……	30
Figure 2.7	:	Basic mechanism of a chemical sensor…….	32
Figure 2.8	:	Modification of electrode……..	35
Figure 2.9	:	The three electrodes system electrochemical cell…….	37
Figure 2.10	:	Nernst diffusion layer model……	40
Figure 3.1	:	Schematic diagram for the preparation of (MWCNTs$_f$ –NGr/CTS)-Cu sensor for the electrochemical detection of NLM……..	50
Figure 3.2	:	Schematic diagram for the preparation of *f*-MWCNTs/CTS-Co/GCE modified sensor for the electrochemical detection of PR...	51
Figure 3.3	:	Synthesis of Co-Ni-Cu MOF/NF by hydrothermal method……..	52
Figure 3.4	:	Mechanism of Co-Ni-Cu MOF/NF by the coordination chemistry of organic linkers and metal nodes for the electrochemical detection of NLM.....	52
Figure 3.5	:	Schematic diagram for the preparation of NC-3DPPY@Ag-Au/GCE modified sensor for the electrochemical detection of MTX and CIF……	54
Figure 4.1	:	(A) FITR of NGr (a) and MWCNTs$_f$ (b). (B) FTIR spectra of MWCNTs$_f$–NGr (a), MWCNTs$_f$–NGr/CTS (b) and (MWCNTs$_f$–NGr/CTS)-Cu (c).....	65
Figure 4.2	:	Raman spectra of pristine (a) and MWCNTs$_f$ (b) in (A), GO (a) and NGr (b) in (B), and MWCNTs$_f$–NGr (a), MWCNTs$_f$–NGr/CTS (b), MWCNTs$_f$–NGr/CTS-Cu (c) in (C)……..	66
Figure 4.3	:	TEM images of MWCNTs$_f$ (A) (inset FESEM image), NGr (B) (inset FESEM image), (MWCNTs$_f$ –NGr) (C) (inset FESEM image), MWCNTs$_f$ –NGr/CTS (D), (MWCNTs$_f$ -NGr/CTS)-Cu/GCE nanocomposite (E). (F) EDS analysis of the synthesized (MWCNTs$_f$–NGr/CTS)-Cu/GCE nanocomposite……	68
Figure 4.4	:	The Nyquist plots of (a) bare GCE, (b) (MWCNTs$_f$-NGr/GCE (c) MWCNTs$_f$-NGr/CTS /GCE, (d) (MWCNTs$_f$ –NGr/CTS)-Cu/GCE in a solution containing 0.1 M KCl solution with 5.0 mM $[Fe(CN)_6]^{3-/4-}$, inset the equivalent circuit is used to do the fitting…….	70
Figure 4.5	:	Cyclic voltammograms of 150 µM NLM on bare GCE (a), (MWCNTs$_f$-NGr/GCE (b), MWCNTs$_f$-NGr/CTS/GCE (c), (MWCNTs$_f$ -NGr/CTS)-Cu/GCE (d) in 0.2 M PBS (pH 7.0) at 50 mVs^{-1}. Inset is CV of (MWCNTs$_f$–NGr/ CTS)-Cu/GCE in absence of NLM……..	71

Figure 4.6 : (A) CV of 150 µM NLM on (MWCNTs$_f$-NGr/CTS)-Cu/GCE at different scan rates in 0.2 M PBS (pH 7.0). (B) The plot of cathodic peak current vs. scan rates. (C) The relationship between cathodic peak potential vs ln υ of scan rate…….. 73
Figure 4.7 : (A) The effect of pH on the CVs of 150 µM NLM at the modified (MWCNTs$_f$-NGr/CTS)-Cu/GCE electrode at 50 mV s^{-1}. (B) The plot of cathodic peak current vs pH. (C) The plot of cathodic peak potential vs. pH……. 74
Figure 4.8 : (A) DPV response at (MWCNTs$_f$-NGr/CTS)-Cu/GCE at different NLM concentrations (0.005–900 µM) in 0.2 M PBS (pH 7.0). (B) Calibration curve of NLM concentration (0.005-10µM). (C) Calibration curve of NLM concentration (20-900 µM)…… 76
Figure 4.9 : The proposed mechanistic pathway for electrochemical reduction mechanism of NLM at the (MWCNTs$_f$–NGr/CTS)-Cu/GCE…….. 78
Figure 4.10 : DPV curve of (MWCNTs$_f$-NGr/CTS)-Cu/GCE in 0.2 M PBS (pH 7.0) containing 2 µM NLM, (a) first signal, (b) 1st week interval, (c) 2nd weeks interval……... 79
Figure 4.11 : (A) Amperometry responses on (MWCNTs$_f$–NGr/CTS)-Cu/GCE with NLM in presence of 60 folds excess concentration of glucose (a), lactose (b), sucrose (c), fructose (d), ascorbic acid (e), dopamine (f), and uric acid (g), and 60 folds of nitro compounds 4-nitrophenol (h), nitrobenzene (i), and 20 fold of Metronidazole drug (j) in 0.2 M PBS (pH = 7.0). (B) DPV in the presence of interfering molecules at same concentration with (A), in 0.2 M PBS (pH = 7.0)……..... 80
Figure 5.1 : FTIR spectra of Pristine (a), *f*-MWCNTs (b), *f*-MWCNTs -CTS (c), *f*-MWCNTs- CTS-Co (d)..... 84
Figure 5.2 : The FESEM images of (A) *f*-MWCNT/GCE, (B) *f*-MWCNTs/CTS/GCE and (C) *f*-MWCNTs/CTS-Co/GCE, (D) SEM image for modified electrode (*f*-MWCNTs/CTS-Co) surface. The circular part in (Figure D) indicates the successful distribution of cobalt. (E) EDX analysis of *f*-MWCNTs/CTS-Co/GCE……. 86
Figure 5.3 : (A) EIS spectra for (a) GCE, (b) CTS/GCE, (c) *f*-MWCNTs/GCE, (d) *f*-MWCNTs/CTS-Co/GCE modified electrode in 0.1 M KCl solution with 0.5 mM $[Fe(CN)_6]^{3-/4-}$. Inset (B) EIS for *f*-MWCNTs/CTS-Co/GCE…….. 88
Figure 5.4 : Cyclic voltammograms of 50 µM PR on a) bare GCE, b) CTS/GCE, c) *f*- MWCNTs/GCE, d) *f*-MWCNTs/CTS/GCE, e) *f*-MWCNTs/CTS-Co/GCE in 0.2 M phosphate buffer solution (pH 7.0) as supporting electrolyte at a scan rate of 0.1 V s^{-1}…….. 89
Figure 5.5 : Cyclic Cyclic voltammetry of 50 µM PR on *f*-MWCNTs/CTS-Co/GCE at scan rates ranges from 10 to 400 mVs^{-1} in 0.2 M phosphate buffer solution (pH 7.0) as the supporting electrolyte (A). The plot of the peak current vs. scan rate (B)…… 90
Figure 5.6 : (A) The pH (5.0 to 10.0) effects on cyclic voltammograms of 50 µM PR at the modified *f*-MWCNTs/CTS-Co electrode at 0.1 V s^{-1}. (B) The plot of solution pH with anodic peak current. (C) The plot of pH vs anodic peak potential (E_{pa})……. 92
Figure 5.7 : DPVs response at *f*-MWCNTs/CTS-Co/GCE for different concentration of PR DPVs response at *f*-MWCNTs/CTS-Co/GCE for different concentration of PR between (0.01 µM – 400 µM) in

		0.2 M phosphate buffer solution (pH 7.0) (A). The calibration curve of peak current and PR concentration (B)……...	93
Figure 5.8	:	Amperometric study of the PR oxidation in the presence of 10-fold concentration of interfering ions……...	94
Figure 6.1	:	XRD diffractogram of Co-Ni-Cu-MOF/NF nanocomposite…….	98
Figure 6.2	:	XPS spectrum of Co 2p (A) Ni 2p (B) and Cu 2p (C) for Co-Ni-Cu-MOF/NF nanocomposite…….	100
Figure 6.3	:	FESEM images of Co-MOF/NF (a), Ni-MOF/NF (b), Cu-MOF/NF (c) and Co-Ni-Cu-MOF/NF (d). The images in the first column are low-magnification at 5000x and second column at high-magnification 10000x……...	101
Figure 6.4	:	EDX and Mapping analysis of the Co-Ni-Cu-MOF/NF nanocomposite…….....	102
Figure 6.5	:	TEM images of Co-Ni-Cu-MOF/NF along with their SAED pattern……	103
Figure 6.6	:	BET analysis of (a) Co-MOF/NF, (b) Ni-MOF/NF (c), Cu-MOF/NF (d) Co-Ni-Cu-MOF/NF…….	104
Figure 6.7	:	The electrochemical investigation in 5.0 mM $[Fe(CN)_6]^{3-/4-}$ in 0.1 M KCl solution (A) Nyquist plots of (a) Co-MOF/NF, (b) Ni-MOF/NF (c), Cu-MOF/NF (d) Co-Ni-Cu- MOF/NF; inset is the equivalent circuit for the fitting. (B) CVs obtained at (a) Co-MOF/NF, (b) Ni-MOF/NF (c), Cu-MOF/NF and (d) Co-Ni-Cu-MOF/NF; scan rate 0.6 V s^{-1} ……	106
Figure 6.8	:	(A) CVs of 300 µM NLM on Co-MOF/NF (a), Ni-MOF/NF (b), Cu-MOF/NF (c) and Co-Ni-Cu-MOF/NF (d) in 0.1 M PBS (pH 7.0) at 0.6 V s^{-1}. (B) Bar diagram shows the different electrode vs current response…….	108
Figure 6.9	:	(A) CVs of 300 µM NLM on Co-Ni-Cu-MOF/NF at different scan rates in 0.1 M PBS (pH 7.0). (B) Relationship between peak current vs. different scan rate. (C) The redox peak potential vs. log of scan rate……	110
Figure 6.10	:	(A) CV response in different solution pH (5.0-9.0) in the presence of 300 µM NLM at Co-Ni-Cu-MOF/NF electrode at 0.6 V s^{-1}. (B) Relationship between pH vs reduction peak potential. (C) Bar diagram between different pH values (5.0-9.0) vs reduction peak current of NLM (n=5)…….....	112
Figure 6.11	:	Differential pulse voltammetry of 0.5 – 900 µM of NLM concentrations at Co-Ni-Cu-MOF/NF in 0.1 M PBS (pH 7.0) at 0.6 V s^{-1}.(B) Relationship between reduction peak current vs. concentration (0.5-70 µM) of NLM. (C) Relationship between reduction peak current vs. concentration (70-900 µM)…….	114
Figure 6.12	:	(A) The interference study of Co-Ni-Cu-MOF/NF electrode to NLM in presence of 60-fold concentration of NO_3^- (a), SO_4^{2-} (b) and CO_3^{2-} (c) and 100-fold concentrations of glucose (d), sucrose (e), fructose (f), ascorbic acid (g), urea (h), dopamine (i) and citric acid (j) in 0.1 M PBS (pH 7.0) at 0.6 Vs^{-1}. (B) Bar diagram shows the current response of NLM in presence of interfering compounds…….....	116
Figure 6.13	:	(A) CV of 3 reproducible cycles of NLM at Co-Ni-Cu-MOF/NF in 0.1 M PBS (pH 7.0) at 0.6 Vs^{-1}. (B) CV of 5 multiple cycles of NLM at Co-Ni-Cu-MOF/NF in 0.1 M PBS (pH 7.0) at 0.6 Vs^{-1} ….	117

Figure 7.1 : FTIR spectra of (A) NC-3DPPY (a), NC-3DPPY@Ag (b) NC-3DPPY@Au (c) and NC-3DPPY@Ag-Au (d). and (B) XRD pattern of NC-3DPPY@Ag-Au nanocomposite……... 121
Figure 7.2 : FESEM images of NC (A), NC-3DPPY (B), Ag-Au (C) and NC-3DPPY@Ag-Au (D)……. 123
Figure 7.3 EDX analysis for NC-3DPPY@Ag-Au nanocomposite……... 123
Figure 7.4 : Elemental Mapping analysis for NC-3DPPY@Ag-Au nanocomposite……... 124
Figure 7.5 : The Nyquist plots of bare GCE (a), NC/GCE (b), NC-3DPPY/GCE (c), NC-3DPPY@Ag/GCE (d), NC-3DPPY@Au/GCE (e) and NC-3DPPY@Ag-Au/GCE (f) in 0.1 M KCl solution with 5.0 mM [Fe (CN) $_6$]$^{3-/4-}$. Inset is the equivalent circuit of the fitting…… 125
Figure 7.6 : (A) CVs of 150 µM MTX and 35 µM CIF in 0.1 M PBS (pH 7.0) at 0.1 V s^{-1} on of bare GCE (a), NC/GCE (b), NC-3DPPY/GCE (c), NC-3DPPY@Ag (d), NC-3DPPY@Au (e), NC-3DPPY@Ag-Au (f). (B) CVs response of bare GCE, NC/GCE, NC-3DPPY/GCE,NC-3DPPY@Ag/GCE,NC-3DPPY@Au/GCE, and NC-3DPPY@Ag-Au/GCE in 0.1 M KCl solution with 5.0 mM [Fe (CN) $_6$]$^{3-/4-}$ at 0.1 V s^{-1}…… 127
Figure 7.7 : CVs of 150 µM MTX and 35 µM CIF on NC-3DPPY@Ag-Au/GCE at 10 mV s^{-1} to 300 mV s^{-1} in 0.1 M PBS (pH 7.0) (A). The calibration plot of oxidation peak current vs. scan rates of MTX (B) and CIF (C)……... 129
Figure 7.8 : (A) The CVs of 150 µM MTX and 35 µM CIF at the NC-3DPPY@Ag-Au/GCE at different pH: 5.0, 6.0, 7.0, 8.0 and 9.0, at 0.1 V s^{-1}. (B) The plot of oxidation peak potential vs. pH of MTX. (C) The plot of oxidation peak potential vs. pH of CIF, (D) The plot of the oxidation peak current vs. pH of MTX, (E) The plot of the oxidation peak current vs. pH of CIF…….. 131
Figure 7.9 : SWVs response at the NC-3DPPY@Ag-Au/GCE for different concentration of MTX and CIF between (10 µM – 350 µM) and (0.5 – 50 µM) in 0.2 M phosphate buffer solution (pH 7.0) (A). The calibration curve of peak current and MTX concentration (B). The calibration curve of peak current and CIF concentration (C)… 134
Figure 7.10 : The bar diagram for stability study of MTX and CIF at NC-3DPPY@Ag-Au modified electrodes, on three consecutive weeks (a) first day; (b) after 1st week; (c) after 2nd weeks (d) after 3rd weeks……. 135
Figure 7.11 : SWVs signal at NC-3DPPY@Ag-Au sensor for interference study of the MTX and CIF oxidation in the presence of interfering ions... 136

LIST OF TABLES

Table 2.1	:	Comparison between enzymatic electrochemical sensor and non-enzymatic electrochemical sensor…….	33
Table 2.2	:	Transition metal ion based nanocomposite for electrochemical sensor applications…….....	44
Table 2.3	:	Transition metal based nanocomposite in other electrochemical applications……	45
Table 3.1	:	List of chemicals and reagents used……..	46
Table 4.1	:	The comparison of various electrodes for the determination of NLM..	77
Table 4.2	:	Determination of NLM in pharmaceutical preparations using differential pulse voltammetry at pH 7.0 (n=5)…….	81
Table 4.3	:	Determination of NLM in human serum sample using differential pulse voltammetry at pH 7.0 (n=5)……	81
Table 5.1	:	The results of various electrodes for the determination of PR……..	94
Table 5.2	:	PR detection in tablet samples (n=3)…….....	96
Table 5.3	:	Results for PR recovery test by using human serum samples (n=3).....	96
Table 6.1	:	EDX data of Co-Ni-Cu-MOF/NF……..	102
Table 6.2	:	The BET analysis of Co-MOF/NF, Ni-MOF/NF, Cu-MOF/NF and Co-Ni-Cu-MOF/NF with their mean pore diameter and pore volume..	104
Table 6.3	:	The comparison of Co-Ni-Cu-MOF/NF sensor for determination of NLM with other published works……..	115
Table 6.4	:	Determination of NLM in pharmaceutical tablets using DPV at Co-Ni-Cu-MOF/NF at pH 7.0 (n=3)……	118
Table 6.5	:	Determination of NLM in human blood serum specimen at Co-Ni-Cu-MOF/NF at pH 7.0 (n=3)…….	118
Table 7.1	:	The comparative study between various electrodes for the detection of MTX and CIF…….....	133
Table 7.2	:	Determination of MTX and CIF in tablets at NC-3DPPY@Ag-Au/GCE using SWV (n=3).....	137
Table 7.3	:	Determination of MTX and CIF in blood serum at NC-3DPPY@Ag-Au/GCE using SWV (n=3)…….....	137
Table 7.4	:	Determination of MTX and CIF in water sample at NC-3DPPY@Ag-Au/GCE using SWV (n=3)…….....	138

LIST OF SYMBOLS AND ABBREVIATIONS

For examples:

°C	:	Degree Celcius
µm	:	Micrometer
AA	:	Ascorbic Acid
Amp	:	Ampere
A.C	:	Alternating current
Ag	:	Silver
APS	:	Ammonium persulfate
atm	:	Atmosphere
Au	:	Gold
BET	:	Brunauer-Emmett-Teller
Co	:	Cobalt
Cu	:	Copper
CE	:	Counter electrode
CTS	:	Chitosan
cm	:	Centimeter
CNT	:	Carbon nanotube
C_3N_4	:	Carbon nitride
CIF	:	Ciprofloxacin
CV	:	Cyclic voltammetry
CVD	:	Chemical vapour deposition
C_{dI}	:	Double-layer capacitance
CMEs	:	Chemically modified electrodes
DA	:	Dopamine

D.C	:	Direct current
DPV	:	Differential pulse voltammetry
DIW	:	Deionized water
eV	:	Electron volt
ECP	:	Electronically conductive polymer
EIS	:	Electrochemical impedance spectroscopy
EDX	:	Energy dispersive X-ray analysis
FESEM	:	Field emission scanning electron microscopy
FRA	:	Frequency response analyzer
FTIR	:	Fourier transform infrared spectroscopy
FTO	:	Fluorine doped tin-oxide
*f*MWCNTs	:	Functionalized multiwall carbon nanotubes
GCE	:	Glassy carbon electrode
GO	:	Graphene oxide
GPES	:	General purpose electrochemical software
Gr	:	Graphene
IUPAC	:	International Union of Pure and Applied Chemistry
ITO	:	Indium tin-oxide
hr	:	Hour
HCl	:	Hydrochloric acid
H_2SO_4	:	Sulphuric acid
K	:	Kelvin
KCl	:	Potassium chloride
KHz	:	Kilohertz
KV	:	Kilovolts
K_2HPO_4	:	Di-potassium hydrogen phosphate

KH_2PO_4	:	Potassium di-hydrogen phosphate
LOD	:	Limit of detection
M	:	Molarity
mHz	:	Millihertz
µA	:	Microampere
µM	:	Micromolar
mg	:	Milligram
mL	:	Milliliter
mv	:	Millivolt
min	:	Minute
mmol	:	Millimol
M	:	Molarity
MOF	:	Metal organic framework
MTX	:	Methotrexate
Ni	:	Nickel
NLM	:	Nilutamide
NC	:	Nanocellulose
nm	:	Nanometer
NF	:	Nickel foam
NPs	:	Noble metal nanoparticles
NNTMs	:	Non-noble transition metals
NTMs	:	Noble transition metals
OTC	:	Over the counter
PBS	:	Phosphate buffer solution
PR	:	Paracetamol
PPY	:	Polypyrrole

Pt	:	Platinum
R_{ct}	:	Charge transfer resistance
R_s	:	Solution resistance
RE	:	Reference electrode
RSD	:	Relative standard deviation
RCF	:	Relative centrifugal field
s	:	Second
SCE	:	Saturated calomel electrode
SAED	:	Selected area electron diffraction
STM	:	Scanning tunneling microscope
SWV	:	Square-wave voltammetry
SWCNTs	:	Single wall carbon nanotube
TMs	:	Transition metals
TEM	:	Transmission emission microscopy
UA	:	Uric acid
W	:	Warburg diffusion elements
WE	:	Working electrode
XRD	:	X-ray diffraction
XPS	:	X-ray photo electron spectroscopy

LIST OF APPENDICES

Appendix A:	The proposed electrochemical reduction mechanism of NLM at the (MWCNTs*f*–NGr/CTS)-Cu/GCE……....	171
Appendix B:	The redox mechanism of paracetamol on the *f*-MWCNT/CTS-Co/GCE electrode surface at a pH range of 5.0-10.0……...	171
Appendix C:	The proposed mechanistic pathway for the electrochemical redox reaction of NLM on Co-Ni-Cu-MOF/NF…….…..	172

CHAPTER 1: INTRODUCTION

1.1 Background

Nanotechnology and its extensive applications have brought a revolutionary impact to the world. For the past few decades, enormous attempts have been made for materials that were considered inactive, especially in bulk form for different technological applications. The nano-scale isolation of these bulk materials overcomes these limitations. The bulk materials in nanoscale isolation show extra-ordinary chemical and physical characteristics, which has been validated through present scientific investigations (Zhang et al., 2008). During at an American Physical Society meeting in 1959, Richard Feynman presented the concept of synthesizing the materials at a nanoscale dimension and stated that; “There is Plenty of Room at the Bottom”. He said that, it is possible to manipulate and control the molecular size of the materials when applied to any electronic system. The implementation of this technology in any system could be applied in chemistry, physics and biology. A Japanese scientist, Norio Taniguchi was the first to mention the term “nanotechnology” during an international conference related to production engineering, that was held in Tokyo. The concept of nanotechnology was first utilized by Gerd Binning and Heinrich Rorhrer for the invention of scanning tunnelling microscope (STM) which brought them a Nobel Prize in Physics in 1986 (Demuth et al., 1986). For the past few decades, researchers have emphasized and paid huge efforts to develop nanostructures due to their outstanding characteristics such as the high surface area to volume ratio which enhance the surface reactivity and accelerate the electrode/electrolyte interaction and the interfacial transfer of electrons that is ultimately beneficial for sensing applications. The transfer of electrons from one state to another enhances the optical emission as well as absorption which is crucial for the optoelectronic nano-devices. It has been proved from the

investigation that, the size, shape, crystallinity and morphology of nanomaterials have a great influence on the optical, magnetic, catalytic and electronic properties (Chen et al., 2018).

Electrochemical technology is a diverse and huge area of science with a combination of chemistry, physics and biology. Electrochemical and bio-nanodevice have profound impacts in different fields of medicine, biomedical and environmental monitoring. The development of sensor devices at a lower cost is a demand for the present time especially in online monitoring, food safety, biomedical and biological determinations, point of care applications (Akbari et al., 2018). The electrochemical devices based on the non-novel metals and their different forms could be an effective strategy for their high sensitivity, selectivity and simultaneous determinations.

The development of electrochemical sensors based on the outstanding physicochemical characteristics of nanomaterials has sparked huge attention among researchers. In recent years, transition metal ions and their nanoparticles of different shapes and morphologies have been synthesized using several approaches. The transition metals are the chemical elements with valence electrons that can participate in the formation of chemical bonds. The transition metals are the metallic elements that serve as a bridge, or transition, between the two sides of the table. They occupy the middle portions of the long periods of the periodic table of elements between the groups on the left side and the groups on the right. The lanthanides and the actinides at the bottom of the table are sometimes known as the inner transition metals because they have atomic numbers that fall between the first and second elements in the last two rows of the transition metals. These transition metal ions and their nanomaterials have been extensively applied for the development of nano-devices due to their excellent electro-

conductivity and catalytic properties which depend on their size, shape, stability and higher surface area (Tyagi et al., 2020; Agnihotri et al., 2021).

Among the first-row transition metals, copper (Cu), cobalt (Co), nickel (Ni) and iron (Fe) are considered the most abundant and cost-efficient transition metals. They are regarded as non-noble transition metals (NNTMs). These metals have sparked interest among researchers due to their outstanding electrical, optical, magnetic and transport properties (Wang et al., 2017; Ren et al., 2020). They have been studied enormously in diverse applications as they can be utilized as substitutes for expensive elements. These transition metal ions and their nanostructures have been at the heart of many dramatic advances in materials science and utilized substantially in the construction of several nano-devices including non-enzymatic determination of glucose (Haldorai et al., 2018), electrochemical determination of different drug molecules (Akhter et al., 2021), energy storage (Jin & Maduraiveeran, 2019), fuel cells (Dai et al., 2021) and supercapacitors (Ren et al., 2020). However, due to their large band gap, low stability and ion-transportation capability, the electrocatalytic effects of these types of transition metals are insufficient for the construction of a high-performance sensor. To alleviate these issues, scientists have incorporated other conductive platforms (e.g. graphene, carbon nanotube, conductive polymers etc) which ultimately enhance the physicochemical properties and sensing efficiency of metal-based nanocomposites.

Metal-organic frameworks (MOFs) are hybrid compounds composed of metal ions and organic ligands as repeating units. Though they have good porous appearance, large surface area, pure MOFs suffer lack of stability in aqueous media and non-conductivity, which limits their electrochemical applications. To overcome these issues, tri-metallic MOFs could be an effective strategy to enhance the stability and electrochemical conductivity (Akhter et al., 2021). Cost-efficient transition metals such as Co, Ni, Cu

have been investigated substantially as replacements for the expensive metals. Several approaches such as, alloy structures, metal catalysts have been utilized to improve their stability and performance, as they tend to aggregate and oxidize easily resulting in loss of performance. Due to the nanostructured configurations, the tri-metallic MOFs possess an outstanding electron transfer process with a highly porous nature, high crystallinity, virtuous stability, excellent selectivity and sensitivity for which they are suitable for the electrochemical applications (Sharma et al., 2017).

Noble metal nanoparticles (NPs), especially silver and gold nanoparticles (Ag and Au), possess several outstanding properties, such as simple operation, economical production, sensitivity and simplicity of construction. These nanomaterials have been widely used for the development of electrochemical sensors and biosensors due to their sensitivity and selectivity. However, the efficiency of the NPs utilized for the electrochemical detection depends on some factors such as the synthesis approach, synthesis parameters, shape and size. (Zhao et al., 2020). The mechanisms for sensors that use NPs are mainly dependent on their unique properties in electrochemical, colorimetric, and fluorescent characteristics. The Ag and Au have a large surface area and small particle size, which increases the sensitivity and selectivity of the detection method. (Shifrina et al., 2019).

Multi-wall carbon nanotubes (MWCNTs) are carbon-based nanomaterials that are composed of sp^2 hybridized nanosheets of graphene rolled into nano-cylinders. MWCNTs have aroused great attention from researchers in different fields of material science due to their several distinctive characteristics such as high electro-conductivity, mechanical strength and prominent electrochemical response. The functionalization of MWCNTs is an effective approach to enhance dispersion, remove the impurities, attachment of more anchoring sites and makes the MWCNTs more electroconductive

and suitable for attachment with other functional groups (Akhter et al., 2018). Recently, huge works have been reported on the functionalized MWCNTs (*f*-MWCNTs) for the development of electrochemical and biosensors (Shalauddin et al., 2017), supercapacitors (Tiwari et al., 2021) and energy conversion (Chai et al., 2021) and others.

Graphene (Gr) is a 2D carbon-based nanomaterial, with an atomic arrangement in the form of honey-comb lattice that possesses extra-ordinary properties such as good electrical conductivity, mechanical and optical properties. Among the dopants, nitrogen (N) is an excellent dopant for the carbon nanomaterials. As N has a comparable atomic size and number of valence electrons, it can form strong valence bonds with graphene. The doping of N on the graphene enhances the electrochemical conductivity of Gr and nitrogen-doped graphene (NGr) able to increases the sensitivity of the nanodevices (Akhter et al., 2020b). Recently, versatile applications of NGr has been observed in different fields such as electrochemical and biosensors (Akhter et al., 2020b), supercapacitors (Dai et al., 2018) and energy storage (Wei et al., 2019).

Chitosan (CTS), a natural polysaccharide composed of d-glucosamine and *N*-acetyl-d-glucosamine and possesses high concentrations of reactive amino (NH_2) and hydroxyl (OH) groups. CTS is used as a binder, which is non-toxic, bio-degradable, biocompatible and inert, has proved its potential for versatile employment in different field of material science (Shalauddin et al., 2017). CTS shows excellent adsorption capacity for several metal ions and some inorganic substances. As CTS enhances the dispersion of nanomaterials and prevents the leaching of nanomaterials from the electrode surface by the formation of films, it helps to enhance the electrochemical response and stability of the sensor. The combination of metal compound and CTS

complex shows excellent catalytic property for several reactions, thus applied enormously for the construction of electrochemical and biosensors (Akhter et al., 2018).

Nanocellulose (NC) is an inexhaustible natural biopolymer obtained from cellulose by nanoscale synthesis. NC is a bio-degradable, biocompatible, cost-effective and eco-friendly green nanomaterial. Furthermore, NC has a high surface to volume ratio, good adsorption capacity for which it can prevent the leaching of nanomaterials and thus enhance the stability of the sensors (Shalauddin et al., 2019). The nanocellulose and three-dimensional polypyrrole (NC-3DPPY) nanocomposite shows a porous appearance with good electroconductivity. NC-3DPPY could be the best loading option for the noble metal nanoparticles. which facilitates the dispersion of several metal ions and metal nanoparticles such as silver (Ag), gold (Au), platinum (pt) etc. NC-3DPPY increase the dispersion of the metal nanoparticles and reduces aggregation (Hanif et al., 2020).

Paracetamol (PR) is one of the most frequently administered drugs which is used for the mitigation of fever and pain (headache, backache, cancer pain, migraine etc). The overdose of PR can cause serious adverse effects such as hepatotoxicity, nephrotoxicity which could be sometimes life-threatening (Anuar et al., 2018). While Nilutamide (NLM) is an anti-androgenic anticancer therapeutic drug which is used for the treatment of metastatic prostate cancer. The overdose of NLM can cause life-threatening side effects such as liver failure, severe pneumonia etc (Akhter et al., 2021). Another anticancer drug is methotrexate (MTX) is used for the treatment of leukemia, neck, head and breast cancer. The excess dose of MTX can cause stomach ulcers, hepato-toxicity and low white blood cell counts (Li et al., 2021). Ciprofloxacin (CIF) is a floroquinolone antibiotic, generally used for the treatment of urinary tract infections, respiratory tract infections and gastro-intestinal diseases. The overdose of CIF causes

severe hypersensitivity, gastric lesions etc. Furthermore, the CIF residues found in water surfaces could cause carcinogenic reactions which are very harmful to humans and animals (Matsunaga et al., 2020). Thus, the development of a facile, cost-efficient and reliable approach for the clinical monitoring, pharmaceutical routine analysis and environmental monitoring are the demand of present research.

In this present study, first-row transition metals such as Cu, Co and their tri-metallic metal-organic frameworks (MOFs) of Cu, Co, Ni were synthesized and used to fabricate nanocomposite for the electrochemical determination of pharmaceutical drugs.

1.2 Problem statements

Due to excellent catalytic activity and high selectivity, the enzyme-based electrochemical nano-device was investigated substantially for different electrochemical applications. However, the enzyme-based electrochemical sensors have some drawbacks such as complex immobilization process, time-consuming, unstable in harsh environmental conditions, poor reproducibility and stability because of the vulnerability of the enzymes. To minimize these limitations, enzyme-free electrochemical sensors have been developed and investigated. The non-enzymatic electrochemical sensor has sparked tremendous attraction due to its fascinating features such as outstanding sensitivity, selectivity, reproducibility and high stability for the broader sensing implementations.

1.3 Objectives of the study

The overall objectives of this study are to fabricate new modified electrodes based on first-row transition metal (Co, Ni, Cu) based nanocomposites. Here, the transition metals have been immobilized with natural biopolymer CTS and incorporated with carbon-based conductive platform such as functionalized carbon nanotubes and

nitrogen-doped graphene. While a tri-metallic MOF composed of Co-Ni-Cu was synthesized on nickel foam (NF) substrate using the solvothermal technique. The combination of two or more components into nanocomposites is expected to improve the properties of the nanocomposite compared to the single component, thus the synergistic effect is a hallmark of good sensing material.

The objectives of the present study are the following:

1. To synthesize a hybrid nanocomposite of functionalized multiwall carbon nanotube, nitrogen-doped Graphene and chitosan with electrodeposited copper for the detection of anticancer drug nilutamide in tablet and biological sample
2. To enhance the amperometric detection of paracetamol by immobilized cobalt on Functionalized MWCNTs - Chitosan thin film
3. To synthesize a tri-metallic Co-Ni-Cu based metal-organic framework nanostructures for the detection of an anticancer drug nilutamide
4. To develop a highly selective nanosensor based on nanocellulose and 3D-polypyrrole decorated with gold-silver bimetallic alloy for the detection of methotrexate and ciprofloxacin in pharmaceuticals, biological medium and water sample

1.4 Scope of the research

The scope of the research clearly represents the content of the research. The main research scope in this thesis are as follows:

1. The structural and morphological properties of the fabricated nanocomposites investigated by Fourier transformed infrared spectroscopy (FTIR), Raman spectroscopy, x-ray diffraction (XRD), field emission scanning electron microscopy (FESEM), transmission emission microscopy (TEM), x-ray photo electron spectroscopy (XPS), Brunauer-Emmett-Teller (BET) analysis

2. The electrochemical investigation of the fabricated electrodes for the analytical determination of different pharmaceutical drugs such as paracetamol, nilutamide, methotrexate, ciprofloxacin.
3. Investigation for the real samples of the modified sensor.

1.5 Thesis outline

This thesis contains eight chapters. Chapter four, five, six and seven represents the research work and findings accomplished during the Ph.D. candidature period including experimental elaborations, results and discussions on different nanocomposites consisting of first-row transition metals with the integration of carbon nanomaterials, their MOF structures and their electrochemical applications

Chapter 1: Introduction

This chapter describes briefly the introduction of the background study, problem statements, research objectives and research scope.

Chapter 2: Literature Review

This chapter illustrates the study of transition metals and their nanomaterials, biopolymers and conductive polymer, carbon-based nanomaterials for the fabrication of modified electrodes. The literature review presents the previous study regarding the use of nanocomposites in the electrochemical detection of a target analyte.

Chapter 3: Methodology

The synthesis approach of the nanocomposite materials and the fabrication of modified electrodes are explained in detail. The characterization techniques such as XRD, BET, SEM, FESEM, TEM, XPS, Raman spectroscopy and FTIR were utilized for the structural and morphological investigation of the nanocomposites.

Chapter 4: Results and Discussions (Part 1)

The characterization of hybrid nanocomposite of functionalized multiwall carbon nanotube, nitrogen-doped graphene and chitosan with electrodeposited copper and the development of an electrochemical sensor for the detection of anticancer drug nilutamide in tablet and biological samples.

Chapter 5: Results and Discussions (Part 2)

The development of an electrochemical sensor for the enhanced amperometric detection of paracetamol by the synthesis and characterization of functionalized MWCNTs - CTS thin film with the immobilized cobalt.

Chapter 6: Results and Discussions (Part 3)

The synthesis and characterization of tri-metallic Co-Ni-Cu based metal organic framework nanostructures and the development of electrochemical sensors for the detection of anticancer drug nilutamide .

Chapter 7: Results and Discussions (Part 4)

Synthesis and characterization of the nanocomposite containing nanocellulose and 3D-polypyrrole decorated with silver-gold bimetallic nanoparticles for the development of an electrochemical sensor for the detection of methotrexate and ciprofloxacin in pharmaceuticals, biological fluid and water samples.

Chapter 8: Conclusions and Future Recommendations

Overall conclusions with an outlook for the future perspective are presented.

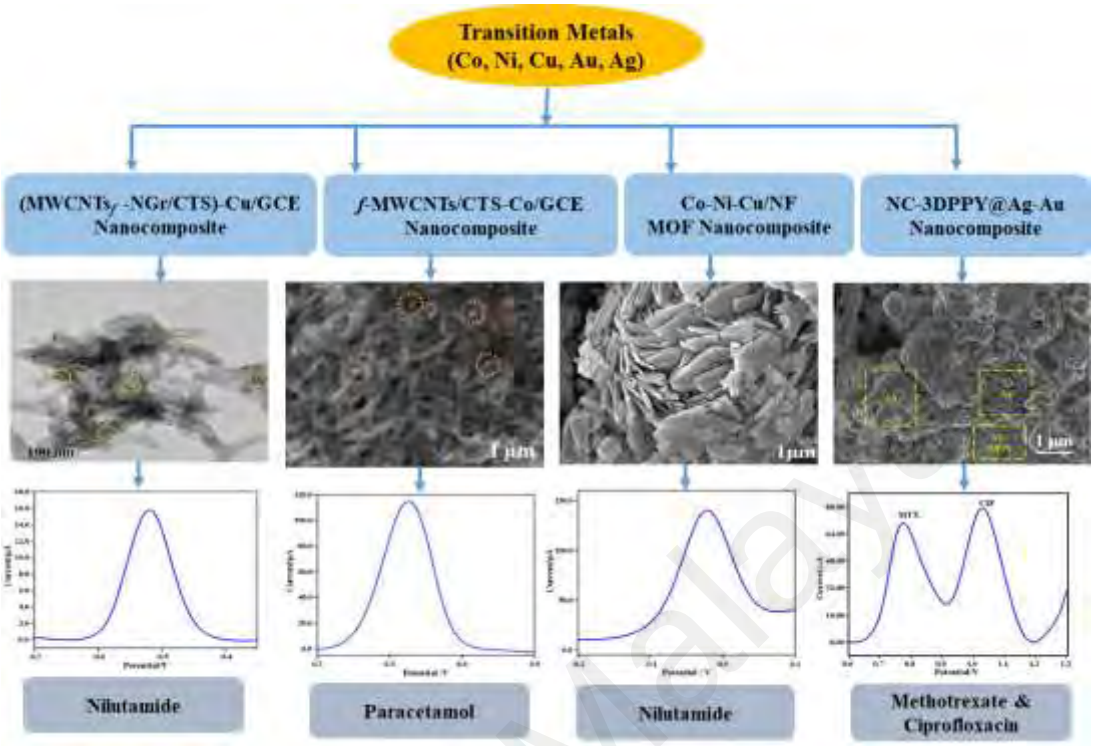

Figure.1.1: Flow chart of the research studies

CHAPTER 2: LITERATURE REVIEW

2.1 Background

The practical applications of different types of metals and their different forms have great roles for human development. Since human civilization, the earth abundant metals have been introduced and utilized enormously for several purposes. Today, as consequence of their usage, the metals and the different sizes and shapes of the metallic structures are used in different fields of science such as biomedical engineering, drug delivery, health care, food packaging and building engineering etc. With the advancements in chemistry and material sciences, the physicochemical properties of the metallic structures could be regulated for a beneficial output to meet the customized demand successfully (Wang & Astruc, 2017).

2.2 Transition metals and their classification

According to the International Union of Pure and Applied Chemistry (IUPAC), transition metals (TMs) are elements that possess an atom with incomplete electrons in the d-sub shell. They can easily donate electrons through the incomplete d-sub shell. Thus, they show their reactivity and tend to be easily oxidized and used in several chemical reactions (Zhao et al., 2020).

TMs and their nanomaterials possess exceptional characteristics such as distinct catalytic effect, produce synergistic effect when conjugated with carbon nanomaterials, mimic the metal surface activation and mimic natural enzymes when conjugated with natural biopolymers such as chitosan and nanocellulose. Due to the aforementioned characteristics, TMs have been applied enormously in biomedical applications (Shalauddin et al., 2017). Some of the TMs are known as non-noble transition metals (NNTMs) such as copper (Cu), cobalt (Co), nickel (Ni), iron (Fe), manganese (Mn) etc.

As these NNTMs are found abundantly in the earth, they are also known as earth-abundant TMs and due to their low production cost they have been used extensively as a substitute for expensive metals. On the other hand, gold (Au), silver (Ag), platinum (Pt) are known as noble transition metals (NTMs) which have been used enormously due to their unique features such as enhanced and improved catalytic and sensing capabilities, efficiently interact with biomolecules and chemical moieties through high adsorption, extra-ordinary electrical and optical properties (Wang & Astruc, 2017).

2.3 Non- noble transition metals (NNTMs)

Non-noble transition metals (NNTMs) such as Cu, Ni, Co, Fe and Mn are found abundantly in the earth and have been used extensively in several electroanalytical applications due to their low energy gap between the different oxidation states, capability to form complexes through the attachment of carbon-based nanomaterials, biopolymers and produce multiple oxidation states. Besides, they are cost-effective, improves the catalytic efficiency of carbon-based nanomaterials. When employed to the surface of the electrode, these metal ions facilitate the transfer of electrons, improve the sensor ability for the adsorption of analytes. Thus, the NNTMs enhance the sensitivity and selectivity of the fabricated electrode (Akhter et al., 2021). The attachment of these types of metals can be achieved by mainly two approaches namely by electrodeposition and the self-assembly approach by immersion. A nanocomposite of functionalized multiwall carbon nanotubes, chitosan and copper was fabricated by the self-assembly technique on GCE surface to prepare the *f*-MWCNT/CTS-Cu for the electrochemical determination of paracetamol (Akhter et al., 2018). While another FMWCNT/CTS-Cu/GCE sensor was fabricated by applying the same technique for the determination of diclofenac sodium (Shalauddin et al., 2017). Another nanocomposite of functionalized multiwall carbon nanotube, nitrogen doped graphene, chitosan and electrodeposited

copper (MWCNT$_f$–NGr/CTS)-Cu was prepared for the electrochemical determination of anticancer drug nilutamide (Akhter et al., 2020).

2.4 Noble transition metals

Over the recent decades, noble transition metals (NTMs) such as Ag, Au based electrochemical sensors have been extensively employed as promising analytical techniques due to their beneficial features such as ease of handling, high sensitivity and selectivity and early detection etc. Due to their outstanding characteristics such as high surface to volume ratios, electron transport capability and adsorption capability to targeted molecules, the NTMs based electrochemical sensors possess remarkable sensitivity. The NTMs possess molecular adsorption ability and suitable attachment with the targeted molecules which ensure sufficient links with the analyte. These properties are significant for the construction of NTMs-based electrochemical sensors for sensing analytes (Siegel et al., 2012). In the past few decades, NTMs based nanocomposites have been applied enormously in different fields of material science such as tissue engineering (Koons et al., 2020), energy storage (Zhu et al., 2020), supercapacitor (Zhu et al., 2019), electrochemical sensing bio-sensing and others. To enhance the stability and catalytic properties, NTMs composites can be synthesized using different strategies such as core-shell, hetero-structure and metallic alloys.

Metallic alloys can be of different types such as monometallic, bimetallic and trimetallic alloys. Bimetallic alloys can be synthesized from different approaches. Sometimes bimetallic alloys can be synthesized by incorporating similar types of transition metals or different types of transition metals. For instance, a first-row transition metal can be incorporated with noble metal nanoparticles or two noble metal nanoparticles that can be incorporated to synthesize the bimetallic alloys using several strategies like ultrasonication and layer by layer electrodeposition etc (Guo et al., 2020).

The bimetallic composition possesses the potential to serve as high energy surface sites in attracting the analytes towards the electrode surface, especially for the rapid and simultaneous detection of analytes. Among these several approaches, the synthesis of bimetallic nanoparticles employing the reducing agents is one of the most efficient synthesis approaches due to its cost-efficiency, and fewer reaction steps. The bimetallic nanoparticles show better electrochemical behavior compared to the monometallic nanoparticles as they possess the synergy of the catalytic effect between the two metals (Agnihotri et al., 2021). The bimetallic nanoparticles such as gold-silver bimetallic nanoparticles, silver-platinum bimetallic nanoparticles, gold-platinum bimetallic nanoparticles have been enormously investigated for sensing applications. Suitable supporting materials can be incorporated for the proper distribution of bimetallic nanoparticles (Anuar et al., 2020). Materials such as graphene, carbon nanotubes and polymeric matrix can be an effective platform for the dispersion of bimetallic nanoparticles and show excellent catalytic effects for enhanced electrochemical responses.

2.5 Metal organic framework based on transition metals

Metal organic frameworks (MOFs) are a type of hybrid compound composed of metal ions and organic linkers in repetitive arrangements, using strong coordination bonds and possess several outstanding physicochemical characteristics such as tunable structures, highly accessible surface area, porous appearance and crystalline configurations etc. The porosity of MOF-based materials permits guest molecules to diffuse into the bulk structure, and the shape and size of the pores produce shape- and size-selectivity over the incorporated guests (Furukawa et al., 2013)

However, the pure MOFs are lack of proper stability in an aqueous medium and have poor conductivity which could limit their electrochemical applications. This

drawback can be minimized by the attachment of other functional compounds. Recently MOFs have been applied enormously in different fields of material science such as gas storage, catalysis, imaging, drug delivery and electrochemical sensing. The preparation of MOFs with cost-effective NNTMs is an effective strategy as a substitute for precious metals. As they tend to become oxidized and aggregated, thus suffer from a loss in performance. Thus, the core-shell, alloy structures and supported metal catalysts have been studied to minimize this issue (Naghian et al., 2020). To improve the physico-chemical properties of MOFs such as mechanical stability, conductivity and catalytic performance, MOFs can be combined with other functional materials like carbon substrates, nanoparticles, enzymes, polymers and conducting substrates. These types of MOFs composites offer enhanced physico-chemical properties that are not possible with pristine MOFs (Li et al., 2018). The MOFs can be synthesized in various approaches such as hydrothermal, microwave absorption, solvothermal, electrodeposition, drop-casting etc. The MOFs can be synthesized using mono-metal, bi-metals or tri-metals as the metal component. Recently, tri-metallic MOFs have sparked a huge interest among researchers. Trimetallic MOFs nanohybrids possess extra-ordinary features compared to mono and bimetallic MOFs. They possess distinct geometric configurations, virtuous stability and porous framework with highly ordered arrangements, diverse morphologies, enhanced electron transfer, high selectivity and sensitivity than the mono- metallic and bi-metallic MOFs (Akhter et al., 2021). Figure 2.1 shows versatile applications of transition metals.

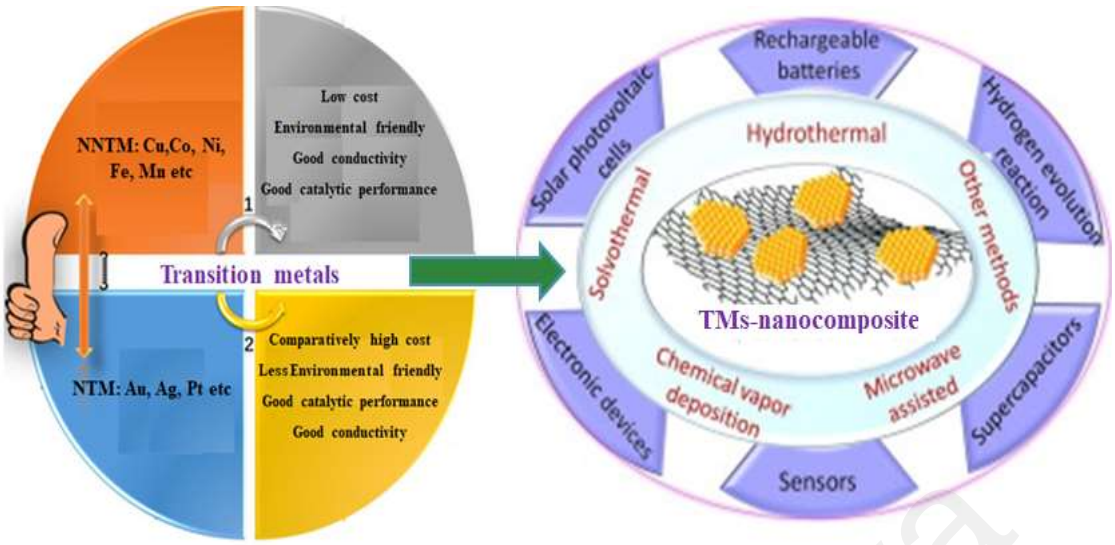

Figure 2.1: Transition metals and their versatile applications (Wang et al., 2016) (Reproduce with permission from the publisher).

2.6 Transition metal and biopolymer composite

2.6.1 Chitosan

Chitosan (CTS) is a natural bio-polysaccharide which is extensively studied and used biopolymers containing the d-glucosamine and *N*-acetyl-d-glucosamine groups with abundant reactive NH_2 and OH groups shown in Figure 2.1. CTS possess several lucrative properties such as biocompatibility, biodegradability, water permeability, low toxicity, inertness, high mechanical strength and film formation capacity. In addition, CTS shows great potential for the adsorption of inorganic compounds and metal ions. For these characteristics, CTS has been applied enormously for the preparation of different nanocomposites especially in metal ion-based nanocomposites (Li et al., 2017). Besides, CTS improves the dispersion of carbon-based nanomaterials, thus minimizes the aggregation of carbon nanomaterials (e.g CNTs, NGr). CTS minimizes the fouling effects of nanomaterials by the film formation, thus the stability of the electrode can be improved (Khan et al., 2016). The incorporation of CTS and metal complex has a favorable catalytic effect due to the synergy between the homogenous and heterogeneous networks. The attachment of CTS polymeric matrix and metal

enables an annulus chelating structure and contains the characteristics of natural enzymes. Moreover, for the development of nanocomposite, the presence of CTS immobilizes the transition metals (Pestov & Bratskaya, 2016). Therefore, CTS has been extensively utilized for the development of enormous nanocomposites for the electrochemical determination of targeted analytes. Surya et al reported a nanocomposite of chitosan, gold nanoparticle molecular imprinted glassy carbon electrode Ch-AuMIP/GCE for the determination of antibiotic ciprofloxacin (Surya et al., 2020). While another nanocomposite of chitosan and yttrium oxide nanoparticle was synthesized on indium tin oxide by the hydrothermal approach CH-nY2O3/ITO for the electrochemical determination of antibiotic norfloxacin (Yadav et al., 2020). Another nanocomposite of functionalized multiwall carbon nanotube, nitrogen-doped graphene, CTS with electrodeposited copper on glassy carbon electrode (MWCNTS$_f$-NGr/CTS)-Cu/GCE was developed for the electrochemical detection of an anticancer drug nilutamide (Akhter et al., 2020). CTS can be synthesized from different sources such as the skeleton of jelly fishes, crabs and others, following the acid hydrolysis method.

2.6.2 Nanocellulose

Nanocellulose (NC) is considered the world's most abundant biopolymers which can be synthesized from cellulose and cellulose is a component of plants and bacteria. Due to the nanoscale isolation, NC becomes free from the inherent limitations present in cellulose and simultaneously, achieve multiple extra-ordinary features such as exceptional mechanical features and surface chemistry, suffice of anchoring sites etc. Moreover, NC possesses several interesting properties such as high specific surface area, biodegradability, biocompatibility, non-toxicity and non-reactivity. Like CTS, NC is capable of film formation and minimize the fouling of the nanomaterials. Thus, it can improve the stability of the electrode. Therefore, NC is considered an ideal option for

the conjugation with CNT, polyaniline, polypyrrole (Shalauddin et al., 2019). Polypyrrole (PPY) is an electronically conductive polymer (ECP) with high electrical conductivity, biocompatibility, good stability, proper redox characteristics, ease of polymerization process compared to other ECP (Shahnaz et al., 2020). In this study, a nanocomposite of NC-3DPPY was developed by a simple sonication method. The 3DPPY was synthesized and incorporated with NC which facilitates the formation of an additional conductive path through the conjugated material and facilitates the charge transfer. The cross-linking structure of the NC and 3DPPY interconnects via the OH and NH groups and form a three-dimensional porous nanostructure and facilitates the dispersion of bimetallic nanoparticles of silver (Ag) and gold nanoparticles (Au), which reduces the aggregation with proper self-assembly of Ag-Au into the skeleton of NC-3DPPY (Shen et al., 2020).

2.7 Carbon-based nanomaterials

Since the past few decades, carbon-based nanomaterials have created a new avenue and technological revolution in different sectors of material science. Due to their extra-ordinary and tunable features, they are suitable for multipurpose applications. These types of materials possess several merits such as excellent mechanical integrity, porous surface, high active surface area, thermal conductivity and electronic distributions. Different forms of carbon-based nanomaterials such as carbon nanotubes (CNTs), graphene (Gr), carbon nanofibers, carbon nanohorns, nanocones-disks, fullerenes, nano-diamonds and their functionalized forms have been developed and studied intensely and successfully applied in different analytical applications (Akhter et al., 2020; Rajakumar et al., 2020).

2.7.1 Carbon nanotubes and their functionalization

Carbon nanotubes (CNTs), is a carbon nano-structured material, containing graphene nano-sheets rolled into a nano-shaped cylinder and possess attractive features such as high electro-conductivity, mechanical robustness and excellent catalytic activity. Carbon nanotubes consist of single-wall or multiple walls of sp^2 hybridized carbon atoms, where the CNTs exists as two types i.e. single-walled carbon nanotubes (SWCNTs) and multi-walled carbon nanotubes (MWCNTs). MWCNTs is comparatively cost-effective and possess excellent features such as high tensile strength, good mechanical and thermal stability, flexible elasticity and high electronic conductivity and catalytic activity (Rajakumar et al., 2020). The pristine CNTs are unsuitable for electrode fabrication as it is hydrophobic. Functionalization of the CNTs is based on the formation of functional groups on the outer walls of the CNTs which could be an effective strategy to increase the solubility of CNTs. The functionalization technique not only removes the impurities but also increases the dispersion ability of CNTs in water and enhances the electrochemical response (Zhu et al., 2020). In addition, abundant binding sites are exposed on CNTs through functionalization that facilitates fabrication of the electrodes. Generally, the functionalization process is accomplished by acid hydrolysis which involves one or two strong acids such as nitric acid, sulfuric acid and hydrochloric acid. Thus, CNTs have been applied enormously for the development of nanocomposites as electrochemical sensors (Shalauddin et al., 2019).

2.7.2 Nitrogen-doped graphene

Doping is an effective approach to modify the characteristics of carbon-based nanomaterials, to increase the density of free charge-carriers and to improve the electrical or thermal conductivity. Among the doping elements, nitrogen (N) is

considered an effective dopant for carbon-based nanomaterials. Due to its comparable size and number of valence electrons, nitrogen forms strong bonds with carbon atoms. Nitrogen-doped graphene (NGr) has good biocompatibility, high surface area and excellent electrochemical response (Anuar et al., 2018). NGr exhibits better electrocatalytic response than graphene (Gr) because of the unique electronic interactions between the lone–pair electrons of nitrogen and the π–π system of graphitic carbon. However, doping on Gr lattice improves the sensing affinity and the catalytic response towards the desired molecules and improves the selectivity of Gr based sensing device. There are several approaches available for the synthesis of NGr such as arc-discharge method, chemical vapour deposition (CVD), solvothermal method, microwave assisted method and plasma treatment etc. In the present study, microwave assisted approach has been applied for the synthesis of NGr (Gowthaman et al., 2017).

2.8 Nanomaterials and their synthesis approach

Nanomaterials are materials with the size of atoms less than 100 nm and possess distinct physicochemical characteristics based on their nano-size and shapes. Nanomaterials can be different types such as carbon nanomaterials (e.g carbon nanotubes, nitrogen-doped graphene), metal nanoparticles (e.g gold nanoparticle, silver nanoparticle), oxide nanoparticles (e.g copper oxide nanoparticle, zinc oxide nanoparticle). Due to their excellent characteristics, they have been enormously utilized for the development of electrochemical and bio-sensors (Pomerantseva et al., 2019).

The first step of an innovative research is to accomplish the preparation the desired nanomaterials successfully. But the development of an effective procedure for the nanomaterials synthesis by retaining the desired structural arrangements and morphology of the synthesized materials are the greatest challenge of nanotechnology. However, the synthetic procedures used for the synthesis of nanomaterials can be

classified into two groups such as the top-down and bottom-up approaches. The top-down approach can be divided into two groups such as the wet method and dry method. While in the milling or grinding methods, the nanomaterials are synthesized from the top-down approach to form tiny particles from the large particles by mechanical disintegration. While in the bottom-up synthesis method, the nanomaterials are generally extracted from the bulk materials and the desired nanomaterials are obtained by following the progressive removal (Gonzalez et al., 2021). On the contrary, nano-capsulation or nano-coatings can be obtained from a molecular levelled precursor and the gradual mobilization of the molecules occurs until the desired composition is formed successfully. Both of the bottom-up and top-down synthetic methods demand similar fundamentals and pre-requisites including fabrication parameters for example concentrations, time, energy from electrons and surrounding conditions for example contaminants, where the temperature should be properly controlled during the synthesis experiments (Rotello, 2004). Thus, nano-scale synthesis investigation requires highly sophisticated fabrication instrumentation accomplished in clean laboratory conditions. The nanomaterials synthesis approaches chart is shown in Figure 2.2. In this thesis, the microwave-assisted method, hydrothermal method and sonochemical method have been used for the synthesis of nanomaterials.

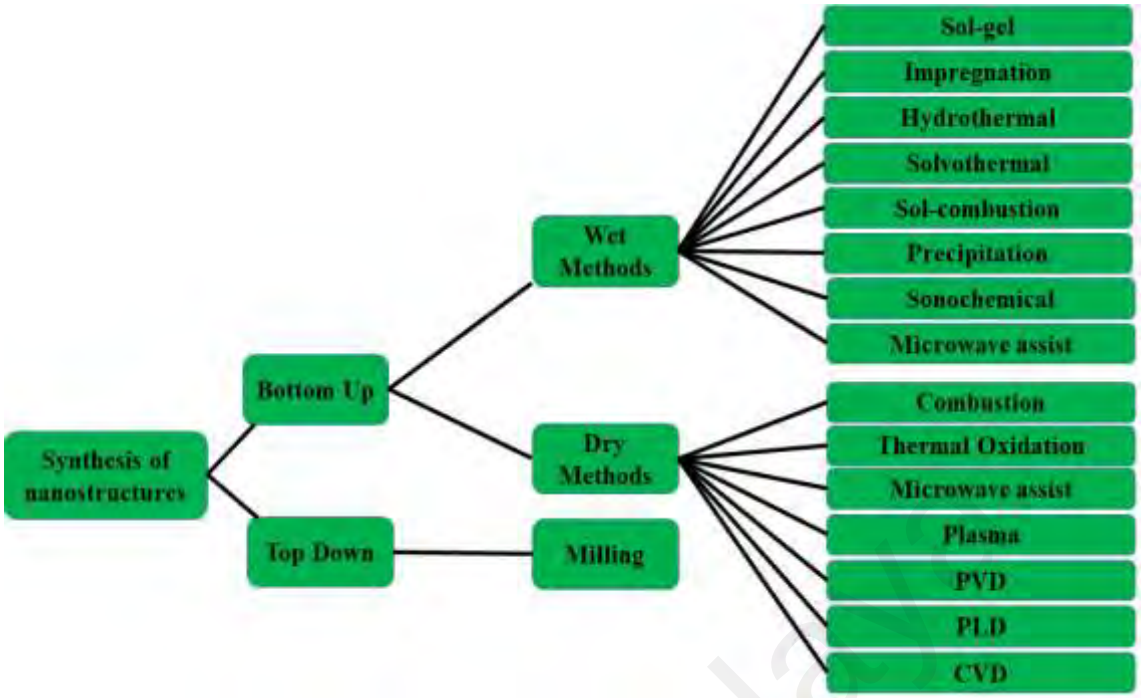

Figure 2.2: Synthetic routes of the nanoparticles (Rotello, 2004) (Reproduce with permission from the publisher).

2.8.1 Microwave-assisted method

Dipolar polarization and ionic transportation are the two mechanisms that are generally activated by microwave irradiation. The basic mechanism of the microwave-assisted method depends on the application of microwave electromagnetic radiation and through this, an excitation is generated on the aligning dipoles of the external area of a material (Sharma & Zalpouri, 2022). This is considered as an effective wet chemical approach for the nanomaterial synthesis with high reproducibility and contains several advantages such as controlled size and shape of nanomaterials by manipulating the reaction parameters including rapid volumetric heating, high reaction rates and energy efficiency etc. However, this microwave irradiation is used for those chemical reactions, where the presented materials are able to absorb the microwave generated energy and convert this energy into heat. The conversion process enables a non-equilibrium condition in the system. The generation of heat from the microwave method minimizes

the reaction time and improves the crystalline nature of the final product (Polshettiwar et al., 2009).

2.8.2 Solvothermal synthesis method

The solvothermal method is analogous to the hydrothermal method, except the synthesis process uses organic solvents instead of water. Alternatively, when alcohols and glycerol are used as the reaction media, the reactions are called alcohothermal and glycothermal, respectively (Nguyen, 2013). These synthetic strategies are important for the synthesis of nanomaterials with good crystalline properties. During the solvothermal approach, the chemical reaction initiates a solvent at a temperature greater than the normal boiling point by containing the reaction mixture within a sealed vessel such as an autoclave. These conditions enhance the solvent's capability to dissolve solids and accelerate the reactions between solid species. The main advantage of this method is that almost any material can be dissolved in the solvent by increasing the temperature and pressure to its critical point. In addition, this method enables the size control, shape distribution and high crystallinity of the metal based nanostructure composites (Jamkhande et al., 2019).

2.8.3 Sonochemical synthesis method

The sonochemical approach for nanomaterial synthesis is an effective approach for the synthesis of nanomaterials with outstanding characteristics. This synthetic route involves both the physical and chemical effects which offer a synergistic impact and can be utilized for the manufacturing of a broad range of nanostructured materials. Here, the molecules undergo chemical reactions due to the application of powerful ultrasound radiation (20 kHz–10 MHz). The basic mechanism of sonochemistry for the modification of nanomaterials arises from acoustic cavitation which is considered as a

physical phenomenon, which includes three steps: formation or construction, growth and collapse of the bubbles in any liquid solution. Some extreme reaction parameters are needed in this process such as high pressure > 500 atm, high temperature >5000 K and >1010 K/s of cooling rate, for the collapse of the cavities. These extreme conditions promote acoustic cavitation which enables the formation of materials possessing outstanding and uncommon features. The irradiation of highly intense ultrasonic energy forces the molecules to undergo high-energy chemical reactions (Bang & Suslick, 2010).

2.9 The development of electrochemical devices using nanocomposites

A composite material is the incorporation of two or more materials which have different chemical and physical properties compared to one another. A nanocomposite consists of at least one material in the nano-scale dimension. Nano structured materials have superior characteristics compared to bulk materials. Different types of nanomaterials such as carbon nanomaterials, metal and metal oxide nanomaterials, mineral nanoparticles, semiconductor nanoparticles have been studied and applied extensively for the fabrication of electrodes and sensing of the desired analytes, energy storage, supercapacitor, bio-fuel etc.

2.10 Analyte of interest

Nilutamide, paracetamol, methotrexate and ciprofloxacin are the analyte of interest, and are used in this research. Thus, the electrochemical determination of these desired analytes is the focus of this research.

2.10.1 Paracetamol

Paracetamol (PR) N-acetyl-P-aminophenol, or acetaminophen is a widely used over the counter (OTC) drug that is mainly used for its analgesic and anti-pyretic effect. In addition, it is used for the mitigation of different types of pain such as headache, toothache, backache and others. PR contains a benzene ring which has two substituent groups of hydroxyl and amide groups on the para (1,4) positions, as shown in Figure 2.3. It is an odorless white crystalline powder with a slightly bitter taste and good solubility in hot water. PR is a safe drug but excess consumption of this drug can cause adverse effects such as nephrotoxicity, increased mortality and liver damage. Thus, it is necessary to determine the overdose concentration of PR as a biomedical quality control via a facile, easy, accurate and sensitive analytical method (Anuar et al., 2018).

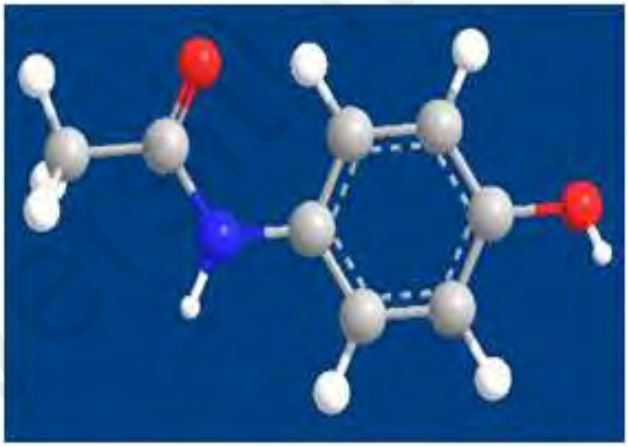

Figure 2.3: The 3D chemical structure of Paracetamol (N-acetyl-P-aminophenol) (Akhter et al., 2021) (Reproduce with permission from the publisher).

Several attempts have been reported for the determination of PR such as titrimetry, (Kumar & Letha, 1997), chromatography (Lohmann & Karst, 2006), chemiluminescence (Easwaramoorthy et al., 2001), high-performance liquid chromatography (HPLC) (Altun, 2002), UV spectrophotometry (Murtaza et al., 2011), capillary electrophoresis (Altria et al., 1994), tandem-mass spectrometry (Lou et al., 2010), thermogravimetric analysis (Calvino et al., 2021). These methods have good

precision, sensitivity and selectivity but they have some demerits such as high cost, complex operation procedures, laborious, tedious sample preparation, time-consuming and others. Thus electrochemical techniques have become the choice of preferences over the years as this method does not have drawbacks like the other traditional methods. Several electrochemical techniques have been investigated for the electrochemical determination of PR (Akhter et al., 2018; Anuar et al., 2018; Alanazi et al., 2021; Kokab et al., 2021; Yang et al., 2021) etc.

2.10.2 Nilutamide

Nilutamide (5,5-dimethyl-3-[4-nitro-3(trifluoromethly)phenyl] imidazolidine-2,4-dion) (NLM) is a synthetic and non-steroidal, anti-androgen compound which blocks the activity of androgen and is used for the treatment of advanced-stage metastatic prostate cancer due to its long half-life and acceptable tolerability shown in Figure 2.4. It has a longer life of $\simeq$ 56 h which is higher compared to other anti-androgen drugs. The elevated dosage of NLM can cause health hazards in the human body such as sexual dysfunction, interstitial pneumonitis, nocturnal amblyopia, nausea, decreased libido, visual disturbance, alopecia, blood in the urine, chest pain, difficulty in breathing, trouble with sleeping and vomiting (Sharma & Hwa, 2021). Considering the health issues, several methods have been developed by the researchers for the determination of NLM such as chromatography (Znaleziona et al., 2011), spectrophotometry (Carvalho et al., 2014), UV-visible spectrophotometry (Silva et al., 2018), automatic micro-flow system (Carvalho et al., 2014) etc. Several electrochemical methods of detection of NLM have been reported recently due to the cost-efficiency, early response, simple operation procedure, high sensitivity and selectivity (Karthik et al., 2017; Karthik et al., 2017; Akhter et al., 2020; Sundaresan et al., 2020; Kokulnathan et al., 2019; Rajendran et al., 2019; Akhter et al., 2021) etc.

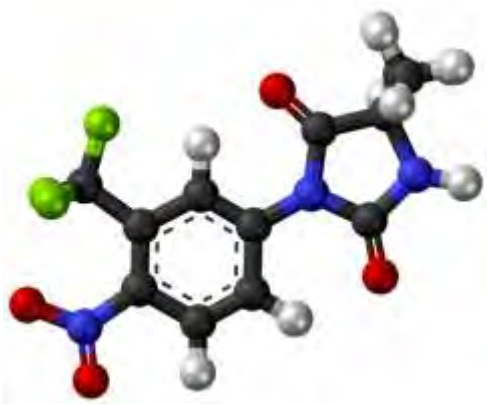

Figure 2.4: The 3D chemical structure of Nilutamide (5,5-dimethyl-3-[4-nitro-3-(trifluoromethyl)phenyl]imidazolidine-2,4-dion) (Sriram et al., 2021) (Reproduce with permission from the publisher).

2.10.3 Methotrexate

Methotrexate (MTX) (2,4-diamino-N-10-methyl folic acid) an anti-metabolite therapeutic agent (shown in Figure 2.5) is administered for the treatment of leukemia, breast cancer, head and neck cancer and autoimmune diseases. The clinical recommendation of MTX is limited due to its severe adverse effects such as ulcer in stomach, myelosuppression, hepatotoxicity and low white blood cell counts of this drug in human body. As MTX has a narrow therapeutic window, it is important to monitor the therapeutic levels to achieve the maximum therapeutic outcomes (Asadian et al., 2017; Jandaghi et al., 2020). Considering the health issues, several approaches have been reported for the detection of MTX including high-performance liquid chromatography (Kim et al., 2021), spectrophotometry (Hamidi et al., 2019), gas chromatography (Zong et al., 2020) etc. Due to the sharp and rapid response, high selectivity and sensitivity, easy and simple on-site and trace level detection, several voltammetric approaches have been reported for the detection of MTX (Salandari-Jolge et al., 2020; Tajik et al., 2021).

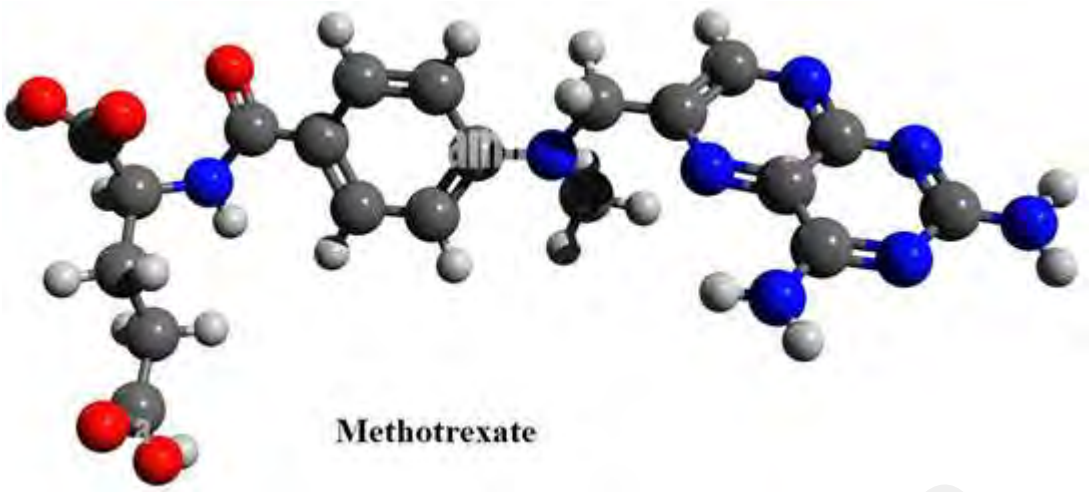

Figure 2.5: The 3D chemical structure of Methotrexate (MTX) (2,4-diamino-N-10-methyl folic acid) (Rana et al., 2020). (Reproduce with permission from the publisher).

2.10.4 Ciprofloxacin

Ciprofloxacin (1-cyclopropyl-6-fluoro-1, 4 dihydro-4-oxo-7-(1-piperazinyl)-3-quinoline carboxylic acid) (CIF) a third generation fluoroquinolone (shown in Figure 2.6), which is widely recommended antibiotics in clinical practice for the mitigation of several gastro-intestinal, urinary and respiratory tract infection. Overdose of CIF can cause severe hypersensitivity reactions, gastro-intestinal lesions etc. Besides, CIF is widely prescribed therapeutic agent for human and livestock animals (Reddy et al., 2018). Considering the health issues, several approaches have been reported for the detection of CIF including high-performance liquid chromatography (Zheng et al., 2019), spectrophotometry (El Demeiry et al., 2020) gas chromatography (Do & Stuckey, 2019) etc. Due to the sharp and rapid response, high selectivity, easy and simple on-site and trace level detection, several voltammetric approaches have been reported for the detection of CIF (Gill et al., 2021; Umesh et al., 2022).

Figure 2.6: The 3D chemical structure of Ciprofloxacin (1-cyclopropyl-6-fluoro-1, 4-dihydro-4-oxo-7-(1-piperazinyl)-3-quinoline carboxylic acid) (Li et al., 2018) (Reproduce with permission from the publisher).

The development of non-enzymatic electrochemical sensors for drug detection is an attractive approach to overcome the drawbacks of enzymatic sensors. Non-enzymatic electrochemical sensors possess advantages of high stability, good reproducibility and facile operation. Therefore, recent efforts for the direct detection of pharmaceutical drugs such as NLM, PR, MTX and CIF without the aid of enzymes could be achieved by the fabrication of modified electrodes based on metal ions and their nanomaterials based nanocomposites.

2.11 Sensor

A sensor is a type of device which responses to the presence of an analyte and the information received will be transduced into a measurable signal such as reduction or oxidation current, potential and impedance etc. Sensors can generate any signals as

thermal, electrical and optical output signals which can be transformed into digital signals for further processing. Generally, sensors can be classified into two groups, which is the chemical and physical sensor. A chemical sensor measures the changes in the composition, concentration and reaction rate of a chemical species. While a physical sensor measures the physical quantity related to the physical changes such as pressure, temperature, force and speed (Sakaguchi et al., 2007).

2.11.1 Chemical sensor

A chemical sensor is a device which transforms the information received from its surrounding chemical species into a useful analytical signal. Generally, a chemical sensor consists of two basic components which are a receptor and a transducer as in the schematic diagram in Figure 2.7. The receptor interacts with the chemical species and converts the chemical information into a form of energy that can be detected by a transducer. Thus, the transducer is used to transform the response from the receptor into a measurable signal. The chemical sensors can be classified into different groups such as optical, electrical and thermal or gas sensors etc. The benefits of these sensors are that they can detect and receive the signal from an analyte from the solid, liquid or gaseous medium (Janata, 2002). An electrochemical sensor is a type of device that can document the electrochemical reaction at the electrode-electrolyte interface and transforms the information into an analytical signal. Since the past few decades, these types of sensors have been developed and applied extensively due to their several advantages such as miniaturization, simple composition and operation procedure, rapid result and cost-effectiveness compared to other types of sensors (Alegret & Merkoçi, 2007).

Electrochemical sensors can be divided into three groups such as the potentiometric, amperometric and conductometric sensor. In amperometric sensors, the current is

measured by the alternating current (A.C) or direct current (D.C) mode. These types of sensors may or may not require an external current source. In the potentiometric sensor, an equilibrium is reached at the electrode interface and the potential of the working electrode is measured against a reference electrode. The composition of an analyte can be obtained by the difference between the potential of the indicator (working) electrode and the reference electrode. Conductometric sensors are based on the measurement of conductivity in multiple frequency series (Janata, 2009; Janata & Bezegh, 1988; Janata & Huber, 1985; Wang, 1988).

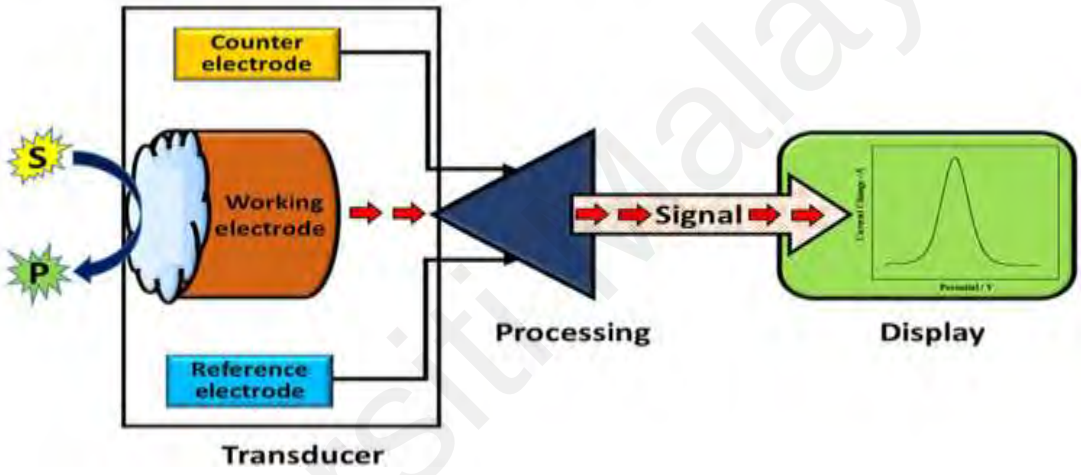

Figure 2.7: Basic mechanism of a chemical sensor (Yin et al., 2018) (Reproduce with permission from the publisher).

Electrochemical sensors can be classified into two groups- enzymatic and non-enzymatic electrochemical sensors. Enzymatic electrochemical sensors are the integrated self-contained receptor-transducer devices which able to provide selectively quantitative analytical information using a biologic recognition element, which is in direct spatial contact with a transducer element (Ji et al., 2020). In enzymatic electrochemical sensors, different types of enzymes are incorporated such as peroxidase, lactase, reductase etc. Here, the enzymes act as the catalyst and facilitate the transfer of electrons between the electrode and analytes during detection. Though this approach has excellent selectivity and sensitivity, the instability of the enzymes is the main drawback for the practical application of this type of sensor. The complex immobilization process

and the instability of the enzyme affect the reproducibility of these sensors. Moreover, the performance the sensor is influenced by environmental factors such as temperature, humidity and pH (Amala & Gowtham, 2017). To minimize these disadvantages, non-enzymatic electrochemical sensors have been studied and developed. The non-enzymatic sensing has been in the research limelight, and most sensors based on the nanomaterials are designed to detect single or multiple analytes. The detection mechanism of non-enzymatic electrochemical sensor relies on the calculation of the current flow or amperometry, which depends on either the oxidation or reduction process, even on both the oxidation and reduction of the analytes. As the non-enzymatic electrochemical sensor does not contain the biological recognition components, they show longer lifetime with greater reproducibility and stability compared to enzymatic electrochemical sensors (Hwang et al., 2018). Due to having improved stability and sensitivity, the non-enzymatic electrochemical sensors have gathered tremendous interest for sensor applications (Rhouati et al., 2018). The comparison between enzymatic electrochemical sensor and non-enzymatic electrochemical sensor is shown in Table 2.1.

Table 2.1: Comparison between enzymatic electrochemical sensor and non-enzymatic electrochemical sensor

Electrochemical sensor	Advantage	Disadvantage	References
Enzymatic electrochemical sensor	High selectivity and sensitivity and catalytically active	A loss of activity when immobilized to transducer	(Ji et al., 2020)
	Improved sensitivity	Expensive and complex immobilization process of enzymes	(Farzin et al., 2018)
	Fairly fast-acting	Poor stability mostly due to the degradation of enzymes	

Table 2.1 continued

Electrochemical sensor	Advantage	Disadvantage	References
Non-enzymatic electrochemical sensor		Temperature, humidity and pH influences the sensitivity of the sensor	
	High stability, selectivity, catalytically active and rapid detection	High working potential,	(Hwang et al., 2018)
	Rapid detection, highly sensitive, simplicity and possibility of continuous analysis on different analytes	Slow electrode kinetics	(Hwang et al., 2018)
	Wide linear range and low detection limit	Poisoning possibilities from intermediate species	
	Low cost and Portable	weak sensing parameters	

2.11.2 Chemically modified electrodes (CMEs)

The application of electrochemical techniques involves the utilization of chemically modified electrodes (CMEs). A chemically modified electrode is prepared by the surface modification with specific materials to produce an electrode with different performance or properties from the unmodified substrate. Thus, the modified electrode shows similar properties as the modifying materials. The schematic diagram of a chemically modified electrode is presented in Figure 2.8. Different types of electrodes have been used for the fabrication of CMEs such as boron-doped diamond electrode, glassy carbon electrode, screen printed electrode, gold electrode, diamond carbon paste electrode and indium tin oxide (ITO), fluorine-doped tin oxide (FTO) as substrate (Smyth & Vos, 1992). At the CMEs, the oxidation or reduction reaction occurs by the transfer of electrons between the electrode and the analyte. CMEs are different compared to other classes of electrodes, as the thin layer of a suitable material is coated or bound on the surface of the electrode to provide special chemical features. One of the distinct properties of CMEs is the electrocatalytic properties used in electroanalytical

measurements (Murray, 1980). They have several advantages such as rapid response, reusable, resistance towards fouling, limiting the effect of interference molecules in any complex solution, enhancing the electrocatalytic effects, chemically and thermally stable, cost-efficient, readily available, high sensitivity and selectivity. Among the methods, the drop-casting method onto a glassy carbon electrode (GCE) was applied in this study. In this method, a small amount of material solution is drop onto the electrode surface followed by the evaporation of the solution. GCE is preferable due to the low cost, chemical inertness, low background current and broad potential window (Raoof et al., 2004).

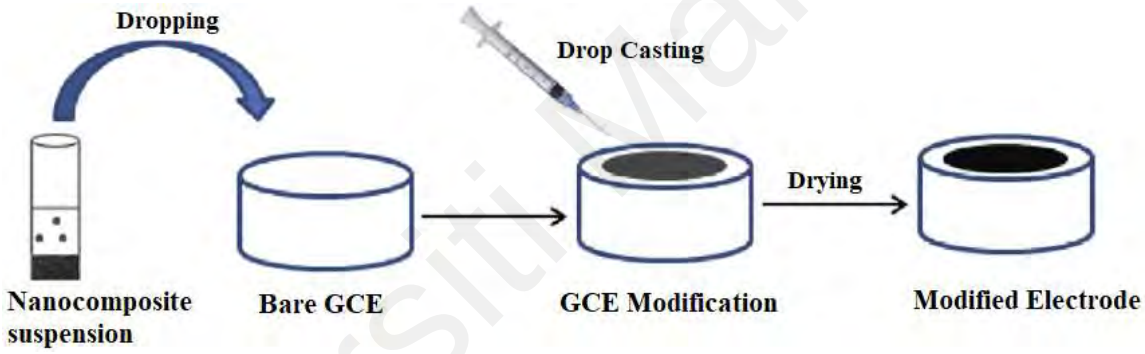

Figure 2.8: Modification of electrode (Beitollahi et al., 2019) (Reproduce with permission from the publisher).

2.12 Electroanalytical techniques

An electrochemical sensor can determine the analytes through qualitative and quantitative analysis. Electroanalytical chemistry is based on quantitative analysis which relies on the electrical characteristics of analytes solution in the electrochemical cell. The electroanalytical methods show high sensitivity with good reproducibility, precision and accuracy and also broad linear range which have been extensively utilized in several fields of science such as environmental, industrial and pharmaceuticals. Electroanalytical techniques are used to determine the concentration or chemical reactivity of an analyte based on the measurement of potential, current or charge. There

are several types of electroanalytical techniques such as voltammetric, potentiometric and coulometric techniques (Bard, 1980).

Voltammetric methods are the measurement of the current variations from the electrochemical reactions of the analyte which occurs at the electrode surface. The basic mechanism of voltammetry involves an electrochemical cell containing three electrodes- working electrodes (WE), counter or auxiliary electrode (CE) and reference electrode (RE). The working electrode is the electrode where an electrochemical reaction under investigation occurs while the counter (CE) or auxiliary electrode is merely to complete the electrical circuit. The potential of the electrochemical cell is simply the potential difference between the WE and the CE. A reference electrode is introduced into the electrochemical cell (three electrode system) when the potential of the CE does not remain constant. The RE maintains its constant potential even the concentration of chemical species changes in the solution. The schematic diagram of a three electrode system electrochemical cell is presented in Figure 2.9. The electrodes are immersed in a container which consists of a supporting electrolyte and chemical species to be examined. The supporting electrolyte should be inert and does not easily oxidize or reduce. The supporting electrolyte is important because decreases the resistance of the solution and removes the influence the electromigration. The flow of current between the WE and CE is a function of potential and is measured by an instrument called potentiostat or galvanostat. This voltammetric measurement is drawn through the current versus potential plot which is referred as the voltammogram (Stradiotto et al., 2003).

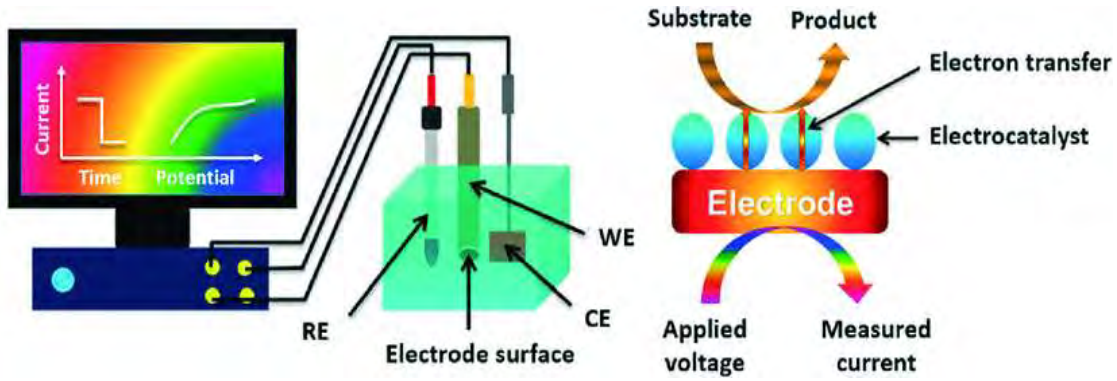

Figure 2.9: The three electrodes system electrochemical cell (Karimi-Maleh et al., 2020) (Reproduce with permission from the publisher).

2.12.1 Cyclic voltammetry

Cyclic voltammetry (CV) is an extensively applied electrochemical technique which is generally used for the preliminary assessment of the oxidation and reduction reaction of the chemical species. The electrochemical characteristics of an analyte in solution or a molecule adsorbed on the electrode surface can be studied by CV. The CV technique is conducted by cycling the potential of the WE versus the RE and measuring the current flow between the WE and the CE. The WE potential is usually measured against a RE which contains a stable and known potential. The applied potential generates an excitation signal (Farghaly et al., 2014). The potential scan can be negative from a more positive potential to a more negative potential. The switching potential is a state where a sufficient voltage is reached to undergo an oxidation or reduction reaction of the analyte. The reversibility or irreversibility of the target analyte can be determined from the voltammograms. Besides that, the parameters such as anodic and cathodic peak current, as well as anodic and cathodic peak potential are also examined from the voltammograms. For the reverse potential, the scan could be from positive to negative. When an oxidation reaction is required for some analytes, the potential is scanned to the positive direction (Cazes, 2004). The voltage rate shifts over time, during each of the phases is called the scan rate of that specific experiment. If the electron transfer is fast on the surface of the WE and when the current is limited by the diffusion of the analytes

to the electrode surface, then the peak current is proportional to the square root of the scan rate. The relationship can be explained through the Randles-Sevcik equation. Then, the experiment samples a little portion of the solution such as the diffusion layer of the electrode surface. In sensor applications, the CV experiments are used to determine the electrochemical performances of the unmodified and different modified electrodes in the presence and absence of the target analytes. The influences of different pH, pH optimization, influences of different scan rates and scan rate optimization are also accomplished by this technique. The active surface area of the electrode can also be calculated using the Randles-Sevcik equation from the CV technique. The Randles-Sevcik equation is as follows:

$$i_p = 2.69 \times 10^5 \, A \, C \, D^{1/2} \, (n)^{3/2} \, \upsilon^{1/2} \qquad (2.1)$$

Here, i_p = redox peak current (Amp), A = surface area of the electrode (cm^2), n = number of transferred electrons, C = concentration of the ferricyanide solution (mol cm^{-3}), D = diffusion coefficient (7.60×10^{-6} cm^2 s^{-1}) and υ = scan rate (V s^{-1}).

2.12.2 Pulse voltammetry:

This voltammetry is often used for the quantitative analysis of the target analyte. Pulse voltammetry is more sensitive than cyclic voltammetry as the double layer charging current is minimized. Pulse voltammetry can be classified into differential pulse voltammetry, normal pulse voltammetry and square wave voltammetry (Sharp et al., 1984).

2.12.3 Differential pulse voltammetry

Differential pulse voltammetry (DPV) is an effective analytical technique for quantitative electrochemical analysis, the investigation of the kinetics, mechanism of the electrochemical reaction. DPV is a sensitive technique which is similar to squarewave voltammetry but offers multiple benefits over other electrochemical techniques. These

techniques possess short pulse time which enhances the measured Faradic current and minimizes the non-Faradaic current. The DPV technique is used for the evaluation of the analytical application of an electrochemical nano-device (Baranowska et al., 2008). The highest to lowest analytic concentration range (linear range) and the lowest concentrations of analytes i.e limit of detection (LOD) can be calculated by the corresponding curves in this technique. The LOD can be calculated by the following equation.

$$LOD = 3 \times S_b/m \tag{2.2}$$

Here, 3 is the signal to noise ratio of 3, S_b denotes the standard deviation of the blank sample and m denotes the slope of the calibration curve.

2.12.4 Chronoamperometry

Chronoamperometry is an amperometric method, where the square-wave potential is applied to the working electrode and a steady-state current is measured as a function of time. The changes in the current arising from the expansion or reduction of the diffusion layer at the electrode. The concept of a diffusion layer was introduced by Nernst and states that there is a stationary thin layer of solution in contact with the electrode surface which is known as the Nernst diffusion layer shown in Figure. 2.10. The solid line represents the actual concentration profile and the dashed line from C surface is the extrapolation of the initial slope. The local analyte concentration drops to zero at the electrode surface and diffusion controls the transfer of analyte from the bulk solution of higher concentration to the electrode. This results in a concentration gradient away from the electrode surface. In the bulk solution the concentration of analyte is maintained at a value of c_o by convective transfer (Gosser, 1993).

In this thesis, voltammetric techniques such as cyclic voltammetry (CV), differential pulse voltammetry (DPV) and square-wave voltammetric (SWV) methods are described. The electrochemical performance and optimization of the electrochemical sensor are studied by cyclic voltammetry. Besides this, the quantitative analysis of the target analyte was performed by DPV and SWV methods.

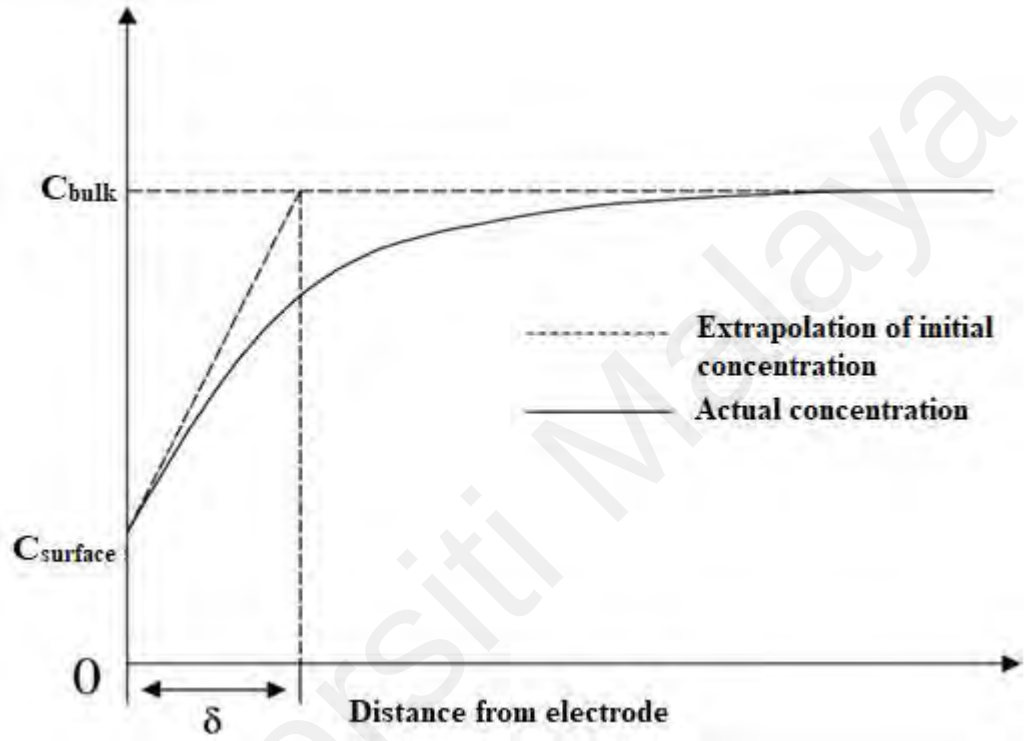

Figure 2.10: Nernst diffusion layer model (Janssen & Hoogland, 1973) (Reproduce with permission from the publisher).

2.13 Electrochemical impedance spectroscopy (EIS)

Electrochemical Impedance Spectroscopy (EIS) introduces a more general concept of resistance. In direct current (DC) circuits, only resistors oppose the flow of electrons. In alternating current (AC) circuits, the capacitors and inductors influence the flow of electrons (impedance) in addition to resistors. Electrochemical impedance spectroscopy is usually measured by applying an AC potential with a small amplitude (Vrms of 5 to 10 mV) to an electrochemical cell and measuring the current flow through the WE (Willner & Katz, 2006). The advantage of EIS is that the electrochemical interface can

be modeled by using purely electrical circuits. An electrode-electrolyte interface undergoing an electrochemical reaction is represented as an electronic circuit consisting of a combination of resistors and capacitors. Thus the Randles circuit consists of a solution resistance (R_s) in series with the parallel combination of the double-layer capacitance (C_{dl}) and an impedance of the Faradaic reaction of interest which consists of charge transfer resistance (R_{ct}) and the Warburg diffusion element W.

2.14 The development of electrochemical sensor using nanocomposite materials

A composite material is the incorporation of two or more materials which are usually different from one another with regards to the chemical and physical properties. While nanocomposites are composite materials, where at least one dimension in the nanometer scale. The rise in the number of publications involving nanocomposite materials in various research areas confirms the extra-ordinary properties of nanostructured materials compared to the bulk materials. The functionalization of nanocomposite materials is very crucial to improve the electrochemical sensor performance by promoting better electrochemical properties such as outstanding electrocatalytic activity, fast electron transfer rate and high conductivity (Munonde & Nomngongo, 2021).

2.14.1 Development of metal-based nanocomposites

In recent years, different metal ions such as copper, cobalt, nickel, etc have been broadly utilized in electrochemical sensor applications especially for their catalytic properties with the incorporation of different carbon-based nanoparticles such as multiwall carbon nanotubes, graphene and nitrogen-doped graphene. The incorporation of metal ions and carbon nanomaterials enhances the electrochemical conductivity due to the synergy of the electrocatalytic effect. In addition, different biopolymers such as

chitosan and nanocellulose have been used for the construction of nanocomposites along with the metal ion and carbon nanomaterials, which ultimately enhances the nanomaterials dispersion, enables a modulus configuration when combined with metal ions and possesses the characteristics of natural enzymes, preventing the fouling of nanomaterials and ultimately increases the catalytic effect of the developed nanocomposites.

Mao et al., 2017 reported a non-enzymatic electrochemical sensor based on multiwall carbon nanotube, chitosan and nickel complex using a self-assembly technique for the determination of metronidazole. They modified a glassy carbon electrode (GCE) with MWCNTs/CTS-Ni and analysed it using a simple and inexpensive CV and DPV method. They demonstrated that the electrode showed excellent electrocatalytic performance for the oxidation of paracetamol in pH 7.0 PBS with good stability, high selectivity and sensitivity, wide linear range and a low detection limit. Shalauddin et al., 2017 reported a nanocomposite of multiwall carbon nanotube, chitosan and copper by a self-assembly technique. They modified the GCE by drop-casting onto a GCE surface and studied by CV and square wave voltammetry. The developed FMWCNTs/CTS-Cu showed a high electrochemical response for the determination of diclofenac sodium from biological fluid and pharmaceutical dosage forms with a broad linear range and low limit of detection. Akhter et al., 2020 developed a nanocomposite of MWCNT, nitrogen-doped graphene, chitosan with electrodeposited of Cu on the surface of GCE for the electrochemical detection of an anticancer drug NLM. They modified the GCE by drop-casting onto GCE surface and studied the CV and DPV. The developed MWCNTs$_f$-NGr/CTS-Cu showed excellent electrochemical behaviour for the determination of NLM from biological fluid and pharmaceutical dosage forms with broad linear range and low limit of detection. While Akhter et al., 2018 reported a nanocomposite of immobilized cobalt on the

functionalized MWCNTs and CTS thin film for the determination of painkiller PR with a broad concentration range and low detection limit. The developed *f*MWCNTs-CTS/Co nanocomposite was studied by CV and DPV method for paracetamol detection from biological fluids and pharmaceutical dosage forms.

Recently, the applications of tri-metallic MOF have been observed in different fields of material science. Compounds based on the first row of transition metals (such as Fe, Co, and Ni) have enhanced the electronic occupancy status by improving the electron transfer ability, and have been widely studied to replace the precious metal-based electrocatalysts. The interaction between various compositions in a multi-metal structure can produce additional synergistic effects and leads to better electronic properties, forming a multi-metallic structure which is widely considered as a new approach for the design of new nanocomposites (Abbas & Tahir, 2021). The tri-metallic MOF sheets accelerate the ion exchange process due to the nanoscale configuration. They are highly crystalline, possess dynamic, porous frameworks of highly ordered networks which enhance the structural flexibility and transformability. In addition, they show prominent chemical reactivity, diverse morphologies, high selective detection and sensitivity, enhanced electronic charged transfer, virtuous stability, lattice strain, distinct geometric effects and chemical transformation compared to the monometallic MOFs (Li et al., 2021). Furthermore, they exhibit greater catalytic effects and improved selective catalysis than monometallic and bimetallic MOFs composites. Due to these excellent features, tri-metallic MOFs have sparked tremendous attention among researchers for various applications especially for the development of sensors. Akhter et al reported a tri-metallic nanocomposite of cobalt, nickel, and copper Co-Ni-Cu synthesized on the nickel foam (NF) for the detection of anticancer drug NLM. The Co-Ni-Cu/NF fabricated sensor showed excellent electrochemical response for the detection of NLM with a broad linear range, low detection limit with high selectivity, stability and

sensitivity (Akhter et al., 2021). Qui et al reported a tri-metallic platinum (Pt), gold (Au) and silver (Ag) nanodendrites (NTs) modified GCE sensor for methanol detection. The fabricated trimetallic Pt.Ag.Au NTs/GCE sensor was studied using CV method and showed high sensitivity and selectivity with a broad linear range and low detection limit (Qiu et al., 2020). Subhan et al developed a tri-metallic molybdate oxide (MoO_2), iron oxide (Fe_3O_4) and copper oxide (CuO) nanocomposite for the fabrication of para-nitrophenol sensor. The developed $MoO_2 \cdot Fe_3O_4 \cdot CuO$/nafion/GCE sensor was analysed using an amperometric method and showed excellent catalytic activity towards the detection of para-nitrophenol with high selectivity and broad linear range and low detection limit (Subhan et al., 2020).

Table 2.2 Transition metal ion-based nanocomposite for electrochemical sensor applications

Nanocomposite	Method	Electrode	Analyte	References
(f-MWCNT-$Ni(OH)_2$)	Synthesis of f-MWCNT by acid treatment and f-MWCNT-$ni(OH)_2$ by ultrasonication	GCE	Folic acid	(Winiarski et al., 2020)
f-MWCNT-CTS/Co	Synthesis of *f*-MWCNT by acid hydrolysis and *f*-MWCNT-CTS/Co by ultrasonication and self-assembly method	GCE	Paracetamol	(Akhter et al., 2018)
Cu/MnO_2/MWCNTs Cu–	Synthesis of Cu/MNO2/MWCNT by ultrasonication and chemical reduction	GCE	Glucose	(Wang et al., 2016)
CS/MWCNT/GCE	Synthesis of Cu–CS/MWCNT/GCE nanocomposite by wet chemical method	GCE	Rutin	(Gholivand, et al., 2016)
OM-MnFeOx	Synthesys of oxidized multiwall carbon nanotubes by acid hydrolysis and OM-MnFeOx/GCE nanocomposite by hydrothermal method	GCE	Hydroquinone and Catechol	(Chen et al., 2019)
MWCNT-CTS/Cu	Functionalized MWCNT by acid treatment and MWCNT-CTS/Cu nanocomposite by ultrasonication and self-assembly method	GCE	Paracetamol	(Mao et al., 2015)

Table 2.2 continued

Nanocomposite	Method	Electrode	Analyte	References
Zn-Co-Ni MOF@CNT	Synthesis of tri-metallic Zn-Co-Ni MOF@CNT nanocomposite by template assisted method	Alumina electrode substrate	Hydrogen sulfide	(Tan et al., 2020)
Au@AgPdNPs-β-CD-IL	Synthesis of Au@AgPdNPs by Frens method using sodium citrate and ascorbic acid. Synthesis of Au@AgPdNPs-β-CD-IL by ultrasonic agitation method	GCE	Carbamazepine	(Daneshvar & Rounaghi, 2017)
Co-Ni-Cu/NF	Synthesis of Co-Ni-Cu/NF by hydrothermal method	Nickel Foam substrate (NF)	Nilutamide	(Akhter et al., 2021)
AuPdPt NPs@RGO	Synthesis of trimetallic AuPdPt NPs@RGO by hydrothermal method	GCE	Retigabine	(Alkahtani et al., 2019)
NiFeCo	Synthesis of NiFeCo by hydrothermal method	GCE	Hydrazine	(Annalakshmi et al., 2019)

Table 2.3 Transition metal-based nanocomposite in other electrochemical applications

Applications	Nanocomposite	References
Supercapacitor	Fe_2O_3 nanoparticle anchored graphene/CNT nanocomposite synthesized by hydrothermal method	(Ding & Wu, 2020)
	(CNFs/PCN) hybrid nanocomposite synthesized by wet chemical method for the development of supercapacitor	(Wang et al., 2020)
	Trimetallic fluoride Ni–Co–M (M = Mn, Fe, Cu, Zn) nanoprisms synthesized by co-precipitation method for supercapacitor	(Zhou et al., 2020)
Tissue engineering	PU-CoNP nanocomposite synthesized by electrospinning method for cardiac tissue applications	(de Laia et al., 2020)
	Cobalt-substituted hydroxyapatite (COHA) synthesized by electrodeposition for bone generation	(Lin et al., 2020)
Energy storage	MnO_2-Cu_2 composite synthesized by hydrothermal approach for energy storage applications	(Racik et al., 2020)
	$CuMnO_2$-gCN nanocomposite synthesized by one step chemical reduction method for energy storage applications	(Siwal et al., 2020)
	Trimetallic Cu_2MSnS_4 composite synthesized by sequential crystallization method for energy storage applications	(Sahoo et al., 2020)
Fuel cell	$CoNiFeO_x$-NC composite synthesized by ion exchanged strategy	(Chen et al., 2021)
	Au-NT-G nanocomposite synthesized by reduction electrode method	(Latif et al., 2020)

CHAPTER 3: METHODOLOGY

This chapter presents the experimental procedures for the synthesis of transition metal-based nanocomposites. The instruments applied in the characterization of the nanocomposites and electrochemical sensors are also described in detail.

3.1 Materials

All chemicals and reagents in this experimental procedure were used as received, without any further purification. All of them are listed in Table 3.1 together with the purities and suppliers.

Table 3.1: List of chemicals and reagents used

Chemical/Reagents	Purity	Supplier
Paracetamol	99.0%	Sigma Aldrich
Pristine MWCNTs	99.4%	Bay Tubes
Cobalt(II) Chloride Hexahydrate	99.0%	Sigma Aldrich
Chitosan	99.0%	Sigma Aldrich
Acetic Acid	99.0%	Sigma Aldrich
Glucose	96.0%	Sigma Aldrich
Dopamine	98.0%	Sigma Aldrich
Ascorbic Acid	99.7%	R&M Chemicals
Uric Acid	99.0%	Sigma Aldrich
Sucrose	99.6%	Sigma Aldrich
Fructose	99.2%	Sigma Aldrich
Sulfuric Acid	98.0%	Sigma Aldrich
Acetone	99.8%	Merck
Nitric Acid	98.0%	Sigma Aldrich
Ethanol	99.9%	Merck
Dipotassium hydrogen phosphate	99.0%	Merck
Potassium dihydrogen phosphate	99.5%	Merck
Potassium hexacyanoferrate (II) trihydrate	98.5%	Sigma Aldrich
Potassium hexacyanoferrate (III)	99.0%	Sigma Aldrich
Hydrazine Hydrate	51.0%	Acros Organic
Nilutamide	99.0%	Sigma Aldrich
Copper (II) Chloride dehydrate	98.0%	Sigma Aldrich
4-Nitrophenol	99.0%	Sigma Aldrich
Nitrobenzene	99.0%	Sigma Aldrich
Metronidazole	97.0%	Sigma Aldrich
nickel (II) chloride hexahydrate	98.0%	R&M Chemicals
Terephthalic Acid	98.0%	R&M Chemicals
Nickel Foam(NF, 110PPi)		R&M Chemicals
Dimethyl Formamide	99.9%	R&M Chemicals
Hydrochloric Acid	37.0%	R&M Chemicals
Ascorbic Acid	99.5%	Sigma Aldrich

Table 3.1 continued

Chemical/Reagents	Purity	Supplier
Phytic Acid	98.2%	Merck
Ammonium Persulfate	99.4%	Merck
Tetra Choloroauric Acid	99.8%	Merck
Silver nitrate	99.8%	Merck

3.2 Preparation of transition metal-based nanocomposite

3.2.1 Preparation of functionalized MWCNTs (MWCNTs$_f$)

The preparation of functionalized MWCNTs was performed by the acid hydrolysis method (Karthik et al., 2017). Firstly, pristine MWCNTs was dissolved in a combined solution of HNO_3 and H_2SO_4 (1:3) and followed by reflux for 24 h. Then the obtained carboxylated MWCNT (MWCNT-COOH) suspension was diluted using (deionized water) DIW and filtered using Whattman filter paper. The collected residue was rinsed several times using DIW until reaching nearly pH 7.0. The final product of MWCNTs$_f$ was properly dried at 80 °C in an oven for 24 h.

3.2.2 Preparation of nitrogen-doped graphene (NGr)

The synthesis of NGr was accomplished using microwave-assisted approach (Anuar et al., 2018), where graphene oxide (GO) was used as the initial substance for the synthesis of NGr. GO was prepared using Hummer's approach. Firstly, the GO suspension was obtained by dispersing 5 mg of graphite in 25 mL distilled water and sonicated in an ultrasonic bath for 40 min. Then 0.2 mg mL^{-1} quantity of GO suspension was ultrasonicated for 30 min to achieve a yellow-brown dispersion. To start the chemical reduction, 0.8 mL of hydrazine was added into the GO dispersion. The solution was irradiated through high power mode activated microwave oven for 5 min. Finally, the desired NGr was obtained by the centrifugation and properly dried at 50 °C.

3.2.3. Synthesis of NC

NC was synthesized from the precursor material micro fibrillated cellulose followed by the previous literature described elsewhere (Shalauddin et al., 2019). The cellulose powder was dissolved in a mixture of HCl and H_2SO_4 (1:3) and was refluxed for 16 hrs. DIW was used to dilute the mixture of solution and centrifuged at 2000 RCF. For neutralization, 0.1M NaOH was added into the mixture until the pH of the solution becomes stable at pH 7.0. Then, a membrane tube was used to wash the solution 3 times with 150 mL of DIW followed by dialyzation with continuous stirring for 24 hrs. Then the obtained product was filtered and dried in an oven at 70 ºC for 24 hrs. The final product was obtained as a powder with a pale white appearance.

3.2.4. Synthesis of 3DPPY

The synthesis of 3DPPY was carried by acid hydrolysis method (Wang et al., 2014). Firstly, 1.15 mL of pyrrole (Py) monomer and 3 mL of phytic acid solution were added into 50 mL of DIW and magnetically stirred for 10 min at 0 –5 °C. An oxidant, ammonium persulfate (APS) (3.5 g) was dispersed in 20 mL of cold water and added to the above mixture under thorough stirring via a mechanical stirrer for 2 min to initiate the polymerisation. Then, the solution was kept still for 15 min to produce the 3D structured PPY. The 3DPPY was collected in a Buchner funnel connected to a suction flask, washed several times with DIW, and subsequently dried to yield a sheet.

3.2.5 Synthesis of bimetallic Ag-Au nanoparticles

The synthesis of Ag-Au bimetallic nanoparticles has been accomplished according to previous work (Hu et al., 2020). At first, 18.0 mL of DIW was added to each of three 50-mL of polypropylene centrifuge tubes. Then, 5.0 mM of chloroauric acid ($HAuCl_4 \cdot 3H_2O$) solution was added to each tube. Next, 10.0 mM of sodium

borohydrate ($NaBH_4$) solutions were prepared immediately before use. Two 1000-µL autopipettors were ready to be used for the rapid injection of the 5.0 mM silver nitrate ($AgNO_3$) and $NaBH_4$ stock solution to the $HAuCl_4$ solution under vortex mixing, to achieve a BH_4 – metallic complex. The resulting solutions, which immediately turned a shade of red to yellow depending on the metal ratio. Additional 20 s of the vortex was continued to produce a uniform bimetallic Ag-Au nanoparticle solution. All solutions were kept at room temperature and stored protected from light.

3.2.6 Activation of glassy carbon electrode (GCE)

Before fabrication, GCE surface was polished to a mirror-like surface on a Buehler microcloth using 0.05 mm alumina and rinsed several times with DIW. Next, the GCE surface was sonicated in the presence of ethanol and water (50% v/v) for 2 min and washed thoroughly and dried properly.

3.3 Fabrication of modified sensor

3.3.1 Fabrication of (MWCNTs$_f$ –NGr/CTS)-Cu nanocomposite

Firstly, MWCNTs$_f$ and NGr powder (1 mg) were dissolved individually in 2 mL of DIW using ultrasonication for 45 min to get a uniform solution. Next, 1 mL solutions were taken from both MWCNTs$_f$ and NGr solution and mixed together via ultrasonication for 1 h to produce a uniform MWCNTs$_f$–NGr suspension. The CTS solution was prepared by dissolving 25 mg amount of CTS powder (white colour) in 50 mL of 0.10 M acetic acid. 0.1 g of $CuCl_2.2H_2O$ powder was dispersed in 100 mL of DIW to afford the $CuCl_2$ solution. 6 µL of MWCNTs$_f$–NGr suspension was micropipette and drop-casted on the surface of GCE. After proper drying at open-air, MWCNTs$_f$–NGr/GCE was dipped into the CTS solution for 20 min for the immobilization of CTS and dried in room temperature. For the electrodeposition of Cu,

the (MWCNTs$_f$ –NGr/CTS)/GCE was placed in an electrochemical cell that contain $CuCl_2$ solution and the CV experiment was performed at - 0.7 V to - 0.1 V potential range, for 50–250 s and at 10 mV s^{-1} scan rate. The schematic diagram for the preparation of (MWCNTs$_f$ –NGr/CTS)-Cu/GCE sensor is shown in Figure 3.1.

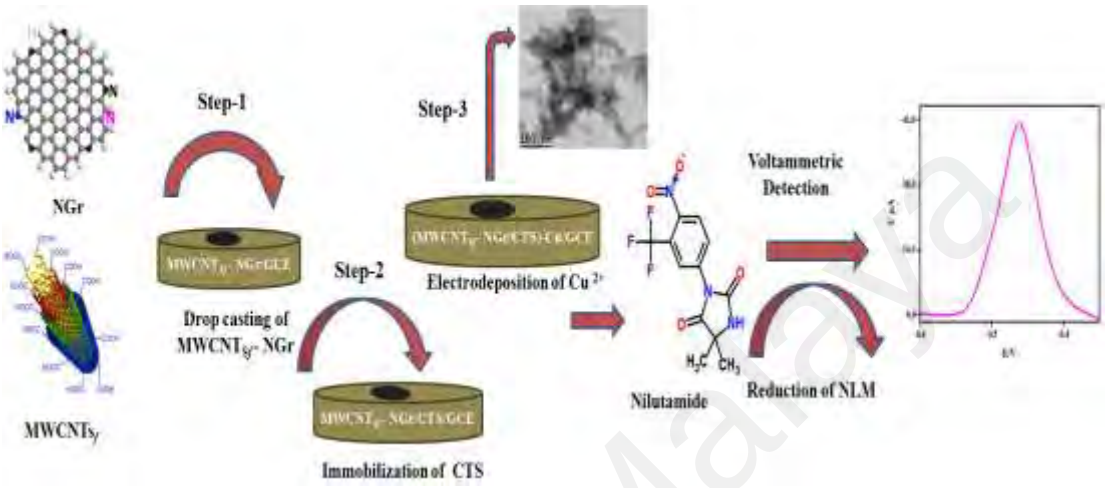

Figure 3.1: Schematic diagram for the preparation of (MWCNTs$_f$ –NGr/CTS)-Cu sensor for the electrochemical detection of NLM.

3.3.2 Fabrication of *f*-MWCNTs/CTS-Co nanocomposite

At first, 2 mg quantity of *f*-MWCNTs powder was dispersed in 2 mL of DIW to produce *f*-MWCNTs suspension through ultrasonication for 15 min to obtain a homogenous solution. Then the CTS solution was produced by 0.25 mg of CTS dispersion into 50 ml 0.10 mol L^{-1} of acetic acid and ultrasonicated for 30 min. Subsequently, cobalt solution was prepared by dispersing 0.1 g of $CoCl_2.6H_2O$ powder in 100 mL of DIW through ultrasonication for 30 min. To fabricate the *f*-MWCNTs/CTS-Co/GCE sensor, 5 µL of *f*-MWCNT dispersion and drop-casted carefully on the surface of GCE and air-dried properly. Next, *f*-MWCNTs/GCE was dipped for 30 min into the solution containing CTS to immobilize CTS and dried properly in the open air. Finally, *f*-MWCNTs/CTS-GCE was dipped in a beaker containing $CoCl_2$ solution for 30 min to produce *f*-MWCNTs/CTS-Co/GCE. Here, Co was deposited onto the surface of CTS through a self-assembly method. The fabricated

electrode was slightly rinsed with DIW and dried properly to obtain the *f*-MWCNTs/CTS-Co/GCE modified sensor. The fabrication of modified electrode is shown in Figure 3.2.

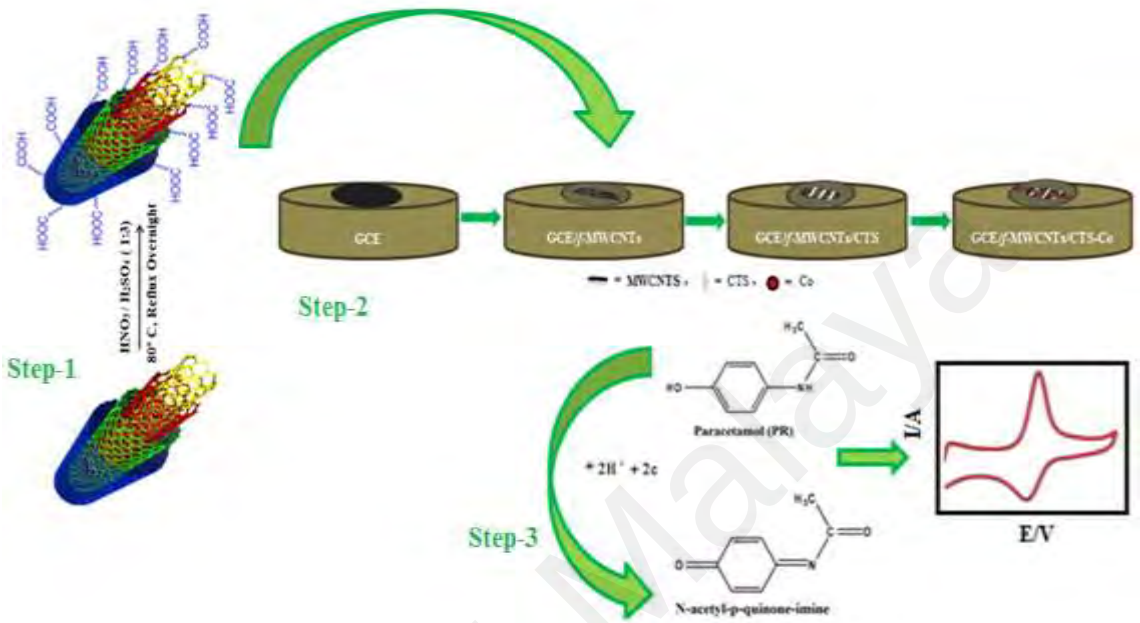

Figure 3.2: Schematic diagram for the preparation of *f*-MWCNTs/CTS-Co/GCE modified sensor for the electrochemical detection of PR.

3.3.3 Fabrication of Co-Ni-Cu MOF/NF nanocomposite

To prepare tri-metallic and mono-metallic MOFs, an organic linker terephthalic acid 0.15 mmol (0.025 g) was dissolved in a beaker containing dimethylformamide (15 mL). In another beaker, 0.05 mmol (0.012 g) of cobalt chloride hexahydrate ($CoCl_2 \cdot 6H_2O$) and nickel chloride hexahydrate, $NiCl_2 \cdot 6H_2O$ and 0.009 g of copper chloride dihydrate $CuCl_2 \cdot 2H_2O$ were dispersed in 10 mL of DIW. This tri-metallic metallic dispersion was added slowly into the organic linker solution and continuously stirred via a magnetic stirrer for 30 min to obtain a pink colour dispersion. Nickel foams (NF) were cleaned using 0.1 M HCl and rinsed with the mixture of DIW and acetone and dried in an oven at 70 °C. At this stage, 10 mL quantity of pink solution and six pieces of NF substrate were introduced into a stainless steel autoclave and heated for 120 °C in an oven for 6 h.

Next, the NFs were withdrawn and washed few times with DIW and ethanol to eliminate the contaminants. The synthesized MOF was named as Co-Ni-Cu-MOF/NF (shown in Figure 3.3). To synthesize the Co-MOF/NF, Ni-MOF/NF, Cu-MOF/NF mono-metallic MOFs, the same procedures were followed where the tri-metal precursor was replaced by the single-metals using 0.15 mmol of (0.036 g) $CoCl_2 \cdot 6H_2O$ and $NiCl_2 \cdot 6H_2O$ and (0.026 g) of $CuCl_2 \cdot 2H_2O$. Fabrication and growth mechanism of Co-Ni-Cu MOF/NF is shown in Figure 3.4.

Figure 3.3: Synthesis of Co-Ni-Cu MOF/NF by hydrothermal method.

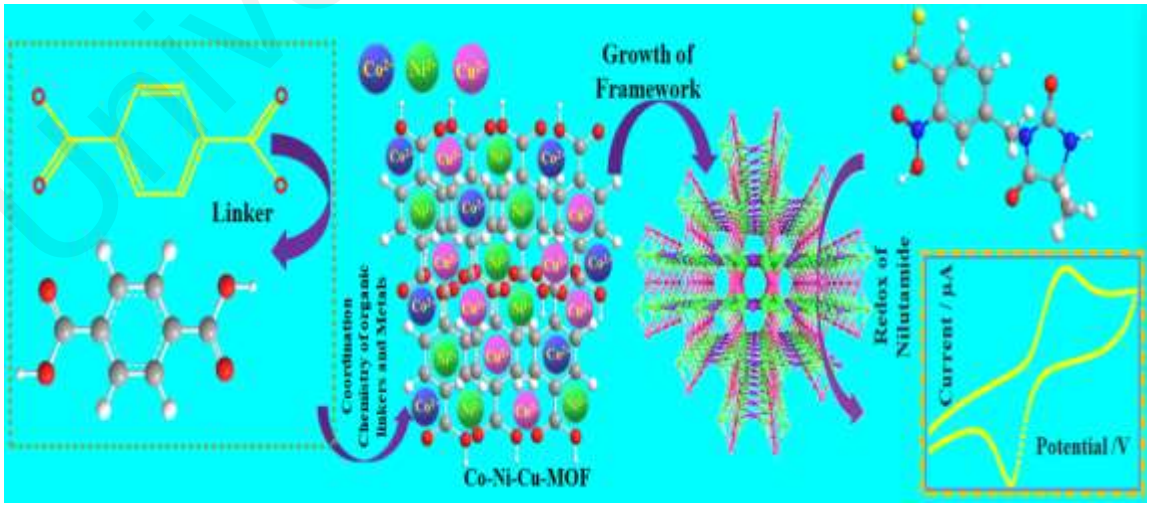

Figure 3.4: Mechanism of Co-Ni-Cu MOF/NF by the coordination chemistry of organic linkers and metal nodes for the electrochemical detection of NLM.

3.3.4 Fabrication of NC-3DPPY@Ag-Au/GCE sensor

Before the fabrication step, glassy carbon electrode (GCE) was polished to obtain a mirror-like surface, on the micro-cloth pad with alumina slurry. Then the GCE was ultra-sonicated in ethanol and then in DIW for 2 min and dried properly at ambient temperature. 1 mg of synthesized NC dispersed in 2 ml of DIW and sonicated for 15 min. On the other hand, 2 mg solid mass of 3DPPY dispersed in 4 ml of DIW and ultrasonicated for 1 hr. Then, 3 mL of 3DPPY uniform dispersion was introduced gradually to NC solution with continuous stirring and stirred for 1 hr. The Ag-Au bimetallic nanoparticle solution was ultrasonicated for 5 min and 5 mL of this solution was introduced to NC-3DPPY dispersion and ultrasonicated for 30 min to obtain NC-3DPPY@Ag-Au. Finally, 5µL of NC-3DPPY@Ag-Au dispersion was drop-cast carefully on GCE surface. The NC-3DPPY@Ag-Au/GCE was air-dried properly at room temperature before starting the experiments. The schematic diagram for the preparation of NC-3DPPY@Ag-Au/GCE modified sensor is shown in Figure 3.5.

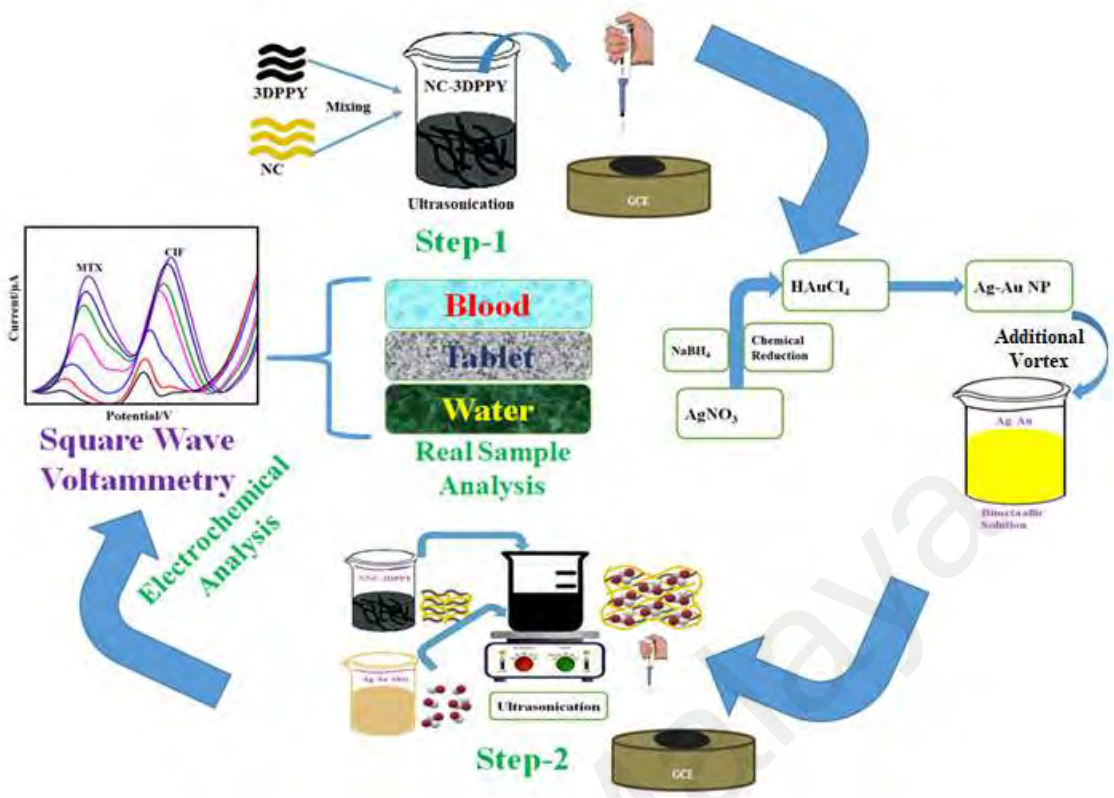

Figure 3.5: Schematic diagram for the preparation of NC-3DPPY@Ag-Au/GCE modified sensor for the electrochemical detection of MTX and CIF.

3.4 Instrumentations

3.4.1 X-ray diffraction (XRD)

X-ray diffraction (XRD) was conducted to investigate the crystalline configuration of prepared nanocomposites according to the characteristic x-ray diffraction pattern. The XRD spectra were obtained from PANalytical Empyrean x-ray diffractometer with Cu Kα radiation (λ=1.541 Å). The finely ground powdered sample was mounted on a sample holder and scanned at 2θ of 10°-90° with a 0.02° step size. Phase identification of the sample was conducted by comparison with the standard reference patterns. The d-spacing and particle size can be also obtained from this analysis.

3.4.2 Raman spectroscopy

Raman spectroscopy is an effective method for the characterization of defects, especially in sp2 hybridized carbon nanomaterials. Raman spectroscopy was conducted by HORIBA XploRA micro Raman microscope using a laser source with 532 nm wavelength. No sample preparation was needed in this analysis. The Raman spectroscopy was carried out in a wavenumber range between 1000 cm^{-1} to 2000 cm^{-1}.

3.4.3 Fourier transform infrared (FTIR) spectroscopy

Fourier transformed infrared (FTIR) spectroscopy was employed to identify the functional groups in a material. The FTIR spectra of carbon nanomaterials and their nanocomposite were recorded on an attenuated total reflection Perkin Elmer Spectrum 400 FTIR spectrometer, in a wavenumber range between 500 cm^{-1} to 4000 cm^{-1}. In principle, the functional group of the molecules in a material absorbs infrared radiation. The FTIR spectra were obtained by measuring the absorbance of a material at various wavelengths, thus undergoes the Fourier transform process.

3.4.4 X-ray photoelectron spectroscopy (XPS)

X-ray photoelectron spectroscopy (XPS) is a spectroscopic technique that determines the chemical and electronic state, and elemental composition on the material surface. The synthesized nanocomposite materials were analyzed using a monochromatic X-ray beam with 4404 eV, from a beam line BL-14 (Indus-2 synchrotron source). The XPS analysis was carried out in an ultra-high vacuum of ~10−8Torr Si (111). A monochromator with double-crystal and hemispherical electron energy analyzer (SPECS PHOIBOS 225 HV) were utilized to obtain the XPS result. The Casa XPS software was utilized to analyze the data with adventitious carbon as the reference. A minimum amount of powder sample was mounted on the sample bars for analysis. The sample was run at the binding energy range of 0 eV to 1000 eV. A

photoelectron spectrum was recorded by measuring the energy of the emitted photoelectrons. The information about the surface elements can be obtained from the intensity and binding energy of the photoelectrons peak.

3.4.5 FESEM and EDX analysis

The morphological characteristics of the nanocomposites were observed by JSM-7800 F JEOL field emission scanning electron microscopy (FESEM), attached to a energy dispersive X-ray (EDX) spectrometer. The EDX spectrometer was employed in combination with the FESEM to measure the composition of element (%) of the nanocomposites. Prior to the analysis, the sample was attached to a double-sided adhesive tape before being placed to the sample holder. The FESEM instrument magnifies the images by using electrons instead of visible light. The FESEM microscopy produces better images in terms of magnification and image resolution compared to the conventional light microscope.

3.4.6 Transmission electron microscopy (TEM)

Transmission electron microscopy (TEM) was employed to observe the morphological features to record high resolution images of the nanocomposites. A Tecnai, G2 F20 FEI transmission electron microscopy (TEM) at 200 kV was used to produce magnified images. However, the TEM involves the transmission of electron beams while FESEM involves the scattering of the electron beams. FESEM only shows the surface morphology of the nanocomposite, whereas TEM provides detailed information about the nanocomposite such as lattice spacing. For the preparation of the TEM sample, a few mg of nanocomposite was dispersed in ethanol and ultrasonicated by a high-powered probe sonicator for 15 minutes. Then, one or two drops of supernatant were drop-casted on the lacy carbon-coated copper grid. Next, the sample was dried for 24 hrs at room temperature before analysis. GATAN software was used to

analyse the TEM, high-resolution transmission electron microscopy (HRTEM), selected area electron diffraction (SAED) pattern of the nanocomposite.

3.4.7 Brunauer-Emmett-Teller (BET) analysis

The Brunauer-Emmett-Teller (BET) adsorption-desorption isotherm study was employed to calculate the specific surface area of the materials by nitrogen multilayer adsorption measured as a pressure-induced automated analyser. This study was used to measure the pore area and specific pore volume utilizing adsorption and desorption. The BET equation illustrates the relationship between the amount of adsorbed gas molecules (X) at a given relative pressure (P/P_0), where C is a second parameter related to the heat of adsorption. The BET study was accomplished employing the Quantachrome ASIQ with the physical adsorption of nitrogen gas on the sorbent at 77 K.

3.4.8 Electrochemical analysis

The electrochemical investigations were conducted with a potentiostat/galvanostat Autolab PGSTAT302 model from Eco Chemie (Netherlands), connected to a computer with Frequency Response Analyzer (FRA) and General Purpose Electrochemical System (GPES) software.

Electrochemical impedance spectroscopy (EIS) experiment was conducted in 0.1 M KCl as the supporting electrolyte with 5.0 mM $K_4[Fe(CN)_6]$ and $K_3[Fe(CN)_6]$. For the paracetamol, nilutamide, methotrexate and ciprofloxacin detection, cyclic voltammetry, differential pulse voltammetry and square-wave voltammetry techniques were carried out in an aqueous solution of 0.2 M phosphate buffer solution (PBS) at pH 7.0. While for the determination of NLM, CV and DPV were performed in aqueous solutions of 0.1 M PBS at pH 7.0. The desired amounts of KH_2PO_4 and K_2HPO_4 were dissolved in deionized water to prepare the PBS supporting electrolyte.

The electrochemical experiments were conducted in a three-electrode electrochemical cell containing the working electrode (WE), reference electrode (RE) and a counter electrode (CE). Here, a glassy carbon electrode (GCE) was employed as the WE which was attached on a disk supported on a peek plastic electrode shaft. The dimensions of the GCE shaft are 52.5 mm in length, with a 3 mm diameter electrode disk and a 10 mm outer diameter electrode shaft. In the polishing step, the GCE was hand-polished with 0.05 μm aluminium oxide powder on a microcloth polishing pad (Buehler) before washing thoroughly with DIW. After that, the GCE was cleaned with ethanol by ultrasonication for 5 min and washed thoroughly with DIW to remove any adsorbed material. Finally, the GCE was dried at room temperature before being modified with the nanocomposite material. A saturated calomel electrode (SCE) was utilized as the RE where the tip of the SCE is made from a porous ceramic junction. The SCE is filled with saturated KCl and stored in 3.0 M KCl when not in use. A platinum wire with 7.0 cm length was used as the counter electrode. Prior to use, the platinum wire was cleaned with ethanol and deionized water.

3.5 Characteristics of the electrochemical sensor

3.5.1 Linearity of calibration curve

A calibration curve is a plot of analytical signal changes with different concentrations of the target analyte. Generally, a calibration curve is used to evaluate the concentration of an unknown by referring to the known concentration of the target analyte. A series of standards solutions with varying concentrations of the desired analyte was prepared, followed by the measurement of the current response of the target analyte to plot the calibration curve. The linearity of the calibration curve was constructed from the straight-line plot. The linear range concentration of the target analyte is given by the minimum to maximum concentration value in the linear

calibration plot. From the calibration curve, the regression model, slope of the line and correlation coefficient can be evaluated.

3.5.2 Sensitivity

The sensitivity of an electrochemical sensor was obtained from the slope of the linear calibration curve and surface area of the electrode (Rahman et al., 2020). The slope can be calculated by selecting any two points in the linear calibration curve which is the ratio between the changes in the current response with respect to the changes in concentrations of the target analyte.

3.5.3 Limit of detection

The limit of detection (LOD) is the lowest concentration of the desired analyte which could be detected by the sensor and distinguished from the blank solution. The LOD can be calculated by using equation 3.1; where 3 is the signal to noise ratio of 3, S_b represents the standard deviation of the blank solution and m is the slope of the calibration curve.

$$LOD = 3 \times S_b/m \quad (3.1)$$

3.5.4 Stability

Stability is a measurement of how much the initial analytical signal remains after a period of time. The stability of a sensor was performed by determining the initial current response value before storage in a refrigerator. The current response was then measured every week for 1 month. The percentage of the remaining current response was evaluated as follows; where x_i represents the initial current response and x_f represents the remaining current response.

$$\text{Percentage decrease} = (x_i - x_f)\, xi \times 100\% \quad (3.2)$$

Percentage remain = 100% - percentage decease (3.3)

3.5.5 Reproducibility

A reproducibility study is very essential to determine the consistency of a result when the entire experiment is repeated. The reproducibility was evaluated by replicating the analysis for the determination of the target analyte by using a similar method. Reproducibility is reported as relative standard deviation (RSD) and the calculations are shown below; where x represents the value of the data for each measurement, $\bar{x}$ represents the mean of measurement and n represents the number of measurements.

$$\text{Standard deviation (SD)} = \sqrt{\Sigma(x - \bar{x})^2/n-1} \quad (3.4)$$

$$\text{Relative standard deviation (RSD)} = SD/\bar{x} \times 100\% \quad (3.5)$$

3.5.6 Selectivity

The selectivity of an electrochemical sensor towards the target analyte is a crucial criterion for a successful sensor. The sensor should respond to any changes in the target analyte concentration, and must not be influenced by the presence of common interfering compounds which also oxidizes or reduces in a similar potential range (Karimi-Maleh et al., 2020). Otherwise, the target analyte concentration will be inaccurate if the interfering compounds are also reactive in a similar potential range. The selectivity study was carried out by analyzing the sensitivity of the electrochemical sensor in the presence and absence of common interfering compounds (Drobek et al., 2016).

3.5.7 Real sample analysis

The real sample study is a crucial characteristic for the sensor, where the sensor can detect the presence of the desired analyte in real or practical samples such as blood

serum, urine and pharmaceutical dosage forms. The concentration of the desired analyte in real samples such as blood serum, urine, pharmaceutical dosage forms was evaluated by the standard addition method. Chapter 4 of this thesis illustrates that the (MWCNTs$_f$-NGr/CTS)- Cu/GCE fabricated sensor showed satisfactory recovery values which were obtained for NLM from 0.85 to 2.35% for blood serum and 0.049 to 2.02 % for tablets. In chapter 5, the *f*-MWCNTs/CTS-Co/GCE modified sensor showed satisfactory recovery values which were obtained for PR from 99.26 to 99.76% for tablets and 99.7 to 98.4%. In chapter 6, the Co-Ni-Cu-MOF/NF modified electrode showed satisfactory recovery values which were obtained for NLM from 98.0 to 102.0% for tablets and 99.0 to 101.5% for blood serum. In chapter 7, the NC-3DPPY@Ag-Au/GCE fabricated sensor showed satisfactory recovery values which were obtained as 99.80% to 100.40% and 99.73% to 100.60% for MTX and CIF tablets respectively. While 99.70 to 100.60% and 100.25 to 100.80% for blood sample with MTX and CIF respectively.

3.5.8 Standard addition method

The standard addition method was carried out to measure the unknown concentration by the extrapolation of a linear calibration curve to the x-axis. An equal volume of the sample solution containing the analyte was added to five different volumetric flasks. Next, the standard solution of the analyte was added into the flasks in increasing volumes, except for the first flask. The solution in all volumetric flasks was diluted with PBS to the same volume. The current response of each solution was measured by the voltammetric technique. The graph of current response vs. the concentration of added standard was plotted and the graph is extrapolated to the x-axis at y = 0. This is the concentration of the analyte in the sample. The recoveries of the concentration obtained from the standard addition method to the actual concentration

were calculated as follows; where X_1 represents the actual concentration and X_2 represents the concentration obtained from the standard addition method.

$$\text{Recovery} = X_2/X_1 \times 100\% \quad (3.6)$$

CHAPTER 4: FUNCTIONALIZED MULTIWALL CARBON NANOTUBE, NITROGEN-DOPED GRAPHENE AND CHITOSAN WITH COPPER FOR NILUTAMIDE DETECTION

This chapter discusses the characterization of functionalized multiwall carbon nanotube, nitrogen-doped graphene and chitosan with copper modified electrode for the electrochemical determination of nilutamide in commercial tablet and blood serum

4.1 (MWCNTs$_f$ –NGr/CTS)-Cu nanocomposite for nilutamide detection

In this section, functionalized multiwall carbon nanotube, nitrogen doped graphene and chitosan with electrodeposited copper (MWCNTs$_f$ –NGr/CTS)-Cu nanocomposite was synthesized and characterized by several analytical techniques such as FTIR spectroscopy, Raman spectroscopy, FESEM and TEM. Then, an electrochemical sensor was prepared for the determination of nilutamide (NLM) by modifying a GCE with the (MWCNTs$_f$–NGr/CTS)-Cu nanocomposite. Voltammetric methods were used to evaluate the electrochemical behavior of NLM. In addition, the linear range, limit of detection, reproducibility, repeatability, stability and selectivity of the electrochemical sensor were studied. The prepared sensor also showed satisfactory results in real sample study using pharmaceuticals and biological samples.

4.2 Aim of the research

The aim of this study is to fabricate a new modified electrode based on MWCNTs$_f$, NGr and CTS with the electrodeposited Cu. The combination of these materials into a nanocomposite is expected to improve the properties of the nanocomposite compared to the single materials. Thus the synergistic effect between MWCNTs$_f$ and NGr with the excellent electrical conductivity with improved dispersion of CTS and excellent

catalytic effect of Cu is a hallmark for the high performance electrochemical sensing of NLM.

4.3 Electrode characterizations

4.3.1 FT-IR spectroscopy analysis

Fourier transformed infrared (FT-IR) (Figure 4.1) spectroscopy was employed to determine the functional groups present in the synthesized nanocomposites. Figure 4.1A shows the FT-IR spectra of NGr (a) and MWCNTs*f* (b). Curve (a) shows that after the reduction reaction, distinguished peaks appear at 1738 cm^{-1}, 1166 cm^{-1} and 1535 cm^{-1} which correspond to C=O, C–N and C=C, respectively, in the NGr (red curve) (Pan et al., 2015). For MWCNTs*f*, a prominent peak is observed at 2931 cm^{-1}, 1745 cm^{-1}, 1604 cm^{-1} and 1159 cm^{-1} which is ascribed to the O-H, C=O, C=C and C=O stretches, respectively (black curve) (Shalauddin et al., 2017). Figure 4.1B shows the FT-IR spectra of MWCNTs*f*–NGr (a), where all of the characteristics peaks are present confirming the presence of NGr and MWCNTs*f* (black curve). Similarly, with regards to MWCNTs*f*–NGr/CTS (b), all the characteristic peaks are present along with the additional peak at 3166 cm^{-1} which corresponds to the O-H and N-H stretch, and confirms the presence of CTS (red curve) (Akhter et al., 2018). For (MWCNTs*f*–NGr/CTS)-Cu (c) all the characteristic peaks for NGr, MWCNTs*f* and CTS are present and an additional peak is observed at around 500 cm^{-1} attributed to the presence of Cu in this nanocomposite (blue curve) (Shalauddin et al., 2017).

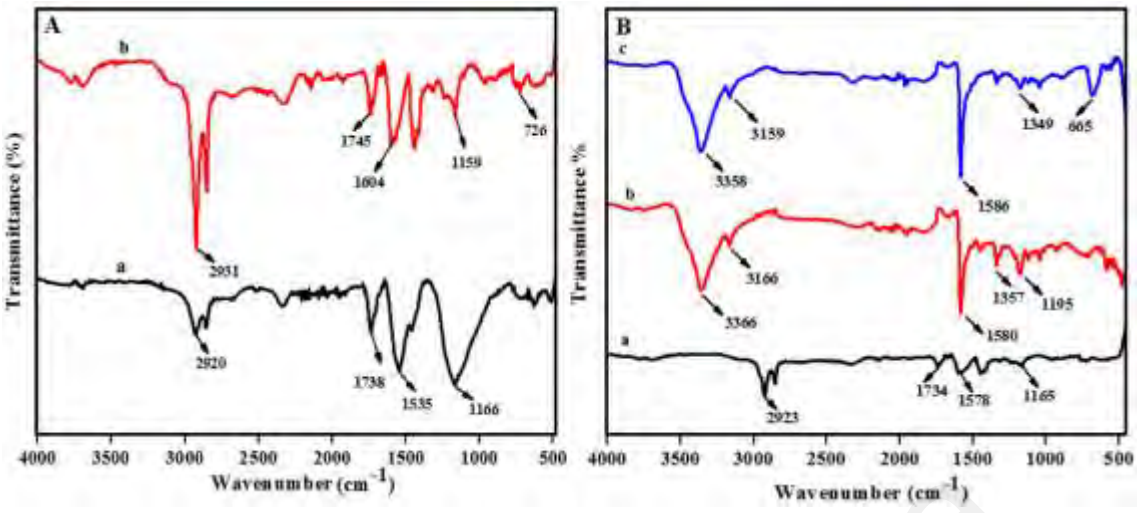

Figure 4.1: (A) FITR of NGr (a) and MWCNTs$_f$ (b). (B) FTIR spectra of MWCNTs$_f$–NGr (a), MWCNTs$_f$–NGr/CTS (b) and (MWCNTs$_f$–NGr/CTS)-Cu (c).

4.3.2 Raman spectroscopy analysis

Raman spectroscopy is an effective technique to investigate carbonaceous materials. The Raman spectra of pristine and MWCNTs$_f$ is shown in Figure 4.2 A. For pristine MWCNT (a), the D and G bands are around 1327 cm^{-1} and 1578 cm^{-1}, accordingly, corresponding to the Raman active E_{2g} analogous to graphite. The D band (1330 cm^{-1}) and G band (1580 cm^{-1}) in the MWCNTs$_f$ (b) spectrum are attributed to the sp^3 amorphous carbons and sp^2 graphitic carbons, respectively. The intensity ratio of the D and G bands (I_D/I_G) is an indicator of the presence of defects. The intensity ratio of the D band to G band (I_D/I_G) increases from 1.28 to 2.84 after functionalization. This confirms the conversion from graphitic into amorphous carbons due to the covalent functionalization of carbons on the surface of MWCNTs (Naeimi et al., 2011; Vinayan et al., 2012). As shown in Figure 4.2B, the D band of GO (a) and NGr (b) appears at 1430 and 1470 cm^{-1}, respectively, while the G band appears at 1600 and 1580 cm^{-1}, respectively. The shift of the G peak from GO to NGr is due to the electron-donating effect of the N heteroatom. In addition, the I_D/I_G ratio is used to evaluate the disorder in graphene materials. The I_D/I_G ratio in GO is 1.10 but increases to 1.15 for NGr. The increase of the I_D/I_G ratio is due to the loss of carbon atoms from the decomposition of

oxygen functional groups (Wei et al., 2009), and the replacement by the N heteroatoms in the graphene lattice (Lin et al., 2010). The MWCNTs*f*–NGr in the curve (a) (Figure 4.2C) shows the combination of MWCNTs*f* and NGr. When MWCNTs*f* and NGr are combined together, the height of D and G band declines. For the MWCNTs*f*–NGr/CTS in curve (b) (Figure 4.2C), when CTS is added with the combination of MWCNTs*f* and NGr, the height of D, G and 2D band increase and these bands are slightly shifted compared to curve (a) (Figure 4.2C). These changes are observed due to the presence of CTS. For (MWCNTs*f*–NGr/CTS)-Cu in curve (c) (Figure 4.2C), an extra small peak appears approximately at 620 cm^{-1} due to the presence of Cu (Akgul et al., 2014) . The D, G and 2D bands are almost similar compared to curve (b) (Figure 4.2C).

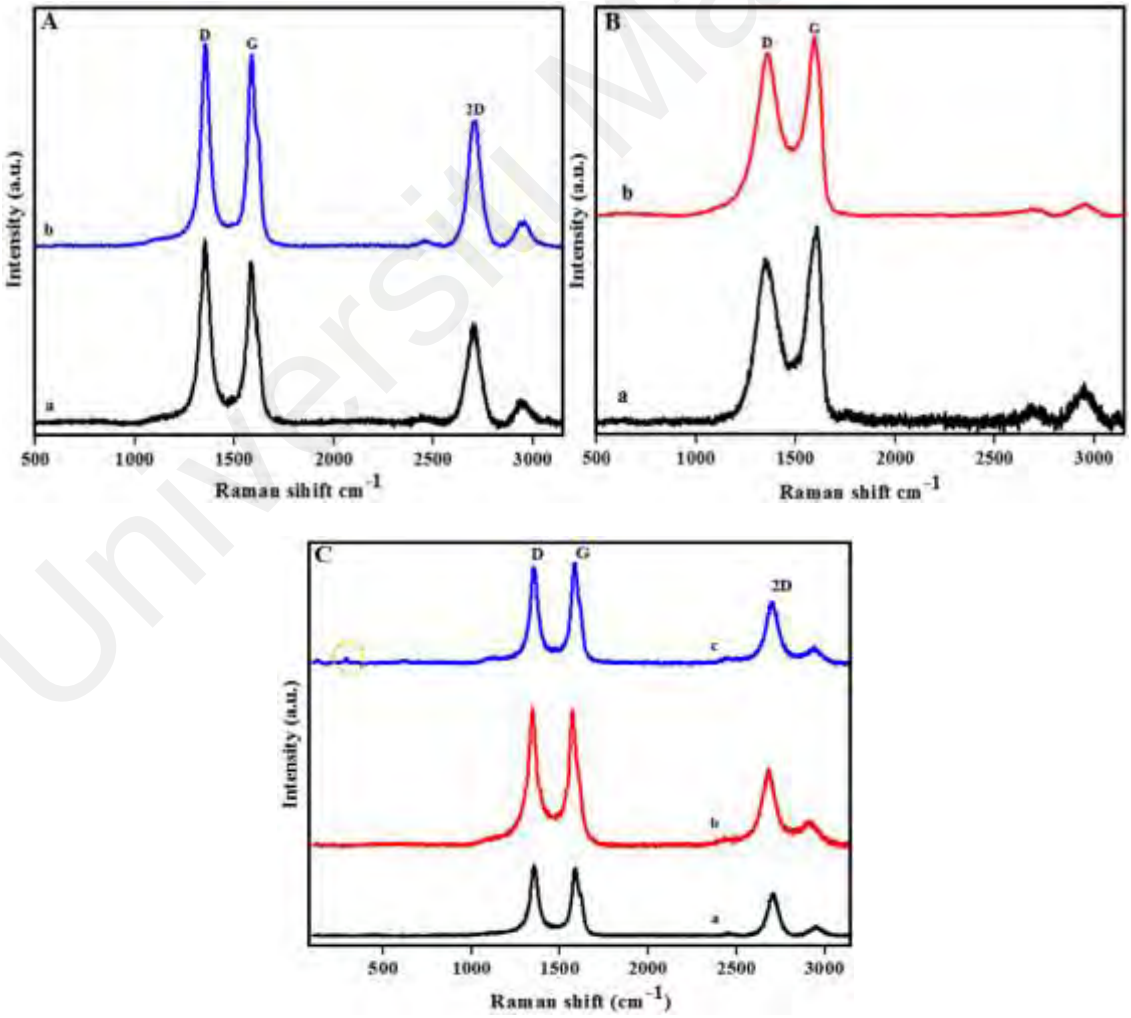

Figure 4.2: Raman spectra of pristine (a) and MWCNTs*f* (b) in (A), GO (a) and NGr (b) in (B), and MWCNTs*f*–NGr (a), MWCNTs*f*–NGr/CTS (b), MWCNTs*f* – NGr/CTS-Cu (c) in (C).

4.3.3 Electron microscopy analysis

The morphological characteristics of the MWCNTs$_f$, NGr and MWCNTs$_f$–NGr, MWCNTs$_f$-NGr/CTS, (MWCNTs$_f$-NGr/CTS)-Cu nanocomposite were observed by electron microscopic imaging techniques such as TEM and FESEM. Figure 4.3A shows the TEM image of MWCNTs$_f$ with 20-60 nm diameter. The inset figure of 4.3A shows the FESEM of MWCNTs$_f$ which was homogenously deposited on the electrode surface. Figure 4.3B shows that the NGr flakes are distributed on several places. The inset figure shows the FESEM image of NGr nanosheets with the wrinkled structure which demonstrates that the 2D configuration of Gr is uninterrupted even after nitrogen doping (Wang et al., 2010). Figure 2C shows that the NGr flakes are distributed on the surroundings of the tubes of MWCNTs$_f$ with few aggregations. Furthermore, the inset of the FESEM figure shows that the tubes of MWCNTs$_f$ are curved due to the encapsulation by NGr. Figure 4.3D shows that the MWCNTs$_f$ and NGr are uniformly distributed due to the CTS. Figure 4.3E shows that Cu was deposited properly on the (MWCNTs$_f$-NGr/CTS). The pointed circles indicate that the Cu are deposited on the surface. The EDS study was employed to determine the elemental percentage in the (MWCNTs$_f$ –NGr/CTS)-Cu/GCE nanocomposite. The EDS spectrum of (MWCNTs$_f$ – NGr/CTS)-Cu/GCE nanocomposite in Figure 4.3F confirms the presence of the major elements such as carbon (69.55%), oxygen (18.67%) and nitrogen (3.25%) and copper (8.53%) which confirms the successful preparation of (MWCNTs$_f$ –NGr/CTS)-Cu on the GCE surface.

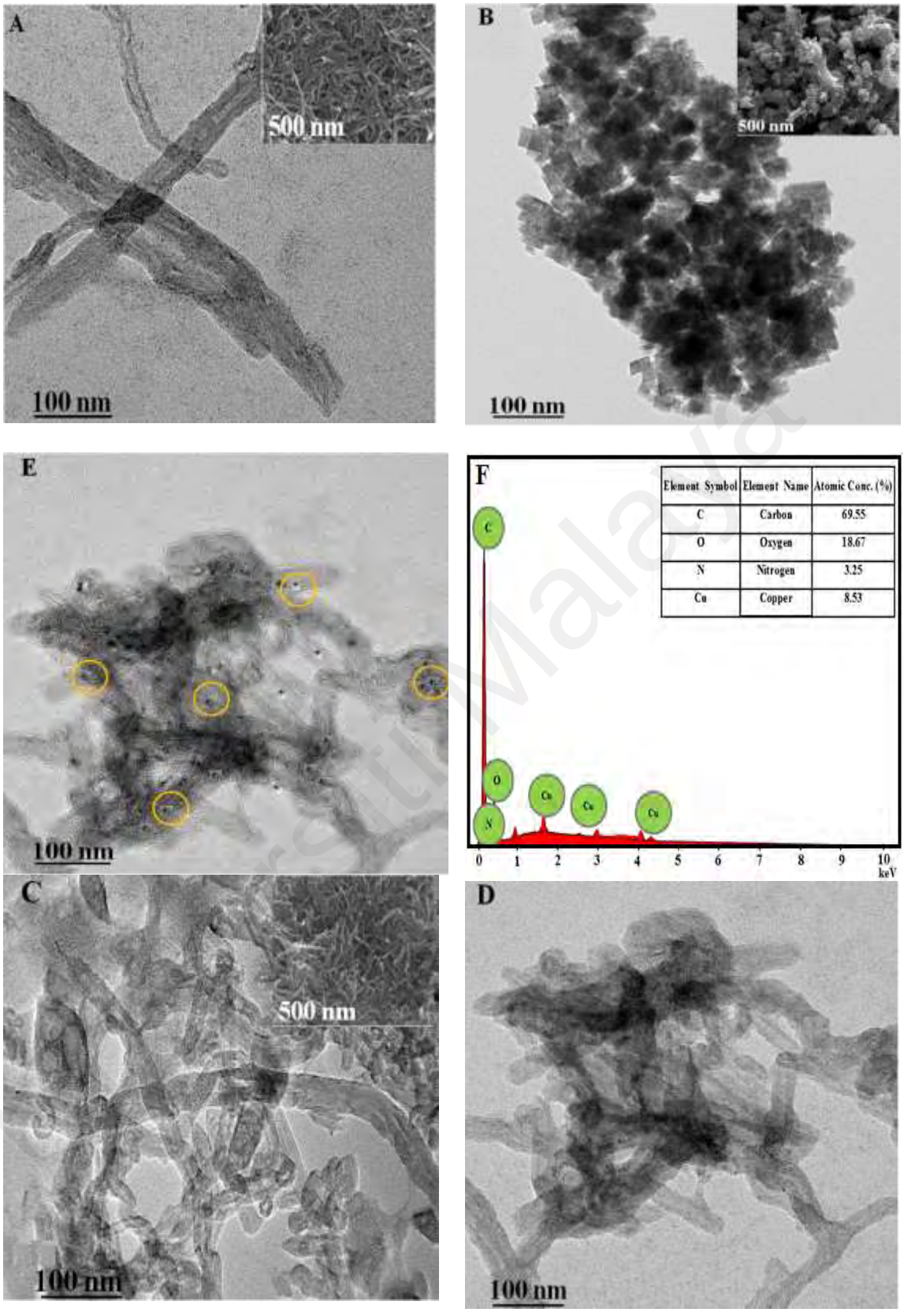

Figure 4.3: TEM images of MWCNTs$_f$ (A) (inset FESEM image), NGr (B) (inset FESEM image), (MWCNTs$_f$–NGr) (C) (inset FESEM image), MWCNTs$_f$–NGr/CTS (D), (MWCNTs$_f$-NGr/CTS)-Cu/GCE nanocomposite (E). (F) EDS analysis of the synthesized (MWCNTs$_f$–NGr/CTS)-Cu/GCE nanocomposite.

4.4 Electrochemical Characterizations

4.4.1 Electrochemical impedance spectroscopy (EIS) analysis

Electrochemical impedance spectroscopy (EIS) was performed to measure the impedance of the electrodes before and after surface modification. The impedance plots for bare GCE (a), MWCNTs$_f$-NGr/GCE (b), MWCNTs$_f$–NGr/CTS/GCE (c), (MWCNTs$_f$-NGr/CTS)–Cu/GCE (d) were compared in the presence of 0.1 M KCl aqueous solution containing 5 mM/L $[Fe(CN)_6]^{3-/4-}$ as shown in Figure 4.4. The semicircle at higher frequencies in the Nyquist plots are attributed to the interfacial electron transfer resistance (R_{ct}), and the linear segment in the lower frequency is associated with the diffusion-controlled phenomena. From the data fitting, the bare GCE (a) shows an R_{ct} value of 950 Ω. The R_{ct} value decreases to 467 Ω due to the surface modification of GCE with MWCNTs$_f$-NGr (b), where the semicircle diameter of MWCNTs$_f$-NGr/GCE decreases considerably compared to the bare GCE. This confirms that the NGr decorated with MWCNTs$_f$ accelerates the electron mobilization process of the $[Fe(CN)_6]^{3/4}$ redox couple. This can be attributed to a significantly improved electrical conductivity of the NGr sheets in the presence of MWCNTs$_f$. The MWCNTs$_f$-NGr/CTS/GCE shows the nearest R_{ct} (385 Ω) value of MWCNTs$_f$-NGr/GCE, because CTS has very low conductivity but it ensures the homogeneous dispersion of nanomaterials on the GCE surface. For (MWCNTs$_f$–NGr/CTS)–Cu/GCE, the R_{ct} value dramatically decreases to 168 Ω which indicates the deposition of Cu with MWCNTs$_f$–NGr/CTS enhances the conductivity of (MWCNTs$_f$–NGr/CTS)–Cu nanocomposite and made this sensor suitable for NLM determination. The impedance data was fitted to an equivalent circuit as shown in inset of Figure 4.4. The R_s, R_p, CPE and W represents the solution resistance, electron transfer resistance, constant phase element and Warburg impedance, respectively.

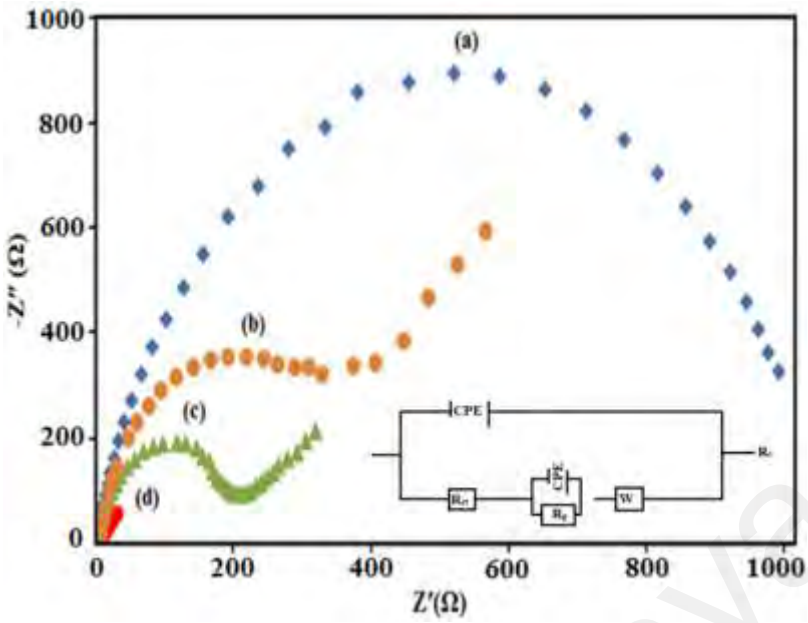

Figure 4.4: The Nyquist plots of (a) bare GCE, (b) (MWCNTs$_f$-NGr/GCE (c) MWCNTs$_f$-NGr/CTS/GCE, (d) (MWCNTs$_f$–NGr/CTS)-Cu/GCE in a solution containing 0.1 M KCl solution with 5.0 mM [Fe (CN) $_6$]$^{3-/4-}$, inset the equivalent circuit is used to do the fitting.

4.4.2 CV of NLM on (MWCNTs$_f$ -NGr/CTS)-Cu/GCE sensor

To investigate the electrochemical response of the unmodified and modified electrodes in the detection of NLM, cyclic voltammetry (CV) was carried out for four different electrodes including the bare GCE (a), MWCNTs$_f$-NGr/GCE (b), MWCNTs$_f$-NGr/CTS/GCE (c), and (MWCNTs$_f$-NGr/CTS)-Cu/GCE (d) in the presence of 150 µM NLM in 0.2 M PBS (pH 7.0) at 50 mV s^{-1} as shown in Figure 4.5. From the inset of Figure 4.5, no redox peaks are observed at the bare GCE and (MWCNTs$_f$-NGr/CTS)-Cu/GCE in the absence of 150 µM NLM in 0.2 M PBS. However, the initial current response of (MWCNTs$_f$-NGr/CTS)-Cu/GCE is higher compared to the bare GCE which confirms an enhanced electrochemical response of the final nanocomposite. The CV results revealed that the fabricated electrode generates a single non -reversible reduction peak from 0.0 to -0.8 V (Figure 4.5). This is due to the reduction of NO_2 group present in NLM (Karthik et al., 2017). For the bare GCE, the reduction peak current of NLM appears at –0.44 V (Figure 4.5 curve a). Besides, the MWCNTs$_f$-NGr/GCE shows a distinguished reduction peak current at -0.47 V (Figure 4.5 curve b). This could be due

to the high electro-active surface area of the MWCNTs$_f$–NGr. The MWCNTs$_f$ prevents the agglomeration of NGr sheets that reveals the active regions in the NGr and enables a large surface area.

MWCNTs$_f$-NGr/CTS/GCE (Figure 4.5 curve c) showed approximately the same peak as the peak of MWCNTs$_f$-NGr/GCE. As CTS is less conductive, thus it could not increase the current. On the other hand, the highest reduction peak was observed for MWCNTs$_f$-NGr/CTS-Cu/GCE at -0.49 V (Figure 4.5 curve d) which is six times higher with a low reduction potential than the bare GCE (-0.44 V). This could be due to the excellent electrocatalytic effect of electrodeposited Cu along with the expanded electroactive surface area which enhances the electro-conductivity of the nanocomposite. Here, the enhanced reduction peak current significantly depends on the presence of the electrodeposited copper on the MWCNTs$_f$-NGr/CTS/GCE surface.

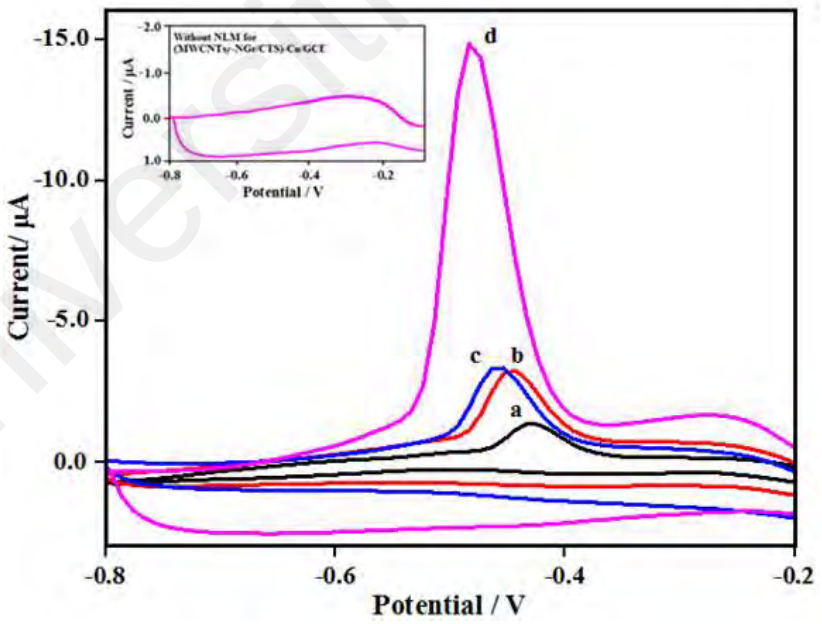

Figure 4.5: Cyclic voltammograms of 150 µM NLM on bare GCE (a), (MWCNTs$_f$-NGr/GCE (b), MWCNTs$_f$-NGr/CTS/GCE (c), (MWCNTs$_f$-NGr/CTS)-Cu/GCE (d) in 0.2 M PBS (pH 7.0) at 50 mVs^{-1}. Inset is the CV of (MWCNTs$_f$–NGr/CTS)-Cu/GCE in absence of NLM.

4.5 Optimization of the fabricated sensor

4.5.1 Scan rate study on (MWCNTs$_f$-NGr/CTS)-Cu sensor

To observe the effect of scan rates, CVs were recorded on the (MWCNTs$_f$-NGr/CTS)-Cu/GCE at different scan rates ranges from 10 to 400 mV s^{-1} in presence of 150 µM NLM in 0.2 M PBS at pH 7.0. Figure 4.6A shows that the cathodic current increases linearly with the increase of scan rates which demonstrates that the reduction of NLM on (MWCNTs$_f$-NGr/CTS)-Cu/GCE is a surface controlled process (Temerk, Ibrahim, & Farhan, 2015). The linear regression equation is as follows (Figure 4.6B):

$$I_{pc}\,(\mu A) = -\,0.148\upsilon\ (mVs^{-1}) - 3.634\ (R^2 = 0.999) \quad (4.1)$$

The Laviron equation was employed to estimate the number of electron participated in the reaction (Laviron, 1979). Figure 4.6C shows a linear relationship between the reduction peak potential and the log of scan rate (ln υ). The regression equation is:

$$E_{pc}\,(mV) = -\,0.024\upsilon\ (mVs^{-1}) - 0.367\ (R^2 = 0.999) \quad (4.2)$$

The Laviron equation for an irreversible reaction can be represented as $E_{pc} = E° - (RT/\alpha nF)\ \ln\ \upsilon$. The estimated value of α is obtained as 0.52 and the number of transported electrons (n) is calculated as ≈ 4. Based on the description, it can be disclosed that the same numbers of electrons and protons participated in the electrochemical reduction of NLM (Appendix 4.1).

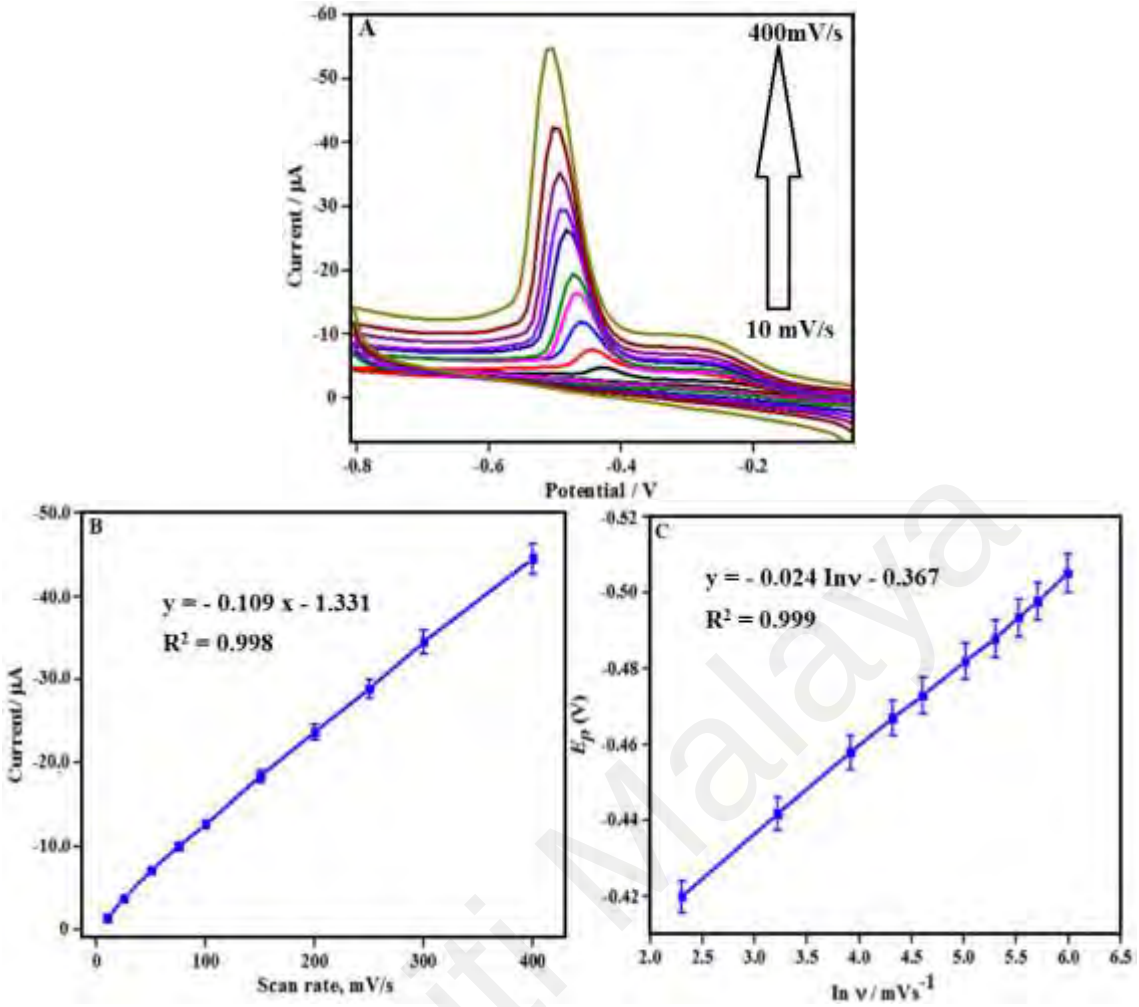

Figure 4.6: (A) CV of 150 µM NLM on (MWCNTs*f*-NGr/CTS)-Cu/GCE at different scan rates in 0.2 M PBS (pH 7.0). (B) The plot of cathodic peak current vs. scan rates. (C) The relationship between cathodic peak potential vs ln υ of scan rate.

4.5.2 CV at different pH

Figure 4.7A exhibits the impact of pH variations by the CV method at the (MWCNTs*f* -NGr/CTS)-Cu/GCE for the determination of 150 µM NLM. The cathodic peak gradually increases with the increase of pH values from 4.0 to 10.0. The cathodic peak moves toward the negative domain with the increase of pH from 7.0 to 10.0, while moves toward to positive region with the decrease of pH from 7.0 to 3.0, which demonstrate that the reduction entails anionic species at greater pH values shown in Figure 4.7B. The maximum peak value was achieved from pH 7.0. The linear relationship between the cathodic peak potential (E_{pc}) and pH values are presented in Figure 4.7C and expressed as:

$$E_{pc} = -0.047\ pH - 0.192 \quad (R^2 = 0.999) \tag{4.3}$$

The slope value of 0.047 V is adjacent to the Nernstian theoretical value of 0.059 V and demonstrates that the electrochemical reduction of NLM at the (MWCNTs$_f$-NGr/CTS)-Cu/GCE sensor entails the identical number of protons and electrons (Fu et al., 2015) (Appendix A).

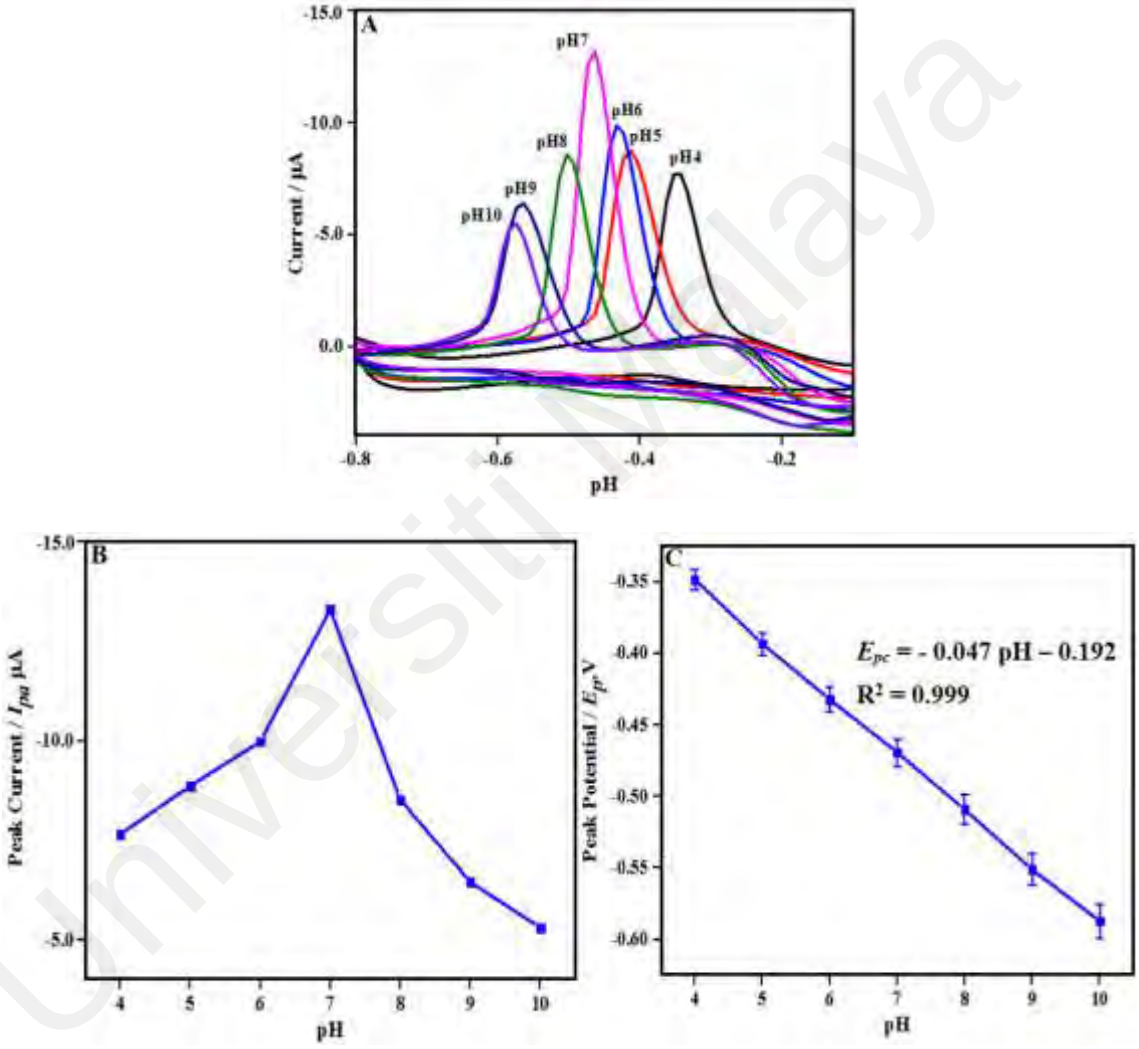

Figure 4.7: (A) The effect of pH on the CVs of 150 µM NLM at the modified (MWCNTs$_f$ -NGr/CTS)-Cu/GCE electrode at 50 mV s^{-1}. (B) The plot of cathodic peak current vs pH. (C) The plot of cathodic peak potential vs. pH.

4.6 Performance evaluation of (MWCNTs$_f$-NGr/CTS)-Cu/GCE sensor

4.6.1 Analytical performance of (MWCNTs$_f$-NGr/CTS)-Cu sensor

Figure 4.8A represents the influence of various NLM concentration on the DPV curves at the (MWCNTs$_f$-NGr/CTS)-Cu/GCE sensor, The DPV voltammograms show that the magnitude of the DPV peak current is enhanced linearly with the increase of the NLM concentration (Figure 4.8A). A couple of linear segments with different slope values were achieved for various concentrations of NLM where the calibration curves reveal a linear relationship of the NLM concentrations (0.005-10 μM) and (20-900 μM) vs. reduction peak at Figure 4.8B and Figure 4.8C respectively, and are proportional with each other. The linear regressions for both calibration ranges are:

$$I_p\ (\mu A) = 0.336C + 2.662 \quad R^2 = 0.999 \quad (0.005\text{-}10\ \mu M) \tag{4.4}$$

$$I_p\ (\mu A) = 0.058C + 5.660 \quad R^2 = 0.999 \quad (20\text{-}900\ \mu M) \tag{4.5}$$

Where, C = NLM concentration, the estimated LOD obtained is 0.15 nM, by employing $3S_b/s$ (according to S/N = 3), S_b = standard deviation of blank and s = sensitivity. The slope (μA/μM) of the plot at a lower concentration range (0.005-10 μM) is around 5 times more sensitive compared to the slope at a higher concentration range (20-900 μM). This could be due to the saturation of the analyte at the interfacial region at a higher concentration range which decreases the sensitivity of the determination. Table 4.1 represents a comparative study between (MWCNTs$_f$-NGr/CTS)-Cu/GCE and previous efforts for the NLM determination in terms of LOD and linear range. From the comparison, it is observed that the (MWCNTs$_f$-NGr/CTS)-Cu/GCE fabricated sensor shows outstanding outcomes compared to earlier attempts (Carvalho et al., 2014; Karthik et al., 2017; Karthik et al., 2017; Sarat & Ramachandran, 2015; Znaleziona et al., 2011). This could be due to the distinctive configurations and remarkable properties

of (MWCNTs$_f$ -NGr/CTS)-Cu electrode which improves the electrochemical behavior of the fabricated electrode for the trace level determination of NLM.

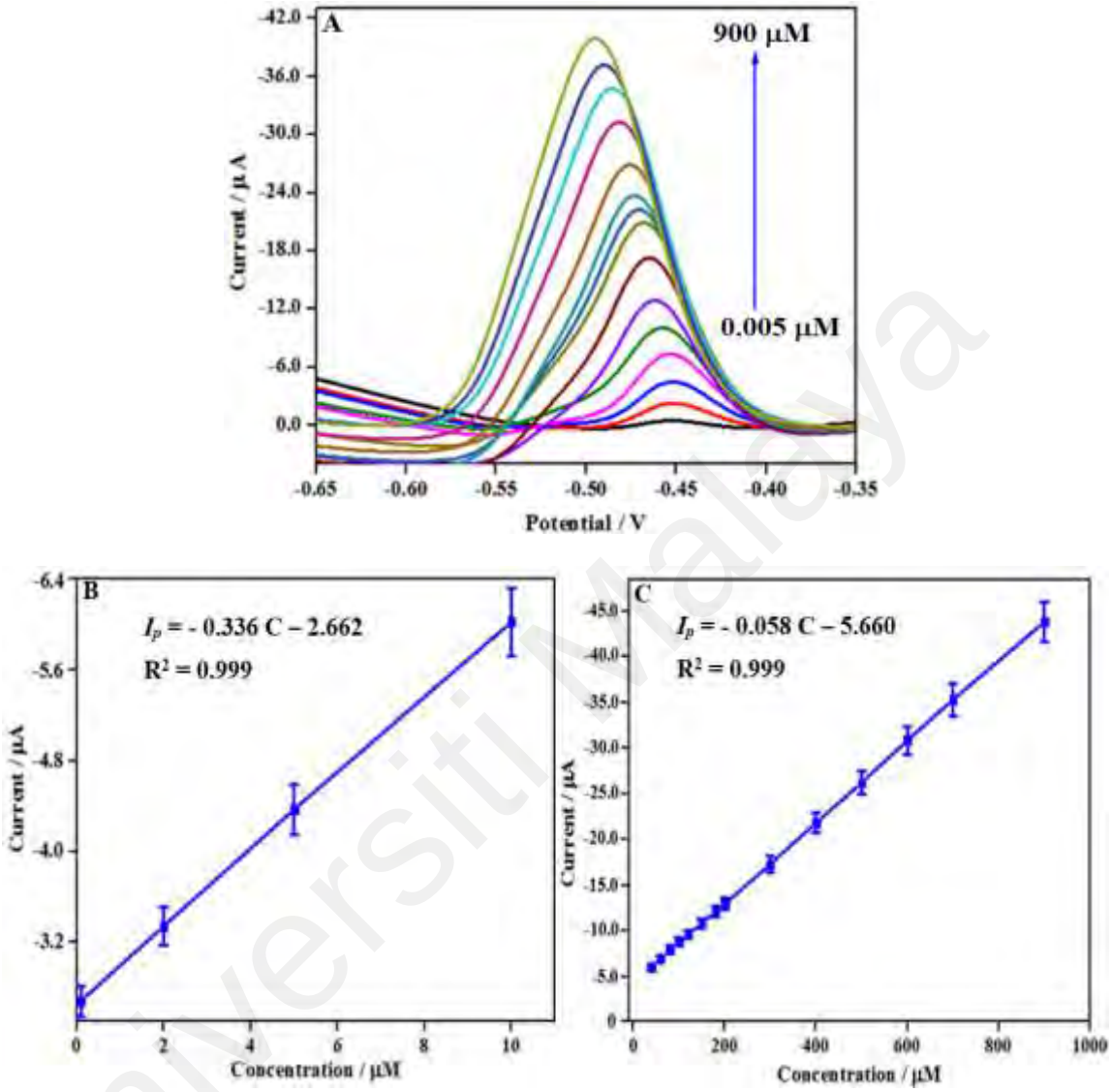

Figure 4.8: (A) DPV response at (MWCNTs$_f$-NGr/CTS)-Cu/GCE at different NLM concentrations (0.005–900 µM) in 0.2 M PBS (pH 7.0). (B) Calibration curve of NLM concentration (0.005-10µM). (C) Calibration curve of NLM concentration (20-900 µM).

Table 4.1. The comparison of various electrodes for the determination of NLM.

Electrode/Material	Linear Range	Detection limit	Reference
f-MWCNTs/GCE	0.01 – 535 µM	0.2nM	(Karthik et al., 2017)
CTAB-ZnONP /CPE	0.03 - 200 µM	3.21 x 10^{-9}mol L^{-1}	(Temerk et al., 2015)
CeV/CNF/GCE	0.01 – 540 µM	2.0 nM	(Kokulnathan, et al., 2019a)
β-CD-AuNP/GO/SPCE	0.01 - 193 µM	0.4nM	(Karthik et al., 2017)
(MWCNTs$_f$-NGr/CTS)-Cu/GCE	0.005 - 900 µM	0.11nM	**This work**

CTAB: Cetyl trimethylammonium bromide, ZnONP: Zinc oxide nanoparticle, CeV: Cerium vanadate, β-CD: Beta-cyclodextrin, CNF: Carbon nanofiber, GO: Graphene oxide, SPCE: Screen printed carbon electrode, CPE: Carbon paste electrode

4.6.2 Mechanistic pathway of the modified sensor

a) Copper loses two electrons: $Cu \rightarrow Cu^{2+} + 2e^-$

b) The two electrons are donated to the nitro group of the NLM. Complexation occurs between the Cu^{2+} and the NO_2^{2-} of the NLM.

c) Water molecule donates one H^+ to the NO_2^{2-} of the NLM.

d) The water molecule donates the second H^+ to the OH group in the NLM to become H_2O^+.

e) The elimination of the water molecule from the NLM.

f) 2 electrons are donated from the electrode to the Cu^{2+} to complete the reaction.

The proposed mechanistic pathway for electrochemical reduction mechanism of NLM at the (MWCNTs$_f$–NGr/CTS)-Cu/GCE is shown in Figure 4.9.

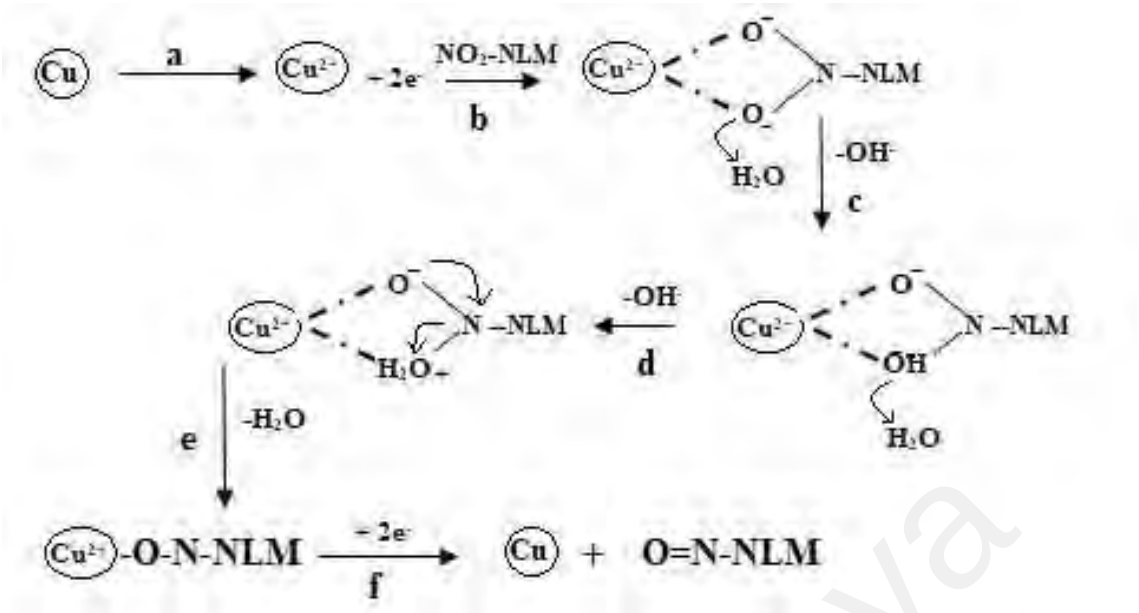

Figure 4.9: The proposed mechanistic pathway for electrochemical reduction mechanism of NLM at the (MWCNTs*f*–NGr/CTS)-Cu/GCE.

4.6.3 Reproducibility, repeatability and stability

The reproducibility was studied on five different (MWCNTs*f* -NGr/CTS)-Cu/GCE modified electrodes and analyzed under optimum conditions in 0.2 M PBS (pH 7.0) with 150 µM NLM. The RSD value was calculated as 4.3%. Besides, the repeatability of (MWCNTs*f* -NGr/CTS)-Cu/GCE was investigated by five independent assays containing 150 µM of NLM with RSD value of 1.68%. These results demonstrate that the electrode shows great reproducibility and repeatability. Moreover, the stability of the fabricated sensor was evaluated by comparing the current responses of the electrode after storage at ambient temperature for 2 weeks and the current response was measured every week as shown in Figure 4.10. The DPV current response was approximately 96% after the 1st week and 90% after the second week, accordingly, which indicate that the current variations are negligible after 2 weeks. Therefore, the overall outcomes disclose that the (MWCNTs*f*-NGr/CTS)-Cu/GCE exhibits great reproducibility, repeatability and stability.

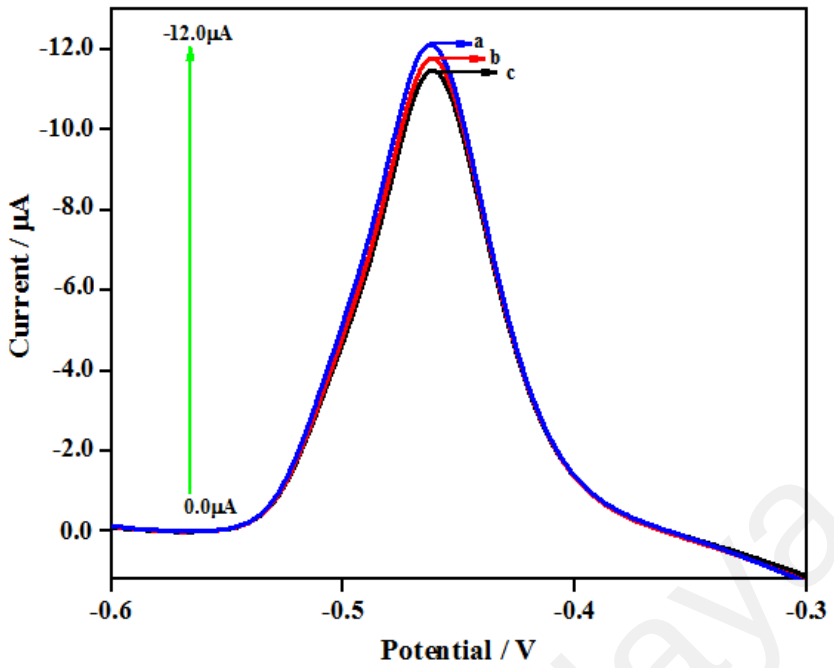

Figure 4.10: DPV curve of (MWCNTs$_f$-NGr/CTS)-Cu/GCE in 0.2 M PBS (pH 7.0) containing 2 µM NLM, (a) first signal, (b) 1st week interval, (c) 2nd weeks interval.

4.6.4 Anti-interference study of modified electrode

To manifest the selectivity of the modified sensor, the anti-interference investigation was performed in the presence of some common biological compounds, interfering molecules and 150 µM NLM in 0.2 M PBS (pH 7.0). From the amperometric study for 600 s, it is observed that even a 60 folds increase of glucose, lactose, sucrose, fructose, ascorbic acid, dopamine, uric acid, nitro compounds (4-nitrophenol, nitrobenzene) and a 20 fold increase of Metronidazole drug do not interfere with the NLM detection (Figure 4.10A), but the current (I_{pa}) increases upon the spike of 150 µM NLM. The DPV response was also recorded in the presence of the same interfering molecules, but no signal was obtained from the interfering compounds except for the desired NLM analyte (Figure 4.11B). It can be concluded from both results that the (MWCNTs$_f$-NGr/CTS)-Cu/GCE sensor can selectively detect NLM even in the presence of interfering compounds.

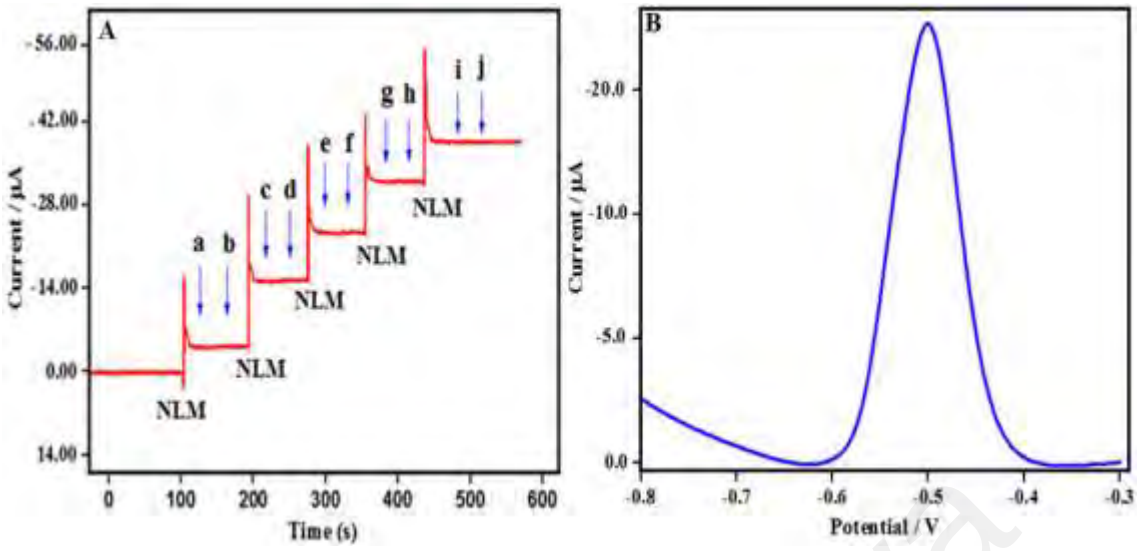

Figure 4.11: (A) Amperometric responses on (MWCNTs$_f$–NGr/CTS)-Cu/GCE with NLM in presence of 60 fold excess concentration of glucose (a), lactose (b), sucrose (c), fructose (d), ascorbic acid (e), dopamine (f), and uric acid (g), and 60 fold of nitro compounds 4-nitrophenol (h), nitrobenzene (i), and 20 fold of Metronidazole drug (j) in 0.2 M PBS (pH = 7.0). (B) DPV in the presence of interfering molecules at same concentration with (A), in 0.2 M PBS (pH = 7.0).

4.6.5 Real sample analysis

To evaluate the potential for real application of (MWCNTs$_f$-NGr/CTS)-Cu/GCE for sensing NLM, real sample investigations were carried out using tablets and human blood serum. The blood sample was collected from a healthy volunteer from University Malaya Hospital Kuala Lumpur. For the blood collection, we prepared a request letter with supervisor's sign on it. After handover the letter to the head of the nurse with proper evidence, we were able to collect the human blood from them. The serum was collected by centrifugation, filtration and then dilution through 0.2 M PBS (pH 7.0). Five NLM tablets (50 mg each) were finely ground into powders, dispersed in ethanol solution and filtered. Table 4.2 and Table 4.3 represent the recovery study of NLM from the tablets and blood serum, accordingly. Satisfactory recovery results and RSD values were achieved for NLM in blood serum (98 – 101.5%) and tablets (98 – 102%) which disclose that the proposed sensor has potential applications for real samples.

Table 4.2: Determination of NLM in pharmaceutical preparations using differential pulse voltammetry at pH 7.0 (n=5).

Sample	Labelled Amount	Added Amount (µM)	Found (mg/tablet)	Recovery (%)	RSD (%)	HPLC (mg)
Tablet	50 mg	0.05	0.049	98.0	2.25	0.051
		0.10	0.101	101	0.55	0.101
		0.5	0.51	102	2.15	0.52
		1.0	1.01	101	0.45	1.01
		2.0	2.02	101	0.57	2.01

Table 4.3: Determination of NLM in human serum sample using differential pulse voltammetry at pH 7.0 (n=5).

Sample	Added (µM)	Found (µM)	Recovery (%)	RSD (%)	HPLC (µM)
Human Serum					
Sample	0.1	0.101	101.0	2.35	0.102
	0.5	0.049	98.0	1.50	0.51
	1.00	0.99	99.0	0.85	1.01
	2.00	2.03	101.5	2.28	2.02
	3.00	2.98	99.33	1.75	3.01

CHAPTER 5: AMPEROMETRIC DETECTION OF PARACETAMOL BY IMMOBILIZED COBALT ON FUNCTIONALIZED MWCNTS - CHITOSAN THIN FILM

This chapter focuses on the characterization of functionalized multiwall carbon nanotubes and chitosan with immobilized cobalt modified electrodes for the electrochemical detection of paracetamol in tablet and biological fluids

5.1 *f*-MWCNTs –CTS-Co nanocomposite for paracetamol detection

In this section, functionalized multiwall carbon nanotubes, chitosan and immobilized cobalt (*f*-MWCNTs/CTS-Co) nanocomposite were synthesized and characterized by several analytical techniques such as FTIR spectroscopy, FESEM and EDX analysis. Then, an electrochemical sensor was fabricated for the detection of paracetamol (PR) by modifying a GCE with the (*f*-MWCNTs/CTS-Co) nanocomposite. Voltammetric methods were used to evaluate the electrochemical behavior of PR. In addition, the linear range, limit of detection (LOD), reproducibility, stability and selectivity of the electrochemical sensor were studied. The prepared sensor also showed satisfactory results in real sample analysis using commercial tablets and biological samples.

5.2 Aim of the research

The aim of this study is to fabricate a new modified electrode based on (*f*-MWCNTs, CTS and Co. The combination of these materials into a nanocomposite is expected to improve the properties of the nanocomposite compared to the single materials. Thus the excellent electrical conductivity of *f*-MWCNTs and improved dispersion of CTS and the catalytic effect of Co is a hallmark for the high performance electrochemical sensing of PR.

5.3 Electrode characterizations

5.3.1 FT-IR spectroscopy analysis

Figure.5.1 shows the FTIR spectra for pristine MWCNTs (a), *f*-MWCNTs (b), *f*-MWCNTs/CTS(c), and *f*-MWCNTs/CTS-Co (d). Curve a and b shows the presence of an asymmetric and symmetric stretch of the CH_2 group at 2923 cm^{-1} and 2852 cm^{-1} respectively (Scheibe et al., 2010). But curve b shows the stretching vibrations of the carboxyl group (COOH) at 1740 cm^{-1} which is absent in curve a (Afkhami et al., 2016; Osswald et al., 2007). Curve b also shows that the peak intensity of the *f*-MWCNTs peaks is higher than the pristine MWCNT. Figure 5.1c is the spectrum of the *f*-MWCNTs/CTS composite. The peaks around 2920 cm^{-1} and 1746 cm^{-1} are attributed to the presence of the CH_2 and COOH groups respectively, in the *f*-MWCNTs. The three characteristics absorption bands are found at 3370 cm^{-1} (O–H and N–H stretching vibrations) and 1558 cm^{-1} (N–H bending vibrations), 1082 cm^{-1} (C–O–C stretching vibrations) are attributed to the CTS molecule (Gregorio-Jauregui et al., 2012). The presence of these functional groups confirms the presence of the *f*-MWCNTs and CTS in the composite. Figure 5.1d is the spectrum of the *f*-MWCNTs/CTS-Co composite where the same characteristics bands are observed as in Figure 5.1c (*f*-MWCNTs/CTS) but with the presence of an additional band for cobalt at around 560 cm^{-1} (Fettkenhauer et al., 2015).

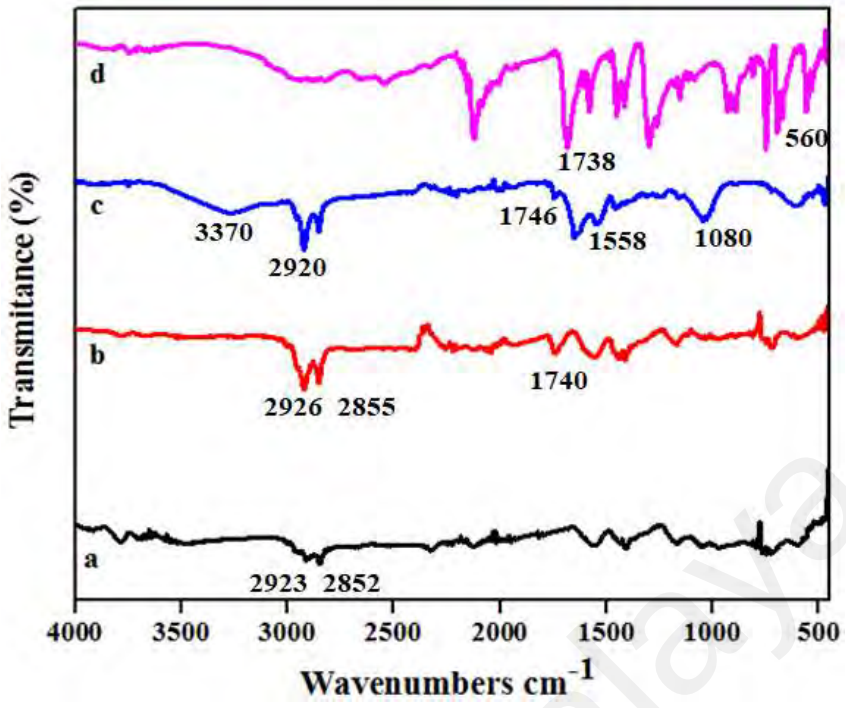

Figure 5.1: FTIR spectra of Pristine (a), *f*-MWCNTs (b), *f*-MWCNTs/CTS (c), *f*-MWCNTs/CTS-Co (d).

5.3.2 FESEM and EDX analysis of *f*-MWCNTs/CTS-Co/GCE

Field emission scanning electron microscopy (FESEM) was used to investigate the surface morphology of the *f*-MWCNTs/CTS-Co/GCE. Figure 5.2A shows a layer of *f*-MWCNTs homogeneously distributed on the electrode surface free from aggregation. Figure 5.2B shows that the morphology of the CTS film markedly differs from the general morphology of *f*-MWCNTs. The inset (5.2) in Figure 5.2B shows clear evidence that the CTS is homogenously dispersed on the *f*-MWCNTs surface. Figure 5.2C is the image of the *f*-MWCNTs/CTS-Co composite on the GCE surface which confirms the successful deposition of cobalt onto the *f*-MWCNTs surface. The cobalt metal is well distributed, spherical in shape and did not alter the morphology of the *f*-MWCNTs and CTS. The presence of cobalt metal is highlighted by circles in the FESEM images (Figure 5.2C to Figure 5.2D). The results demonstrate the successful preparation of *f*-MWCNTS/CTS-Co composite and the incorporation on the GCE surface which increases the electrode surface area to enhance the PR adsorption. Figure 5.2D presents

the image of *f*-MWCNTS/CTS-Co composite where the circles represent the successful deposition of cobalt ions. The energy dispersive X-ray (EDX) analysis (Figure 5.2E) of the electrode surface confirms the presence of cobalt (2.53%), carbon (67.87%), nitrogen (12.86%) and oxygen (16.74%) as the main elements of the composite. This result clearly shows that cobalt is dispersed homogenously on the surface of the *f*-MWCNTs layer.

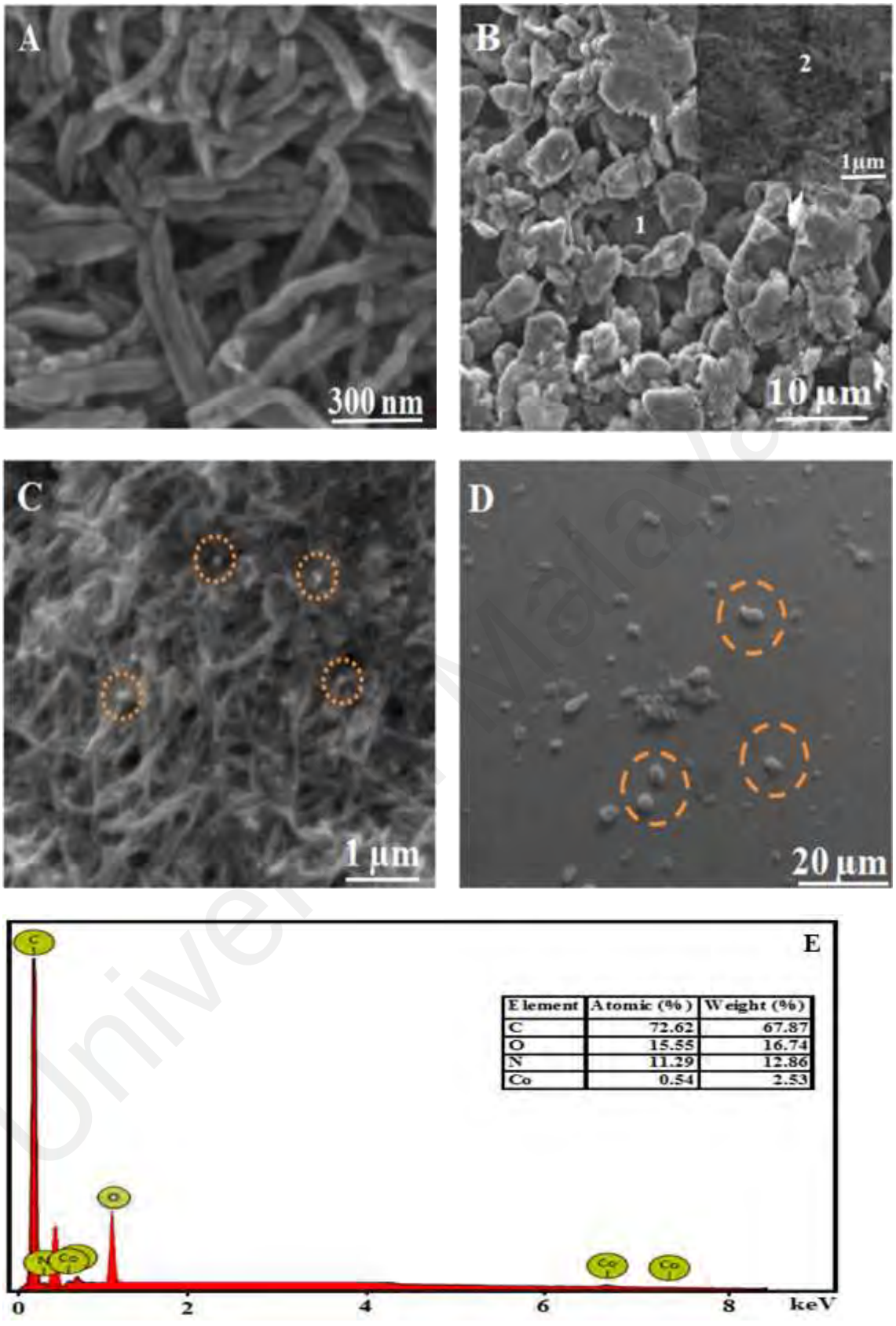

Figure 5.2: The FESEM images of (A) *f*-MWCNT/GCE, (B) *f*-MWCNTs/CTS/GCE and (C) *f*-MWCNTs/CTS-Co/GCE, (D) SEM image for modified electrode (*f*-MWCNTs/CTS-Co) surface. The circular part in (Figure D) indicates the successful distribution of cobalt. (E) EDX analysis of *f*-MWCNTs/CTS-Co/GCE.

5.4 Electrochemical characterization

5.4.1 Electrochemical impedance spectroscopy (EIS) analysis

Electrochemical impedance spectroscopy (EIS) is utilized to investigate the interfacial electron transfer kinetics of the modified electrode. The charge transfer resistance (R_{ct}) value depends on the dielectric and insulating characteristics at the electrode/electrolyte interface, which can be derived from the semicircle diameters of the Nyquist plots. This resistance controls the electron transfer kinetics of the redox reaction at the electrode-electrolyte interface. Figure 5.3 (A) is the Nyquist plots of the impedance spectrum of the GCE (curve a), CTS/GCE (curve b) *f*-MWCNTs/GCE (curve c), *f*-MWCNTS/CTS-Co/GCE (curve d) in 0.1 M potassium chloride solution with 5.0 mM/L $[Fe(CN)_6]^{3-/4-}$. From the data fitting, the bare GCE and CTS/GCE (curve b) show R_{ct} value of 580 Ω and 420 Ω. Compared to the bare GCE (curve a), *f*-MWCNTs/GCE (curve c) shows a distinctively decreased R_{ct} value of 140 Ω which indicates the successful absorption of *f*-MWCNTs on the GCE surface. The decreased resistance is due to the improved electrical conductivity of *f*-MWCNTs. The R_{ct} of the *f*-MWCNTs/CTS-Co/GCE modified electrode (curve d), is 47 Ω indicating a lower electron transfer resistance compared to *f*-MWCNTs/GCE. The R_{ct} value of *f*-MWCNTS/CTS-Co/GCE is lower than the *f*-MWCNTs/GCE suggesting that the CTS-Co complex was dispersed successfully in the presence of *f*-MWCNTs on the GCE surface. Though chitosan is an electrical insulator but is a good ion conductor, thus the electrochemical response of the $[Fe(CN)_6]^{3-/4-}$ redox couple could be enhanced by the incorporation of the complex in the chitosan matrix with Co. The impedance data was fitted to an equivalent circuit as shown in inset of Figure 5.3. The R_s, R_{ct}, C_{dl} and W represents the solution resistance, electron transfer resistance, double layer capacitance and Warburg impedance, respectively.

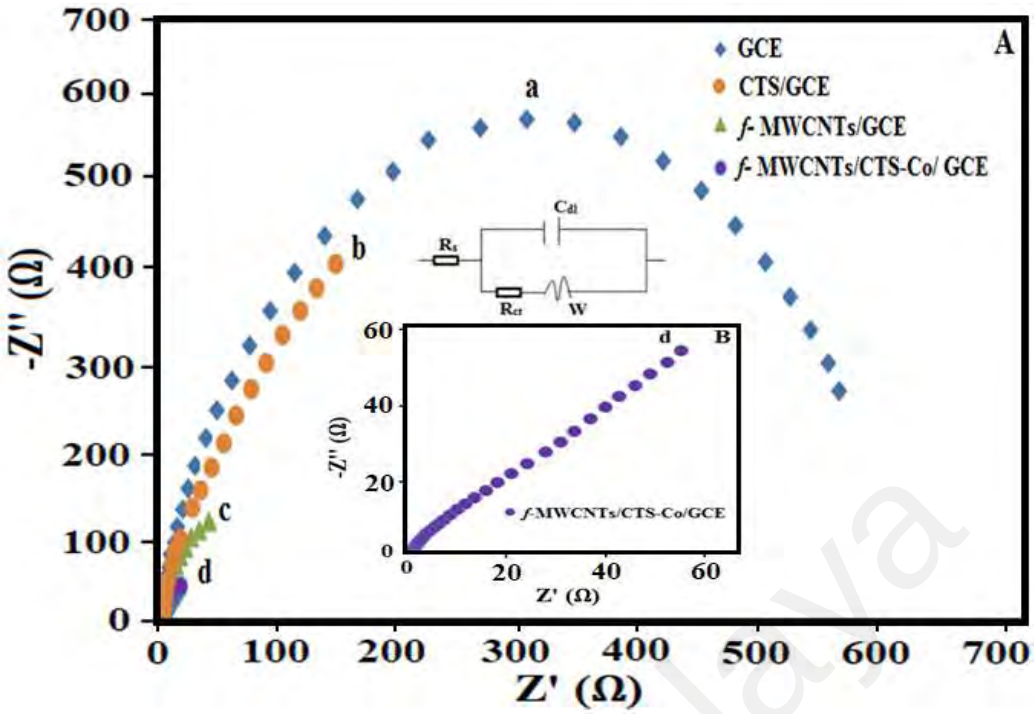

Figure 5.3: (A) EIS spectra for (a) GCE, (b) CTS/GCE, (c) *f*-MWCNTs/GCE, (d) *f*-MWCNTs/CTS-Co/GCE modified electrode in 0.1 M KCl solution with 5 mM $[Fe(CN)_6]^{3-/4-}$. Inset (B) EIS for *f*-MWCNTs/CTS-Co/GCE.

5.4.2 CV of PR on *f*-MWCNTs/CTS/-Co/GCE electrode

The electrochemical study of PR was performed by cyclic voltammetry (CV) on (a) bare GCE, (b) CTS/GCE, (c) *f*-MWCNTs/GCE, (d) *f*-MWCNTs/CTS/GCE and (e) *f*-MWCNTs/CTS-Co/GCE in the presence of 50 µM PR in 0.2 M PBS (pH 7) at 0.1 V s^{-1}. The inset of Figure 5.4 shows small oxidation peaks for GCE and CTS/GCE at 0.43 V attributed to paracetamol but with the absence of the reduction peak on the surface of the bare GCE. Due to the slow electron transfer rate, no significant current change was observed for the GCE and CTS/GCE. However, Fig. 5.4c shows the presence of a redox peak at 0.34 V due to the higher electrical conductivity of *f*-MWCNTs. Figure 4d reveals that the *f*-MWCNTs/CTS/GCE composite shows no significant current change compared to the *f*-MWCNTs/GCE. This is because although CTS has very low electrical conductivity, it facilitates the dispersion of *f*- MWCNTs on the electrode surface via the hydrogen bonding between CTS and *f*-MWCNTs. In the *f*-MWCNTs/CTS-Co (Figure 5.4e) composite, a remarkably sharp redox peak is

observed due to the higher electrochemical redox activity of the PR on the modified electrode. In addition, the oxidation peak potential is shifted to positive region compared to the *f*-MWCNTs and *f*-MWCNTs/CTS electrodes. The increased current of the *f*-MWCNTs/CTS-Co composite is attributed to the synergistic effects of CTS and Co. The CTS immobilizes the Co into the polymeric matrix, while the *f*-MWCNT forms an electronic conducting network in the composite which enhances the electrocatalytic activity of Co and increases the redox peak current significantly (Mao et al., 2015). The CTS with OH functional groups provide and an ideal platform for the immobilization of PR through hydrogen bonding before the electrocatalytic reaction on Co occurs. This phenomenon is confirmed in Section 5.1.3.1 where the electrochemical redox behavior of PR on the *f*-MWCNTs/CTS-Co modified electrode is a surface-confined process. Thus, the composite of *f*-MWCNTs/CTS-Co/GCE was further investigated for the detection of PR.

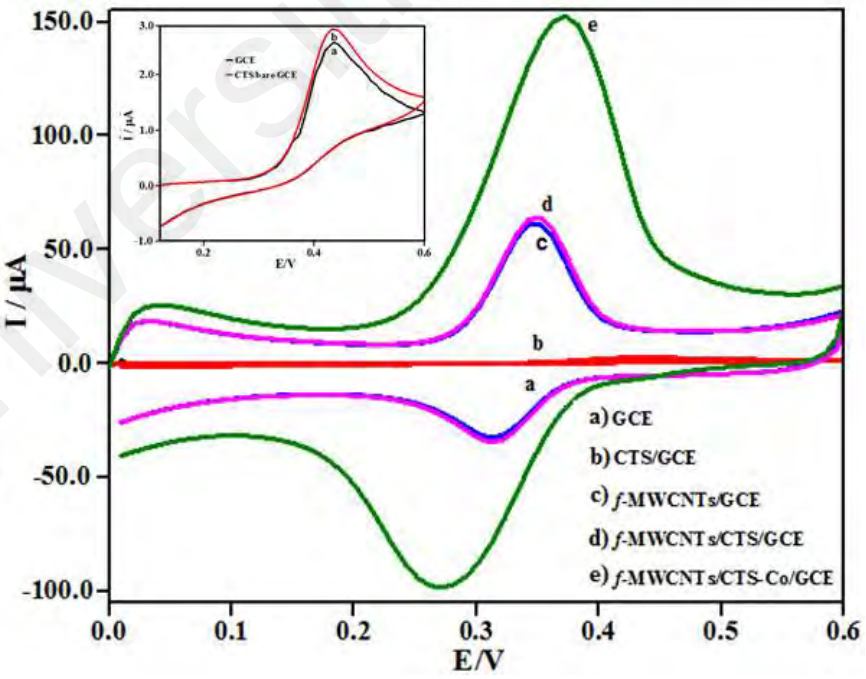

Figure 5.4: Cyclic voltammograms of 50 µM of PR on a) bare GCE, b) CTS/GCE, c) *f*-MWCNTs/GCE, d) *f*-MWCNTs/CTS/GCE, e) *f*-MWCNTs/CTS-Co/GCE in 0.2 M phosphate buffer solution (pH 7.0) as supporting electrolyte at a scan rate of 0.1 V s^{-1}.

5.5 Optimization of the fabricated sensor

5.5.1 Scan rate study of *f*-MWCNTs/CTS-Co sensor

The redox behavior of 50 µM PR (in 0.2 M L^{-1} PBS at pH 7) at the *f*-MWCNTs/CTS-Co modified electrode was investigated by varying the scan rates (10-400 mV^{-1}) in cyclic voltammetry as shown in Figure 5.5A. The redox peak currents of PR increase linearly with the increase of scan rate. In Figure 5.5B, the parameters from the linear regression equations are: I_{pa} (µA) = 0.0045 + 0.807 with a correlation co-efficient R^2 = 0.997; and I_{pc} (µA) = -0.0025 + 0.196 and correlation co-efficient R^2 = 0.999. This confirms that the redox process of PR at the *f*-MWCNTs/CTS-Co modified electrode is a surface-confined process (Teng et al., 2015).

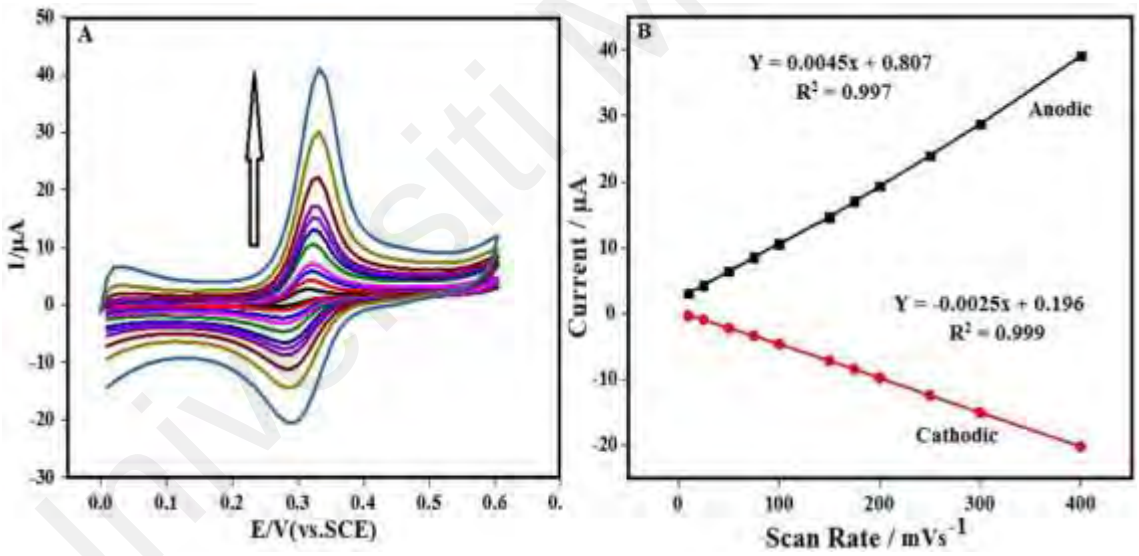

Figure 5.5: Cyclic voltammetry of 50 µM of PR on *f*-MWCNTs/CTS-Co/GCE at scan rates ranges from 10 to 400 mVs^{-1} in 0.2 M phosphate buffer solution (pH 7.0) as the supporting electrolyte (A). The plot of the peak current vs. scan rates (B).

5.5.2 Analysis of pH variation

The pH of the electrolyte affects the electrochemical response of the *f*-MWCNTs/CTS-Co modified electrode due to the redox behavior of PR. Figure 5.6A presents the cyclic voltammetry of 50 µM PR solution between pH 5.0-10.0. Figure

5.6B shows that the anodic peak current of PR increases as the pH increases from 5.0 to 7.0 but decreases beyond pH 7.0. This is due to the slower kinetics of the PR redox reaction with the presence of the phenoxide anion (Lu & Tsai, 2011). On the other hand, PR is hydrolyzed to p-aminophenol at very low pH values (Arvand & Gholizadeh, 2013). Therefore, the maximum peak current occurs at pH 7.0 and was selected as the working pH for further electrochemical experiments. Figure 5.6C shows a good linear relationship of the anodic peak potential with pH and the resultant linear regression equation is E_{pa} = -0.032 pH + 0.584 and R^2 = 0.996. Zhou *et al*. reported the following equation, dEpa/dpH = (-2.303mRT)/(nF) (Zhou et al., 2009). Here, *n* is the number of electrons transferred, *m* is the proton number, *R* is the gas constant, *T* is the Kelvin temperature, E_{pa} is the anodic peak potential and *F* is the Faraday constant. From this equation, it is clear that the redox reaction involves the same number of electrons and protons (2) (Fanjul-Bolado et al., 2009). The anodic and cathodic peak potentials are 0.36 V and 0.31 V, respectively, for the redox reaction of PR to N-acetyl-P-quinone-imine. The electrooxidation reaction of PR is given as below (Appendix B). For the fabrication *f*-MWCNTs/CTS-Co modified GCE, metallic cobalt has been used. The metallic cobalt does not produce any ions when goes into solution. The metallic Co becomes Co (II) and becomes oxidized and covalently bonded with the COOH- groups of f-MWCNTs and NH_2 group of CTS. Thus, Co shows the catalytic effect. A simple three steps mechanism for the electrooxidation reaction of PR on the surface of the *f*-MWCNTs/CTS-Co modified GCE can be proposed as below:

PR+*f*-MWCNTs/CTS-Co → PR-*f*-MWCNTs/CTS-Co (5.1)

PR-*f*-MWCNTs/CTS-Co → PR-*f*-MWCNTs/CTS-Co (II) + $2e^-$ (5.2)

PR-*f*-MWCNTs/CTS-Co (II) → N-acetyl-p-quinone-imine + *f*-MWCNTs/CTS-Co+$2H^+$ (5.3)

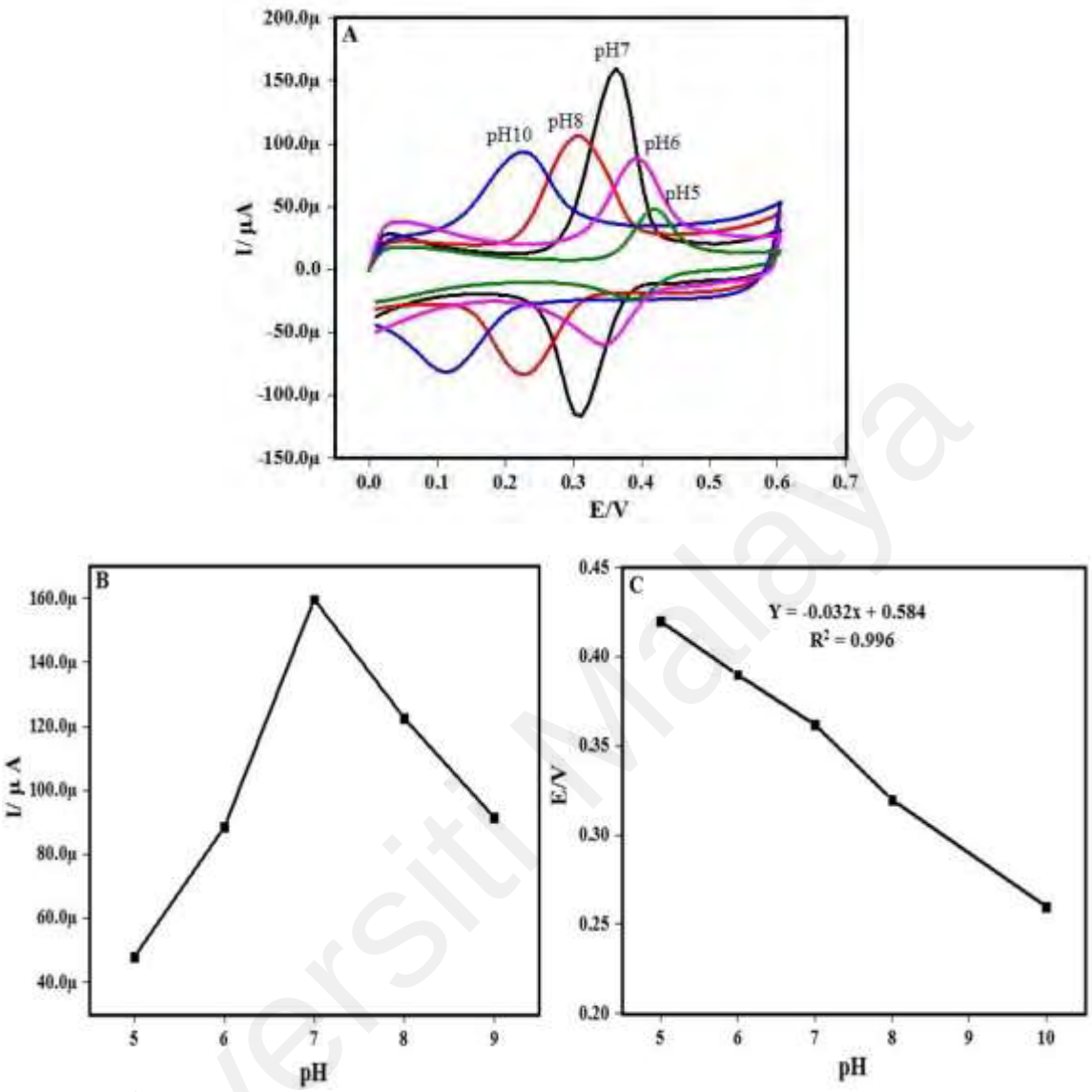

Figure 5.6: (A) The pH (5.0 to 10.0) effects on cyclic voltammograms of 50 µM of PR at the modified *f*-MWCNTs/CTS-Co electrode at 0.1 V s^{-1}. (B) The plot of solution pH with anodic peak current. (C) The plot of pH vs anodic peak potential (E_{pa}).

5.6 Performance evaluation of *f*-MWCNTs/CTS-Co/GCE sensor

5.6.1 Analytical characterization and method validation

Differential pulse voltammetry (DPV), a sensitive electrochemical technique was utilized to evaluate the performance of the *f*-MWCNTs/CTS-Co modified electrode and the quantitative determination of PR. The calibration plot for PR was determined by the

DPV technique in 0.2 M PBS. Figure 5.7A presents the DPV response for various concentrations of PR (0.1-400 µmol L^{-1}) at the *f*-MWCNTs/CTS-Co modified electrode. A well-defined and sharp anodic peak current occurs at 0.32 V with the increase of PR concentration. Figure 5.7B presents the calibration plot of current with PR concentration with a linear regression equation I_{pa} (µA) = 0.636 C_{PR} (µmol L^{-1}) + 0.273 (R^2 = 0.99). The limit of detection (LOD) was estimated by following $3S_b/m$, where S_b refers to the standard deviation of the blank sample while *m* refers to the slope of the calibration curve. A comparative study of the *f*-MWCNTs/CTS-Co modified electrode with other electrodes for PR determination is presented in table 1. It is clear that the newly developed electrode has a wider linear range and showed better LOD compared to the other electrodes. This result indicates the reliability of the fabricated electrode for the quantitative detection of PR.

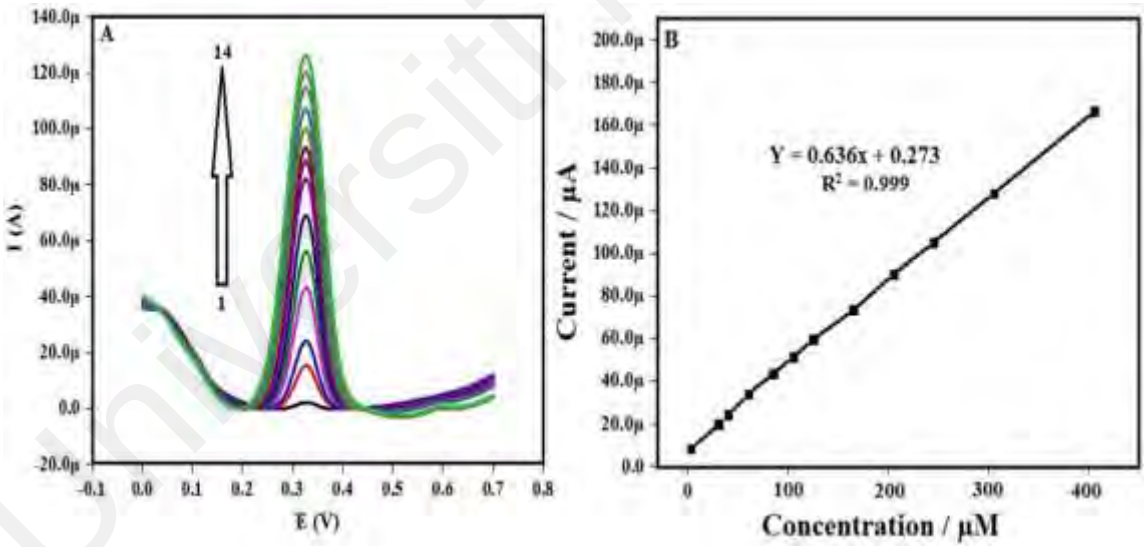

Figure 5.7: DPVs response at *f*-MWCNTs/CTS-Co/GCE for different concentration of PR between (0.01 µM – 400 µM) in 0.2 M phosphate buffer solution (pH 7.0) (A). The calibration curve of peak current and PR concentration (B).

Table 5.1: The results of various electrodes for the determination of PR.

Electrode	Linear Range (µM)	Detection limit (µM)	Reference
C60/GCE	50-150	50	(Goyal & Singh, 2006)
N-DHPB-MWCNT/CPE	15-270	10	(Li & Jing, 2007)
Poly (taurin)-MWCNT/GCE	1-100	0.50	(Wan et al., 2009)
Chitosan -MWCNT/GCE	1-145	0.10	(Razmi & Habibi, 2010)
f-MWCNT/GCE	3-300	0.60	(Alothman et al., 2010)
f-MWCNTs/CTS-Co/GCE	0.1-400	0.01	**This work**

5.6.2 Interference Study

Generally, the analytical detection of paracetamol suffers from interference due to the presence of some biological compounds. The amperometric method was utilized to investigate the selectivity of PR at 0.45 V. Figure 5.8 shows the amperometric responses of PR with a 10-fold concentration increase of interfering ions such as dopamine, ascorbic acid, uric acid, fructose and glucose. The results confirm that the analytical detection using the modified electrode is free from interferences and is highly selective for the detection of PR in biological samples.

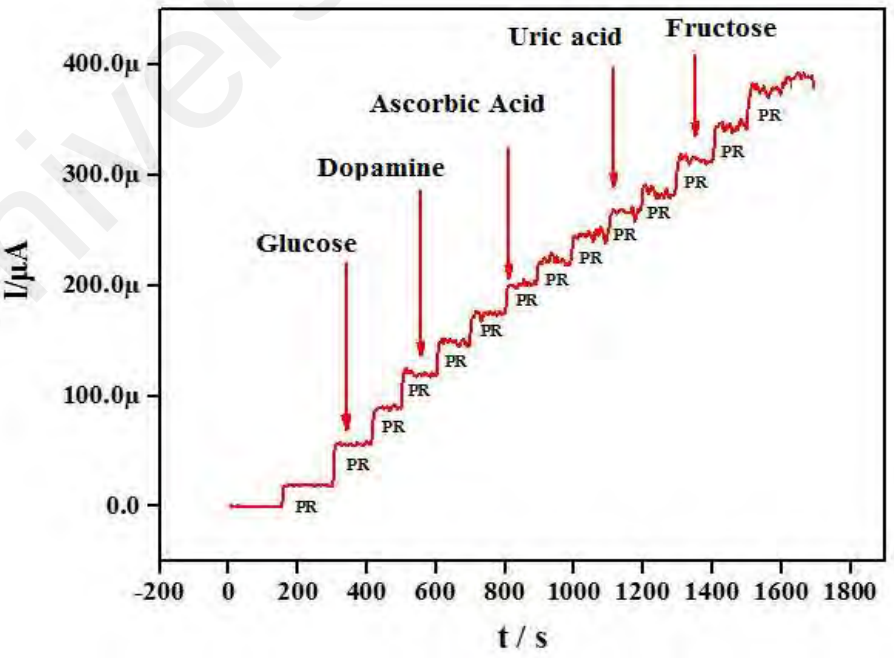

Figure 5.8: Amperometric study of the PR oxidation in the presence of 10-fold concentration of interfering ions.

5.6.3 Reproducibility and stability of the fabricated electrode

Reproducibility and stability are two of the most important criteria for a successful sensor. The reproducibility of the modified electrode for the detection of PR was conducted in the same PR standard solution and using the same modified electrode. The relative standard deviation (RSD) of 3.009% was obtained for the anodic peak current of PR, which indicates a good reproducibility of the modified sensor. After a week of storage in a refrigerator at 4 °C, the PR peak current at the *f*-MWCNTs/CTS-Co/GCE modified electrode retained 90% of its initial value. Furthermore, the peak current slightly decreased to 85% of the initial value after a month of storage. These results confirmed that the *f*-MWCNTs/CTS-Co/GCE maintains satisfactory storage stability.

5.6.4 Recovery Study and analytical test results for real samples

To assess the viability of the newly developed *f*-MWCNTs/CTS-Co/GCE sensor, a recovery test of PR was conducted on spiked tablet samples and from human serum. Human blood specimens were collected from University Malaya Hospital for the blood collection, we prepared a request letter with supervisor's sign on it. After handover the letter to the head of the nurse with proper evidence, we were able to collect the human blood from them. The blood serum was collected by centrifugation before the experiments. The spiked sample consists of 1% human serum and PR in 0.2 M PBS. From the analysis of recovery test results (Table 2 and 3), it can be considered that the recovery of PR at the *f*-MWCNTs/CTS-Co/GCE modified electrode was satisfactory. Furthermore, the values obtained from the modified electrode have close similarities with the results obtained from the HPLC technique.

Table 5.2: PR detection in tablet samples (n=3)

Sample	Labeled (mg/tablet)	Found (mg/tablet)	Recovery (%)	RSD (%)	HPLC (mg)
250 mg	250	249.4	99.76	2.8	250.2
500 mg	500	497.6	99.52	2.2	500.8
650 mg	650	645.2	99.26	1.9	651.6

Table 5.3: Results for PR recovery test by using human serum samples (n=3)

Added (µM)	Found (µM)	Recovery (%)	RSD (%)	HPLC (µM)
0	ND[a]	-	-	ND[a]
10	9.97	99.7	1.8	10.13
50	49.20	98.4	2.6	50.34
100	98.88	98.88	2.4	98.44

CHAPTER 6: TRI-METALLIC COBALT-NICKEL-COPPER BASED METAL ORGANIC FRAMEWORK NANOSTRUCTURES FOR THE DETECTION OF AN ANTICANCER DRUG NILUTAMIDE

This chapter discusses about the Tri-Metallic cobalt-nickel-copper (Co-Ni-Cu) based metal organic framework for the electrochemical detection of nilutamide in tablet and biological fluids

6.1 Detection of nilutamide using Co-Ni-Cu-MOF/NF sensor

In this section, tri-metallic Co-Ni-Cu based metal organic framework nanocomposite was synthesized and characterized by several analytical techniques such as XRD, XPS spectroscopy, FESEM, TEM, EDX and BET analysis. The electrochemical sensor was fabricated for the detection of nilutamide (NLM) by modifying the nickel foam (NF) with the trimetallic Co-Ni-Cu-MOF. Voltammetric methods were used to evaluate the electrochemical behavior of NLM. In addition, the linear range, LOD, reproducibility, repeatability, stability and selectivity of the electrochemical sensor were studied. The prepared sensor also showed satisfactory results in real sample analysis using commercial tablets and biological samples.

6.2 Aim of the research

The aim of this study is to fabricate a new modified electrode based on Co-Ni-Cu-MOF on the NF. The combination of the Co-Ni-Cu tri-metals into MOF nanocomposite is expected to improve the properties of the nanocomposite compared to the single MOF nanocomposite. Thus the synergistic effect of Co-Ni-Cu tri-metals with the excellent electrical conductivity and excellent catalytic effect is a hallmark for the high performance electrochemical sensing of NLM.

6.3 Electrode characterizations

6.3.1 X-ray diffraction analysis

The crystalline properties of the tri-metallic Co-Ni-Cu-MOF/NF was investigated by X-ray diffraction (XRD) spectroscopy as shown in Figure 6.1(a). The presence of high intensity peaks is due to the crystalline phase of the MOFs. The metallic phase of cobalt (Co) and nickel (Ni) occurs at 44.26° (111), 51.58° (002) and 76.18° (022) in accordance to the ICSD No. 98-008-6621 and 98-006-2718 of Co and Ni, respectively (Qiu et al., 2020), while copper (Cu) is present at 43.02° (111) and at 50.32° (002) in accordance to the ICSD No. 98-006-2672.

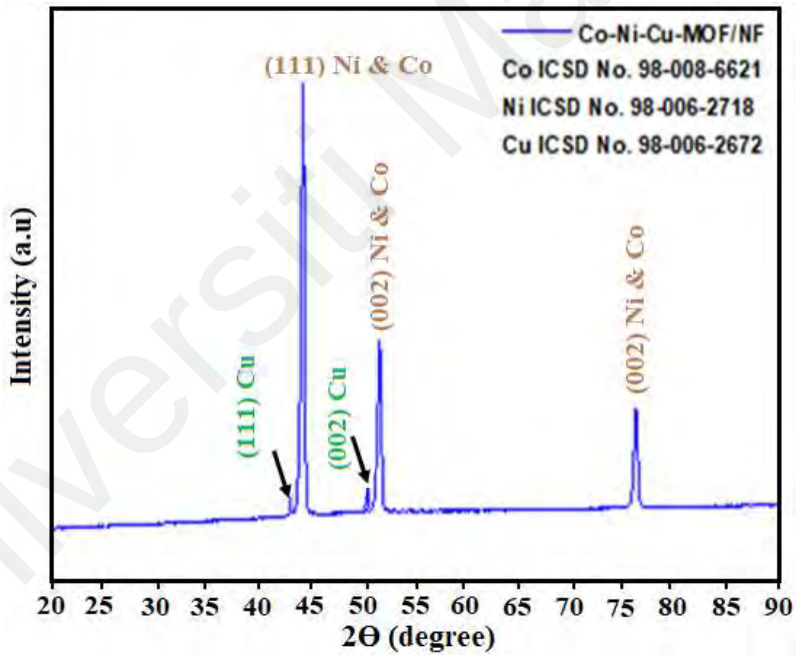

Figure 6.1: XRD diffractogram of Co-Ni-Cu-MOF/NF nanocomposite.

6.3.2 X-ray photoelectron spectroscopy analysis

X-ray photoelectron spectroscopy (XPS) provides useful information on the binding energy and the elemental composition of the material. The surface chemistry of Co-Ni-Cu-MOF was analyzed by XPS. The high-resolution scan of Co 2p (Figure 6.2A) reveals two prominent peaks at 775.2 eV and 790.5 eV binding energies corresponding

to the Co $2p_{3/2}$ and Co $2p_{1/2}$ levels, respectively, with a spin-orbital splitting (SOS) of Δ_{Co} = 15.3 eV. The presence of Co^{2+} was confirmed in the hybrid MOF composite from the fitting of the Co peaks and the SOS value (Topcu, 2020) . The narrow scan of Ni 2p could be deconvoluted into four different peaks as observed in Figure 6.2B, which consists of the Ni $2p_{3/2}$ and Ni $2p_{1/2}$ peaks, in addition to the shake-up satellite peaks (denoted as "sat"). The Ni $2p_{3/2}$ and Ni $2p_{1/2}$ peaks occur at binding energies of 848.1 eV and 865.7 eV with a SOS value of 17.6 eV. The satellite peaks adjacent to the Ni $2p_{3/2}$ and Ni $2p_{1/2}$ peaks confirmed the presence of Ni (II) oxidation state in the Co-Ni-Cu tri-metallic MOF (Mohd Zain et al., 2018). The Cu 2p spectrum (Figure 6.2C) demonstrates a pair of predominant peaks at 929.1 eV and 946.2 eV binding energies, attributed to the Cu $2p_{3/2}$ and Cu $2p_{1/2}$ levels, respectively. The satellite peaks at 935.4 eV and 955.3 eV binding energies confirmed the presence of Cu (II) oxidation state in the Co-Ni-Cu tri-metallic MOF. The SOS value of 17.1 eV suggests the formation of a hybrid organic network with the presence of Cu^{2+} (Wang et al., 2019). The XPS spectra substantiate the formation of the tri-metallic Co-Ni-Cu-MOF/NF where the Co, Ni and Cu are attached to the terephthalate linkers in the hybrid MOF.

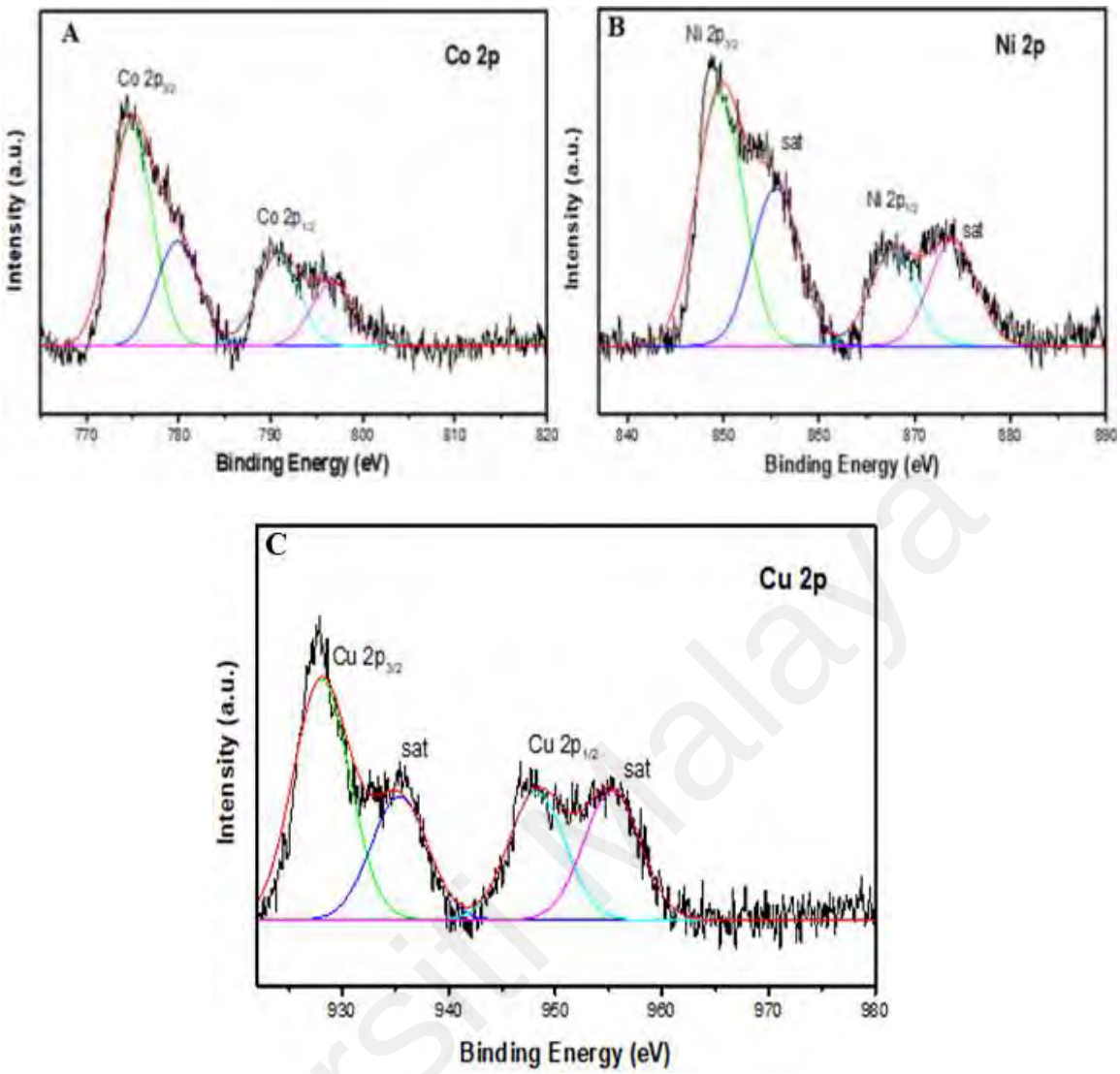

Figure 6.2: XPS spectrum of Co 2p (A) Ni 2p (B) and Cu 2p (C) for Co-Ni-Cu-MOF/NF nanocomposite.

6.3.3 FESEM, TEM, and EDX analysis

Further investigations on the morphology and structure of the tri-metallic Co-Cu-Ni-MOF/NF was performed using field emission scanning electron microscope (FESEM) in Figure (6.3) and energy dispersive X-ray (EDX) with mapping (Figure 6.4). Table 6.1 shows the elemental percentage of the composite, respectively and transmission emission microscope (TEM) imaging, (Figure 6.5).

The morphology of the synthesized Co-Ni-Cu-MOF/NF was investigated using FESEM imaging. The FESEM image shows that the growth of MOF occurs uniformly

through the NF substrate, the amount of materials grown calculated from several samples is ~1.5-2.0 mg/cm^2. Figure 6.3a shows the irregular aggregation and compression of the Co-MOF/NF thin flakes. While Figure 6.3b shows a similar surface morphology of the Ni-MOF/NF but with thicker flakes compared to the Co-MOF. Figure 6.3c reveals a granular appearance of the Cu-MOF/NF, while Figure 6.3d shows the aggregation of the tri-metallic Co-Ni-Cu-MOF/NF flakes, with the formation of thin cuboid structures and the presence of cavities. The tri-metallic MOF possesses a rough surface and larger surface area with the presence of cavities compared to other single metal MOFs.

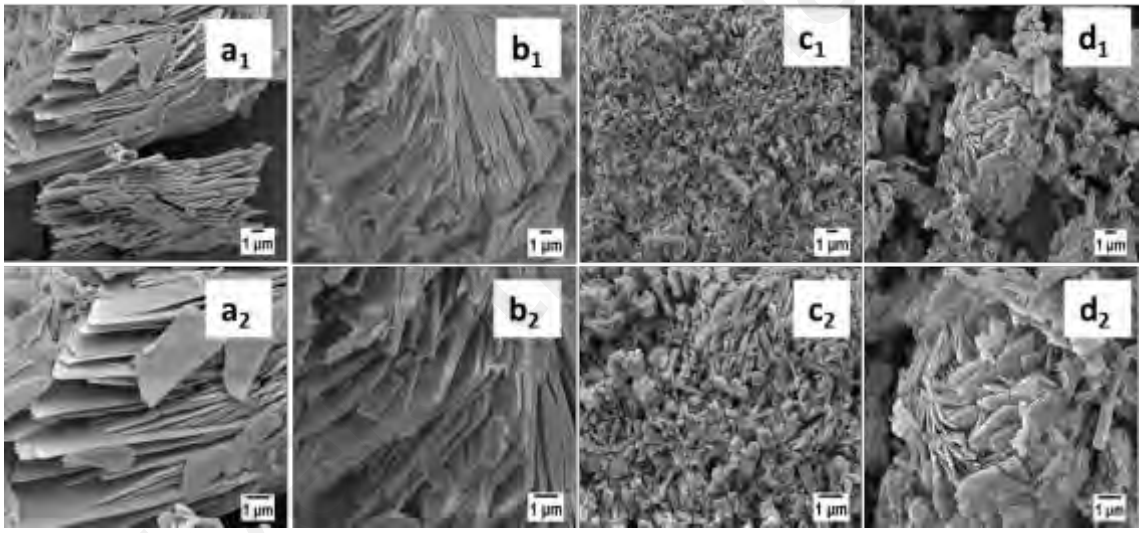

Figure 6.3: FESEM images of Co-MOF/NF (a), Ni-MOF/NF (b), Cu-MOF/NF (c) and Co-Ni-Cu-MOF/NF (d). The images in the first column are low-magnification at 5000x and second column at high-magnification 10000x.

Energy dispersive X-ray spectroscopy (EDX) analysis and elemental mapping were performed to obtain the elemental composition and distribution of the Co-Ni-Cu-MOF/NF as shown in Figure 6.4. The EDX spectrum shows that the main elements of the tri-metallic Co-Ni-Cu-MOF/NF composite are Co, Ni, Cu. It is confirmed that the tri-metallic MOF is free from chemical contaminants. Table 6.1 shows the elemental percentage of the C, O, Co, Ni and Cu are 44.73%, 44.90%, 0.70%, 7.50% and 2.17% respectively. The percentage of Ni is greater than the other metal elements as the Co-Ni-

Cu-MOF was grown on the Ni foam substrate. The elemental mapping from the EDX analysis indicates the homogeneous distribution of the three metals in the tri-metallic MOF.

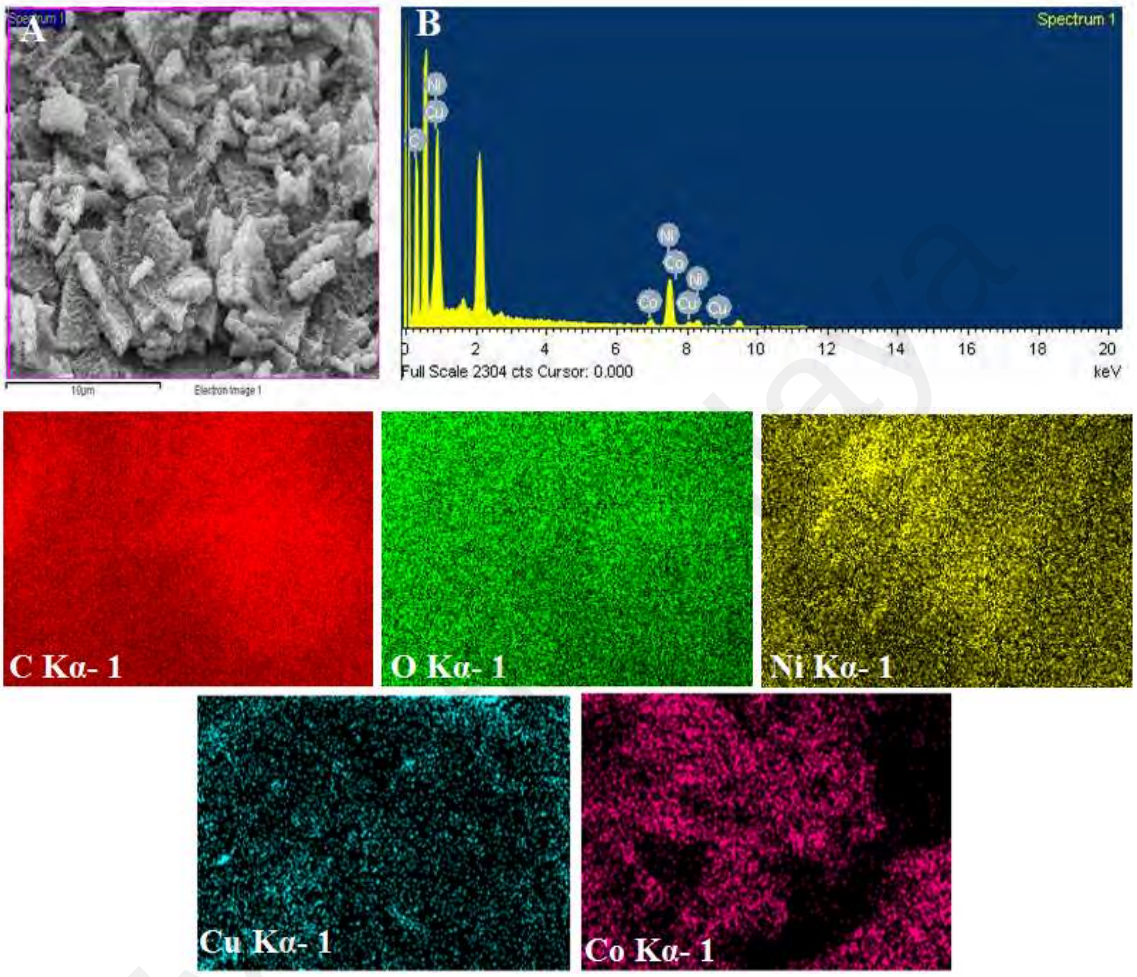

Figure 6.4: EDX and Mapping analysis of the Co-Ni-Cu-MOF/NF nanocomposite.

Table 6.1 EDX data of Co-Ni-Cu-MOF/NF.

Element	Weight %	Atomic %
C	28.65	44.73
O	38.30	44.90
Co	2.21	0.70
Ni	23.49	7.50
Cu	7.35	2.17
Totals	100.00	100.00

Figure 6.5 shows TEM images with different magnifications of Co-Ni-Cu-MOF/NF nanocomposite. Figure a and b show TEM images of Co-Ni-Cu-MOF/NF with a regular cuboid structure of the flakes stacked closely together. The TEM images at higher

magnifications (Figure 6.5d and 6.5e) reveal that the cuboid flakes are decorated with thin crumpled sheets that are concentrated on the edge of the structures. Figure 6.5c and 6.5f are the selected area electron diffraction (SAED) patterns which indicates the high crystallinity of the MOF material.

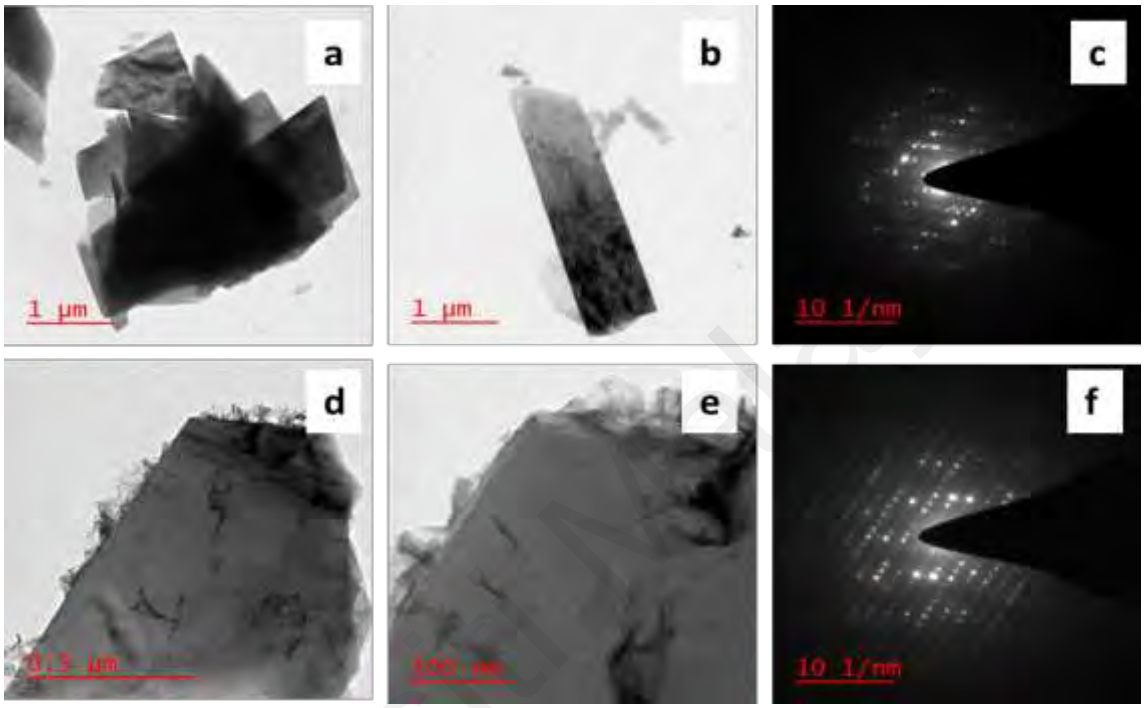

Figure 6.5: TEM images of Co-Ni-Cu-MOF/NF along with their SAED pattern.

6.3.4 BET analysis of fabricated sensor

The BET adsorption-desorption isotherm analysis was performed to determine the surface area, porosity and mean pore diameter of the synthesized a) Co-MOF/NF, b) Ni-MOF/NF, c) Cu-MOF/NF and d) Co-Ni-Cu-MOF/NF and shown in Figure 6.6. The BET surface areas of a) Co-MOF/NF, b) Ni-MOF/NF, c) Cu-MOF/NF and d) Co-Ni-Cu-MOF/NF were found to be 143.47 m^2/g, 153.65 m^2/g, 158.93 m^2/g and 382.87 m^2/g respectively, which confirms that the Co-Ni-Cu-MOF/NF possesses the largest surface area compared to Co-MOF/NF, Ni-MOF/NF, and Cu-MOF/NF. The nitrogen adsorption-desorption isotherm of Co-Ni-Cu-MOF/NF exhibits a big hysteresis loop at high relative pressure (P_s/P_0) range and the adsorption curve displays an abrupt

enhancement in the high pressure region (> 0.5 P_s/P_0) which indicates the high porous structure of Co-Ni-Cu-MOF/NF sample. In addition, the total pore diameter and pore volume of the Co-Ni-Cu-MOF/NF were found to be higher than the Co-MOF/NF, Ni-MOF/NF, and Cu-MOF/NF as summarized in Table 6.2. The large surface area and pore diameter facilitate the rapid electron transport between the electrode and electrolytic solution.

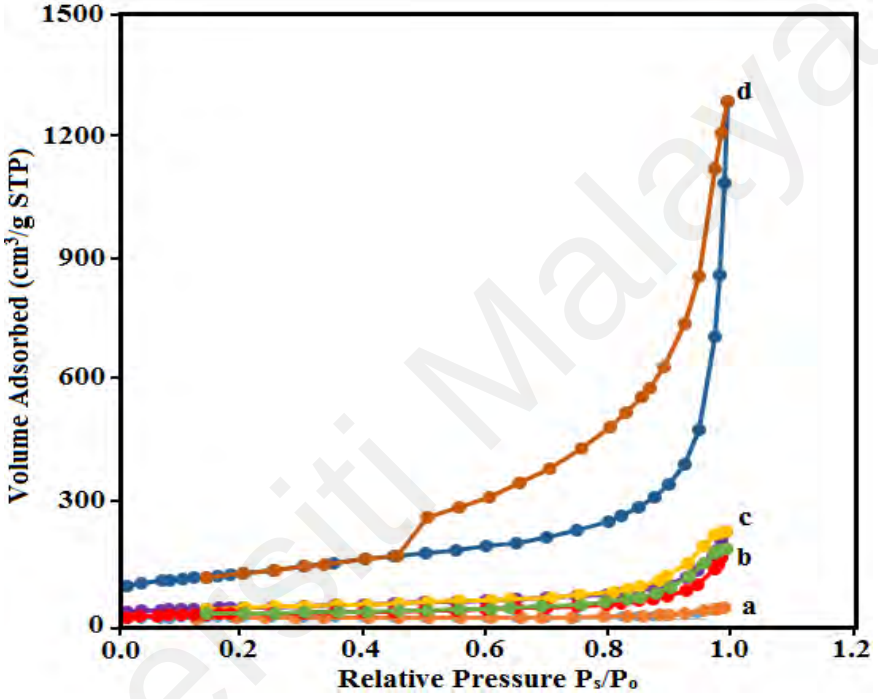

Figure 6.6: BET analysis of (a) Co-MOF/NF, (b) Ni-MOF/NF (c), Cu-MOF/NF (d) Co-Ni-Cu-MOF/NF.

Table 6.2: The BET analysis of Co-MOF/NF, Ni-MOF/NF, Cu-MOF/NF and Co-Ni-Cu-MOF/NF with their mean pore diameter and pore volume.

Sample	Surface Area (m^2/g)	Mean pore diameter (nm)	Pore volume (cm^3/g)
Co-MOF/NF	143.47	18.4	0.071
Ni-MOF/NF	153.65	18.7	0.082
Cu-MOF/NF	158.93	19.2	0.086
Co-Ni-Cu-MOF/NF	382.87	35.4	0.436

6.4 Electrochemical characterization of Co-Ni-Cu-MOF/NF sensor

6.4.1 EIS analysis and characterization of effective surface area

In order to investigate the electrode performance, the active surface area of the modified electrodes was calculated using electrochemical impedance spectroscopy (EIS) and cyclic voltammetry (CV) (Fig. 6.7). The results showed that the fabricated electrodes possess an enhanced surface area and increased electrical conductivity.

Electrochemical impedance spectroscopy (EIS) was performed to study the interfacial charge transfer resistance of the MOF sensor. The charge transfer resistance (R_{ct}) relies on the dielectric and insulating properties of the electrode/electrolyte interface that was calculated from the diameter of the semicircular region in the Nyquist plot. Figure 6.7A shows the Nyquist plots of the Co-MOF/NF (a), Ni-MOF/NF (b), Cu-MOF/NF (c), Co-Ni-Cu-MOF/NF (d) in 0.1 M KCl aqueous solution with 5 mM $[Fe(CN)_6]^{3-/4}$. From the data fitting, the R_{ct} value of Co-MOF/NF, Ni-MOF/NF, Cu-MOF/NF and Co-Ni-Cu-MOF/NF was found to be 2180 Ω, 1280 Ω, 870 Ω and 435 Ω, respectively. The lowest R_{ct} value of the Co-Ni-Cu-MOF/NF indicates the synergistic catalytic effect of the three metals which enhances the interfacial electron transfer rate compared to the single metal MOFs. The impedance data was fitted to an equivalent circuit as shown in inset of Figure 6.7 A. The R_s, R_p, and W represents the solution resistance, electron transfer resistance, and Warburg impedance, respectively.

To confirm the above results, the CV response (Figure 6.7B) was recorded in 5 mM $[Fe(CN)_6]^{3-/4}$ redox couple with 0.1 M KCl at 0.6 V s^{-1} for the measurement of active surface areas of the Co-MOF/NF (a), Ni-MOF/NF (b), Cu-MOF/NF (c) and Co-Ni-Cu-MOF/NF (d) fabricated electrodes using the Randles-Sevcik equation (Rawool & Srivastava, 2019).

$$I_p = 2.69 \times 10^5 \, A \, C \, D^{1/2} \, (n)^{3/2} \, \upsilon^{1/2} \quad (6.1)$$

The electrochemical active surface area was measured by the peak currents, where I_p = redox peak current (Amp), A = surface area of the electrode (cm^2), *n* = number of transferred electrons, C = concentration of the ferricyanide solution (mol cm^{-3}), D = diffusion coefficient (7.60×10^{-6} cm^2 s^{-1}) and υ = scan rate (V s^{-1}). The calculated electrochemical active surface area of Co-MOF/NF (a), Ni-MOF/NF (b), Cu-MOF/NF (c) and Co-Ni-Cu-MOF/NF (d) electrodes were found to be 0.0158 cm^2, 0.0164 cm^2, 0.0171 cm^2 and 0.0379 cm^2, respectively. The result shows that the tri-metallic Co-Ni-Cu-MOF/NF possesses the largest electrochemical active surface area which is approximately 2 folds larger than other single metal MOF electrodes. This effect is attributed to the enhanced porosity which increases the total surface area of the tri-metallic MOF.

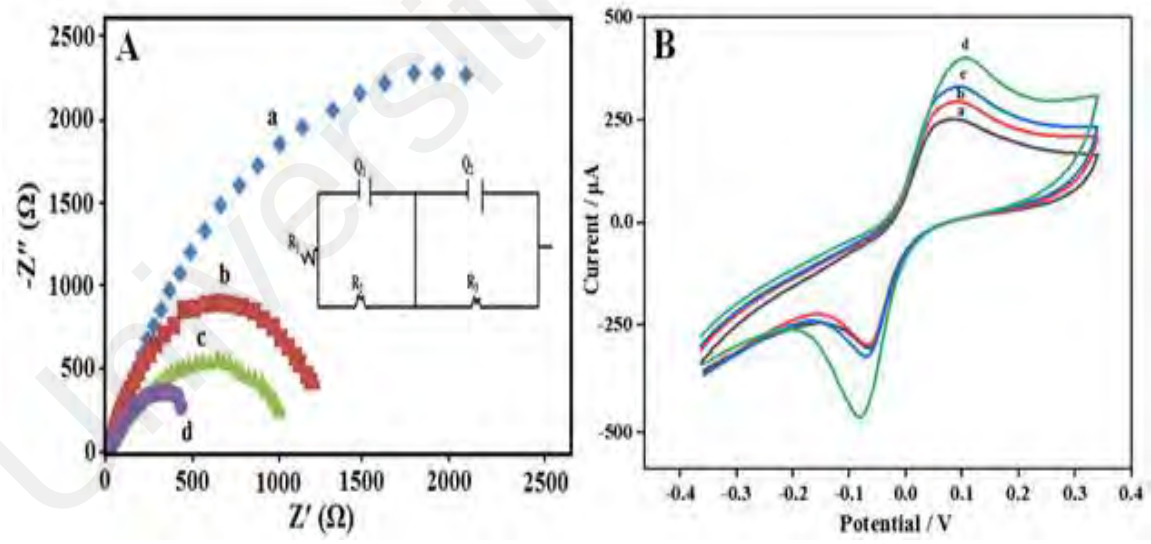

Figure 6.7: The electrochemical investigation in 5.0 mM $[Fe(CN)_6]^{3-/4-}$ in 0.1 M KCl solution (A) Nyquist plots of (a) Co-MOF/NF, (b) Ni-MOF/NF (c), Cu-MOF/NF (d) Co-Ni-Cu-MOF/NF; inset is the equivalent circuit for the fitting. (B) CVs obtained at (a) Co-MOF/NF, (b) Ni-MOF/NF (c), Cu-MOF/NF and (d) Co-Ni-Cu-MOF/NF; scan rate 0.6 V s^{-1}.

6.4.2 Electrochemical analysis of Co-Ni-Cu-MOF/NF sensor

The electrochemical behavior of 300 μM NLM was investigated using cyclic voltammetry (CV) of the Co-MOF/NF (a), Ni-MOF/NF (b), Cu-MOF/NF (c) and Co-Ni-Cu-MOF/NF (d) sensor electrodes at 0.6 V s^{-1} between -0.4 and 0.3 V in 0.1 M PBS at pH 7.0 (Figure 6.8). The prepared MOF sensor electrodes were assessed for the redox reaction of NLM. The MOF electrodes showed redox peaks of NLM but variations in the current were observed for each electrode. The tri-metallic Co-Ni-Cu-MOF/NF electrode showed the highest redox current response towards NLM compared to the single metal MOF electrodes. This confirms that the electron transfer rate of the tri-metallic Co-Ni-Cu-MOF/NF is remarkably enhanced due to the superior electrical conductivity which enhances the electrocatalytic activity of the tri-metallic Co-Ni-Cu-MOF/NF. At curve a-c, the single metal MOFs shows well-defined redox peaks of the NLM but the tri-metallic Co-Ni-Cu-MOF/NF (curve d) exhibits the strongest electrocatalytic effect of the redox reaction of NLM. The enhancement in the peak height of the Co-Ni-Cu-MOF/NF electrode could be attributed to the larger surface area due to the greater porosity, in addition to the greater affinity towards NLM due to the presence of cavities and the synergy of the catalytic effect among the three metals in the tri-metallic MOF. This increases the electrical conductivity which enhances the electrocatalytic effects for the detection of NLM.

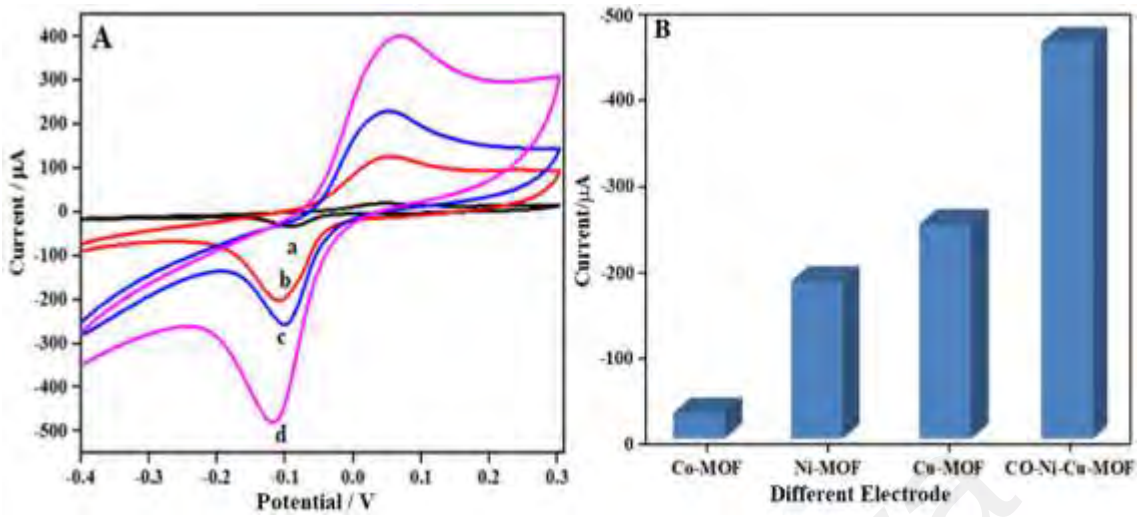

Figure 6.8: (A) CVs of 300 µM NLM on Co-MOF/NF (a), Ni-MOF/NF (b), Cu-MOF/NF (c) and Co-Ni-Cu-MOF/NF (d) in 0.1 M PBS (pH 7.0) at 0.6 V s^{-1}. (B) Bar diagram shows the different electrode vs current responses.

6.5 Optimization of Co-Ni-Cu-MOF/NF sensor

6.5.1 Effect of scan rate

The scan rate study was performed to investigate the kinetics of the NLM redox reaction whether the reaction is adsorption or a diffusion-controlled process. The effect of different scan rates from 10 to 1000 mV s^{-1} was investigated on the redox behavior of NLM at the Co-Ni-Cu-MOF/NF in the presence of 300 µM NLM in 0.1 M PBS (pH 7.0) as shown in Figure 6.9A. The results confirm that the peak currents of NLM were enhanced linearly with the scan rate with a slight shift of the peak potential at high scan rates. The oxidation peak potentials were shifted from 0.012 V to 0.068 V while the reduction peak potentials were shifted from -0.062 V to -0.119 V. The linear relationships of the peak current (I_p) and scan rate (υ) are illustrated by the following equations (Figure 6.9B):

$$I_{pa}\,(\mu A) = 0.430\upsilon + 42.537 \qquad (R^2 = 0.991) \qquad (6.2)$$

$$I_{pc}\,(\mu A) = -0.453\upsilon - 52.686 \qquad (R^2 = 0.992) \qquad (6.3)$$

From these equations, it is clear that the redox reaction of NLM on the tri-metallic MOF electrode is an adsorption-controlled process (Karthik et al., 2017). The Laviron equation was used to calculate the electron transfer coefficient and the number of transferred electrons (Anuar et al., 2018). The linear relationship of redox peak current vs. natural logarithm of the scan rate is shown in Figure 6.9C. The regression equations are as follows:

$$E_{pa} = 0.010 \log \upsilon - 0.002 \ (R^2 = 0.952) \quad (6.4)$$

$$E_{pc} = -0.017 \log \upsilon - 0.037 \ (R^2 = 0.999) \quad (6.5)$$

The slopes of the anodic and cathodic curves are 2.303RT/(1-α)nF and -2.303RT/nF, respectively. The values for the electron transfer coefficient and the number of electrons transferred in the reduction reaction are estimated as 0.35 and 3.7 ≈ 4, respectively. The 4 electrons electrochemical redox reaction of NLM from previous works (Karthik et al., 2017; Kokulnathan et al., 2019a; Rajendran et al., 2019; Sundaresan et al., 2020b) is shown in Appendix C.

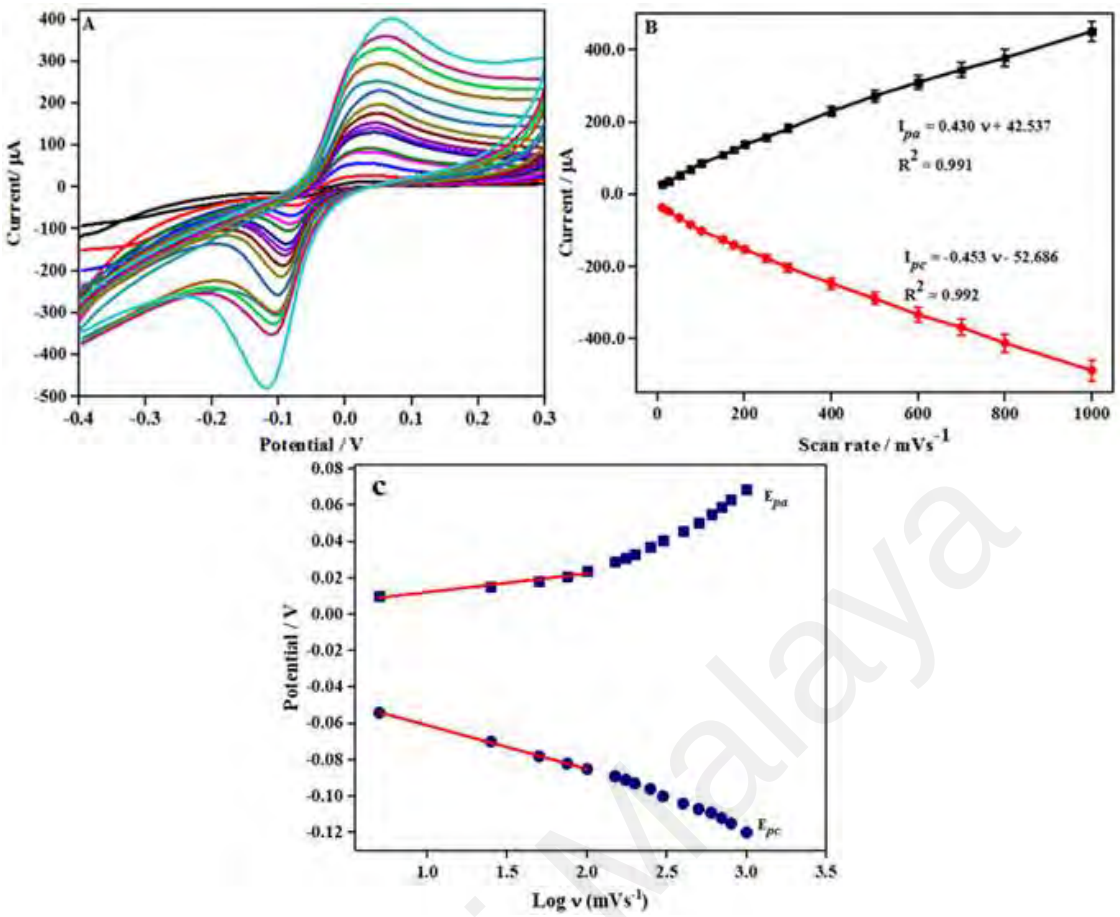

Figure 6.9: (A) CVs of 300 µM NLM on Co-Ni-Cu-MOF/NF at different scan rates in 0.1 M PBS (pH 7.0). (B) Relationship between peak current vs. different scan rates. (C) The redox peak potential vs. log of scan rate.

Previous studies on the electrochemical detection of NLM using functionalized multi-walled carbon nanotubes (MWCNT) (Karthik et al., 2017), ZnO modified on carbon paste (Temerk et al., 2015), Au nanoparticles (NPs)/graphene oxide (GO) (Karthik et al., 2017), vanadium tetrasulfide nanorods on nitrogen-doped carbon nanofibers (Rajendran et al., 2019), cerium vanadate (Kokulnathan et al., 2019a), samarium tungstate (Sundaresan et al., 2020b) and MWCNT/nitrogen-doped graphene (NDG)/chitosan (Akhter et al., 2020a) gave a single reduction peak without a reversible oxidation peak in the reverse scan. The electroreduction of NLM is attributed to the four-electron reduction of the nitro into hydroxylamine group between -0.5 V to -0.6 V (vs. Ag/AgCl) at pH 7 (Karthik et al., 2017; Karthik et al., 2017; Kokulnathan et al., 2019a; Rajendran et al., 2019; Sundaresan et al., 2020b; Temerk et al., 2015). The scan to further positive potential gave a redox couple at around 0.05 V – 0.15 V (Karthik et

al., 2017; Karthik et al., 2017; Kokulnathan et al., 2019a; Rajendran et al., 2019), which is attributed to the 2 electron redox process between the hydroxylamine and nitroso (Appendix 6.1, ESI). A totally different behavior was observed on the tri-metallic MOF where the NLM shows a pair of redox peaks between -0.1 V and 0.05 V (Fig. 6.7A) with a peak shift at higher scan rates.

It should be noted that the previous electro-active materials utilized for the detection of NLM such as MWCNT (Karthik et al., 2017), Au NPs, GO (Karthik et al., 2017), VS_4 (Rajendran et al., 2019), $CeVO_4$ (Kokulnathan et al., 2019), $Sm_2(WO_4)_3$ (Sundaresan et al., 2020) and NDG (Akhter et al., 2020) were not the constituents of the tri-metallic MOF electrode, thus a different electrochemical response was observed in the present investigation.

The redox peaks are attributed to the 4 electrons redox process between the nitro and hydroxylamine group in the NLM which was not observed in previous reports (Akhter et al., 2020; Karthik et al., 2017; Karthik et al., 2017; Kokulnathan et al., 2019; Rajendran et al., 2019; Sundaresan et al., 2020; Temerk et al., 2015). This effect could be due to the presence of the terephthalate linkers in the tri-metallic MOF, with an abundance of COO^- linkers and high porosity, which are efficient binding sites for the electronegative fluorine atoms in the NLM and gives a pair of redox peaks.

6.5.2 Influence of pH

The electrochemical behavior of 300 µM NLM was studied by CV at different solution pH (5.0-9.0) in 0.1 M PBS at 0.6 V s^{-1} for the optimization of the solution pH. Figure 6.10A reveals that the electrochemical behavior of NLM depends on the pH of the solution. The redox peak potentials of NLM were shifted to the negative region with the increase of pH from pH 5.0 to 9.0. The cathodic peak potential of NLM was shifted from -0.028 V to -0.258 V, which indicates that the NLM undergoes an electrochemical

reaction with the transport of protons. The highest redox current for NLM was obtained at pH 7.0 and the peak current declines beyond pH 7.0 (Figure 6.10C). Thus, pH 7.0 is the optimum pH and is used for all subsequent electrochemical measurements. Figure 6.10B shows the plot of redox peak potential (E_{pc}) and pH, while the linear regression relationship is as follows:

$$E_{pc} = -0.058\ pH - 0.271 \quad (R^2 = 0.944) \tag{6.6}$$

The slope value of the plot (eq. 6.6) is close to the theoretical value of a Nernstian behavior. This indicates that an equal number of electrons and protons participates in the electrochemical redox reaction of NLM (Temerk et al., 2015).

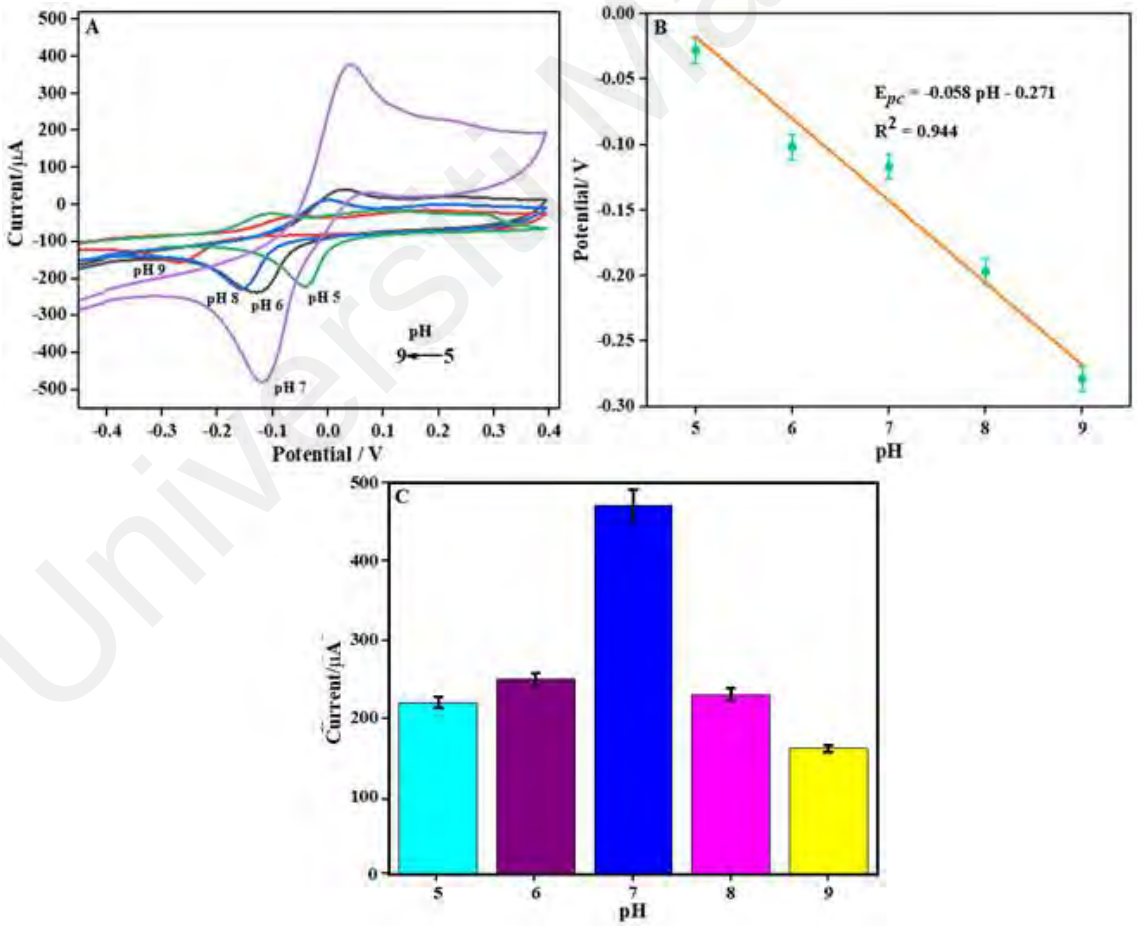

Figure 6.10: (A) CV response in different solution pH (5.0-9.0) in the presence of 300 µM NLM at Co-Ni-Cu-MOF/NF electrode at 0.6 V s^{-1}. (B) Relationship between pH vs reduction peak potential. (C) Bar diagram shows the relationship between different pH values (5.0-9.0) vs reduction peak current of NLM (n=5).

6.6 Performance evaluation of Co-Ni-Cu-MOF/NF sensor

6.6.1 Analytical application of the Co-Ni-Cu-MOF/NF sensor

Differential pulse voltammetry (DPV) is an effective electroanalytical technique that yields better signal to background response compared to the CV method. Distinguishable peaks with negligible background current can be obtained even at low analyte concentrations by this technique. The investigation focuses on the development of a sensitive MOF sensor electrode which could detect low and high concentrations of NLM. Thus, the DPV technique was employed to investigate the analytical application of the fabricated MOF sensor electrode with different concentrations of NLM (0.5-900 μM) in 0.1 M PBS (pH 7.0) at 0.6 V s^{-1}. Figure 6.11A shows that the peak current is directly proportional to the NLM concentration. The DPV showed two linear segments with different slope values at different concentrations ranges of NLM. The first linear segment is in the range of 0.5-70 μM (Figure 6.11B) while the second linear segment is in the range of 70-900 μM (Figure 6.11C). The linear regression equations for the calibrated ranges are as follows:

$$i_p\ (\mu A) = -3.464C - 130.088 \quad (0.5\text{-}70\ \mu M) \qquad (R^2 = 0.999) \tag{6.7}$$

$$i_p\ (\mu A) = -0.406C - 396.630 \quad (70\text{-}900\ \mu M) \qquad (R^2 = 0.997) \tag{6.8}$$

The obtained limit of detection (LOD) is 0.48 ± 0.021 nM from the second linear regression equation (70-900 μM) from S/N= 3, where 'S' is the standard deviation of the blank response and 'N' is the slope of the calibration curves. The limit of quantification (LOQ) was calculated as 1.6 nM from S/N=10 from the linear plots of (0.5-70 μM) and (70-900 μM). The sensitivity was calculated from the following formula:

$$\text{Sensitivity} = m/A \tag{6.9}$$

Where m = slope of the calibration curve,

A = surface area of the electrode (Rahman et al., 2020)

According to the formula, the calculated sensitivity value is found to be 10.712 µA μM^{-1} cm^{-2} which was calculated from second linear regression equation. The performance of the tri-metallic MOF sensor towards the quantitative determination of NLM was compared with the previous works with regards to the linear range, LOD and sensitivity and summarized in table 6.3.

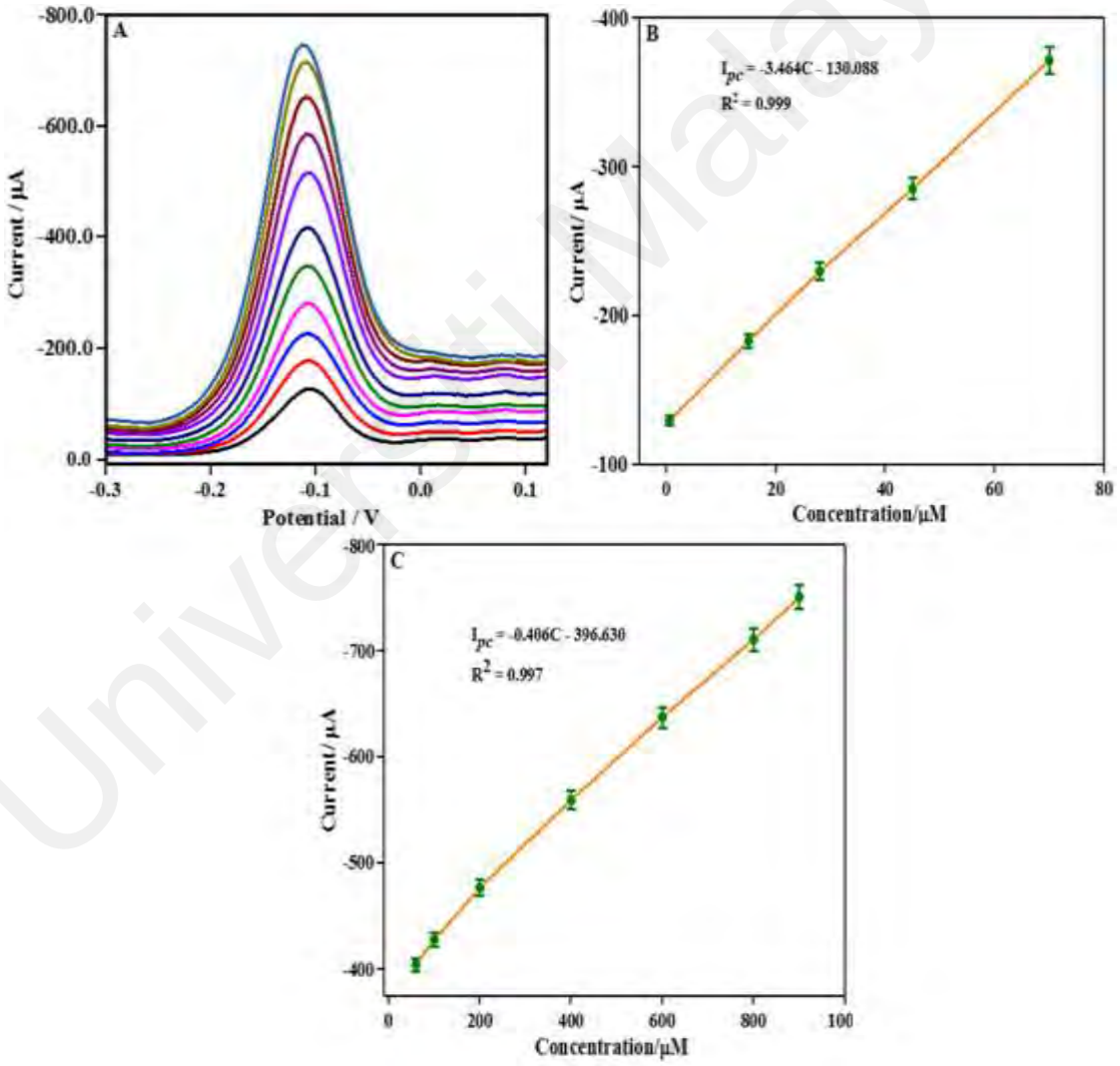

Figure 6.11: (A) Differential pulse voltammetry of 0.5 – 900 µM of NLM concentrations at Co-Ni-Cu-MOF/NF in 0.1 M PBS (pH 7.0) at 0.6 V s^{-1}. (B) Relationship between reduction peak current vs. concentration (0.5-70 µM) of NLM. (C) Relationship between reduction peak current vs. concentration (70-900 µM).

It is concluded that the Co-Ni-Cu-MOF/NF sensor shows very low LOD and wide linear range with very high sensitivity compared to previous reports (Karthik et al., 2017; Kokulnathan et al., 2019b; Sundaresan et al., 2020a). This could be attributed to the synergy of the catalytic effect of Co, Ni, Cu tri-metals, large electroactive surface area which remarkably enhanced electrochemical performance of the Co-Ni-Cu-MOF/NF for the determination of NLM even at low concentrations.

Table 6.3: The comparison of Co-Ni-CuMOF/NF sensor for determination of NLM with other published works.

Electrode Materials	Method	Linear range (µM)	LOD (nM)	Sensitivity $\mu A \mu M^{-1} cm^{-2}$	Reference
CeV/CNF/GCE	DPV	0.01-540 .00	2.0	1.36	(Kokulnathan et al., 2019b)
VS_4/NCNF/GCE	AMP	0.001-760	0.9	6.59	(Rajendran et al., 2019)
f-MWCNT/GCE	DPV	0.01 – 535	1.8	1.412	(Karthik et al., 2017)
SWNPs/SPCE	DPV	0.05-918.65	2.6	0.9185	(Sundaresan et al., 2020a)
β-CD-AuNP/GO/SPCE	DPV	0.01–193.00	0.4	1.167	(Karthik et al., 2017)
(MWCNTs*f*–NGr/CTS)-Cu/GCE	DPV	0.005-900.00	1.6	0.058	(Akhter et al., 2020b)
Co-Ni-Cu-MOF/NF	DPV	0.5-900.00	0.48±0.021	10.712	**Present work**

Carbon nano-fibers (CNF), Cerium vanadate (CeV), chitosan (CTS), cyclo-dextrin (CD), glassy carbon electrode (GCE), amperometry (AMP), graphene oxide (GO), gold nanoparticles (AuNP), multi-walled carbon nanotubes (MWCNT), nitrogen-doped carbon nanofibers (NCNF), nitrogen-doped graphene (NDG), screen printed carbon electrode (SPCE), samarium tungstate nanoparticles (SWNP).

6.6.2 Interference study of the coexisting substances

Selectivity is an essential parameter for a successful sensor must possess and can be determined by the interference study. One of the main objectives of the present work is to investigate the ability of the tri-metallic MOF sensor electrode to quantify the NLM concentrations in biological mediums such as human blood. This is due to the presence of interfering ions which coexist with NLM in human blood.

The interference study of NLM at the Co-Ni-Cu-MOF/NF electrode was investigated in the presence of interfering ions in 0.1 M PBS (pH 7.0) at 0.6 Vs^{-1} using DPV method. shown in Figure 6.12 A. It was observed that, 60-fold concentration of some common ions such as NO_3^- (a), SO_4^{2-} (b) and CO_3^{2-} (c) and 100-fold concentrations of glucose (d), sucrose (e), fructose (f), ascorbic acid (g), urea (h), dopamine (i) and citric acid (j) did not interfere with the redox peak of NLM.

Figure 6.12B shows the bar diagram of DPV current response of NLM and other interferents. The DPV current did not deviate after addition of each interferents in presence of NLM. Which demonstrates that, after adding each of the interfering compounds, the DPV current responses remained almost similar confirming that the Co-Ni-Cu-MOF/NF sensor is highly selective towards the determination of NLM in pharmaceutical products and biological samples.

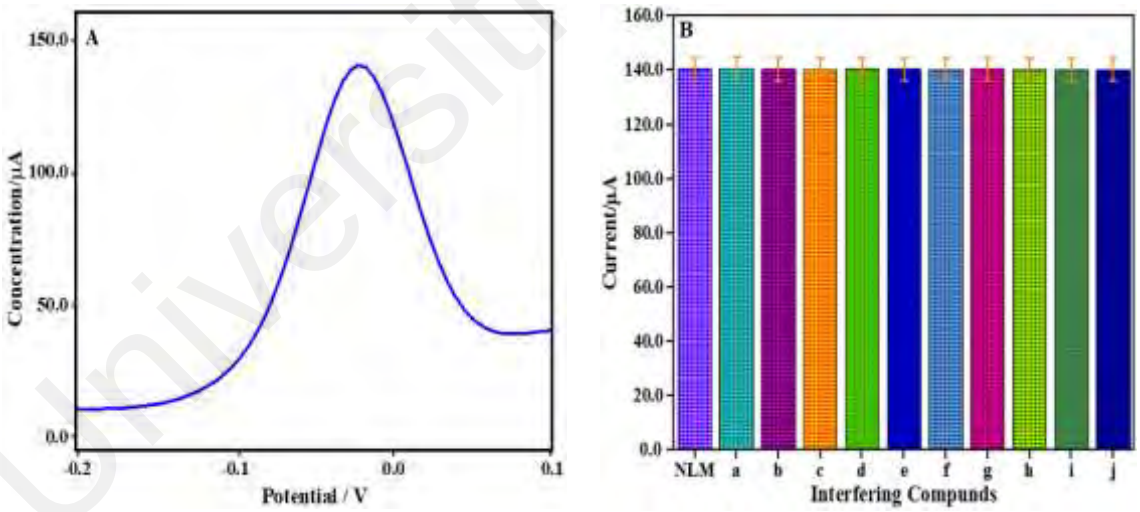

Figure 6.12: (A) The interference study of Co-Ni-Cu-MOF/NF electrode to NLM in presence of 60-fold concentration of NO_3^- (a), SO_4^{2-} (b) and CO_3^{2-} (c) and 100-fold concentrations of glucose (d), sucrose (e), fructose (f), ascorbic acid (g), urea (h), dopamine (i) and citric acid (j) in 0.1 M PBS (pH 7.0) at 0.6 Vs^{-1}. (B) Bar diagram shows the current response of NLM in presence of interfering compounds.

6.6.3 Reproducibility, repeatability and stability of the prepared sensor

A successful sensor must possess good reproducibility, repeatability and stability. The reproducibility of the Co-Ni-Cu-MOF/NF sensor was studied using the CV

technique for NLM in 0.1 M PBS (pH 7.0) at 0.6 V s^{-1} (Figure 6.13A). The CV was recorded three times under the same conditions using three individual freshly prepared electrodes. The CV curves obtained from all three electrodes show almost similar peak currents which indicate that the proposed sensor possesses acceptable reproducibility. Furthermore, the CV curves for NLM at Co-Ni-Cu-MOF/NF showed almost similar peak currents with the relative standard deviation (RSD) value of 1.2%, which confirms that the fabricated electrode was not poisoned by the redox product and good repeatability of the electrodes were obtained. The stability of the Co-Ni-Cu-MOF/NF sensor for NLM was evaluated by CV curve which showed almost unchanged peak currents and integral area after 5 cycles which assured that the proposed Co-Ni-Cu-MOF/NF possesses good stability (Figure 6.13B).

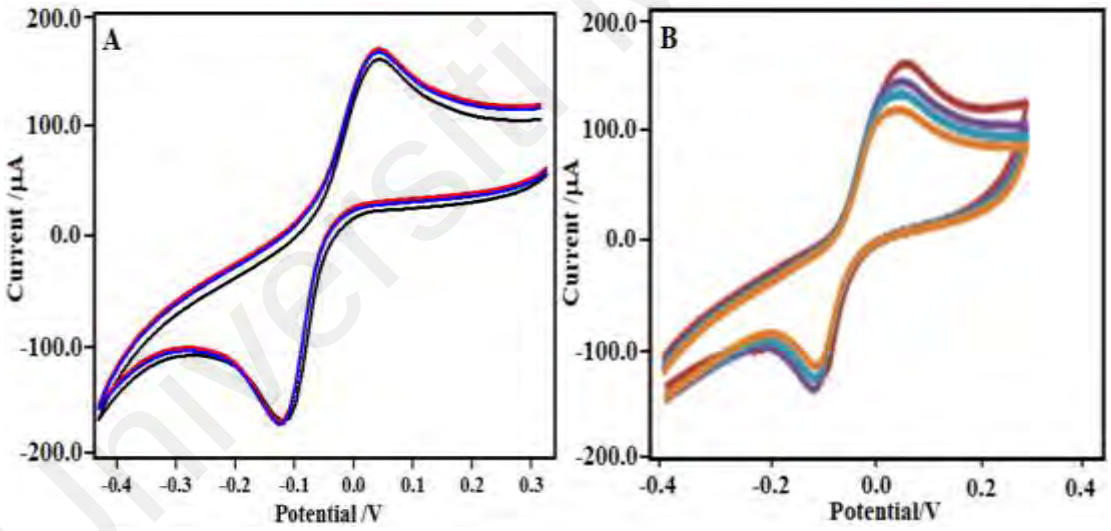

Figure 6.13: (A) CV of 3 reproducible cycles of NLM at Co-Ni-Cu-MOF/NF in 0.1 M PBS (pH 7.0) at 0.6 Vs^{-1}. (B) CV of 5 multiple cycles of NLM at Co-Ni-Cu-MOF/NF in 0.1 M PBS (pH 7.0) at 0.6 Vs^{-1}.

6.6.4 Study of real samples

The practical feasibility of the fabricated Co-Ni-Cu-MOF/NF sensor was investigated with NLM tablet and blood serum sample. Human blood specimens were collected from University Malaya Hospital while human urine specimens were collected

from healthy volunteer. For the blood collection, we prepared a request letter with supervisor's sign on it. After handover the letter to the head of the nurse with proper evidence, we were able to collect the human blood from them. The blood serum is isolated by the centrifugation before the experiments. DPV current responses were recorded for the blood sample in the presence of 0.1 M PBS (pH 7.0) at 0.6 V s^{-1}. The voltammetric response of the Co-Ni-Cu-MOF/NF sensor was performed at standard spiked solutions of NLM and the % recovery is calculated. The % recovery values were calculated by the comparison of the DPV peak current before and after the spike of the blood serum and tablet solution. The calculated RSD (%) values for the NLM tablet are between 98% and 102%, while the human blood serum recovery is between 99% and 101.5% which are summarized in Tables 4 and 5 respectively**.** From these results, it is confirmed that the Co-Ni-Cu-MOF/NF sensor exhibits acceptable recovery values.

Table 6.4: Determination of NLM in pharmaceutical tablets using DPV at Co-Ni-Cu-MOF/NF at pH 7.0 (n=3).

Sample	Labelled Amount	Added Amount (µM)	Found (mg/tablet)	Recovery (%)	RSD (%)	HPLC (mg)
Tablet	50 mg	1.0	0.98	98.0	0.45	1.01
		2.0	2.02	101.0	0.57	2.02
		5.0	5.01	102.0	1.15	5.02

Table 6.5: Determination of NLM in human blood serum specimen at Co-Ni-Cu-MOF/NF at pH 7.0 (n=3).

Sample	Added (µM)	Found (µM)	Recovery (%)	RSD (%)	HPLC (µM)
Human Serum	1.00	0.99	99.0	0.85	1.02
	2.00	2.03	101.5	2.28	2.01
	5.00	4.98	99.6	1.05	5.03

CHAPTER 7: NANOCELLULOSE AND 3D-POLYPYRROLE DECORATED WITH SILVER-GOLD BIMETALLIC NANOPARTICLES FOR THE DETECTION OF METHOTREXATE AND CIPROFLOXACIN.

This chapter focuses on the characterization of nanocellulose and 3D-polypyrrole decorated with silver-gold bimetallic nanoparticles for the simultaneous detection of methotrexate and ciprofloxacin in pharmaceuticals, biological fluid and water samples.

7.1 NC-3DPPY@Ag-Au nanocomposite for the detection of methotrexate and ciprofloxacin.

In this section, nanocellulose (NC) and 3D polypyrrole (PPY) decorated with silver (Ag) and gold (Au) bimetallic nanoparticles were synthesized and characterized by several analytical techniques such as FTIR spectroscopy, XRD analysis, FESEM and EDX analysis. Then, an electrochemical sensor was fabricated for the simultaneous detection of methotrexate (MTX) and ciprofloxacin (CIF) by modifying GCE with NC-3DPPY@Ag-Au nanocomposite. Voltammetric methods were used to evaluate the electrochemical behavior of MTX and CIF. In addition, the linear range, limit of detection, reproducibility, stability and selectivity of the electrochemical sensor were studied. The prepared sensor also showed satisfactory results in real sample analysis using commercial tablets, biological and water samples.

7.2 Aim of the research

The aim of this study is to fabricate a new modified electrode based on NC-3DPPY@Ag-Au nanocomposite. The combination of NC-3DPPY and Ag-Au bimetallic nanocomposite is expected to improve the properties of the nanocomposite compared to the single metal nanocomposite. Thus the excellent electrical conductivity

of NC-3DPPY, synergistic effect of Ag-Au with excellent catalytic effect is a hallmark for the high performance electrochemical sensing of MTX and CIF.

7.3 Structural characterizations of NC-3DPPY@Ag-Au nanocomposite

7.3.1 FTIR spectroscopy analysis

The synthesized NC-3DPPY@Ag-Au nanocomposites were investigated by different analytical techniques for morphological and structural analysis. The FTIR was performed to determine the presence of functional groups and chemical compositions of NC-3DPPY@Ag-Au. Figure 7.1A shows the FTIR spectra of NC-3DPPY (a), NC-3DPPY@Ag (b) NC-3DPPY@Au (c) and NC-3DPPY@Ag-Au. Curve (a) shows some characteristic peaks at 3728 cm^{-1}, 2919 cm^{-1} and 1181 cm^{-1} which correspond to the free OH, C-H and C-C stretch which confirms the presence of NC (Shalauddin et al., 2019). While a characteristic peak is observed at 1540 cm^{-1} which could be assigned to the C-C stretching vibrations present in the pyrrole ring while the peak at 891 cm^{-1} represents the doping state of 3DPPY (Shahnaz et al., 2020). In curve (b), two absorption peaks appear at 1624 cm^{-1} attributed to the C=O and transmittance peak at around 455 cm^{-1} which confirms the presence of Ag (Deng et al., 2021). The characteristic peaks for NC-3DPPY are also present in curve C. In curve (c), where the characteristic peaks appear at 1678 cm^{-1} and 812 cm^{-1} corresponding to C=C and C-H stretch which confirms the presence of Au (Weng et al., 2020). The characteristic peaks for NC-3DPPY are present here. Curve (d) shows the characteristic peaks of Ag, Au, NC and 3DPPY but with the slight shift in the peak wavenumbers. This result confirms that the NC-3DPPY layer was successfully attached with the Ag-Au nanoparticles.

7.3.2 XRD analysis

To observe the crystalline characteristics, the powder XRD pattern of NC-3DPPY@Ag-Au is shown in Figure 7.1B. NC shows some distinct peaks at 2Θ = 15.44°, 22.62° and 34.66° which could be attributed to the presence of NC. While another peak at 2Θ = 26.05° is attributed to the presence of 3DPPY (Tasrin et al., 2021). The 2θ values of the Ag–Au nanoparticles are very close to each other since Ag and Au have very similar lattice constants. The distinct peaks at 2θ = 38.1°, 44.2°, 64.5° and 77.4° and the crystal planes correspond to (1 1 1), (2 0 0) ,(2 2 0) and (3 1 1) which could be attributed to the face centered cubic (fcc) structure of Ag and Au nanoparticles (Garcia et al., 2020).

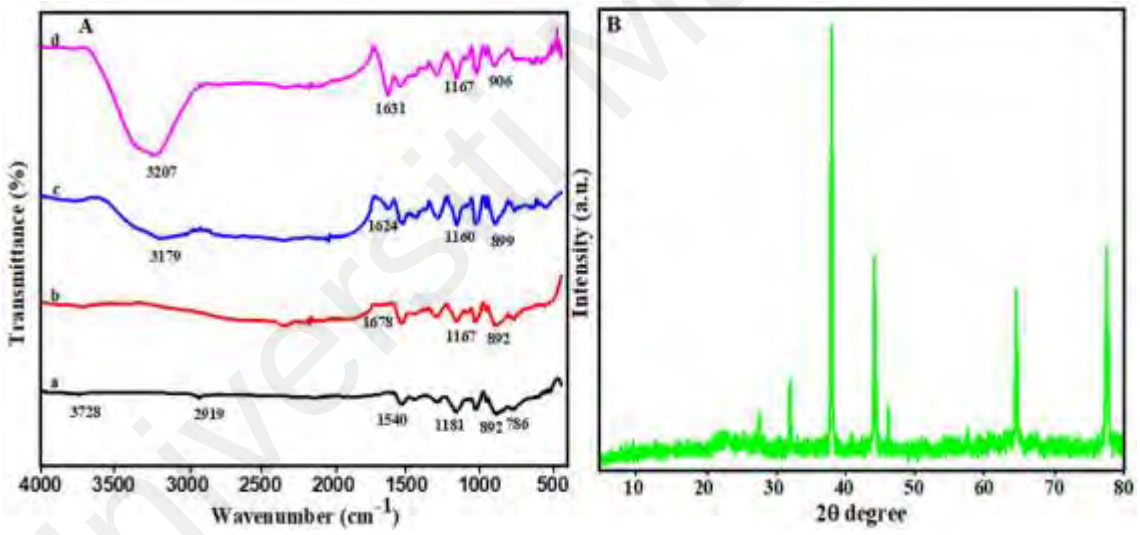

Figure 7.1: FTIR spectra of (A) NC-3DPPY (a), NC-3DPPY@Ag (b) NC-3DPPY@Au (c) and NC-3DPPY@Ag-Au (d). and (B) XRD pattern of NC-3DPPY@Ag-Au nanocomposite.

7.3.3 Surface morphology analysis of modified electrode

Field emission scanning electron microscopy (FESEM) was used to investigate the morphology of the modified electrode. Figure 7.2A shows the dispersion of NC with a rough surface. Figure 7.2B shows a uniform mixture of NC-3DPPY fibers with a porous foam-like network composed of NC-3DPPY. The fibers of NC are entangled and

embedded on the layer of 3DPPY and formed a 3D network (Wang et al., 2014). Figure 7.2 C shows the homogeneous deposition of Ag-Au with spherical shapes. Figure 7.2D shows the homogeneous deposition of Ag-Au nanoparticles on the NC-3DPPY layer. The presence of carbon, oxygen, nitrogen, gold and silver in the NC-3DPPY@Ag-Au nanocomposite were detected by EDX analysis as shown in Figure 7.3. The inset table shows the percentage of major elements along with Ag and Au percentage. EDX elemental mapping was used to investigate the distribution of Ag and Au nanoparticles on the NC-3DPPY surface. Figure 7.4 illustrates the elemental mapping images of carbon, oxygen, nitrogen, silver and gold. The EDX elemental mapping shows the presence of bimetallic Ag–Au nanoparticles on the NC-3DPPY surface.

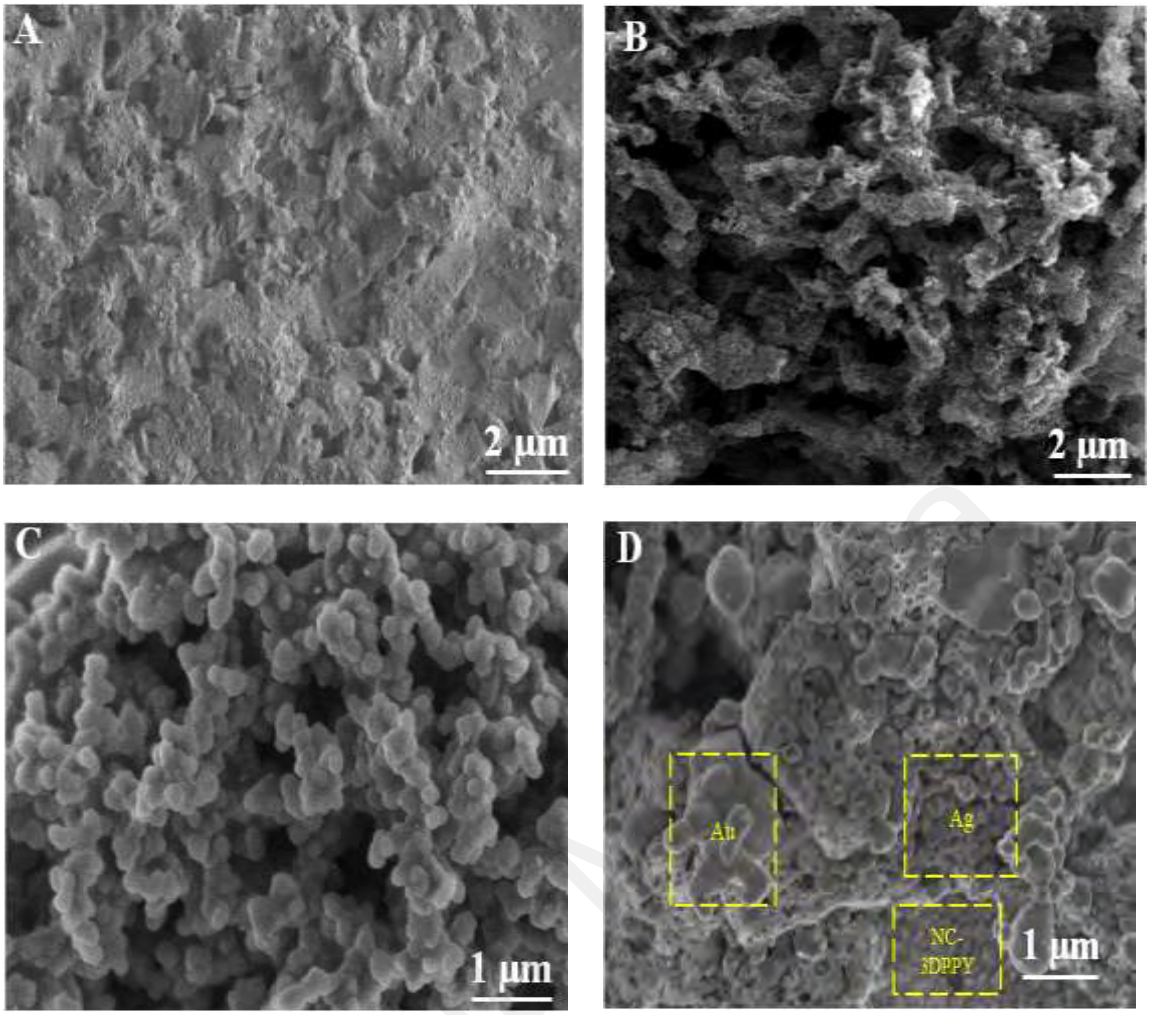

Figure 7.2: FESEM images of NC (A), NC-3DPPY (B), Ag-Au (C) and NC-3DPPY@Ag-Au (D).

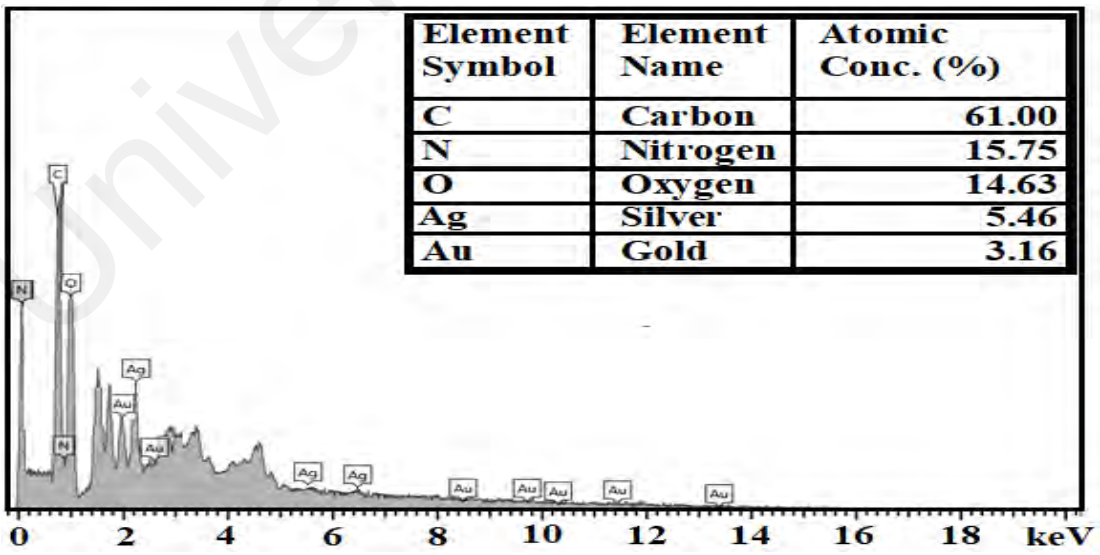

Element Symbol	Element Name	Atomic Conc. (%)
C	Carbon	61.00
N	Nitrogen	15.75
O	Oxygen	14.63
Ag	Silver	5.46
Au	Gold	3.16

Figure 7.3: EDX analysis for NC-3DPPY@Ag-Au nanocomposite.

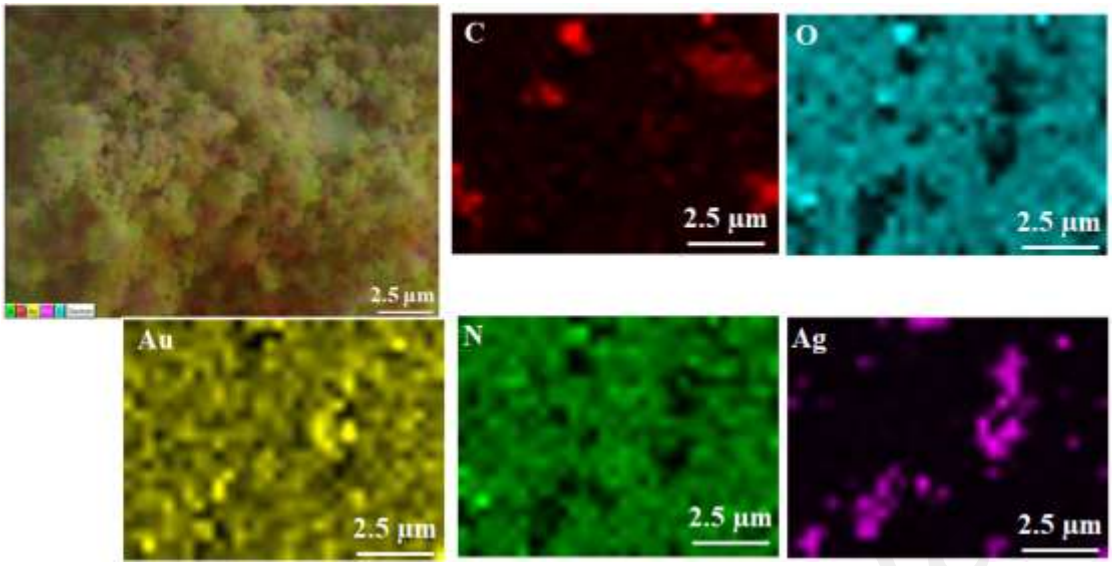

Figure 7.4: Elemental Mapping analysis for NC-3DPPY@Ag-Au nanocomposite.

7.4 Electrochemical characterizations

7.4.1 EIS and active surface area calculation for modified sensor

The EIS analysis was conducted to investigate the interfacial electron transfer properties on the electrode-electrolyte interface. The optimized operational parameters for the study were: frequency ranges from 100 kHz to 100 mHz and V_{rms} potential of 10 mV. Figure 7.5 shows the Nyquist plots of different electrodes, the bare GCE (a), NC/GCE (b), NC-3DPPY/GCE (c), NC-3DPPY@Ag/GCE (d), NC-3DPPY@Au/GCE (e) and NC-3DPPY@Ag-Au/GCE (f) and in presence of 0.1M KCl and 5mM $[Fe(CN)_6]^{3-/4-}$. The GCE shows the largest R_{ct} value of 460 Ω which could be attributed to the poor interfacial electrons transfer. The R_{ct} values obtained for NC and NC-3DPPY are 420 and 310 Ω, respectively, which is attributed to the lower electrical conductivity of NC and comparatively good electrical conductivity of NC-3DPPY. The R_{ct} values obtained for NC-3DPPY@Ag and NC-3DPPY@Au are 115 and 105 Ω which could be attributed to the excellent electrical conductivity of Ag and Au. The lowest R_{ct} value is 42 Ω when the GCE is modified with NC-3DPPY@Ag-Au, which could be attributed to the synergy of the enhanced electrochemical conductivity and excellent catalytic effect

of bimetallic Ag and Au nanoparticles with the combination of NC-3DPPY which facilitates the electronic mobility.

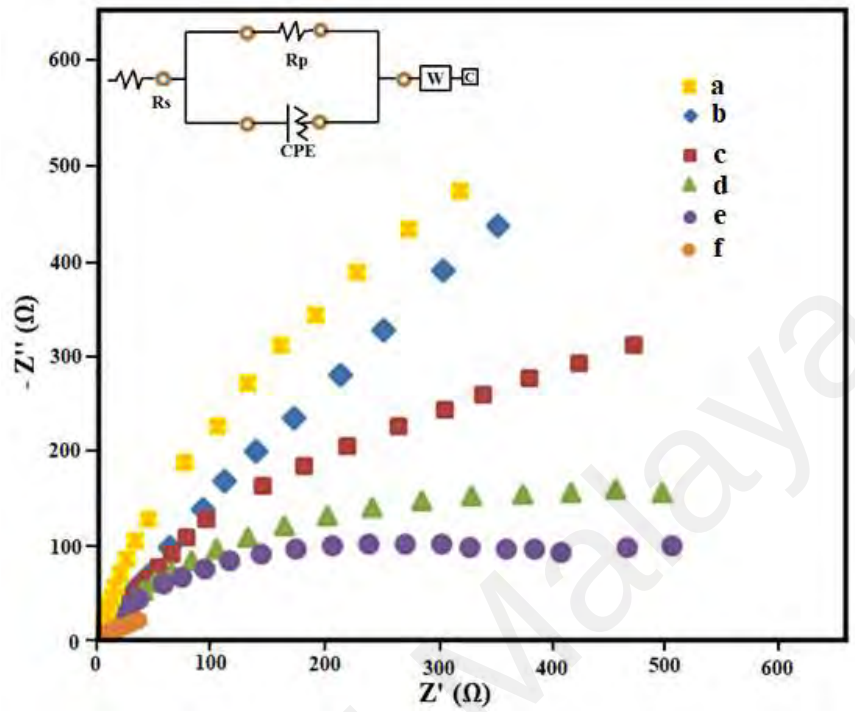

Figure 7.5: The Nyquist plots of bare GCE (a), NC/GCE (b), NC-3DPPY/GCE (c), NC-3DPPY@Ag/GCE (d), NC-3DPPY@Au/GCE (e) and NC-3DPPY@Ag-Au/GCE (f) in 0.1 M KCl solution with 5.0 mM [Fe (CN) $_6$]$^{3-/4-}$. Inset is the equivalent circuit of the fitting.

Cyclic voltammetry (CV) was performed on different modified electrodes in the presence of 0.1M KCl and 5mM $[Fe(CN)_6]^{3-/4-}$ at 50 mVs^{-1} as shown in Figure 7.6B. It can be observed that bare GCE (a), NC/GCE (b), NC-3DPPY/GCE (c), NC-3DPPY@Ag/GCE (d), NC-3DPPY@Au/GCE (e), and NC-3DPPY@Ag-Au/GCE (f) has a set of obvious redox peaks due to the transfer of electrons in the presence of $[Fe(CN)_6]^{3-}$ and $[Fe(CN)_6]^{4-}$. Compared to the bare GCE and NC/GCE, the intensity of the redox peaks of NC-3DPPY/GCE, NC-3DPPY@Ag/GCE, NC-3DPPY@Au/GCE has a certain increase. The highest redox peak current value is obtained from NC-3DPPY@Ag-Au/GCE and calculated from the Randles-Sevcĭk equation below:

$$I_p = 2.69 \times 10^5 n^{3/2} A D^{1/2} v^{1/2} C \quad (7.1)$$

Where I_p is the peak current value, n is the number of electrons transferred (n= 1), A is

the effective area of the working electrode, D is the diffusion coefficient (7.6×10^{-6} cm^2 s^{-1}), v is the scan rate, and C (mol mL^{-1}) is the concentration of $[Fe(CN)_6]^{4-/3-}$. Employing Eq. 7.1, the estimated effective surface area of the different working electrodes, i.e. bare GCE, NC/GCE, NC-3DPPY/GCE, NC-3DPPY@Ag/GCE, NC-3DPPY@Au/GCE, and NC-3DPPY@Ag-Au/GCE is 0.052 cm^2 (a), 0.067 cm^2 (b), 0.082 cm^2 (c), 0.105 cm^2 (d), 0.110 cm^2 (e) and 0.122 cm^2 (f).

7.4.2 CV of MTX and CIF at NC-3DPPYT@Ag-Au sensor

To investigate the electrochemical behavior of different modified electrodes, cyclic voltammetric (CV) responses were recorded. Figure 7.6A exhibits the CV curves of bare GCE (a), NC/GCE (b), NC-3DPPY/GCE (c), NC-3DPPY@Ag (d), NC-3DPPY@Au (e), NC-3DPPY@Ag-Au (f) for 150 μM MTX and 35 μM CIF in 0.1 M PBS at 0.3 V s^{-1} scan rate. The bare GCE and NC/GCE exhibit almost similar oxidation peak currents for MTX and CIF. The low conductivity of NC, could not promote the electron transfer process. In addition, NC-3DPPY/GCE exhibited better electrochemical response than the bare GCE and NC/GCE which could be assigned to the good electro-conductivity of NC-3DPPY. When GCE is fabricated with NC-3DPPY@Ag and NC-3DPPY@Au, an increased well-defined oxidation peaks are observed which could be ascribed to the excellent electrical conductivity and catalytic activity of Ag and Au. The presence of Ag and Au nanoparticles on the NC-3DPPY surface accelerates the electron transport during the electrochemical detection of MTX and CIF. The NC-3DPPY@Ag-Au shows the highest oxidation peak current for MTX and CIF compared to the NC-3DPPY@Ag and NC-3DPPY@Au, confirming the outstanding electro-catalytic activity of NC-3DPPY@Ag-Au towards the simultaneous detection of MTX and CIF. The remarkable increment of the oxidation peak current is due to the synergy between the Ag-Au bimetallic nanoparticles and NC-3DPPY. The unique combination of Ag-Au

bimetal possesses excellent electrocatalytic behaviour and superior electronic conductivity compared to the single metal Ag and Au nanoparticles. Furthermore, the inclusion of Ag and Au bimetallic nanoparticles on the high surface area of NC-3DPPY expose more electroactive sites for the efficient electron transfer between the modified electrode and analyte (Aazam & Zaheer, 2021). Therefore, the NC-3DPPY@Ag-Au nanocomposite modified GCE is recommended for the electrochemical detection of MTX and CIF due to the superior conductivity, excellent electrocatalytic activity and high surface area.

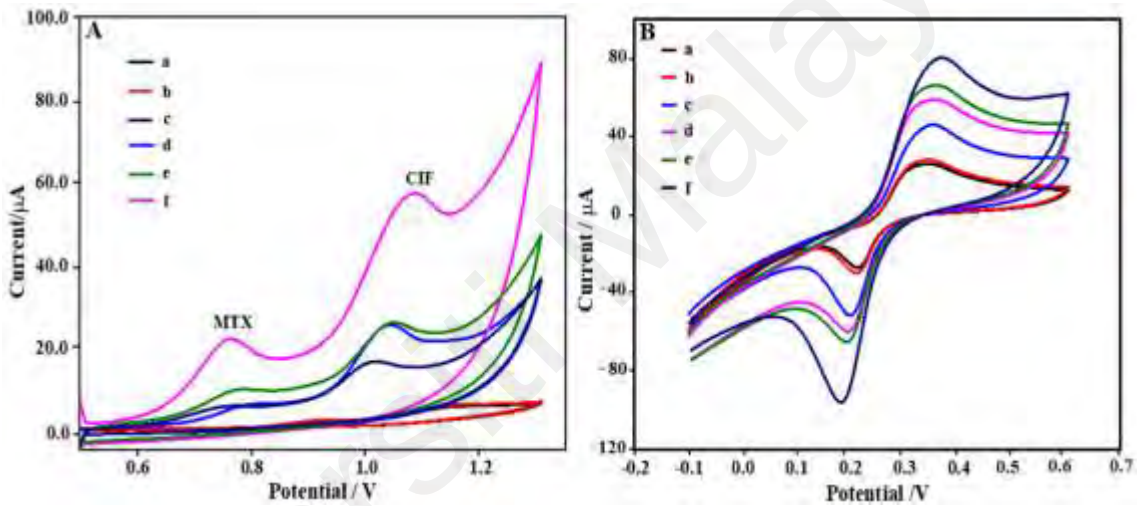

Figure 7.6: (A) CVs of 150 µM MTX and 35 µM CIF in 0.1 M PBS (pH 7.0) at 0.1 V s^{-1} on of bare GCE (a), NC/GCE (b), NC-3DPPY/GCE (c), NC-3DPPY@Ag (d), NC-3DPPY@Au (e), NC-3DPPY@Ag-Au (f). (B) CVs response of bare GCE, NC/GCE, NC-3DPPY/GCE, NC-3DPPY@Ag/GCE, NC-3DPPY@Au/GCE, and NC-3DPPY@Ag-Au/GCE in 0.1 M KCl solution with 5.0 mM $[Fe(CN)_6]^{3-/4-}$ at 0.1 V s^{-1}.

7.5 Optimization of the fabricated sensor

7.5.1 Influence of scan rate

To understand the reaction mechanism of MTX and CIF, the influence of scan rate was investigated on the peak current and peak potential. Figure 7.7 show the CVs of 150 µM MTX and 35 µM CIF at the NC-3DPPY@Ag-Au modified electrode in the presence of 0.1 M PBS pH 7.0 at different scan rates from 10-300 mVs^{-1}. It is observed from Figure 7.7A that the oxidation peak currents of MTX and CIF increase linearly with the increase of scan rates. This entailed that the electrochemical reactions of MTX

and CIF on the NC-3DPPY@Ag-Au follows an adsorption controlled mechanism (Gayen & Chaplin, 2016; Jandaghi et al., 2020). Both MTX and CIF contain benzene ring in their chemical structure. Therefore, during the interaction between MTX and NC-3DPPY@Ag-Au, the van der Waals force is involved while the electrostatic interactions are involved during the interaction of CIF and NC-3DPPY@Ag-Au and both are absorbed onto the surface of NC-3DPPY@Ag-Au. In addition, a variation of the oxidation peak current of MTX and CIF appear with the variation of scan rates, which reveals that the electrochemical redox reaction of MTX and oxidation reaction of CIF is surface controlled process on the NC-3DPPY@Ag-Au nanocomposite (Karami et al., 2019; Matsunaga et al., 2020). The oxidation currents of MTX and CIF are shifted toward the positive direction which is due to the kinetic effect of the NC-3DPPY@Ag-Au on the oxidation of MTX and CIF (Figure 7.7 B and C). The linear regression equation for MTX and CIF are as following;

$$I_{pa}\,(\mu A) = 0.556\,\upsilon + 1.732\ (R^2 = 0.999)\ \ (MTX) \tag{7.2}$$

$$I_{pc}\,(\mu A) = -0.154\,\upsilon + 5.960\ (R^2 = 0.998)\ (CIF) \tag{7.3}$$

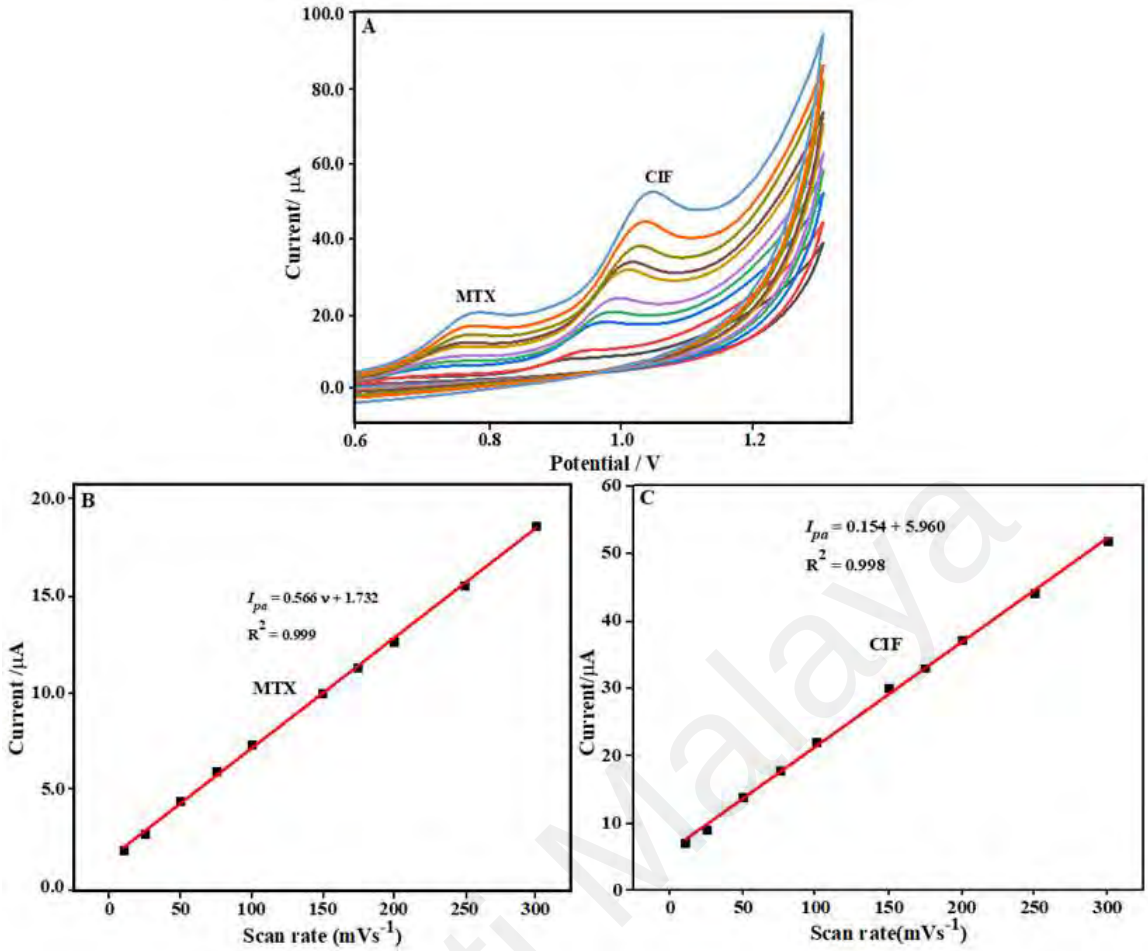

Figure 7.7: CVs of 150 µM MTX and 35 µM CIF on NC-3DPPY@Ag-Au/GCE at 10 mV s^{-1} to 300 mV s^{-1} in 0.1 M PBS (pH 7.0) (A). The calibration plot of oxidation peak current vs. scan rates of MTX (B) and CIF (C).

7.5.2 Analysis of pH variation

The electrochemical behavior of MTX and CIF at NC-3DPPY@Ag-Au are greatly influenced by the variations of pH. The CV responses of 150 µM MTX and 35 µM CIF are recorded at 0.3 V s^{-1} in the presence of 0.1 M PBS (pH 7.0) in different pH ranges from pH 5.0 to 9.0 as shown in Figure 7.8A. It is observed that the highest current response is obtained from pH 7.0. When the pH increases from 5.0 to 9.0, the oxidation peak potential of MTX and CIF are gradually shifted to the negative regions. The oxidation peak potential of MTX is shifted from 0.84 V to 0.73 V, while the oxidation peak potential of CIF is shifted from 1.10 V to 0.90 V which indicates that the oxidation of MTX and CIF requires the transfer of protons (Kummari et al., 2019; Matsunaga et

al., 2020). Figures 7.8B and 7.8C represent the relationship between the oxidation peak potential (E_{pa}) and different pH for MTX and CIF, respectively. A linear relationship between E_{pa} and different pH values is observed with slope values of -0.065 V pH^{-1} and -0.052 V pH^{-1} for MTX and CIF respectively. The linear regression equations for the oxidation peak potential of MTX and CIF are as follows:

$$E_p \text{ (MTX)} = -0.052 \text{ pH} + 0.963 \ (R^2 = 0.967) \quad (7.4)$$

$$E_p \text{ (CIF)} = -0.065 \text{ pH} + 1.422 \ (R^2 = 0.981) \quad (7.5)$$

From Eqs. 7.4 and 7.5, it is observed that both the slope value of MTX and CIF are close to the Nernst equation value (0.059 V pH^{-1}), indicating that identical numbers of electrons and protons are involved in the reactions of MTX and CIF (n= 2). Figures 7.8 D and E for MTX and CIF show an increment in the peak current when the pH changes from 5.0 to 7.0 but decline beyond the pH 7.0. Due to the low current detection, the oxidation reactions of MTX and CIF are less favorable in low and high pH values (Chauhan et al., 2020; Jandaghi et al., 2020). The highest current response was observed at pH 7.0, thus pH 7.0 was selected as optimum pH for whole experiments. It can be concluded that the electrochemical reactions of MTX and CIF at the NC-3DPPY@Ag-Au/GCE solely depend on the pH and NC-3DPPY@Ag-Au/GCE which show great improvements in the oxidation peak current of MTX and CIF.

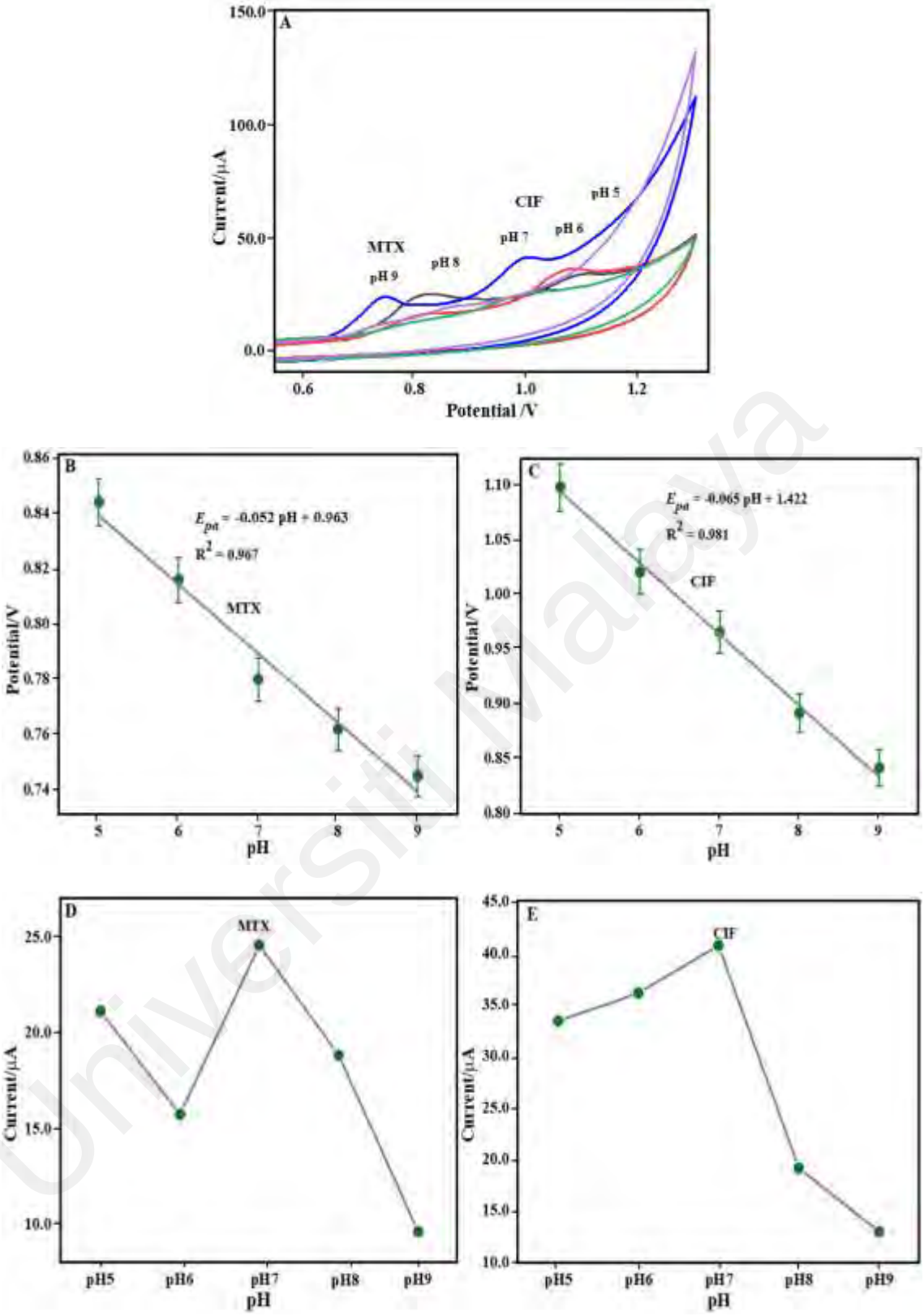

Figure 7.8: (A) The CVs of 150 µM MTX and 35 µM CIF at the NC-3DPPY@Ag-Au/GCE at different pH: 5.0, 6.0, 7.0, 8.0 and 9.0, at 0.1 V s^{-1}. (B) The plot of oxidation peak potential vs. pH of MTX. (C) The plot of oxidation peak potential vs. pH of CIF, (D) The plot of the oxidation peak current vs. pH of MTX, (E) The plot of the oxidation peak current vs. pH of CIF.

7.6 Performance evaluation of NC-3DPPY@Ag-Au/GCE sensor

7.6.1 Analytical application of NC-3DPPY@Ag-Au/GCE sensor

The square-wave voltammetric (SWV) method was employed for the quantitative analysis of NC-3DPPY@Ag-Au/GCE sensor for the simultaneous detection of MTX and CIF. Figure 7.9A reveals the effect of different concentration ranges from 10 to 350 μM for MTX and from 0.5 to 50 μM for CIF at the NC-3DPPY@Ag-Au/GCE in the presence of 0.1M PBS (pH 7.0) at 0.1 V s^{-1}. A gradual increase was observed for the oxidation peaks of MTX and CIF with the increase of MTX and CIF concentrations. Figure 7.9B shows the calibration curve between the oxidation peak current and different concentrations of MTX, where the linear range starts from 10- 350 μM. Similarly, Figure 7.9C shows the calibration curve between the oxidation peak currents and different concentrations of CIF, with the linear range from 0.5 - 50 μM. The linear regressions for the calibrated ranges are the following:

$$I_p(\mu A) = 0.191C + 1.395 \ (0.1 – 350\ \mu M)\ (MTX)\ (R^2 = 0.992) \quad (7.6)$$

$$I_p\ (\mu A) = 1.537 + 11.383\ (0.05 - 50\ \mu M)\ (CIF)\ (R^2 = 0.993) \quad (7.7)$$

The LOD value of MTX and CIF are calculated from the linear regression equation (Eqs. 7.6 and 7.7), respectively, from $3S_b/m$, where, S_b = standard deviation of the blank sample, m = slope of the calibration curve. The estimated limit of detection (LOD) value for MTX and CIF is 0.0062 μM and 0.0007 μM, respectively. A comparative study is presented between the present work and previous works in terms of LOD and linear ranges. It is observed that the NC-3DPPY@Ag-Au/GCE shows impressive results with lower LOD and broad linear ranges compared to the other modified electrodes. These results demonstrate the excellent electrochemical conductivity and catalytic activity of bimetallic Ag-Au nanoparticles with porous configuration and the

mechanically robust structure of the NC-3DPPY network remarkably accelerates the electronic mobility and enhances the electrochemical performance of the NC-3DPPY@Ag-Au/GCE for the simultaneous determination of MTX and CIF at very low concentrations.

Table 7.1 The comparative study between various electrodes for the detection of MTX and CIF.

Analytes	Electrode	Method	Linear ranges(µM)	Detection limit(µM)	References
MTX	STAB/ABPE	CV	0.005-75.0	0.307	(Deng et al., 2020)
	NiO/GCE	CV	0.05-300	0.146	(Khand et al., 2021)
	PANI-Co_3O_4 NP/GCE	LSV	5.0-75	0.198	(Qureshi et al., 2021)
CIF	Ag nps- β-CD/GCE	DPV	0.1-500	0.028	(Gill et al., 2021)
	g-C_3N_4/Ti_3C_2/GCE	IV	0.4-1000	0.13	(Yuan et al., 2021)
	AuNPs/Ac/GCE	DPV	0.25-250	0.20	(Gissawong et al., 2021)
MTX & CIF	NC-3DPPY@Ag-Au	SWV	10-350 (MTX) 0.5-50 (CIF)	0.0062 (MTX) 0.0007 (CIF)	**This Work**

STAB: stearyl trimethyl ammoniumbromide, ABPE: Acetylene black paste electrode, NiO: Nickel oxide nanostructure, PANI: Polyaniline, Co_3O_4 NP: Cobalt oxide nanoparticle, g-C_3N_4: Graphitic carbon nitride, Ti_3C_2 : Titanium carbide, AuNPs: Gold nanoparticle, AC: Activated carbon

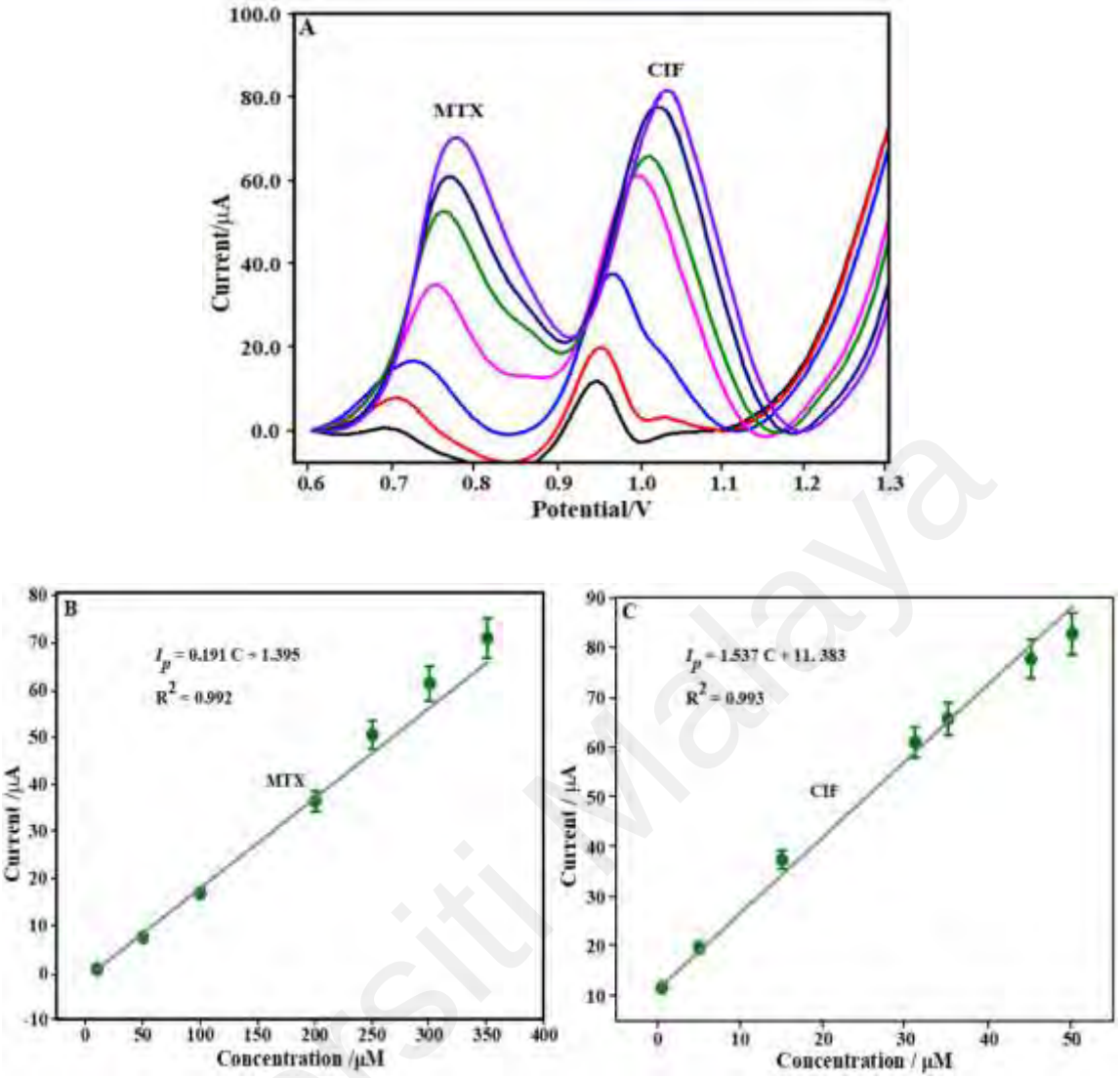

Figure 7.9: SWVs response at the NC-3DPPY@Ag-Au/GCE for different concentration of MTX and CIF between (10 – 350 µM) and (0.5 – 50 µM) in 0.2 M phosphate buffer solution (pH 7.0) (A). The calibration curve of peak current and MTX concentration (B). The calibration curve of peak current and CIF concentration (C).

7.6.2 Stability and reproducibility of NC-3DPPY@Ag-Au/GCE

The stability and reproducibility of NC-3DPPY@Ag-Au/GCE electrode were carried out by SWV method in 0.1M PBS containing MTX and CIF. The fabricated electrode was preserved at refrigerator for 21 days and the current responses was recorded after every week. The current responses after the 1st, 2nd and 3rd weeks from its initial response were 97.17%, 96.92 and 90.76% for MTX and 97.46%, 96.87% and

90.71% for CIF (Figure 7.10), confirming the greater stability of the NC-3DPPY@Ag-Au/GCE sensor. Besides, for the reproducibility test, a series of NC-3DPPY@Ag-Au/GCE prepared electrodes are taken and the estimated relative standard deviation (RSD) values for MTX and CIF are 2.75% and 3.15% respectively. From these results, it can be demonstrated that, the NC-3DPPY@Ag-Au/GCE sensor possess good stability and reproducibility.

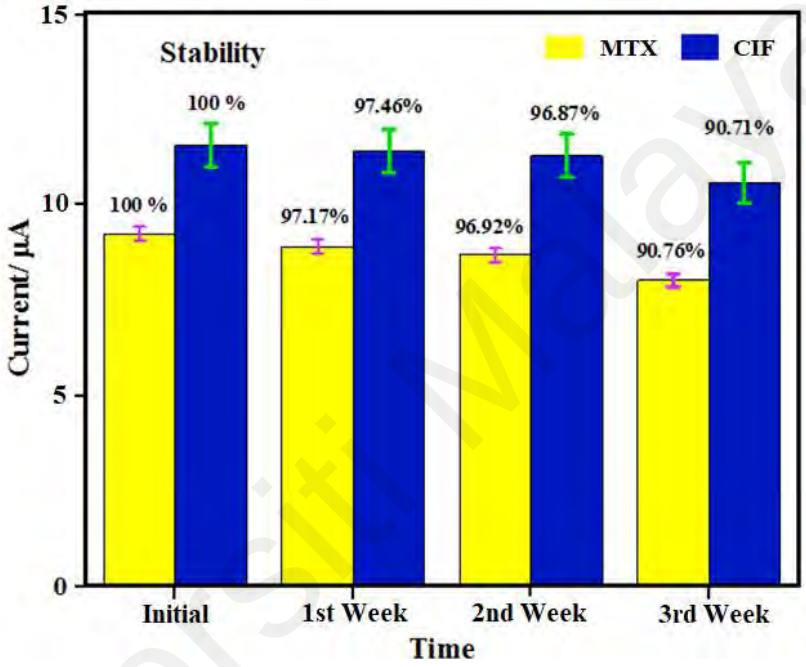

Figure 7.10: The bar diagram for stability study of MTX and CIF at NC-3DPPY@Ag-Au modified electrodes, on three consecutive weeks (a) first day; (b) after 1st week; (c) after 2nd weeks (d) after 3rd weeks.

7.6.3 Selectivity test of NC-3DPPY@Ag-Au/GCE sensor

The presence of interfering compounds in the biological fluid can affect the sensor response, thus it is necessary to evaluate the sensor selectivity toward the detection of MTX and CIF in the presence of the non-targeted entities. The selectivity analysis was carried out by adding the interfering molecules in the PBS solution containing MTX and CIF. Figure 7.11 showed 500 fold of Fe^{2+},Na^{+}, K^{+}, Cl^{-} and SO_4^{2-}, 30 fold of glycine, glucose, ascorbic acid (AA) and dopamine (DA), and 10 fold of cephalexin (CX), paracetamol (PR) and tetracycline (TC) could not influence the detection of MTX and

CIF except DA. However, the distinct peak separation of DA, MTX and CIF indicates that the presence of DA did not interrupt the simultaneous detection of MTX and CIF. From this result, it can be disclosed that the NC-3DPPY@Ag-Au/GCE sensor is highly selective for the detection of MTX and CIF.

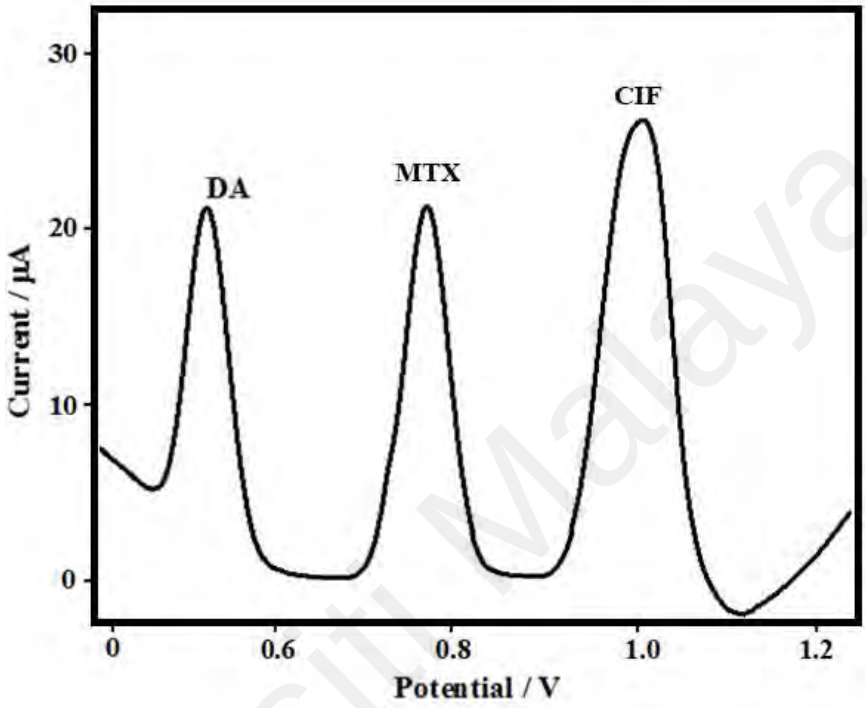

Figure 7.11: SWVs signal at NC-3DPPY@Ag-Au sensor for interference study of the MTX and CIF oxidation in the presence of interfering ions.

7.6.4 Real samples analysis

Human serum specimens were collected from University Malaya Hospital while human urine specimens were collected from healthy volunteer. For the blood collection, we prepared a request letter with supervisor's sign on it. After handover the letter to the head of the nurse with proper evidence, we were able to collect the human blood from them. Then, 10 mL of the human blood serum was centrifuged at 2000 rpm for 15 minutes. The supernatant was filtered by a filter paper (0.45 mm) and the filtered solution was diluted with 0.1 M PBS (pH 7.0). The tablet dosage forms of MTX and CIF were collected from a local pharmacy and crushed into fine powders and dissolved in DIW. Then the solutions of MTX and CIF were filtered and diluted using 0.1 M PBS.

The practical application of the fabricated NC-3DPPY@Ag-Au sensor was investigated using the human blood sample and pharmaceutical tablet dosage forms. The SWV method was utilized to determine the concentrations of MTX and CIF using the standard addition method. The recovery and relative standard deviation (RSD %) values were calculated from this experiment shown in Table 7.2 (tablet) and Table 7.3 (blood). Good recovery results and low RSD values confirm the suitability, efficiency and practical application of the NC-3DPPY@Ag-Au sensor towards the detection of MTX and CIF.

Table 7.2: Determination of MTX and CIF in tablets at NC-3DPPY@Ag-Au/GCE using SWV (n=3).

Tablet	Sample	Labelled (µM)	Found (µM)	Recovery (%)	RSD (%)	HPLC (mg)
MTX	1	10	10.04	100.40	1.25	10.05
	2	15	15.05	100.33	0.86	15.08
	3	20	19.96	99.80	1.45	20.07
CIF	1	10	10.06	100.60	1.05	10.04
	2	15	14.96	99.73	0.95	15.09
	3	20	20.05	100.25	1.36	20.06

Table 7.3: Determination of MTX and CIF in blood serum at NC-3DPPY@Ag-Au/GCE using SWV (n=3).

Blood Serum	Sample	Labelled (µM)	Found (µM)	Recovery (%)	RSD (%)	HPLC (µM)
MTX	1	10	10.06	100.60	1.75	10.08
	2	20	19.94	99.70	0.86	20.06
	3	30	30.08	100.26	1.42	30.05
CIF	1	10	10.08	100.80	0.95	10.04
	2	15	15.10	100.66	1.55	15.03
	3	20	20.05	100.25	1.37	20.06

7.6.5 Determination of MTX and CIF in water sample

The performance of the fabricated NC-3DPPY@Ag-Au/GCE sensor was evaluated in real water samples using the standard addition method. The water sample was collected from the tap water. The tap water was preserved and filtered through 0.30 µm

membrane filters to remove the impurities. Then different concentrations of MTX and CIF (0.3 to 08 μM) were added to the filtered water. The electrochemical response of the NC-3DPPY@Ag-Au/GCE sensor for the detection of MTX and CIF is illustrated in table 7.4 in terms of the recovery (%) and RSD (%). Excellent electrochemical response with good recovery of 99.92 – 100.66 % and 99 – 102% was observed for the MTX and CIF, respectively. The RSD value of 0.85 – 2.35 % and 0.78 – 1.75 was observed for the MTX for CIF, respectively, which confirms the feasibility and applicability of the fabricated NC-3DPPY@Ag-Au/GCE sensor for the simultaneous determination of MTX and CIF in the water samples.

Table 7.4: Determination of MTX and CIF in water sample at NC-3DPPY@Ag-Au/GCE using SWV (n=3)

Sample		Spiked (mM)	Found (nM)	Recovery (%)	RSD (%)
water sample	MTX	15	15.10	100.66	2.35
		25	24.88	99.52	1.25
		35	35.06	100.17	0.85
	CIF	5	5.10	102.00	1.75
		10	10.05	100.5	0.78
		15	14.85	99.00	1.35

CHAPTER 8: CONCLUSIONS AND FUTURE RECOMMENDATIONS

8.1 Conclusions

The present research illustrates the synthesis of transition metal-based nanocomposite for the fabrication of electrochemical sensors. The functionality of transition metal-based nanocomposites was improved either by the incorporation of carbon-based nanomaterials and biopolymers or by the introduction of tri-metals into a metallic foam as a substrate to develop a tri-metal based metal-organic framework. We have developed four sensing platforms and illustrated in the present study. Chapter 4 of this thesis focuses on the development of a nanocomposite of functionalized multiwall carbon nanotubes, nitrogen-doped graphene and chitosan with electrodeposited copper for nilutamide detection. Chapter 5 focuses on the nanocomposite of functionalized multiwall carbon nanotubes, chitosan and cobalt for the detection of paracetamol. Chapter 6 illustrates the design of a tri-metallic MOF employing cobalt, nickel and copper tri-metals based metal-organic framework onto the nickel foam for the determination of nilutamide. While chapter 7 focuses on the incorporation of silver and gold bimetallic nanoparticles on the nanocellulose and 3D polypyrrole nanocomposite for the simultaneous detection of methotrexate and ciprofloxacin.

The key findings of each sensing platforms are summarized in the following:

1. A nanocomposite of (MWCNTs$_f$–NGr/CTS)-Cu was synthesized successfully and characterized using various analytical techniques. The XRD results confirmed the presence of Cu on the MWCNTs$_f$–NGr/CTS nanocomposite. The TEM images confirm the deposition of Cu on the high surface area of MWCNTs$_f$–NGr/CTS. The electrochemical reduction of NLM was achieved on the (MWCNTs$_f$–NGr/CTS)-Cu nanocomposite modified GCE. The high electroactive surface area and synergy between

the MWCNTs*f* and NGr improves the mobility of ions and electrons, while improved the dispersion of nanomaterials by CTS and enhanced the electrocatalytic effect of electrodeposited copper greatly improve the reduction peak current of NLM. The fabricated sensor can detect NLM in a linear range of 0.005 to 900 μM with a correlation co-efficient of 0.999 and low LOD of 1.6 nM. The sensor showed high selectivity toward the detection of NLM even in the presence of interfering compounds. The modified electrode was successfully applied to blood serum sample and commercial tablets with the great recovery of 98.0–101.5% and 98.0–102.0% respectively.

2. While a nanocomposite comprising of *f*-MWCNTs/CTS-Co was successfully synthesized and characterized by several techniques. The XRD results confirmed the successful incorporation of Co on the *f*-MWCNTs/CTS nanocomposite. The FESEM images showed that the spherical shaped Co was deposited on the surface of *f*-MWCNTs/CTS. The electrochemical performance of the *f*-MWCNTs/CTS-Co modified electrode towards the oxidation of PR was studied by cyclic voltammetry and differential pulse voltammetry. The outstanding electrical conductivity of *f*-MWCNTs, excellent adsorption ability and dispersion profile of CTS which assures the homogenous dispersion of *f*-MWCNTs, and catalytic effect of Co, facilitates the electrons transfer between the modified electrode and PR, which greatly improved the redox response of the PR. The developed sensor is able to detect PR in a linear concentration range between 0.1 and 400 μmol L^{-1} with a low LOD of 0.01 μmol L^{-1}. This modified electrode exhibited a satisfying reproducibility and also good selectivity in the presence of some common interferences. Finally, the modified electrode was successfully tested for the detection of PR in the real sample.

3. While another nanocomposite comprising of Co, Ni and Cu based tri-metallic metal-organic framework grown at nickel foam was successfully synthesized and

characterized by several analytical methods. The XRD results confirmed the successful formation of tri-metallic Co-Ni-Cu-MOF/NF nanocomposite. The FESEM and TEM images of nanocomposite showed the uniform deposition of Co, Ni and Cu on the surface of the NF substrate. The information about the chemical state of Co, Ni and Cu in the Co-Ni-Cu-MOF/NF nanocomposite was determined by XPS analysis. The BET spectrum gave the surface area of the Co-Ni-Cu-MOF/NF nanocomposite. The electrochemical behaviour of the Co-Ni-Cu/NF modified electrode towards the redox response of NLM was studied by cyclic voltammetry and differential pulse voltammetry. The fabricated electrode presented superior electrocatalytic activity towards the redox response of NLM. The synergistic combination of Co, Ni and Cu tri-metals makes this nanocomposite as better electrocatalyst for NLM detection. In addition, the 3D network of tri-metals with greater catalytic activity, efficient binding sites and high electro-active surface area accelerates the electron transfer process. The developed sensor is able to detect NLM in a linear concentration range between from 0.5 to 900 μM. The sensitivity and limit of detection at the Co-Ni-Cu-MOF/NF was 10.712 μA $\mu M^{-1}cm^{-2}$ and 0.48 ± 0.02 nM, respectively. This modified electrode exhibited good selectivity in the presence of some common interferences. Finally, the modified electrode was successfully tested for the detection of NLM in the real sample.

4. Another nanocomposite composed of Ag-Au bimetallic nanoparticles and NC-3DPPY was successfully synthesized and characterized by several techniques. The XRD results confirmed the successful formation of bimetallic Ag-Au in the NC-3DPPY nanocomposite. The FESEM images of NC-3DPPY@Ag-Au/GCE nanocomposite confirmed deposition of the Ag-Au bimetallic nanoparticles on the surface of the NC-3DPPY support. The electrochemical performance of the NC-3DPPY@Ag-Au/GCE modified electrode towards the oxidation of MTX and CIF was studied by cyclic voltammetry and squarewave voltammetry. The fabricated electrode showed excellent

electrocatalytic activity towards the oxidation of MTX and CIF. The synergistic combination of Ag-Au bimetallic nanoparticles with porous appearance of NC-3DPPY makes the nanocomposite an excellent electrocatalyst for MTX and CIF detection. In addition, an increase in the electroactive sites for the efficient electron transfer process between MTX, CIF and the modified electrode is due to the deposition of Ag-Au bimetallic nanoparticles on the high surface area of NC-3DPPY. The developed sensor can detect MTX and CIF in a linear concentration range between 0.1 μM to 600 μM and 0.5 μM to 500 μM respectively. The modified electrode showed high selectivity towards the detection of MTX and CIF in presence of some common interference with a low LOD of 0.005 μM for MTX and 0.04 μM for CIF. Finally, the modified electrode was successfully tested for the detection of MTX and CIF in the real sample.

The present study represents different electrochemical sensing platforms for the quantitative detection of pharmaceutical drugs. Furthermore, the study explores the different applications of the proposed sensors in clinical, pharmaceutical and environmental monitoring aspect which proves the potential of this research investigation and could contribute to the research community. By comparing the advantages and sensing performances of all the developed sensing platforms included in this study, the Co-Ni-Cu-MOF/NF electrochemical sensing platform might be selected for commercialization purpose for pharmaceutical routine analysis and clinical monitoring due to its novelty, simplicity and fewer fabrication steps, cost-effectivity, very low LOD and broad linear ranges.

8.2 Future recommendations

The current research work focuses on the synthesis of nanocomposite by the incorporation of transition metals such as cobalt and copper with the assimilation of carbon-based nanostructured materials such as multiwall carbon nanotubes and nitrogen-doped graphene. While the design of cobalt, nickel and copper tri-metals MOF

network with this transition metal on porous metallic nickel foam with enhanced catalytic effect and electrochemical response. In this work, the synthesized transition metal-based nanocomposite was utilized as a sensing platform for the electrochemical determination of pharmaceutical drugs in commercial preparations and biological fluids. The attachment of transition metal ions along with carbon-based nanomaterials and biopolymers facilitated the efficient electron transfer at the electrode and electrolyte interface, provides synergy in the catalytic effect, thus enhances the electrochemical signals. From these results it can be demonstrated that, some future works can be explored based on improved and the scopes could be widened with the incorporation of novel concepts which are listed below:

(1) The scope of electrochemical sensors could be expanded with the synthesis of the transition metals with different nanostructured morphology (nanorods, nanowires, nanobelts, nanotubes etc), bimetallic nanostructures are yet to be explored.

(2) The electrochemical performances of the transition metal-based nanocomposite could be modified by the selection of carbon-based nanomaterials of the different nanostructured forms such as nanorods, nanotubes, nanobeads, nanoribbons, nanofibers and others are yet to be explored.

(3) The synthesis of tri-metallic MOFs could be modified by the incorporations of other transition metals such as zinc, iron, manganese and others with the incorporation of other metallic substrates such as titanium, aluminium, silica and others.

(4) The sensitivity and flexibility of the transition metals-based nanocomposite could be further improved by the incorporation of different synthesized forms of biopolymers such as chitosan nanoparticle, carboxylated nanocellulose, nanocellulose aerogels etc or other conductive polymers such as polyaniline. Both approaches contribute to an improvement in the electrocatalytic activity of the nanocomposite towards analyte detection.

(5) The proposed transition metal-based nanocomposites could be efficiently used for the electrochemical determination of other analytes, supercapacitors and solar cell applications. However, more studies are needed for the synthesis and preparation of different types of transition metal-based nanocomposites for the fabrication of advanced electrochemical sensors.

REFERENCES

Aazam, E. S., & Zaheer, Z. (2021). Gold@ Silver bimetallic nanoparticles: fabrication and removal of toxic chromium (VI). *Journal of Materials Science: Materials in Electronics, 32*(8), 11043-11058.

Abbas, T., & Tahir, M. (2021). Tri-metallic Ni–Co modified reducible TiO2 nanocomposite for boosting H2 production through steam reforming of phenol. *International Journal of Hydrogen Energy, 46*(13), 8932-8949.

Afkhami, A., Bahiraei, A., & Madrakian, T. (2016). Gold nanoparticle/multi-walled carbon nanotube modified glassy carbon electrode as a sensitive voltammetric sensor for the determination of diclofenac sodium. *Materials Science and Engineering: C, 59*, 168-176.

Agnihotri, A. S., Varghese, A., & Nidhin, M. (2021). Transition metal oxides in electrochemical and bio sensing: A state-of-art review. *Applied Surface Science Advances, 4*, 100072.

Akbari, A., Amini, M., Tarassoli, A., Eftekhari-Sis, B., Ghasemian, N., & Jabbari, E. (2018). Transition metal oxide nanoparticles as efficient catalysts in oxidation reactions. *Nano-Structures & Nano-Objects, 14*, 19-48.

Akgul, F. A., Akgul, G., Yildirim, N., Unalan, H. E., & Turan, R. (2014). Influence of thermal annealing on microstructural, morphological, optical properties and surface electronic structure of copper oxide thin films. *Materials Chemistry and Physics, 147*(3), 987-995.

Akhter, S., Basirun, W. J., Alias, Y., Johan, M. R., Bagheri, S., Shalauddin, M., . . . Anuar, N. S. (2018). Enhanced amperometric detection of paracetamol by immobilized cobalt ion on functionalized MWCNTs-Chitosan thin film. *Analytical Biochemistry, 551*, 29-36.

Akhter, S., Basirun, W. J., Shalauddin, M., Johan, M. R., Bagheri, S., Akbarzadeh, O., & Anuar, N. S. (2020b). Hybrid nanocomposite of functionalized multiwall carbon nanotube, nitrogen doped graphene and chitosan with electrodeposited copper for the detection of anticancer drug nilutamide in tablet and biological samples. *Materials Chemistry and Physics, 253*, 123393.

Akhter, S., Zain, N. K. M., Shalauddin, M., Singh, V. K., Misnon, I. I., Sharma, R. K., . . . Jose, R. (2021). Tri-metallic Co-Ni-Cu based metal organic framework nanostructures for the detection of an anticancer drug nilutamide. *Sensors and Actuators A: Physical, 325*, 112711.

Alanazi, K., Cruz, A. G., Di Masi, S., Voorhaar, A., Ahmad, O. S., Cowen, T., . . . Sims, M. R. (2021). Disposable paracetamol sensor based on electroactive molecularly imprinted polymer nanoparticles for plasma monitoring. *Sensors and Actuators B: Chemical, 329*, 129128.

Alegret, S., & Merkoci, A. (Eds.) (2007). *Electrochemical sensor analysis*: Elsevier.

Alkahtani, S. A., El-Wekil, M. M., Mahmoud, A. M., Mahnashi, M. H., & Oraby, M. (2019). One pot synthesis of AuPdPt trimetallic nanohybrid decorated reduced graphene oxide nanosheets for ultrasensing of anti-convulsant drug retigabine (ezogabine). *Journal of The Electrochemical Society, 166*(12), H521.

Alothman, Z. A., Bukhari, N., Wabaidur, S. M., & Haider, S. (2010). Simultaneous electrochemical determination of dopamine and acetaminophen using multiwall carbon nanotubes modified glassy carbon electrode. *Sensors and Actuators B: Chemical, 146*(1), 314-320.

Altria, K., Clayton, N., Hart, M., Harden, R., Hevizi, J., Makwana, J., & Portsmouth, M. (1994). An inter-company cross-validation exercise on capillary electrophoresis testing of dose uniformity of paracetamol content in formulations. *Chromatographia, 39*(3-4), 180-184.

Altun, M. L. (2002). HPLC method for the analysis of paracetamol, caffeine and dipyrone. *Turkish Journal of Chemistry, 26*(4), 521-528.

Amala, G., & Gowtham, S. (2017). Recent advancements, key challenges and solutions in non-enzymatic electrochemical glucose sensors based on graphene platforms. *RSC Advances, 7*(59), 36949-36976.

Annalakshmi, M., Balasubramanian, P., Chen, S.-M., & Chen, T.-W. (2019). One pot synthesis of nanospheres-like trimetallic NiFeCo nanoalloy: A superior electrocatalyst for electrochemical sensing of hydrazine in water bodies. *Sensors and Actuators B: Chemical, 296*, 126620.

Anuar, N. S., Basirun, W. J., Ladan, M., Shalauddin, M., & Mehmood, M. S. (2018). Fabrication of platinum nitrogen-doped graphene nanocomposite modified electrode for the electrochemical detection of acetaminophen. *Sensors and Actuators B: Chemical, 266*, 375-383.

Anuar, N. S., Basirun, W. J., Shalauddin, M., & Akhter, S. (2020). A dopamine electrochemical sensor based on a platinum–silver graphene nanocomposite modified electrode. *RSC Advances, 10*(29), 17336-17344.

Arvand, M., & Gholizadeh, T. M. (2013). Simultaneous voltammetric determination of tyrosine and paracetamol using a carbon nanotube-graphene nanosheet nanocomposite modified electrode in human blood serum and pharmaceuticals. *Colloids and Surfaces B: Biointerfaces, 103*, 84-93.

Asadian, E., Shahrokhian, S., Zad, A. I., & Ghorbani-Bidkorbeh, F. (2017). Glassy carbon electrode modified with 3D graphene–carbon nanotube network for sensitive electrochemical determination of methotrexate. *Sensors and Actuators B: Chemical, 239*, 617-627.

Bang, J. H., & Suslick, K. S. (2010). Applications of ultrasound to the synthesis of nanostructured materials. *Advanced Materials, 22*(10), 1039-1059.

Baranowska, I., Markowski, P., Gerle, A., & Baranowski, J. (2008). Determination of selected drugs in human urine by differential pulse voltammetry technique. *Bioelectrochemistry, 73*(1), 5-10.

Bard, A. (1980). Electrochemical Methods. *Fundamentals and applications, 290*.

Beitollahi, H., Movahedifar, F., Tajik, S., & Jahani, S. (2019). A review on the effects of introducing CNTs in the modification process of electrochemical sensors. *Electroanalysis, 31*(7), 1195-1203.

Calvino, M. M., Lisuzzo, L., Cavallaro, G., Lazzara, G., & Milioto, S. (2021). Non-isothermal thermogravimetry as an accelerated tool for the shelf-life prediction of paracetamol formulations. *Thermochimica Acta, 700*, 178940.

Carvalho, M. M., Ribeiro, D. S., Santos, J. L., & Prior, J. A. (2014). pH-sensitive spectrophotometric control of nilutamide in an automatic micro-flow system. *New Journal of Chemistry, 38*(7), 2856-2864.

Cazes, J. (2004). *Analytical instrumentation handbook*: CRC Press.

Chai, L., Hu, Z., Wang, X., Zhang, L., Li, T.-T., Hu, Y., Huang, S. (2021). Fe7C3 nanoparticles with in situ grown CNT on nitrogen doped hollow carbon cube with greatly enhanced conductivity and ORR performance for alkaline fuel cell. *Carbon, 174*, 531-539.

Chauhan, R., Gill, A. A., Nate, Z., & Karpoormath, R. (2020). Highly selective electrochemical detection of ciprofloxacin using reduced graphene oxide/poly (phenol red) modified glassy carbon electrode. *Journal of Electroanalytical Chemistry, 871*, 114254.

Chen, C., Tuo, Y., Lu, Q., Lu, H., Zhang, S., Zhou, Y., Feng, X. (2021). Hierarchical trimetallic Co-Ni-Fe oxides derived from core-shell structured metal-organic frameworks for highly efficient oxygen evolution reaction. *Applied Catalysis B: Environmental, 287*, 119953.

Chen, S., Huang, R., Yu, J., & Jiang, X. (2019). Simultaneous voltammetric determination of hydroquinone and catechol by using a glassy carbon electrode modified with a ternary nanocomposite prepared from oxidized multiwalled carbon nanotubes, manganese dioxide and manganese ferrite. *Microchimica Acta, 186*(9), 1-8.

Chen, Y., Fan, Z., Zhang, Z., Niu, W., Li, C., Yang, N., Zhang, H. (2018). Two-dimensional metal nanomaterials: synthesis, properties, and applications. *Chemical Reviews, 118*(13), 6409-6455.

Dai, S., Liu, Z., Zhao, B., Zeng, J., Hu, H., Zhang, Q., Liu, M. (2018). A high-performance supercapacitor electrode based on N-doped porous graphene. *Journal of Power Sources, 387*, 43-48.

Dai, Y., Ding, J., Li, J., Li, Y., Zong, Y., Zhang, P., Liu, X. (2021). N, S and Transition-Metal Co-Doped Graphene Nanocomposites as High-Performance Catalyst for Glucose Oxidation in a Direct Glucose Alkaline Fuel Cell. *Nanomaterials, 11*(1), 202.

Daneshvar, L., & Rounaghi, G. H. (2017). An electrochemical sensing platform for carbamazepine determination based on trimetallic Au-Ag-Pd dendritic nanopatricles, supramolecular β-cyclodextrin and [bmim] NTF2 ionic liquids. *Journal of The Electrochemical Society, 164*(6), B177.

de Laia, A. G. S., Barrioni, B. R., Valverde, T. M., de Goes, A. M., de Sá, M. A., & de Magalhães Pereira, M. (2020). Therapeutic cobalt ion incorporated in poly (vinyl alcohol)/bioactive glass scaffolds for tissue engineering. *Journal of Materials Science, 55*(20), 8710-8727.

Demuth, J., Hamers, R., Tromp, R. M., & Welland, M. (1986). A scanning tunneling microscope for surface science studies. *IBM Journal of Research and Development, 30*(4), 396-402.

Deng, S., Zhao, B., Xing, Y., Shi, Y., Fu, Y., & Liu, Z. (2021). Green synthesis of proanthocyanidins-functionalized Au/Ag bimetallic nanoparticles. *Green Chemistry Letters and Reviews, 14*(1), 45-50.

Deng, Z., Li, H., Tian, Q., Zhou, Y., Yang, X., Yu, Y., Zhou, T. (2020). Electrochemical detection of methotrexate in serum sample based on the modified acetylene black sensor. *Microchemical Journal, 157*, 105058.

Ding, B., & Wu, X. (2020). Transition metal oxides anchored on graphene/carbon nanotubes conductive network as both the negative and positive electrodes for asymmetric supercapacitor. *Journal of Alloys and Compounds, 842*, 155838.

Do, M. T., & Stuckey, D. C. (2019). Fate and removal of Ciprofloxacin in an anaerobic membrane bioreactor (AnMBR). *Bioresource Technology, 289*, 121683.

Drobek, M., Kim, J.-H., Bechelany, M., Vallicari, C., Julbe, A., & Kim, S. S. (2016). MOF-based membrane encapsulated ZnO nanowires for enhanced gas sensor selectivity. *ACS Applied Materials & Interfaces, 8*(13), 8323-8328.

Easwaramoorthy, D., Yu, Y.-C., & Huang, H.-J. (2001). Chemiluminescence detection of paracetamol by a luminol-permanganate based reaction. *Analytica Chimica Acta, 439*(1), 95-100.

El Demeiry, M., Ali, A., Abouleila, Y., Shimizu, Y., Masujima, T., Salam, R. A., Emara, S. (2020). Quantification and targeted detection of ciprofloxacin in dosage form and human urine by direct injection nano-electrospray ionization multi-stage mass spectrometry. *Microchemical Journal, 153*, 104534.

Fanjul-Bolado, P., Lamas-Ardisana, P. J., Hernández-Santos, D., & Costa-Garcia, A. (2009). Electrochemical study and flow injection analysis of paracetamol in pharmaceutical formulations based on screen-printed electrodes and carbon nanotubes. *Analytica Chimica Acta, 638*(2), 133-138.

Farghaly, O. A., Hameed, R. A., & Abu-Nawwas, A.-A. H. (2014). Analytical application using modern electrochemical techniques. *Int. J. Electrochem. Sci, 9*(1), 3287-3318.

Farzin, L., Shamsipur, M., Samandari, L., & Sheibani, S. (2018). Advances in the design of nanomaterial-based electrochemical affinity and enzymatic biosensors for metabolic biomarkers: A review. *Microchimica Acta, 185*(5), 1-25.

Fettkenhauer, C., Wang, X., Kailasam, K., Antonietti, M., & Dontsova, D. (2015). Synthesis of efficient photocatalysts for water oxidation and dye degradation reactions using CoCl 2 eutectics. *Journal of Materials Chemistry A, 3*(42), 21227-21232.

Fu, L., Lai, G., & Yu, A. (2015). Preparation of β-cyclodextrin functionalized reduced graphene oxide: application for electrochemical determination of paracetamol. *RSC Advances, 5*(94), 76973-76978.

Furukawa, H., Cordova, K. E., O'Keeffe, M., & Yaghi, O. M. (2013). The chemistry and applications of metal-organic frameworks. *Science, 341*(6149).

Garcia, P. R., Prymak, O., Grasmik, V., Pappert, K., Wlysses, W., Otubo, L., Oliveira, C. L. (2020). An in situ SAXS investigation of the formation of silver nanoparticles and bimetallic silver–gold nanoparticles in controlled wet-chemical reduction synthesis. *Nanoscale Advances, 2*(1), 225-238.

Gayen, P., & Chaplin, B. P. (2016). Selective electrochemical detection of ciprofloxacin with a porous nafion/multiwalled carbon nanotube composite film electrode. *ACS Applied Materials & Interfaces, 8*(3), 1615-1626.

Gill, A. A., Singh, S., Nate, Z., Pawar, C., Chauhan, R., Thapliyal, N. B., Patel, R. (2021). One-pot synthesis of β-cyclodextrin modified silver nanoparticles for highly sensitive detection of ciprofloxacin. *Journal of Pharmaceutical and Biomedical Analysis*, 114219.

Gissawong, N., Srijaranai, S., Boonchiangma, S., Uppachai, P., Seehamart, K., Jantrasee, S., Mukdasai, S. (2021). An electrochemical sensor for voltammetric detection of ciprofloxacin using a glassy carbon electrode modified with activated carbon, gold nanoparticles and supramolecular solvent. *Microchimica Acta, 188*(6), 1-13.

González, C. M. O., Kharissova, O. V., González, L. T., Méndez-Rojas, M. A., Quezada, T. S., & Méndez, Y. P. (2021). Scalable Synthesis of Nanomaterials. *Handbook of Nanomaterials and Nanocomposites for Energy and Environmental Applications*, 899-921.

Gosser, D. K. (1993). *Cyclic voltammetry: simulation and analysis of reaction mechanisms*: VCH New York.

Gowthaman, N., Raj, M. A., & John, S. A. (2017). Nitrogen-doped graphene as a robust scaffold for the homogeneous deposition of copper nanostructures: A nonenzymatic disposable glucose sensor. *ACS Sustainable Chemistry & Engineering, 5*(2), 1648-1658.

Goyal, R. N., & Singh, S. P. (2006). Voltammetric determination of paracetamol at C60-modified glassy carbon electrode. *Electrochimica Acta, 51*(15), 3008-3012.

Gregorio-Jauregui, K. M., Pineda, M., Rivera-Salinas, J. E., Hurtado, G., Saade, H., Martinez, J. L., Lopez, R. G. (2012). One-step method for preparation of magnetic nanoparticles coated with chitosan. *Journal of Nanomaterials,4,(1-8) 2012*.

Guo, L., Zheng, H., Zhang, C., Qu, L., & Yu, L. (2020). A novel molecularly imprinted sensor based on PtCu bimetallic nanoparticle deposited on PSS functionalized graphene with peroxidase-like activity for selective determination of puerarin. *Talanta, 210*, 120621.

Haldorai, Y., Choe, S. R., Huh, Y. S., & Han, Y.-K. (2018). Metal-organic framework derived nanoporous carbon/Co3O4 composite electrode as a sensing platform for the determination of glucose and high-performance supercapacitor. *Carbon, 127*, 366-373.

Hamidi, S., Azami, A., & Aghdam, E. M. (2019). A novel mixed hemimicelles dispersive micro-solid phase extraction using ionic liquid functionalized magnetic graphene oxide/polypyrrole for extraction and pre-concentration of methotrexate from urine samples followed by the spectrophotometric method. *Clinica Chimica Acta, 488*, 179-188.

Hanif, Z., Shin, D., Choi, D., & Park, S. J. (2020). Development of a vapor phase polymerization method using a wet-on-wet process to coat polypyrrole on never-dried nanocellulose crystals for fabrication of compression strain sensor. *Chemical Engineering Journal, 381*, 122700.

Hu, X., Xu, X., Fu, F., Yang, B., Zhang, J., Zhang, Y., Liu, X. (2020). Synthesis of bimetallic silver-gold nanoparticle composites using a cellulose dope: Tunable nanostructure and its biological activity. *Carbohydrate Polymers, 248*, 116777.

Hwang, D.-W., Lee, S., Seo, M., & Chung, T. D. (2018). Recent advances in electrochemical non-enzymatic glucose sensors–a review. *Analytica Chimica Acta, 1033*, 1-34.

Jamkhande, P. G., Ghule, N. W., Bamer, A. H., & Kalaskar, M. G. (2019). Metal nanoparticles synthesis: An overview on methods of preparation, advantages and disadvantages, and applications. *Journal of Drug Delivery Science and Technology, 53*, 101174.

Janata, J. (2002). Electrochemical Sensors and their impedances: a tutorial. *Critical Reviews in Analytical Chemistry, 32*(2), 109-120.

Janata, J. (2009). *Principles of chemical sensors*: Springer.

Janata, J., & Bezegh, A. (1988). Chemical sensors. *Analytical Chemistry, 60*(12), 62R-74R.

Janata, J., & Huber, R. J. (1985). *Solid state chemical sensors*: Academic Press Orlando.

Jandaghi, N., Jahani, S., Foroughi, M. M., Kazemipour, M., & Ansari, M. (2020). Cerium-doped flower-shaped ZnO nano-crystallites as a sensing component for simultaneous electrochemical determination of epirubicin and methotrexate. *Microchimica Acta, 187*(1), 1-11.

Janssen, L., & Hoogland, J. (1973). The effect of electrolytically evolved gas bubbles on the thickness of the diffusion layer—II. *Electrochimica Acta, 18*(8), 543-550.

Ji, C., Zhou, Y., Leblanc, R. M., & Peng, Z. (2020). Recent developments of carbon dots in biosensing: A review. *ACS sensors, 5*(9), 2724-2741.

Jin, W., & Maduraiveeran, G. (2019). Recent advances of porous transition metal-based nanomaterials for electrochemical energy conversion and storage applications. *Materials Today Energy, 13*, 64-84.

Karami, F., Ranjbar, S., Ghasemi, Y., & Negahdaripour, M. (2019). Analytical methodologies for determination of methotrexate and its metabolites in pharmaceutical, biological and environmental samples. *Journal of Pharmaceutical Analysis, 9*(6), 373-391.

Karimi-Maleh, H., Karimi, F., Alizadeh, M., & Sanati, A. L. (2020). Electrochemical sensors, a bright future in the fabrication of portable kits in analytical systems. *The Chemical Record, 20*(7), 682-692.

Karthik, R., Karikalan, N., Chen, S.-M., Gnanaprakasam, P., & Karuppiah, C. (2017). Voltammetric determination of the anti-cancer drug nilutamide using a screen-printed carbon electrode modified with a composite prepared from β-cyclodextrin, gold nanoparticles and graphene oxide. *Microchimica Acta, 184*(2), 507-514.

Karthik, R., Sasikumar, R., Chen, S.-M., Kumar, J. V., Elangovan, A., Muthuraj, V., Elshikh, M. S. (2017). A highly sensitive and selective electrochemical determination of non-steroidal prostate anti-cancer drug nilutamide based on f-MWCNT in tablet and human blood serum sample. *Journal of Colloid and Interface Science, 487*, 289-296.

Khan, S. A., Khan, S. B., Kamal, T., Asiri, A. M., & Akhtar, K. (2016). Recent Development of Chitosan Nanocomposites for Environmental Applications. *Recent Patents on Nanotechnology, 10*(3), 181-188.

Khand, A. A., Lakho, S. A., Tahira, A., Ubaidullah, M., Alothman, A. A., Aljadoa, K., . . . Ibupoto, Z. H. (2021). Facile Electrochemical Determination of Methotrexate (MTX) Using Glassy Carbon Electrode-Modified with Electronically Disordered NiO Nanostructures. *Nanomaterials, 11*(5), 1266.

Kim, D. H., Yoo, Y. S., Yoo, H. J., Choi, Y. J., Kim, S. A., Sheen, D. H., Cho, K. (2021). Analysis of hair and plasma samples for methotrexate (MTX) and metabolite using high-performance liquid chromatography triple quadrupole mass spectrometry (LC-MS/MS) detection. *Journal of Mass Spectrometry, 56*(4), e4648.

Kokab, T., Shah, A., Khan, M. A., Arshad, M., Nisar, J., Ashiq, M. N., & Zia, M. A. (2021). Simultaneous Femtomolar Detection of Paracetamol, Diclofenac, and Orphenadrine Using a Carbon Nanotube/Zinc Oxide Nanoparticle-Based Electrochemical Sensor. *ACS Applied Nano Materials 4,5,* 4699-4712.

Kokulnathan, T., Karthik, R., Chen, S.-M., Kumar, J. V., & Sakthinathan, S. (2019a). A cerium vanadate interconnected with a carbon nanofiber heterostructure for electrochemical determination of the prostate cancer drug nilutamide. *Microchimica Acta, 186*(8), 579.

Koons, G. L., Diba, M., & Mikos, A. G. (2020). Materials design for bone-tissue engineering. *Nature Reviews Materials, 5*(8), 584-603.

Kumar, K. G., & Letha, R. (1997). Determination of paracetamol in pure form and in dosage forms using N, N-dibromo dimethylhydantoin. *Journal of Pharmaceutical and Biomedical Analysis, 15*(11), 1725-1728.

Kummari, S., Kumar, V. S., Satyanarayana, M., & Gobi, K. V. (2019). Direct electrochemical determination of methotrexate using functionalized carbon nanotube paste electrode as biosensor for in-vitro analysis of urine and dilute serum samples. *Microchemical Journal, 148*, 626-633.

Latif, H., Wasif, D., Rasheed, S., Sattar, A., Rafique, M. S., Anwar, A. W., Qutab, M. (2020). Gold nanoparticles mixed multiwall carbon nanotubes, supported on graphene nano-ribbons (Au-NT-G) as an efficient reduction electrode for Polymer Electrolyte Membrane fuel cells (PEMFC). *Renewable Energy, 154*, 767-773.

Laviron, E. (1979). General expression of the linear potential sweep voltammogram in the case of diffusionless electrochemical systems. *Journal of Electroanalytical Chemistry and Interfacial Electrochemistry, 101*(1), 19-28.

Li, C., Sun, Z., Zhang, W., Yu, C., & Zheng, S. (2018). Highly efficient g-C3N4/TiO2/kaolinite composite with novel three-dimensional structure and enhanced visible light responding ability towards ciprofloxacin and S. aureus. *Applied Catalysis B: Environmental, 220*, 272-282.

Li, C., Wu, Z., Yang, H., Deng, L., & Chen, X. (2017). Reduced graphene oxide-cyclodextrin-chitosan electrochemical sensor: Effective and simultaneous determination of o-and p-nitrophenols. *Sensors and Actuators B: Chemical, 251*, 446-454.

Li, H., Wang, K., Sun, Y., Lollar, C. T., Li, J., & Zhou, H.-C. (2018). Recent advances in gas storage and separation using metal–organic frameworks. *Materials Today, 21*(2), 108-121.

Li, J., Chen, D., Zhang, T., & Chen, G. (2021). Highly sensitive electrochemical determination of methotrexate based on a N-doped hollow nanocarbon sphere modified electrode. *Analytical Methods, 13*(1), 117-123.

Li, M., & Jing, L. (2007). Electrochemical behavior of acetaminophen and its detection on the PANI–MWCNTs composite modified electrode. *Electrochimica Acta, 52*(9), 3250-3257.

Li, S., Gao, Y., Li, N., Ge, L., Bu, X., & Feng, P. (2021). Transition metal-based bimetallic MOFs and MOF-derived catalysts for electrochemical oxygen evolution reaction. *Energy & Environmental Science, 14*(4), 1897-1927.

Lin, W., Chuang, C., Yao, C., & Tang, C. (2020). Effect of cobalt precursors on cobalt-hydroxyapatite used in bone regeneration and MRI. *Journal of Dental Research, 99*(3), 277-284.

Lin, Z., Yao, Y., Li, Z., Liu, Y., Li, Z., & Wong, C.-P. (2010). Solvent-assisted thermal reduction of graphite oxide. *The Journal of Physical Chemistry C, 114*(35), 14819-14825.

Lohmann, W., & Karst, U. (2006). Simulation of the detoxification of paracetamol using on-line electrochemistry/liquid chromatography/mass spectrometry. *Analytical and Bioanalytical Chemistry, 386*(6), 1701-1708.

Lou, H.-g., Yuan, H., Ruan, Z.-r., & Jiang, B. (2010). Simultaneous determination of paracetamol, pseudoephedrine, dextrophan and chlorpheniramine in human plasma by liquid chromatography–tandem mass spectrometry. *Journal of Chromatography B, 878*(7-8), 682-688.

Lu, T.-L., & Tsai, Y.-C. (2011). Sensitive electrochemical determination of acetaminophen in pharmaceutical formulations at multiwalled carbon nanotube-alumina-coated silica nanocomposite modified electrode. *Sensors and Actuators B: Chemical, 153*(2), 439-444.

Mao, A., Li, H., Jin, D., Yu, L., & Hu, X. (2015). Fabrication of electrochemical sensor for paracetamol based on multi-walled carbon nanotubes and chitosan–copper complex by self-assembly technique. *Talanta, 144*, 252-257.

Matsunaga, T., Kondo, T., Osasa, T., Kotsugai, A., Shitanda, I., Hoshi, Y., Yuasa, M. (2020). Sensitive electrochemical detection of ciprofloxacin at screen-printed diamond electrodes. *Carbon, 159*, 247-254.

Mohd Zain, N. K., Vijayan, B. L., Misnon, I. I., Das, S., Karuppiah, C., Yang, C.-C., Jose, R. (2018). Direct Growth of Triple Cation Metal–Organic Framework on a Metal Substrate for Electrochemical Energy Storage. *Industrial & Engineering Chemistry Research, 58*(2), 665-674.

Munonde, T. S., & Nomngongo, P. N. (2021). Nanocomposites for Electrochemical Sensors and Their Applications on the Detection of Trace Metals in Environmental Water Samples. *Sensors, 21*(1), 131.

Murray, R. W. (1980). Chemically modified electrodes. *Accounts of Chemical Research, 13*(5), 135-141.

Murtaza, G., Hussain, I., Khan, S. A., Shabbir, A., Mahmood, A., Asad, M. H. H. B., Malik, N. S. (2011). Development of a UV-spectrophotometric method for the simultaneous determination of aspirin and paracetamol in tablets. *Scientific Research and Essays, 6*(2), 417-421.

Naeimi, H., Mohajeri, A., Moradi, L., & Rashidi, A. (2011). Solubilization of multi walled carbon nanotubes under a facile and mild condition. *Journal of Nanoscience and Nanotechnology, 11*(10), 8903-8906.

Naghian, E., Khosrowshahi, E. M., Sohouli, E., Ahmadi, F., Rahimi-Nasrabadi, M., & Safarifard, V. (2020). A new electrochemical sensor for the detection of fentanyl lethal drug by a screen-printed carbon electrode modified with the open-ended channels of Zn (ii)-MOF. *New Journal of Chemistry, 44*(22), 9271-9277.

Nguyen, T.-D. (2013). From formation mechanisms to synthetic methods toward shape-controlled oxide nanoparticles. *Nanoscale, 5*(20), 9455-9482.

Osswald, S., Havel, M., & Gogotsi, Y. (2007). Monitoring oxidation of multiwalled carbon nanotubes by Raman spectroscopy. *Journal of Raman Spectroscopy: An International Journal for Original Work in all Aspects of Raman Spectroscopy, Including Higher Order Processes, and also Brillouin and Rayleigh Scattering, 38*(6), 728-736.

Pan, Y., Yang, N., Chen, Y., Lin, Y., Li, Y., Liu, Y., & Liu, C. (2015). Nickel phosphide nanoparticles-nitrogen-doped graphene hybrid as an efficient catalyst for enhanced hydrogen evolution activity. *Journal of Power Sources, 297*, 45-52.

Pestov, A., & Bratskaya, S. (2016). Chitosan and its derivatives as highly efficient polymer ligands. *Molecules, 21*(3), 330.

Polshettiwar, V., Nadagouda, M. N., & Varma, R. S. (2009). Microwave-assisted chemistry: a rapid and sustainable route to synthesis of organics and nanomaterials. *Australian Journal of Chemistry, 62*(1), 16-26.

Pomerantseva, E., Bonaccorso, F., Feng, X., Cui, Y., & Gogotsi, Y. (2019). Energy storage: The future enabled by nanomaterials. *Science, 366*(6468).

Qiu, Q., Jiang, N., Ge, L., Li, X., & Chen, X. (2020). The electrochemical sensor for methanol detection based on trimetallic PtAuAg nanotubes. *Journal of Materials Science, 55*(33), 15681-15694.

Qiu, Y., Lin, Y., Yang, H., Wang, L., Wang, M., & Wen, B. (2020). Hollow Ni/C microspheres derived from Ni-metal organic framework for electromagnetic wave absorption. *Chemical Engineering Journal, 383*, 123207.

Qureshi, I. N., Tahira, A., Aljadoa, K., Alsalme, A. M., Alothman, A. A., Nafady, A., Ibupoto, Z. H. (2021). Polyaniline as a sacrificing template for the synthesis of controlled Co 3 O 4 nanoparticles for the sensitive and selective detection of methotrexate (MTX). *Journal of Materials Science: Materials in Electronics*, 1-11.

Racik, K. M., Manikandan, A., Mahendiran, M., Prabakaran, P., Madhavan, J., & Raj, M. V. A. (2020). Fabrication of manganese oxide decorated copper oxide (MnO2/CuO) nanocomposite electrodes for energy storage supercapacitor devices. *Physica E: Low-dimensional Systems and Nanostructures, 119*, 114033.

Rahman, M. M., Alam, M., & Alamry, K. (2020). A reliable alternative approach for the ultra-sensitive detection of l-glutathione with wet chemically synthesized Co 3 O 4-doped SnO 2 nanoparticles decorated on a glassy carbon electrode. *New Journal of Chemistry, 44*(37), 16020-16030.

Rajakumar, G., Zhang, X.-H., Gomathi, T., Wang, S.-F., Azam Ansari, M., Mydhili, G., Chung, I.-M. (2020). Current Use of Carbon-Based Materials for Biomedical Applications—A Prospective and Review. *Processes, 8*(3), 355.

Rajendran, K., Kokulnathan, T., Chen, S.-M., Allen, J. A., Viswanathan, C., & Therese, H. A. (2019). Nitrogen doped carbon nanofibers loaded with hierarchical vanadium tetrasulfide for the voltammetric detection of the non-steroidal anti-prostate cancer drug nilutamide. *Microchimica Acta, 186*(3), 141.

Rana, R. M., Rampogu, S., Abid, N. B., Zeb, A., Parate, S., Lee, G., Lee, K. W. (2020). In silico study identified methotrexate analog as potential inhibitor of drug resistant human dihydrofolate reductase for cancer therapeutics. *Molecules, 25*(15), 3510.

Raoof, J. B., Ojani, R., & Rashid-Nadimi, S. (2004). Preparation of polypyrrole/ferrocyanide films modified carbon paste electrode and its application on the electrocatalytic determination of ascorbic acid. *Electrochimica Acta, 49*(2), 271-280.

Rawool, C. R., & Srivastava, A. K. (2019). A dual template imprinted polymer modified electrochemical sensor based on Cu metal organic framework/mesoporous carbon for highly sensitive and selective recognition of rifampicin and isoniazid. *Sensors and Actuators B: Chemical, 288*, 493-506.

Razmi, H., & Habibi, E. (2010). Amperometric detection of acetaminophen by an electrochemical sensor based on cobalt oxide nanoparticles in a flow injection system. *Electrochimica Acta, 55*(28), 8731-8737.

Reddy, K. R., Brahman, P. K., & Suresh, L. (2018). Fabrication of high performance disposable screen printed electrochemical sensor for ciprofloxacin sensing in biological samples. *Measurement, 127*, 175-186.

Ren, Y., Du, H., Zhou, X., Liu, Y., Wang, Q., Li, S., Dong, X. (2020). Three-dimensional Al-substituted quasi-concentration gradient Ni-Co layered double hydroxide nanosheets for high-performance asymmetric supercapacitors. *Materials Today Energy, 18*, 100514.

Rhouati, A., Majdinasab, M., & Hayat, A. (2018). A perspective on non-enzymatic electrochemical nanosensors for direct detection of pesticides. *Current Opinion in Electrochemistry, 11*, 12-18.

Rotello, V. (2004). *Nanoparticles: building blocks for nanotechnology*: Springer Science & Business Media.

Rotello, V. M. (2004). *Nanoparticles: building blocks for nanotechnology*: Springer Science & Business Media.

Sahoo, M. K., Gusain, M., Thangriyal, S., Nagarajan, R., & Rao, G. R. (2020). Energy storage study of trimetallic Cu2MSnS4 (M: Fe, Co, Ni) nanomaterials prepared by sequential crystallization method. *Journal of Solid State Chemistry, 282*, 121049.

Sakaguchi, T., Morioka, Y., Yamasaki, M., Iwanaga, J., Beppu, K., Maeda, H., Tamiya, E. (2007). Rapid and onsite BOD sensing system using luminous bacterial cells-immobilized chip. *Biosensors and Bioelectronics, 22*(7), 1345-1350.

Salandari-Jolge, N., Ensafi, A. A., & Rezaei, B. (2020). A novel three-dimensional network of CuCr 2 O 4/CuO nanofibers for voltammetric determination of anticancer drug methotrexate. *Analytical and Bioanalytical Chemistry, 412*(11), 2443-2453.

Sarat, P., & Ramachandran, D. (2015). Two new UV-visible spectrophotometric methods for the determination of nilutamide in pure and their tablets using 2, 3-Dichloro-5, 6-Dicyano-1, 4-benzoquinone (DDQ) and Para Chloranilic acid (PCA). *Int J Pharm Pharm Res, 2*, 161-171.

Scheibe, B., Borowiak-Palen, E., & Kalenczuk, R. J. (2010). Oxidation and reduction of multiwalled carbon nanotubes—preparation and characterization. *Materials Characterization, 61*(2), 185-191.

Shahnaz, T., Padmanaban, V., & Narayanasamy, S. (2020). Surface modification of nanocellulose using polypyrrole for the adsorptive removal of Congo red dye and chromium in binary mixture. *International journal of Biological Macromolecules, 151*, 322-332.

Shalauddin, M., Akhter, S., Bagheri, S., Abd Karim, M. S., Kadri, N. A., & Basirun, W. J. (2017). Immobilized copper ions on MWCNTS-Chitosan thin film: Enhanced amperometric sensor for electrochemical determination of diclofenac sodium in aqueous solution. *International Journal of Hydrogen Energy, 42*(31), 19951-19960.

Shalauddin, M., Akhter, S., Basirun, W. J., Bagheri, S., Anuar, N. S., & Johan, M. R. (2019). Hybrid nanocellulose/f-MWCNTs nanocomposite for the electrochemical sensing of diclofenac sodium in pharmaceutical drugs and biological fluids. *Electrochimica Acta, 304*, 323-333.

Sharma, G., Bhogal, S., Naushad, M., Kumar, A., & Stadler, F. J. (2017). Microwave assisted fabrication of La/Cu/Zr/carbon dots trimetallic nanocomposites with their adsorptional vs photocatalytic efficiency for remediation of persistent organic pollutants. *Journal of Photochemistry and Photobiology A: Chemistry, 347*, 235-243.

Sharma, P., & Zalpouri, R. (2022). Microwave-assisted extraction of proteins and carbohydrates from marine resources. *Innovative and Emerging Technologies in the Bio-marine Food Sector*, 361-374.

Sharma, T. S. K., & Hwa, K.-Y. (2021). Rational design and preparation of copper vanadate anchored on sulfur doped reduced graphene oxide nanocomposite for electrochemical sensing of antiandrogen drug nilutamide using flexible electrodes. *Journal of Hazardous Materials, 410*, 124659.

Sharp, T., Maidment, N., Brazell, M., Zetterstro, T., Ungerstedt, U., Bennett, G., & Marsden, C. (1984). Changes in monoamine metabolites measured by simultaneousin vivo differential pulse voltammetry and intracerebral dialysis. *Neuroscience, 12*(4), 1213-1221.

Shen, M., Gao, K., Xiang, F., Wang, B., Dai, L., Zheng, L., Sun, S. (2020). Nanocellulose-assisted synthesis of ultrafine Co nanoparticles-loaded bimodal micro-mesoporous N-rich carbon as bifunctional oxygen electrode for Zn-air batteries. *Journal of Power Sources, 450*, 227640.

Shifrina, Z. B., Matveeva, V. G., & Bronstein, L. M. (2019). Role of polymer structures in catalysis by transition metal and metal oxide nanoparticle composites. *Chemical Reviews, 120*(2), 1350-1396.

Siegel, J., Kvítek, O., Ulbrich, P., Kolská, Z., Slepička, P., & Švorčík, V. (2012). Progressive approach for metal nanoparticle synthesis. *Materials Letters, 89*, 47-50.

Silva, F. V., Resende, S., Araújo, A. N., & Prior, J. A. (2018). Determination of pKa (s) of nilutamide through UV-visible spectroscopy. *Microchemical Journal, 138*, 303-308.

Siwal, S. S., Zhang, Q., Sun, C., & Thakur, V. K. (2020). Graphitic carbon nitride doped copper–manganese alloy as high–performance electrode material in supercapacitor for energy storage. *Nanomaterials, 10*(1), 2.

Smyth, M. R., & Vos, J. G. (1992). *Analytical Voltammetry* (Vol. 27): Elsevier.

Sriram, B., Baby, J. N., Hsu, Y.-F., Wang, S.-F., George, M., Veerakumar, P., & Lin, K.-C. (2021). Electrochemical sensor-based barium zirconate on sulphur-doped graphitic carbon nitride for the simultaneous determination of nitrofurantoin (antibacterial agent) and nilutamide (anticancer drug). *Journal of Electroanalytical Chemistry, 901*, 115782.

Stradiotto, N. R., Yamanaka, H., & Zanoni, M. V. B. (2003). Electrochemical sensors: a powerful tool in analytical chemistry. *Journal of the Brazilian Chemical Society, 14*(2), 159-173.

Subhan, M. A., Saha, P. C., Ahmed, J., Asiri, A. M., Al-Mamun, M., & Rahman, M. M. (2020). Development of an ultra-sensitive para-nitrophenol sensor using tri-metallic oxide MoO 2· Fe 3 O 4· CuO nanocomposites. *Materials Advances, 1*(8), 2831-2839.

Sundaresan, P., Yamuna, A., & Chen, S.-M. (2020a). Sonochemical synthesis of samarium tungstate nanoparticles for the electrochemical detection of nilutamide. *Ultrasonics Sonochemistry, 67*, 105146.

Surya, S. G., Khatoon, S., Lahcen, A. A., Nguyen, A. T., Dzantiev, B. B., Tarannum, N., & Salama, K. N. (2020). A chitosan gold nanoparticles molecularly imprinted polymer based ciprofloxacin sensor. *RSC Advances, 10*(22), 12823-12832.

Tajik, S., Beitollahi, H., Shahsavari, S., & Nejad, F. G. (2021). Simultaneous and selective electrochemical sensing of methotrexate and folic acid in biological fluids and pharmaceutical samples using Fe3O4/ppy/Pd nanocomposite modified screen printed graphite electrode. *Chemosphere*, 132736.

Tan, J., Hussain, S., Ge, C., Zhan, M., Liu, J., Liu, S., . . . Qiao, G. (2020). Construction of hierarchical trimetallic organic framework leaf-like nanostructures derived from carbon nanotubes for gas-sensing applications. *Journal of Hazardous Materials, 400*, 123155.

Tasrin, S., Fazil, S. M. M., Senthilmurugan, S., & Selvaraju, N. (2021). Facile preparation of nanocellulose embedded polypyrrole for dye removal: unary and binary process optimization and seed toxicity. *International Journal of Environmental Science and Technology, 18*(2), 365-378.

Temerk, Y., Ibrahim, H., & Farhan, N. (2015). Square wave adsorptive stripping voltammetric determination of anticancer drug nilutamide in biological fluids using cationic surfactant cetyltrimethylammonium bromide. *Analytical Methods, 7*(21), 9137-9144.

Teng, Y., Fan, L., Dai, Y., Zhong, M., Lu, X., & Kan, X. (2015). Electrochemical sensor for paracetamol recognition and detection based on catalytic and imprinted composite film. *Biosensors and Bioelectronics, 71*, 137-142.

Tiwari, P., Janas, D., & Chandra, R. (2021). Self-standing MoS2/CNT and MnO2/CNT one dimensional core shell heterostructures for asymmetric supercapacitor application. *Carbon, 177*, 291-303.

Topçu, E. (2020). Three-dimensional, free-standing, and flexible cobalt-based metal-organic frameworks/graphene composite paper: A novel electrochemical sensor for determination of resorcinol. *Materials Research Bulletin, 121*, 110629.

Tyagi, A., Banerjee, S., Cherusseri, J., & Kar, K. K. (2020). Characteristics of transition metal oxides *Handbook of Nanocomposite Supercapacitor Materials I* (pp. 91-123): Springer.

Umesh, N. M., Jesila, J. A. A., & Wang, S.-F. (2022). Amperometric detection of antibiotic drug ciprofloxacin using cobalt-iron Prussian blue analogs capped on carbon nitride. *Microchimica Acta, 189*(1), 1-10.

Vinayan, B., Jafri, R. I., Nagar, R., Rajalakshmi, N., Sethupathi, K., & Ramaprabhu, S. (2012). Catalytic activity of platinum–cobalt alloy nanoparticles decorated functionalized multiwalled carbon nanotubes for oxygen reduction reaction in PEMFC. *International Journal of Hydrogen Energy, 37*(1), 412-421.

Wan, Q., Wang, X., Yu, F., Wang, X., & Yang, N. (2009). Poly (taurine)/MWNT-modified glassy carbon electrodes for the detection of acetaminophen. *Journal of Applied Electrochemistry, 39*(6), 785-790.

Wang, D., & Astruc, D. (2017). The recent development of efficient Earth-abundant transition-metal nanocatalysts. *Chemical Society Reviews, 46*(3), 816-854.

Wang, J. (1988). *Electroanalytical techniques in clinical chemistry and laboratory medicine*: Vch New York.

Wang, K., Bi, R., Huang, M., Lv, B., Wang, H., Li, C., Zhang, Q. (2020). Porous cobalt metal–organic frameworks as active elements in battery–supercapacitor hybrid devices. *Inorganic Chemistry, 59*(10), 6808-6814.

Wang, S., Li, Z., Duan, F., Hu, B., He, L., Wang, M., Zhang, Z. (2019). Bimetallic cerium/copper organic framework-derived cerium and copper oxides embedded by mesoporous carbon: Label-free aptasensor for ultrasensitive tobramycin detection. *Analytica chimica acta, 1047*, 150-162.

Wang, Y.-H., Huang, K.-J., & Wu, X. (2017). Recent advances in transition-metal dichalcogenides based electrochemical biosensors: A review. *Biosensors and Bioelectronics, 97*, 305-316.

Wang, Y., Shao, Y., Matson, D. W., Li, J., & Lin, Y. (2010). Nitrogen-doped graphene and its application in electrochemical biosensing. *ACS Nano, 4*(4), 1790-1798.

Wang, Y., Zhang, S., Bai, W., & Zheng, J. (2016). Layer-by-layer assembly of copper nanoparticles and manganese dioxide-multiwalled carbon nanotubes film: a new nonenzymatic electrochemical sensor for glucose. *Talanta, 149*, 211-216.

Wang, Z., Tammela, P., Zhang, P., Huo, J., Ericson, F., Strømme, M., & Nyholm, L. (2014). Freestanding nanocellulose-composite fibre reinforced 3D polypyrrole electrodes for energy storage applications. *Nanoscale, 6*(21), 13068-13075.

Wang, Z., Zhao, C., Gui, R., Jin, H., Xia, J., Zhang, F., & Xia, Y. (2016). Synthetic methods and potential applications of transition metal dichalcogenide/graphene nanocomposites. *Coordination Chemistry Reviews, 326*, 86-110.

Wei, D., Liu, Y., Wang, Y., Zhang, H., Huang, L., & Yu, G. (2009). Synthesis of N-doped graphene by chemical vapor deposition and its electrical properties. *Nano Letters, 9*(5), 1752-1758.

Wei, N., Yu, L., Sun, Z., Song, Y., Wang, M., Tian, Z., Zhao, L. (2019). Scalable salt-templated synthesis of nitrogen-doped graphene nanosheets toward printable energy storage. *ACS Nano, 13*(7), 7517-7526.

Weng, Y., Li, J., Ding, X., Wang, B., Dai, S., Zhou, Y., Tian, B. (2020). Functionalized gold and silver bimetallic nanoparticles using deinococcus radiodurans protein extract mediate degradation of toxic dye malachite green. *International Journal of Nanomedicine, 15*, 1823.

Willner, I., & Katz, E. (Eds.). (2006). *Bioelectronics*: *from theory to applications.* John Wiley & Sons.

Winiarski, J. P., Rampanelli, R., Bassani, J. C., Mezalira, D. Z., & Jost, C. L. (2020). Multi-walled carbon nanotubes/nickel hydroxide composite applied as electrochemical sensor for folic acid (vitamin B9) in food samples. *Journal of Food Composition and Analysis, 92*, 103511.

Yadav, A. K., Dhiman, T. K., Lakshmi, G., Berlina, A. N., & Solanki, P. R. (2020). A highly sensitive label-free amperometric biosensor for norfloxacin detection based on chitosan-yttria nanocomposite. *International Journal of Biological Macromolecules, 151*, 566-575.

Yang, L., Zhang, B., Xu, B., Zhao, F., & Zeng, B. (2021). Ionic liquid functionalized 3D graphene-carbon nanotubes–AuPd nanoparticles–molecularly imprinted copolymer based paracetamol electrochemical sensor: Preparation, characterization and application. *Talanta, 224*, 121845.

Yin, M.-j., Gu, B., An, Q.-F., Yang, C., Guan, Y. L., & Yong, K.-T. (2018). Recent development of fiber-optic chemical sensors and biosensors: Mechanisms, materials, micro/nano-fabrications and applications. *Coordination Chemistry Reviews, 376*, 348-392.

Yuan, C., He, Z., Chen, Q., Wang, X., Zhai, C., & Zhu, M. (2021). Selective and efficacious photoelectrochemical detection of ciprofloxacin based on the self-assembly of 2D/2D g-C3N4/Ti3C2 composites. *Applied Surface Science, 539*, 148241.

Zhang, Y., Chen, Y., Wang, T., Zhou, J., & Zhao, Y. (2008). Synthesis and magnetic properties of nanoporous Co3O4 nanoflowers. *Microporous and Mesoporous Materials, 114*(1-3), 257-261.

Zhao, X., Zhao, H., Yan, L., Li, N., Shi, J., & Jiang, C. (2020). Recent developments in detection using noble metal nanoparticles. *Critical Reviews in Analytical Chemistry, 50*(2), 97-110.

Zheng, Y., Wang, Z., Lui, G., Hirt, D., Treluyer, J. M., Benaboud, S., Gana, I. (2019). Simultaneous quantification of levofloxacin, pefloxacin, ciprofloxacin and moxifloxacin in microvolumes of human plasma using high-performance liquid chromatography with ultraviolet detection. *Biomedical Chromatography, 33*(5), e4506.

Zhou, C., Liu, Z., Dong, Y., & Li, D. (2009). Electrochemical Behavior of o-Nitrophenol at Hexagonal Mesoporous Silica Modified Carbon Paste Electrodes. *Electroanalysis: An International Journal Devoted to Fundamental and Practical Aspects of Electroanalysis, 21*(7), 853-858.

Zhou, X., Dai, H., Huang, X., Ren, Y., Wang, Q., Wang, W., Dong, X. (2020). Porous trimetallic fluoride Ni–Co–M (M= Mn, Fe, Cu, Zn) nanoprisms as electrodes for asymmetric supercapacitors. *Materials Today Energy, 17*, 100429.

Zhu, P., Ou, H., Kuang, Y., Hao, L., Diao, J., & Chen, G. (2020). Cellulose nanofiber/carbon nanotube dual network-enabled humidity sensor with high sensitivity and durability. *ACS Applied Materials & Interfaces, 12*(29), 33229-33238.

Zhu, Y., Huang, C., Li, C., Fan, M., Shu, K., & Chen, H. C. (2019). Strong synergetic electrochemistry between transition metals of α phase Ni− Co− Mn hydroxide contributed superior performance for hybrid supercapacitors. *Journal of Power Sources, 412*, 559-567.

Zhu, Y., Liao, X., Qiu, H., An, S., Zhang, Y., & He, W. (2020). Mixed metals oxides with strong synergetic electrochemistry as battery-type electrodes for ultrafast energy storage. *Journal of Alloys and Compounds, 848*, 156395.

Znaleziona, J., Maier, V., Petr, J., Chrastina, J., & Ševčík, J. (2011). MEKC determination of nilutamide in human serum using sweeping in high salt sample matrix. *Chromatographia, 74*(1-2), 151.

Zong, J., Cheng, J., Fu, Y., Song, J., Pan, W., Yang, L., . . . Zhou, M. (2020). Serum metabolomic profiling reveals the amelioration effect of methotrexate on imiquimod-induced psoriasis in mouse. *Frontiers in Pharmacology*, 1783.

LIST OF PUBLICATIONS AND PAPERS PRESENTED

List of Publications

1. **Akhter, S.**, Zain, N. K. M., Shalauddin, M., Singh, V. K., Misnon, I. I., Sharma, R. K., . . . Jose, R. (2021). Tri-metallic Co-Ni-Cu based metal organic framework nanostructures for the detection of an anticancer drug nilutamide. *Sensors and Actuators A: Physical, 325*, 112711.

2. **Akhter, S.**, Basirun, W. J., Shalauddin, M., Johan, M. R., Bagheri, S., Akbarzadeh, O., & Anuar, N. S. (2020). Hybrid nanocomposite of functionalized multiwall carbon nanotube, nitrogen doped graphene and chitosan with electrodeposited copper for the detection of anticancer drug nilutamide in tablet and biological samples. *Materials Chemistry and Physics, 253*, 123393.

3. **Akhter, S.**, Basirun, W. J., Alias, Y., Johan, M. R., Bagheri, S., Shalauddin, M., . . . Anuar, N. S. (2018). Enhanced amperometric detection of paracetamol by immobilized cobalt ion on functionalized MWCNTs-Chitosan thin film. *Analytical Biochemistry, 551*, 29-36.

4. Anuar, N. S., Basirun, W. J., Shalauddin, M., & **Akhter, S**. (2020). A dopamine electrochemical sensor based on a platinum–silver graphene nanocomposite modified electrode. *RSC Advances, 10*(29), 17336-17344.

5. Akbarzadeh, O., Mohd Zabidi, N.A., Shalauddin, Md., Abdul Wahab, Y., Hamizi, N.A., **Akhter, S.**, (2019). Effects of cobalt loading, particle size, and calcination condition on Co/CNT catalyst performance in Fischer-Tropsch reaction. *Symmetry 11*(1), 7-11.

6. Shalauddin, M., **Akhter, S**., Basirun, W. J., Bagheri, S., Anuar, N. S., & Johan, M. R. (2019). Hybrid nanocellulose/f-MWCNTs nanocomposite for the electrochemical sensing of diclofenac sodium in pharmaceutical drugs and biological fluids. *Electrochimica Acta, 304*, 323-333.

7. Akbarzadeh, O., Mohd Zabidi, N.A., Shalauddin, Md., Hamizi, N.A., Abdul Wahab Y., **Akhter, S.**, (2019). Effect of pH, Acid and Thermal Treatment Conditions on Co/CNT catalyst performance in Fischer-Tropsch Reaction. *Symmetry 11*(1) 50-54.

8. Shalauddin, M., **Akhter, S.,** Bagheri, S., Abd Karim, M. S., Kadri, N. A., & Basirun, W. J. (2017). Immobilized copper ions on MWCNTS-Chitosan thin film: Enhanced amperometric sensor for electrochemical determination of diclofenac sodium in aqueous solution. *International Journal of Hydrogen Energy, 42*(31), 19951-19960.